
01 Sep 1971

The analysis and behavior of thin-steel hyperbolic paraboloid shells

Peter Gergely

P. V. Banavalkar

J. E. Parker

Follow this and additional works at: <https://scholarsmine.mst.edu/ccfss-library>



Part of the [Structural Engineering Commons](#)

Recommended Citation

Gergely, Peter; Banavalkar, P. V.; and Parker, J. E., "The analysis and behavior of thin-steel hyperbolic paraboloid shells" (1971). *Center for Cold-Formed Steel Structures Library*. 19.
<https://scholarsmine.mst.edu/ccfss-library/19>

This Technical Report is brought to you for free and open access by Scholars' Mine. It has been accepted for inclusion in Center for Cold-Formed Steel Structures Library by an authorized administrator of Scholars' Mine. This work is protected by U. S. Copyright Law. Unauthorized use including reproduction for redistribution requires the permission of the copyright holder. For more information, please contact scholarsmine@mst.edu.

Department of Structural Engineering
School of Civil and Environmental Engineering
Cornell University

Report No. 338

THE ANALYSIS AND BEHAVIOR OF THIN-STEEL
HYPERBOLIC PARABOLOID SHELLS

by

Peter Gergely
P. V. Banavalkar
and
J. E. Parker

A Research Project Sponsored by the
American Iron and Steel Institute

Ithaca, New York

September 1971

INDEX

	<u>Page</u>
ABSTRACT	i
NOMENCLATURE	1
I. INTRODUCTION	7
1. HYPAR ROOFS	7
2. LITERATURE REVIEW	9
3. SCOPE AND OBJECTIVES OF THE PRESENT INVESTIGATION	16
4. ACKNOWLEDGMENTS	17a
II. DECK PROPERTIES	18
1. INTRODUCTION	18
2. ELASTIC PROPERTIES OF DECK	19
A. MEMBRANE PROPERTIES	20
B. BENDING PROPERTIES	22
C. ELASTIC PROPERTIES FOR ARBITRARILY ORIENTED CO-ORDINATE AXES	24
3. SHEAR RIGIDITY OF ORTHOTROPIC DECKS	25
4. DETERMINATION OF THE EFFECTIVE SHEAR RIGIDITY FOR ORTHOTROPIC HYPARS	28
III. FINITE ELEMENT METHOD FOR STIFFNESS AND STRESS ANALYSIS	31
1. INTRODUCTION	31
2. ELEMENT STIFFNESS	33
A. DISPLACEMENT FUNCTIONS	33
B. CURVED ELEMENT (METHOD "a")	36
C. FLAT ELEMENT (METHOD "b")	40
D. EDGE MEMBER	43
E. ECCENTRICALLY CONNECTED NON- COMPATIBLE SUPPORTING EDGE MEMBER	45
F. ELASTIC SPRINGS	47

	<u>Page</u>
3. MASTER STIFFNESS MATRIX	47
4. LOADING	53
5. BOUNDARY CONDITIONS	54
6. SOLUTIONS OF EQUATIONS	56
7. STRESS ANALYSIS	57
A. DECK STRESSES	58
B. BEAM STRESSES	59
IV. GENERAL COMPARATIVE STUDY	61
1. INTRODUCTION	61
2. COMPARISON OF METHOD 'a' WITH OTHER NUMERICAL SOLUTIONS	62
3. COMPARISON OF METHOD 'a' AND METHOD 'b'	63
4. DISCUSSION OF METHOD 'a'	67
5. COMPARISON OF ANALYTICAL AND EXPERIMENTAL WORK	71
A. EDGE-SUPPORTED HYPARS	72
B. CONCRETE UMBRELLA SHELLS	75
C. UMBRELLA SHELLS WITH STANDARD CORRUGATED DECKS	79
1. INVERTED UMBRELLA SHELL WITH FLEXIBLE EDGE MEMBERS	81
2. INVERTED UMBRELLA SHELL WITH STIFF EDGE MEMBERS	86
6. SUMMARY	91
V. QUALITATIVE EFFECTS OF PRINCIPAL VARIABLES ON BEHAVIOR OF HYPARS	92
1. INTRODUCTION	92
2. GEOMETRICAL SHAPE	92
3. DECK PROPERTIES	94
A. SHEAR RIGIDITY	94

	<u>Page</u>
B. THICKNESS OF THE CORRUGATED DECK	95
C. NUMBER OF DECKS	96
4. BOUNDARY CONDITIONS	97
A. EDGE MEMBER PROPERTIES	98
B. EDGE MEMBER AND DECK CONNECTION	99
5. LOADING	100
A. EDGE MEMBER WEIGHT	100
VI. INSTABILITY ANALYSIS OF HYPARS	104
1. INTRODUCTION	104
2. INCREMENTAL MATRIX FOR DECK AND EDGE MEMBERS	107
3. CHECKING OF THE INCREMENTAL MATRICES	108
4. INSTABILITY OF HYPARS	111
5. DETERMINATION OF THE BUCKLING LOAD	112
6. NUMERICAL RESULTS AND THEIR DISCUSSION	114
7. DECK BUCKLING BY THE ENERGY METHOD	120
8. STABILITY OF ISOLATED EDGE MEMBERS	123
VII. EXPERIMENTAL INVESTIGATION	126
1. INTRODUCTION	126
2. FLAT SHEAR TESTS	127
3. SADDLE-SHAPED HYPAR TESTS	131
4. MEDIUM-SCALE INVERTED UMBRELLAS WITH VERY STIFF EDGE BEAMS	134
5. INVERTED UMBRELLAS WITH VERY FLEXIBLE EDGE BEAMS	135
6. DISCUSSION OF EXPERIMENTAL RESULTS	137
VIII. SUMMARY, CONCLUSIONS AND RECOMMENDATIONS	145
BIBLIOGRAPHY	152
APPENDIX A. DECK PROPERTIES	158

	<u>Page</u>
APPENDIX B. STIFFNESS MATRICES	166
APPENDIX C. DECK STRESSES	172
APPENDIX D. INCREMENTAL MATRIX FOR DECK	175
APPENDIX E. STIFFNESS AND INCREMENTAL MATRICES FOR A FULLY COMPATIBLE ECCENTRIC STIFFENER	179

ABSTRACT

An extensive experimental and analytical investigation of thin-steel hyperbolic paraboloid (hypar) structures was carried out to provide design information. As a result of this work, empirical data is provided regarding the behavior of such structures and computer programs are presented for the analysis of thin steel hypar structures.

Hyperbolic paraboloid structures possess a unique combination of structural and architectural properties; some of them are the following: 1) Due to the double curvature of the surface the internal stresses in the deck are generally low and the deflections are small. 2) Since a hypar surface can be generated by straight lines, thin-steel or light-gage panels may be used to form the shell; furthermore such panels are well suited to carry the in-plane shear forces in hypar shells. 3) Basic hypar units can be combined in a large variety of ways to produce attractive roofs (Fig. 1-2, page 212). 4) The dead load to live load ratio is very low in the case of thin-steel shell structures.

A hypar unit is a warped surface bounded by straight lines (Fig. 1-1, page 211). The equation of the surface is $z = Cxy/AB$. According to the simple membrane theory, a uniform load p produces pure shear forces $N_{xy} = ABp/2C$. This membrane shear transmits uniform eccentric axial forces to the edge members.

The following are the major problems associated with the design of thin-steel hypar structures: 1) The deflections,

stresses, and the stability of hypars depends greatly on the shear rigidity of the thin-steel deck. This property must be evaluated experimentally for each combination of decking, connections to edge members, and seam connections. Furthermore, in the case of hypars the deck is warped and thus the shear rigidity may be different from that of an equivalent flat diaphragm. 2) The deck may buckle due to the shear stresses, and the buckling load must be evaluated for highly orthotropic shells. 3) The design of thin-steel hypar structures is generally governed by stiffness (deflections or buckling) requirements. The evaluation of the deflections is a very complex matter because it depends on the deck rigidity, the edge member axial and bending stiffnesses, and on the eccentricity of the deck-to-edge member connection. 4) If the curvature (or rise-to-span ratio) of a hypar is small, the deflections may be large and a considerable portion of the load is carried by bending rather than by membrane shear. 5) Partial or concentrated loads may cause large local deflections, especially if single-layer decks are used.

The present investigation studied all the above-mentioned factors. The experimental and the analytical studies are summarized briefly in the following paragraphs.

The experimental investigation consisted of four types of tests: a) Four medium-scale (12 ft by 12 ft in plan) inverted umbrella tests to study the stresses, deflections, and the deck buckling; b) Test on a small-scale (2 ft by 2 ft) inverted umbrella structure to study scaling effects and the overall

buckling of hypars; c) Sixteen flat shear tests to determine the shear rigidity of the decks used in the hypar tests; d) Twelve saddle-shaped hypar tests (5 ft by 5 ft in plan) with various rise-to-span ratios to evaluate the effect of rise or warping on the shear rigidity and to study other factors such as partial loading and single versus double layered decks. Photos of the various types of tests are shown in Figs. 7.1 to 7.5. The experimental program is described in detail in Chapter VII.

Prior to the main test program, several small-scale (2 ft by 2 ft) four-quadrant tests and medium-scale single-quadrant tests were also conducted. These tests were however discontinued because of the severe scaling effects in the case of the small-scale models and the violation of the symmetry conditions in the case of single-quadrant experiments where the neighboring quadrants were missing. Nevertheless, these tests produced useful qualitative information and experience with manufacturing and testing thin-steel hypar structures.

The edge members of the umbrella-type specimens were made of tubular members since this afforded easy connection of the warped surface to the straight edges. The decking consisted of single or double layers of standard corrugated panels. One layer was connected to the edge members with sheet metal screws at various spacings. The seam connections between the panels were also made by means of sheet metal screws. In the case of shells with two layers, the top layer was connected to the bottom layer in a similar manner.

The medium-scale umbrella models were loaded using air bags under each of the four quadrants. The saddle-shaped hypars were loaded with sand, whereas the small-scale models were loaded through loading pads and suspended weights.

The following are the principal conclusions of the experimental part of this investigation:

The effective shear stiffness of the cold-formed deck and the rise (or curvature) of the structure are the most important factors influencing the behavior of hypars. For low shear stiffnesses and for small rise-to-span ratios the deflections may be large, the bending stresses tend to increase relative to the membrane stresses, and the possibility of deck buckling increases. As in the case of flat shear diaphragms, the shear stiffness depends strongly on the seam and edge connections.

The increase in shear stiffness due to the addition of a second layer of deck was found to be only about $1/3$ if the second layer was connected only to the first layer and not directly to the edge members. Similarly, the deflections of a double-layered shell are more than half of those of a corresponding single shell. If the two layers are interconnected with sheet metal screws (on an 8 in. grid in the present saddle-shaped hypar tests), the deflections are further reduced by about 10 to 20%, depending on the rise ratio.

A particular problem of certain types of hypar structures is the deflection of unsupported outside corners (see Fig. 1-2, page 212). The membrane shear cannot carry the load over such flat corners and thus considerable bending and deflections may develop. The tests showed that the bending stiffness of the

edge members has a great effect on the corner deflections, in fact, they indicate that the design of the edge members in hypars with flat corners is usually governed by deflection limitations.

The measured bending strains in flat saddle shells (rise-to-span ratio of 1.8) was much greater than the bending in hypars with greater curvature (rise ratio of 1/3). The membrane theory is insufficient for the design of flat hypar structures. However, the design of the connections (seam or edge) may be based on the shear forces obtained from the simple membrane theory.

Several single and double layered saddle-shaped models were tested under partial loading. Since such loads must be carried mainly by bending of beam strips along the deformations of single decks, relatively large deflections were noted. The deflections under the 8 in. by 8 in. loaded area were about three times greater in the single decks than on the double-layered structures.

Since the effective shear rigidity of the deck is of paramount importance, the effect of curvature (warping) on it is an important question. The effective shear rigidity of various deck, edge member, and connection configurations are determined by tests on flat diaphragms. The comparison of the measured deflections for saddle hypars with various rise-span ratios and the evaluation of the effective shear rigidities backwards from the measured deflections indicated that the shear rigidity is reduced by about 20% due to the warping effect.

The buckling of the deck is one of the design factors. For small rise-span ratios and for low deck shear rigidities the deck may buckle. As an example, a 12 ft by 12 ft model

having a single layer 24 gage corrugated sheet deck buckled at a uniform load of 70 psf (see Fig. 6.14). This model had relatively stiff edge members (3 in. dia. tubular sections). The corner deflections remained linear with increasing load beyond the buckling load.

The buckling load of double-layered structures is much larger than that for single deck shells. A model, similar to the above but with two layers of 28 gage standard corrugated decks, did not buckle up to a load of 145 psf, when the test was discontinued.

The major part of the analytical investigation consisted of two finite element approaches for the calculation of deflections, stresses, and instability. In addition, two simple methods were developed for estimating the deck buckling load and the buckling of the compression edge members, which would suffice in preliminary designs.

Two types of finite elements were used: curved shallow shell elements and flat elements. The details of the analysis are described in Chapter III. Both approaches were verified by comparisons with existing experimental and analytical results.

The stiffness of the eccentric edge members were properly accounted for in the mathematical representation of the structure. The connection of the decks to the edge members may allow rotation about the axis of the edge members and movement normal to the edges due to slip at the connections. These possibilities were also considered in the analysis.

The instability of the decks was studied with the help of the incremental stiffness matrix approach. The effective stiff-

ness of the system is reduced due to the in-plane forces in the deck. The in-plane forces depend on the deflections of the shell and to obtain the buckling load, the eigenvalues of a large order system need to be evaluated. In the present study the load incrementation method was used instead. The effect of the in-plane forces was evaluated iteratively at successive load increments. The buckling load is obtained from the nonlinear load-deflection curve, (Fig. 6-6, Page 276).

The comparison of the results of the flat element and the curved element approaches reveals that both give good results for shells supported around the perimeter. However, the flat element method gave better results in the neighborhood of unsupported flat corners.

The analysis of the structures tested in this and in other studies confirmed the conclusions of the experimental part of the investigation. The stresses in most types of hypars are low and the design is usually controlled by deflection or buckling limitations.

The relative stiffness of the deck and the edge members is an important factor. For stiff edge members the deck tends to bend between opposite edges, whereas in the case of flexible cantilevered edge members the shell partially supports the edge members. Analysis of a structure including the weight of the edge members indicated that this effect may have to be considered in the design of hypar structures.

The analysis of buckling of hypar decks showed that the buckling load of double-layered shells is three to four times

greater than that of single decks. The predicted buckling loads compared well with experimental or previous analytical evidence. The buckling load does not depend much on pre-buckling deflections, however it depends on the axial stiffness of the edge members.

The finite element analysis was also used to calculate the deflection of an unsymmetrically loaded inverted umbrella structure. The results, which compared well with experimental data, showed that these deflections are about four times greater than those due to symmetric loading. This increase of deflections obviously depends on the type of structure; in this case much of the flexibility was due to the bending of the central column of the umbrella structure.

Since the instability analysis of hypars by the finite element method involves considerable amount of computer capacity and expense, approximate methods were developed for the calculation of buckling loads. The buckling of the compression edge members was studied by isolating them from the structure. The instability of columns loaded by tangential axial forces that remain parallel to the member during deflection was evaluated. The results are tabulated in Fig. 6-13, page 284.

The buckling of hypar decks was also investigated by the energy method (Section VI-7. The resulting equation has to be minimized to get the critical load; this can easily be done with the help of a computer. This approach is much simpler than the finite element instability analysis and is preferable in preliminary designs.

A few buckling analyses of cold-formed hypar shells showed that the critical load for double-layers is about three to four times greater than a shell with a single deck.

The finite element analysis computer program will be made available to designers by the American Iron and Steel Institute.

GLOSSARY OF TERMS

A	Length of hypar quadrant in x-direction, inch.
A_b	Cross-sectional area of the beam, inch^2 .
A_x	Area of deck along x-direction, inch^2 .
A_y	Area of deck along y-direction, inch^2 .
A_c	Area enclosed by the cellular portion, inch^2 .
A_i, B_i, C_i	Dimensions of the i-th quadrant.
a	Length of the element in x-direction, inch.
B	length of hypar quadrant in y-direction, inch.
b	Length of the element in y-direction, inch.
C	Rise of hypar quadrant, inch.
D	Bending rigidity of an isotropic deck, $\text{lb-inch}^2/\text{inch}$.
D_1	Rigidity due to Poisson's effect, $\text{lb-inch}^2/\text{inch}$.
D_x	Bending rigidity of the deck in x-direction, $\text{lb-inch}^2/\text{inch}$.
D_{xy}, D_{yx}	Torsional rigidities of the deck, $\text{lb-inch}^2/\text{inch}$.
D_y	Bending rigidity of the deck in y-direction, $\text{lb-inch}^2/\text{inch}$.
E	Young's Modulus, lb/inch^2 .
E_x	Modulus of elasticity in x-direction, lb/inch^2 .
E_{xt}	Extensional rigidity of the deck along the x-direction, lb/inch .
E_{xyt}	Inplane shear rigidity of the deck, lb/inch .
E_y	Modulus of elasticity in y-direction, lb/inch^2 .
E_{yt}	Extensional rigidity of the deck along the y-direction, lb/inch .
E_1	Modulus of elasticity due to Poisson's effect, lb/inch^2 .
E_{1t}	Inplane coupling rigidity of the deck accounting for Poisson's effect, lb/inch .

G	Shear modulus, lb/inch ² .
G'	Shear rigidity of deck (=E _{xyt}), lb/in.
G _{eff}	Effective shear modulus, lb/inch ² .
I _{ed}	Effective moment of inertia of a corrugated deck, inch ⁴ /inch.
I _o	Moment of inertia of the deck section, $\frac{t^3}{12}$, inch ⁴ /inch.
I _y	Moment of inertia of a beam about the y-axis, inch ⁴ .
I _{yd}	Moment of inertia of a repetitive deck unit about the x-axis, inch ⁴ /inch.
I' _y	Moment of inertia of a repetitive deck unit about the line of connection parallel to the x-axis, inch ⁴ /inch.
I _z	Moment of inertia of a beam about the z-axis, inch ⁴ .
J	St. Venant torsional constant, inch ⁴ .
K _x	Bending curvature in x-direction, inch ⁻¹ .
K _{xy}	Twisting curvature, inch ⁻¹ .
K _y	Bending curvature in y-direction, inch ⁻¹ .
[k]	Stiffness matrix.
[k] _{bb}	Element stiffness matrix for plate bending.
[k] _{bbm}	Element stiffness matrix for w-displacement.
[k] _{bm}	Flexural and membrane coupling element stiffness matrix.
[k] _{curved}	Element stiffness matrix for the curved element.
[k] _{eb}	Effective stiffness matrix of the supporting edge member with respect to the eccentric axes.
[k] _{eff}	Effective stiffness of the deck after inclusion of the instability effects.
[k] _{eℓ}	Stiffness matrix of the plate element in the global co-ordinate.
[k] _{flat}	Element stiffness matrix for the flat element.

k_{ij}	Element of the stiffness matrix in the i-th row and the j-th column.
$[k]_m$	Element membrane stiffness matrix.
ℓ	Length of a basic repetitive unit of the deck, inch.
ℓ_x, ℓ_y, ℓ_z	Direction cosines of the local element axes.
M_x	Moment about y-axis, inch-lb/inch.
M_{xy}	Twisting moment about x and y axis, inch-lb/inch.
M_y	Moment about x-axis, inch-lb/inch.
m_x, m_y, m_z	Direction cosines of the local element axes.
$[N]$	Incremental matrix.
$[N]_e$	Incremental stiffness for the flexural displacements (w).
$[N]_{\text{global}}$	Incremental matrix for deck in the global coordinate system.
N_{ij}	Element of the incremental matrix in the i-th row and j-th column.
N_x	Force per unit length along the x-direction, lb/inch.
N_{xy}	Shear force, lb/inch.
N_y	Force per unit length along the y-direction, lb/inch.
n_x, n_y, n_z	Direction cosines of the local element axes.
ox', oy'	Generators of the hyper surface
$ox\bar{,} oy\bar{,} oz\bar{}$	Local orthogonal element axes.
oz'	Normal to the hyper surface at point o.
$[P]$	Load vector.
q_o	Uniformly distributed load, lb/inch ² .
R_{red}	Reduction factor for the torsional rigidity of a cellular deck.
S	Developed length of a basic repetitive unit of the deck, inch.

S_i	Stiffness of the i-th spring.
$[T]$	Component transformation matrices for the plate element.
T_F	Coefficient for torsional fixity between the deck and the edge member.
T_H	The coefficient for inplane fixity between the deck and the edge member.
$[T]_R$	Rotational transformation matrix for the beam element.
$[T]_S$	Translational transformation matrix for a beam element.
t	Thickness of the deck, inch.
t_1	Thickness of the base plate in a cellular deck, inch.
t_2	Thickness of the hat section in a cellular deck, inch.
U	Strain energy, inch-lb.
U_b	Strain energy due to bending of deck, inch-lb.
U_{bb}	Strain energy of a beam, inch-lb.
U_c	Average axial displacement of a beam section measured at its centroid, inch.
U_m	Strain energy due to the membrane action of the deck, inch-lb.
U_{warp}	Strain energy due to the warping of the deck, inch-lb.
u	Displacement along x-axis, inch.
u_i, v_i, w_i	Displacements of the i-th node.
V	Potential energy of the applied loads, inch-lb.
V_N	Potential energy of the in-plane forces, inch-lb.
V_s	Displacement of the shear center measured along y-axis, inch.
v	Displacement along y-axis, inch.
W_s	Displacement of the shear center measured along Z-axis, inch.

w_x, w_y	Differentiation of w-displacement with respect to x and y.
w	Displacement along z-axis, inch.
\bar{x}_i	x-coordinate of the local origin of a hyper quadrant with respect to the global coordinate system.
x_o, y_o, z_o	Cartesian coordinates of the center point o of an element.
x, y, z	Orthogonal cartesian global coordinates.
x', y', z'	Orthogonal axes other than the global cartesian axes.
Y_c	Eccentricity of the centroid of the cross-section of the beam in the y-direction from the shell surface, inch.
Y_s	Eccentricity of the shear center of the cross section of the beam in the y-direction from the shell surface, inch.
\bar{y}_i	y-coordinate of the local origin of a hyper quadrant with respect to the global coordinate system.
Z_c	Eccentricity of the centroid of the cross-section of the beam in the z-direction from the shell surface, inch.
Z_s	Eccentricity of the shear center of the cross section of the beam in the z-direction from the shell surface, inch.
Z_x, Z_y	Derivatives of the surface $Z(x, y)$ with respect to x and y.
α	Ratio of shear rigidity of a corrugated deck to that of a flat deck with the same thickness.
Γ	Warping constant of the deck, inch ⁶ /inch.
Γ_b	Warping constant of a beam, inch ⁶ .
γ_{xy}	Shearing strain in the x-y plane.
$[\Delta]$	Generalized displacement vector.
Δ_i	Generalized displacement at the i-th node.
δ_a	w-displacement at the point a.

δp	Load increment used in load incrementation method, lb/inch ² .
$\delta \Delta$	Increment in the displacements due to the application of the incremental load δp .
ϵ_x	Strain in x-direction.
$\epsilon_x', \epsilon_y', \gamma_{x'y'}$	Strains measured along x' and y' axes
ϵ_y	Strain in y-direction.
η	Number of interconnected decks.
θ	Twist rotation of a beam, radian.
θ'	Rate of change of twist rotation, radians/inch.
θ_i	Angle of twist of a beam at the i-th end, radian.
θ'_{ix}	Rate of change of angle of twist at the i-th end, radians/inch.
θ_x	Rotation about x-axis, radian.
θ_{xy}	Rate of change of rotation, radians/inch.
θ_y	Rotation about y-axis, radian.
λ	Eigenvalue for the critical buckling load.
ν	Poisson's ratio.
ν_{xy}, ν_{yx}	Poisson's ratios in x and y-directions respectively for the equivalent orthotropic plate.
σ_x	Stress in x-direction, lb/inch ² .
$\sigma_x', \sigma_y', \tau_{x'y'}$	Stresses measured along x' and y' axes.
σ_y	Stress in y-direction, lb/inch ² .
τ_{xy}	Shearing stress, lbs/inch ² .
ϕ	Total potential energy of a system, inch-lb.

CHAPTER I

INTRODUCTION

I.1. HYPAR ROOFS

The hyperbolic paraboloid shell roof, like any other form of shell is one of the types of construction that makes efficient use of materials by depending primarily upon the form or shape for strength rather than on mass. The doubly curved surface of a hypar shell is composed of straight lines in two directions (Fig. 1.1). From the construction point of view, this property is very attractive. It facilitates the use of straight members for formwork and reinforcing steel in the case of concrete hypars. This very feature also allows the use of light gage steel deck panels, which could be easily warped to the required degree to form the hypar surface.

The hypar surface shown in Fig. 1.1, can be generated in two ways¹: (1) The surface can be defined by moving a convex parabola ODC in a direction parallel to itself, over a concave parabola BDA. The parabola ODC lies in the plane perpendicular to that of BDA. (2) The surface can also be defined as a warped parallelogram. The surface can be generated (Fig. 1.1) by moving along y-axis, a straight line that remains parallel to the xz-plane at all times but pivots while sliding along the straight line AC. Physically the surface can be visualized as a warped parallelogram OBCA, obtained by depressing the corner H through a distance CH. By means of

similar triangles (Fig. 1.1), it can be easily shown that the surface equation is,

$$PQ = Z = Kxy \text{ where } K = \frac{CH}{OA \times OB}$$

The surface is called hyperbolic paraboloid because any plane parallel to the xy-plane, intersects it in a hyperbola; whereas a plane perpendicular to ODC intersects it in a parabola.

For simplicity, the structural action of a hypar can be visualized as a net of intersecting arches and cables. The convex parabolas (arches) parallel to ODC carry compressive stresses, whereas the concave parabolas (cables) parallel to ADB carry tensile stresses. This implies that the element I is in a state of biaxial stress, compression parallel to the arches and tension parallel to the cables. On the other hand, the element II is in a state of pure shear. In the interior, the membrane shear is carried by the shell. Along the free edges, stiffening edge members are usually provided to sustain the membrane action. These edge members themselves carry gradually increasing tensile or compressive forces depending upon the geometry of the structure.

By the combination of a basic hypar unit, such as shown in Fig. 1.1, different elegant hypar structures can be built. Four such configurations are shown in Fig. 1.2. The edge members are provided to build up the membrane action and also to stiffen the structure. Tension tie rods are commonly employed to balance the horizontal reactions between the low corners.

Because of its architectural beauty, ease of construction and ability to provide large column-free working space, the hyperbolic paraboloid shell has been used for industrial plants, churches, assembly halls, etc. In Mombasa², the hypar structure was used as a footing on low bearing capacity soil. A 225-foot double cantilever hypar roof is under construction at Los Angeles for the American Airlines jet hangar. The roof uses a cellular form of deck. This structure may very well prove to be the forerunner of many more similar structures.

I.2. LITERATURE REVIEW

Like any other shell, hypars carry load by both membrane and bending actions. The membrane theory, as indicated before, results in a state of pure shear. The limitations of this theory were realized by the most investigators and the necessity of probing into the bending behavior of the shells became apparent.

The shallow shell theory of Marguerre³ and Vlassov⁴ is often used to analyze the bending action. Though this theory is approximate, it is considered fairly accurate for a shell surface where the slopes of the tangents are very small compared to unity. Two basic approaches were used to formulate the shallow shell theory.

In the first approach, two fourth-order coupled partial differential equations in terms of normal displacement w and Airy-stress function F are formed. Reissner⁵ using this approach, determined the buckling load of a uniformly loaded

isotropic hyper with moment-free rigid edges, with the edge members of infinite axial rigidity but negligible bending rigidity in planes tangential to the shell. Apeland and Popov⁶ reduced these two equations to a single eight-order differential equation. Using Levy-type boundary conditions (with two opposite edges knife edge supported) they tried to establish the effect of edge disturbances in the same way as that for cylindrical shells. Their important conclusion was that the effect of the edge moment does not die off very rapidly in the case of hyper shells.

The formulation in terms of middle-surface displacement $u-v-w$, results in three coupled partial differential equations, two second-order ($u-v$) and one fourth-order (w). Salvadori and Bleich⁷ using Vlassov's shallow shell equations followed this approach. Assuming $u=v=0$ all over the middle surface, the fourth-order differential equation reduced to that of a plate on an elastic foundation.

However, it must be emphasized that in order to obtain the solutions to these mathematically complicated equations, simplifying assumptions were made. The choice of boundary conditions was dictated by the possibility of obtaining solutions rather than simulating the exact boundary conditions in a physical model.

The shortcomings of the classical solutions resulted in the realization of the importance of numerical approaches for the solution of these differential equations.

Chetty and Tottenham⁸ applied a variational method

for the analysis of shallow shell equations (W-F). However, the choice of approximating functions limited its applicability to the specific boundary conditions. Besides, non-classical boundary conditions presented serious difficulties.

The numerical scheme of finite difference provided a very useful tool in the solution of these equations. Das Gupta⁹, Mirza¹⁰, Russell and Gerstle^{11,12} using the W-F approach applied this method to different hyper structures using meaningful boundary conditions. The edge members were also incorporated in their analysis. Everybody used the classical beam theory. Mirza solved an umbrella shell. However, the magnitude of the corner deflections obtained for an umbrella shell and the boundary conditions used along the line of symmetry, raise serious doubts about the validity of the method¹³. Russell and Gerstle¹² mainly analyzed two-corner and four-corner supported hypars. Non-dimensionalized design parameters were provided. The main contribution of their work was to show the importance of the line-load along the edge members. Croll and Scrivener^{14,15} used the u-v-w formulation. The effect of the eccentric connection of the beam to the shell is discussed. One of the important features of their work is a complete discussion of the convergence characteristic of the solution with relation to the relative proportions of the shell and the edge member stiffnesses. A comprehensive review of the above mentioned method is presented by Brebbia¹⁶.

The finite element method, which is nothing else but the matrix formulation of Rayleigh-Ritz method of variational

principle, was successfully employed by several workers. The ease with which this method can handle realistic boundary conditions, made this method very suitable for hypars. It is also believed that the variational principle used in the finite element method will yield better results than the finite difference method because it involves integration rather than differentiation as used in the latter method.

Connor and Brebbia¹⁷ using shallow shell approximation, formulated the stiffness matrix for a thin shell curved element, rectangular in plan. Similar formulations were worked out by Deak¹⁸ and Parker¹⁹. Pecknold and Schnobrich^{20,21} working along the same lines, extended the work to the skewed shallow shells. All these workers used linear displacement field for u , v displacements. The major difference was the displacement field they used for the normal displacement w .

Deak¹⁸ and Pecknold²⁰ both used the Birkhoff-Garabedian interpolation formula. Connor¹⁷ used a twelve-term polynomial whereas Parker¹⁹ used the Lagrange interpolation formula. Parker extended the work to orthotropic light gage steel hypars and compared the results with the experiments. None of the Refs. 17, 18, 20, 21 mentioned any correlation with experimental results but were content with the comparison to solutions obtained by other numerical methods.

The buckling and nonlinear analysis of hypars are also reported in the literature. Ralston²² continued Reissner's⁵ work by investigating the buckling of a hypar under its own weight. Dayaratnam and Gerstle²³ presented a

solution to the buckling problem of hypars with edge beams, simply supported at their corners. The in-plane displacements u and v were assumed equal to zero. A double sine series deflected shape was assumed and the total potential energy of the system was minimized using Ritz procedure. The critical load was determined by equating the determinant of the resulting matrix to zero. It was concluded that for all positive values of the ratio of bending rigidity of the edge member to the deck, the deck buckling always preceded the edge member buckling. The study in Ref. 19, indicates that for a very flexible edge member, the possibility of overall buckling prior to the deck buckling does exist. The erroneous conclusion of Ref. 23 was reached because of two reasons:

(i) A non-compatible displacement field between the shell and the edge beams.

(ii) In determining the eigenvalue the off diagonal terms were neglected.

These points are discussed at length in Ref. 19. Muskat²⁴ studied the buckling of hypars with corrugated orthotropic deck. A method for determining the buckling load of the deck, considering pre-critical deflections of the entire structure was developed, using the energy approach.

Brebbia and Connor²⁵ presented a consistent finite-element displacement formulation applicable to the shallow shell elements using the Newton-Raphson iteration scheme, by linearizing the incremental equation. The load deflection curve for fixed hypar was presented.

A large number of experimental studies have been reported for hypar shells. A major portion of the experiments were carried out to measure deflections and stresses on small to medium scale models. The results were correlated with the approximate theories and by changing the design parameters, certain predictions on the overall behavior of the hypar shells were made. Rowe and Mirza²⁶ tested plastic models with two adjacent edges fixed and the other two free. The effect of rise to span ratio was studied on the free corner deflections and axial strains. By changing the depth of edge beams along the free edges, it was concluded that by increasing the depth of the edge beam both the axial strains and the vertical deflections are decreased in the shell portion. Rowe²⁷ also tested medium to small scale concrete models and used unsymmetrical loading. In order to study the ultimate load carrying capacity of the umbrella shell hypars, an experimental research program is underway at the Cornell University, where small scale concrete umbrella shells are being tested to failure⁶⁵.

Muskat²⁴ and Leet²⁸ tested small scale models to determine the buckling characteristics. Leet tested plastic models subjected to uniform normal load. The effect of imperfection was studied on the fixed shells. Edge beams were used to study the effects of different edge conditions on stresses, deflections, shell buckling and overall buckling. The effect of different boundary conditions was not very pronounced on the shell buckling. By studying the effect of different beam

sizes Leet concluded that the cross-sectional areas of the edge beams have a significant effect on the deck buckling.

Most of the experiments were conducted with medium scale models. Ref. 19 has listed most of them. Bertaro and Choi²⁹ tested an 8' x 8' model. The model with edge beams and two diagonally opposite corners supported was chemically prestressed by using expansive cement. The model was tested in the inverted position using air pressure loading. Deflection profiles, crack patterns, and stresses were presented.

In the last 8 years or so, the use of light gage steel decks as a hypar shell has gained some momentum. McDermott³⁰ tested two 8' x 8' orthotropic light gage steel, saddle-shaped (Fig. 1.2b) models. In the first case, the steel deck was welded to the edge members whereas in the second case the steel deck was glued. The rubberized canvas bags were pressurized by water in the first case whereas air was used in the second case. He also tested a large-scale model with a single layer standard corrugated deck. The edge members consisted of built-up sections. The loading was applied with sand bags. Strains and deflections were measured.

Yu and Kriz³¹ tested a concrete inverted umbrella shell 24' x 24' in plan, in which upturned edge beams were used. The symmetrical and unsymmetrical loading was simulated by the discrete loads. The measured strains and deflections were presented.

Three large scale tests were conducted for hypars using orthotropic deck as a shell surface:

Nilson³² tested a 15' x 15' hypar quadrant with simulated boundary conditions of the adjacent quadrant. A single layer of cellular deck was connected to the channels, which were used as the edge members, by means of a warped plate. Uniform loading was applied by 25 jacks. The load deflection curve and the measured membrane stresses were reported.

Two large scale hypar models 50' x 30' in plan, were tested recently³³. Two different cellular orthotropic single layer decks were used in each case. 14 WF sections were used as the edge members, which were allowed to move freely in the plane of the hypar but were supported against the vertical movement. The normal uniformly distributed load was applied by creating a vacuum in the enclosed chamber.

1.3 SCOPE AND OBJECTIVES OF THE PRESENT INVESTIGATION

The main purpose of the present investigation was to determine the deflections, stresses, buckling and collapse loads of light gage steel hypar shell roofs and to provide design information. An analytical procedure was developed so that it could be extended to include the analysis of hypars with various support conditions as well as hypars subjected to partial loadings.

The finite element method was selected because of its versatility. The entire project was approached from an engineering point of view. The validity of the method was established by comparing the theoretical and experimental results for different kinds of hypar structures.

Two separate computer programs were written, (1) For

stiffness analysis; (2) For instability analysis.

(1) Stiffness Analysis

A linear elastic analysis of the structure was performed and the deflections, the edge member and deck stresses were computed. The program can handle the following variables:

- (a) Different types of orthotropic decks.
- (b) Different configurations of the hypar structure.
- (c) Realistic physical boundary conditions such as eccentric connections of the edge members and discontinuity between the deck and the supporting edge members.
- (d) Different loading conditions such as uniform, unsymmetrical, line loads, etc.

(2) Instability Analysis

A linear load incrementation method was used for the instability analysis. The effect of the in-plane forces N_x , N_y and N_{xy} was included.

The experimental part of the investigation included the determination of the effective shear rigidities of standard corrugated decks and the determination of deflections, stresses, and buckling loads in inverted umbrellas and saddle-shaped hypars constructed of corrugated steel decking and tubular edge beams.

1.4 ACKNOWLEDGMENTS

This investigation was sponsored by the American Iron and Steel Institute. The financial assistance and the technical guidance provided by the Institute is gratefully acknowledged. We thank the Task Group on Shell Roof Structures, and especially its chairman, Dr. J. B. Scalzi, for their interest in this project.

Special thanks are due to Dr. George Winter, principal investigator of the project, for his great interest in the investigation and for the many wise suggestions throughout the work. His insight into structural behavior often steered the study back from tangents and away from pitfalls.

The nonconservative stability analysis was carried out by Dr. R. Muskat. His and Mr. A. Banerjee's help with the experimental program was very valuable.

CHAPTER II

DECK PROPERTIES

II.1. INTRODUCTION

A material in which resistance to mechanical actions is different in different directions, is called anisotropic. Orthotropy is a special case of anisotropy, where the body possesses elastic properties which are symmetric about three mutually perpendicular planes.

Orthotropy can be further classified into two categories namely, natural and geometric. The natural orthotropy is a result of the material property itself. A classical example of natural orthotropy is timber, where the modulus of elasticity, along the direction of its grain in tension, is substantially higher than the corresponding modulus in the direction perpendicular to it.

In the geometric type of orthotropy, the difference in elastic properties in the perpendicular direction, as shown in Fig. 2.1, is due to the geometrical configuration of the structural element even though it is made up of an isotropic homogeneous material. Different types of decks belonging to this category are shown in Fig. 2.2.

In both the cases, the definition of elastic constants in two mutually perpendicular directions is required. However, geometric orthotropy is of particular interest for the hypar structure dealt with in this work.

In the following analysis the decks, shown in Fig. 2.2, are replaced by equivalent orthotropic plates, having the same physical properties as the decks, such as extensional and bending stiffnesses. It is impossible to achieve a complete equivalence between the actual physical system and the idealized orthotropic plate, in all respects such as strain energy, deflections or moments at different points under different criteria. The properties of the idealized system can be determined either by equivalence of stiffness or equivalence of strain energy between the idealized and the physical system³⁴. The equivalence of stiffness is established by equating only the deformations between the actual and the idealized system. The equivalence of strain energy is obtained by equating the work done by the internal forces in both the systems when subjected to identical loading and boundary conditions.

The elastic constant for the idealized plate material is assumed to be the same as that of the parent material. The properties calculated depend only upon the direction considered and not on the position of the corresponding point on the actual deck. The orthotropic plate theory is applicable to the decks, shown in Fig. 2.2, provided the ratio of the dimensions of the repetitive unit (ℓ) and the overall span of the deck, is very small, i.e., $\ll 1$.

II.2. ELASTIC PROPERTIES OF DECK

In the case of a geometrical orthotropy, as present in corrugated or closed formed decks, in order to calculate elastic properties in two mutually perpendicular directions,

it is necessary to separate the in-plane membrane and the bending action.

A. MEMBRANE PROPERTIES

The principal directions of elasticity in an orthotropic deck are those along which the extensional rigidities are either minimum or maximum. When the axes x and y coincide with its principal direction of elasticity, the equation of generalized Hooke's law for plane stress-strain can be written as

$$\epsilon_x = \frac{\sigma_x}{E_x} - \frac{\nu_{xy}}{E_y} \sigma_y \quad 2-1a$$

$$\epsilon_y = \frac{-\nu_{yx}}{E_x} \sigma_x + \frac{\sigma_y}{E_y} \quad 2-1b$$

$$\gamma_{xy} = \frac{\tau_{xy}}{G_{eff}} \quad 2-1c$$

Solving the equations for the stresses we get,

$$\begin{bmatrix} \sigma_x \\ \sigma_y \\ \tau_{xy} \end{bmatrix} = \frac{1}{(1-\nu_{xy}\nu_{yx})} \begin{bmatrix} E_x & \nu_{xy}E_x & 0 \\ \nu_{yx}E_y & E_y & 0 \\ 0 & 0 & (1-\nu_{xy}\nu_{yx})G_{eff} \end{bmatrix} \begin{bmatrix} \epsilon_x \\ \epsilon_y \\ \gamma_{xy} \end{bmatrix} \quad 2-2$$

The terms ν_{xy} and ν_{yx} represent the coupling effect of the actions (stress or strain) applied in two perpendicular directions. From Fig. 2.2, it is obvious that these coefficients (ν_{xy} and ν_{yx}) cannot be equal. For example, consider the cellular deck shown in Fig. 2-2c, where a uniform stress applied along the bottom plate of the deck in the x-direction will produce a negligibly small strain in the y-direction, in the hat portion. Whereas a uniform stress applied over the entire cross-section along the y-direction will produce a

strain in the bottom plate proportional to the material constant ν , (Poisson's Ratio). Though $\nu_{xy} \neq \nu_{yx}$, by Maxwell-Betti reciprocal theorem the following relationship holds:

$$E_x \nu_{xy} = \nu_{yx} E_y = E_1 \quad 2-3$$

As explained by the physical behavior above, ν_{xy} is equal to ν and hence,

$$\nu_{yx} = \frac{E_x}{E_y} \nu \quad 2-4$$

The value of G_{eff} is given by,

$$G_{\text{eff}} = \alpha G \quad 2-5$$

where α is called the relative shear rigidity factor, the value of which depends upon a number of factors. A complete discussion of α , together with a description of the experimental method of determination of α , is given in Section II-3. The methods for the determination of constants E_x , E_y , ν_{xy} and ν_{yx} , for both closed and open form decks, are given in Appendix A.

Since the decks are idealized as uniform orthotropic plates of constant thickness, it is convenient to express the membrane stiffness constants and the forces in terms of their thicknesses. Multiplying the first row of Eq. 2-2,

$$\sigma_x t = \frac{E_x t}{(1-\nu\nu_{yx})} \epsilon_x + \frac{E_1 t}{(1-\nu\nu_{yx})} \epsilon_y \quad 2-6$$

$$N_x = E_{xt} \epsilon_x + E_{1t} \epsilon_y \quad 2-7$$

where $N_x = \sigma_x t$; $E_{xt} = \frac{E_x t}{(1-\nu\nu_{yx})}$; $E_{1t} = \frac{E_1 t}{(1-\nu\nu_{yx})}$. 2-8

The other rows can be modified similarly (see Eq. 3-13).

Depending upon the method of connections the elastic

constants, calculated above purely on the basis of geometrical configuration, thickness and material properties, need modifications.

The elastic constant E_x for an open deck is given by, (Appendix A)

$$E_x = \frac{I_o E}{I_y'} \quad 2-9$$

The value of I_y' depends upon the line of application of the load. A substantial reduction in the value of E_x results from the eccentric connection. The cellular decks (Fig. 2-2c) are usually connected to the supporting member along the bottom plate leaving the hat portions free. As shown in Fig. 2-3, the forces applied along the bottom plate will be partly resisted by the vertical sides of the hat. Depending upon the joint efficiency between the hat and the bottom plate, the effective area of the hat section in resisting the forces σ_y will vary. In the absence of the test data, it will be conservative to consider the bottom plate only as being effective in resisting the in-plane forces σ_y . In the computer programs, a provision is made to include the effective width of the web plates of the hat.

B. BENDING PROPERTIES

The bending rigidities, D_x , D_y , D_{xy} and D_1 , for a geometrically orthotropic plate cannot be obtained directly from the directional elastic constants given in Eq. 2-2. The relationship between the bending rigidities and the moments, is given in Eq. 3-16. In the case of a light-gage orthotropic deck (corrugated or cellular) $D_y \gg 50.D_x$. This property can

be used to approximate properties such as D_1 and ν_{yx} . Since the twisting rigidity D_{xy} is not equal to D_{yx} (see Appendix A), the average of the directional twisting rigidities is used³⁵.

In the case of an open formed deck there is a tendency for the warping of the surface. The method of calculating the warping constant Γ , based on the assumption that an individual unit³⁵ of a plate twists about its center of rotation is well known³⁶. However, considering the plate as a whole unit, the plane of twisting changes, depending upon the distance of a point from the support. The extent to which this warping restraint alters the behavior of the deck is not very clear.

The moment of inertia used for the computation of D_y is calculated at the centroid of the repetitive section. The effect of eccentric location of the ribs or hats in the case of decks, on the bending properties is discussed in great detail by Massonnet and Barés³⁷. However its use in practical problems is difficult. Due to the local buckled form for high width to thickness ratio for a compression flange³⁹ (Fig. 2.4), the effective moment of inertia for both deflections and stress analysis is reduced. The reduction in the moment of inertia is a function of the stress level. This factor may be of importance in the cellular deck. Depending upon this reduction of the effective section, a second analysis of the hypar shells may be necessary though in most cases the stresses are small. The procedure of calculating I_{ed} is discussed in Refs. 38, 39.

The mechanism of reduction in bending rigidities due to the connection between the different panels is not very clear. Experimental results on the determination of these rigidities for a continuous single panel have been reported⁴⁰. The bending rigidities D_x and D_{xy} are particularly affected by the discontinuities between connections of different panels. Examination of structural problems solved in this study shows that the magnitude of both these constants (D_x and D_{xy}) is so small for an open formed deck that the reduction even of the order of 1/10, does not affect the results significantly (<<5% variation).

The properties for two or more decks placed perpendicularly can be calculated by adding the corresponding directional constants.

C. ELASTIC PROPERTIES FOR ARBITRARILY ORIENTED CO-ORDINATE AXES

When the structural axes and the principal axes of orthotropy coincide, the elastic properties of the deck calculated on the basis of principal axes can be directly used in the analysis without any modifications. As explained in the Section I.1, the structural behavior of a hypar can be broken up into mutually orthogonal arches and cables. When the decks are placed along the axes of arches and cables (Fig. 2.5), the structural axes x and y , do not coincide with the principal axes of orthotropy x' and y' . The elastic constants in terms of the structural axes are expressed by the principle of work equivalence^{41,42}. The membrane strain energy in two systems

of axes can be given by,

$$V = \frac{1}{2} \sigma_x \epsilon_x + \frac{1}{2} \sigma_y \epsilon_y + \frac{1}{2} \tau_{xy} \gamma_{xy} \quad 2-10a$$

$$V' = \frac{1}{2} \sigma_x' \epsilon_x' + \frac{1}{2} \sigma_y' \epsilon_y' + \frac{1}{2} \tau_{x'y'} \gamma_{x'y'} \quad 2-10b$$

Expressing strains in terms of stresses in both the systems of axes and equating,

$$V' = V \quad 2-10c$$

one can obtain the equivalent elastic constants. The equivalent bending constants can be determined by equating the bending strain energy along both axes (Eq. 3-17). The elastic properties for an orthotropic material in terms of any arbitrarily oriented co-ordinate axes are given in detail by Lekhnitskii⁴¹.

II.3. SHEAR RIGIDITY OF ORTHOTROPIC DECKS

The shear stiffness of an orthotropic plate, assuming $N_{xy} = N_{yx}$ (Section III.2 B), is given by the expression

$$E_{xyt} = G' = \alpha G nt \quad 2-11$$

where n is the number of interconnected decks, t is the thickness of each deck and G is the shear modulus of the material. α is the relative shear rigidity coefficient giving the ratio of the shear stiffness of the actual orthotropic deck system and the isotropic plates of thickness nt . In the case of an isotropic plate, the vertical load on a hypar is partly carried by the membrane action in shear and therefore the shear stiffness of the deck is of utmost importance in its structural behavior. Experimental and theoretical determination of α was carried out by several workers. The factor α depends

upon a number of factors listed below:

(a) The different shapes (corrugated sine form, N-type, etc.) of diaphragms (Fig. 2.2), show different resistances to the in-plane shear loads. The shearing loads produce bending and twisting of the corrugations and also set up membrane stresses and shearing strains. On the basis of the assumed displacement field of the corrugations, energy stored due to each of these above mentioned actions (bending, twisting, etc.) is reported in Refs. 43, 44.

(b) The spacing of the connectors, between the deck and the edge members, transverse to the corrugations have a pronounced effect on the value of K , whereas the spacing along the directions of the corrugations has a very minor effect. Flat shear tests on a 26-G. standard corrugated deck, 6' x 6' in plan, were conducted in this investigation (Chapter VII). Two tests were performed with the connectors between the deck and the edge members at each valley and one with the connectors spaced over every third valley. The other factors, in the above tests, being the same, the value of the shear stiffness obtained for the former cases was reported nearly three times as large as that of the latter.

(c) According to Luttrell⁴⁵, the shear stiffness of a panel also depends upon the length along the corrugations. Accordion-like warping results due to the connection of the diaphragm to the edge members. It was found⁴⁵ that the length of penetration of this warping is independent of the overall span of the diaphragm and this warping reduces the shear stiff-

ness, particularly for short spans.

(d) According to Ref. 43, the seam-slip between the adjoining deck panels and the connection of the deck to the edge members contributes substantially to the shear flexibility.

(e) As found in the experiments (Chapter VII), for the limited range of thickness of panels studied, the shear rigidity increases linearly with the effective thickness as given by Eq. 2-11. However, consideration should be given to the connections between two or more decks and their connections to the edge members. The results are reported in Chapter VII. The two layers of corrugated decks placed perpendicular to each other were connected to the edge members through the connection of the lower deck (Fig. 2.6). The additional flexibility provided by the lower deck corrugations, reduces the effectiveness of the upper deck. The position of the screws with respect to the direction of the applied shear also affected the stiffness of the shear panel. It was found that only 33% increase in E_{xyt} was noted for two decks connected as shown in Fig. 2.6, whereas the value of nt doubled.

All the factors mentioned above are important for open form decks as shown in Fig. 2.2a,b. In the case of cellular decks or stiffened panels (Figs. 2.2c,d) the flat plate of the deck is directly connected to the edge members. In view of the low shear carrying capacity of the out-of-plane hats, a major portion of the shear is carried by the flat plate. Knowing the seam-slip characteristics between the adjoining panels, the shear stiffness for the cellular deck can be estimated conser-

vatively as that of the flat plate.

The dependence of the relative shear rigidity coefficient α on some other factor such as connection with the intermediate purlins, etc., is discussed in detail in Ref. 43.

II.4. DETERMINATION OF THE EFFECTIVE SHEAR RIGIDITY FOR ORTHOTROPIC HYPARS

The theoretical determination of shear rigidity coefficient α , was done by equating the work done by the applied shearing force with the strain energy stored in the deck panels due to deformations. In Ref. 43, an excellent correlation between the theoretical and experimental results was reported. Since a major contribution to the shear flexibility was from the connection between the deck panels⁴³ and the connections of decks to the edge members, a previous knowledge of the seam-slip characteristic is required. Based on an experimental investigation, the method for the determination of the shear rigidity from flat shear test is given in Ref. 45.

The next question arises as to whether the relative shear rigidity determined by the flat shear test can be directly used for hypar structures without any modification. To correlate the shear rigidity coefficient α determined by the flat shear tests and that of the warped deck in the actual hypar surface, twelve saddle-shaped hypars, uniformly loaded, with tubular edge members of 3" diameter and $\frac{1}{4}$ " thickness (vertically supported all around) were tested (Chapter VII). The lower corners were connected by $2\frac{1}{2}$ " x $\frac{1}{4}$ " tie bars, in order to restrict the horizontal spreading. The tests were conducted

for both single and double decks with varying rise to span ratios.

It was found that for the lower values of α (<0.12), the center deflection of all-supported hypars was proportional to the value of α . Both single and double deck hypars were tested for three different rise to span ratios (1/8, 1/5, 1/3). The theory developed in Chapter III correctly predicts the effect of α and rise independently on the central deflection δ_0 (Key Sketch, Table II.1, II.2). The value of α in the actual hypar surface was interpolated from the structures analyzed with different assumed α values for the constant rise to span ratio.

The results obtained for the effective value of α are compared with the results given by Parker¹⁹, who analyzed the same shells on the basis of plate on an elastic foundation ($u=v=0$) and did not include the effect of the tie bar. For both single and double deck, a certain amount of increase in the value of α was noted for the low rise to span ratio (1/8) but with the increase of the ratio, the value of effective α reduces. The results obtained by direct interpolation for single deck hypars appear quite reasonable (Table II.1). The direct interpolation if applied to the double decks, results in extremely low effective value of α particularly for the ratio of 1/5 and 1/3 (Table II.2). The fallacy in the method of interpolation can be explained as follows:

All the test results marked with an index (I) (821(I)) were the tests where two transversely placed corrugated decks

were inter-connected whereas in the rest of the tests, the top deck was connected only along its periphery to the bottom deck which in turn was connected to the edge member. The center deflections obtained for Case (I) is roughly 20-30% less than that where the decks were not inter-connected. In the mathematical model there is a complete coupling between the in-plane displacements of u - v and the normal displacement w (see Chapter III). Secondly when two decks are placed on top of each other in the analysis, the in-plane stiffnesses of the top deck E_{xt} , E_{yt} , E_{xyt} and E_{lt} are assumed to be fully effective in resisting the load.

In case of the decks only connected at the edges, the deviation between the mathematical and physical model is very drastic, and therefore the deflections given by the analysis are very low. With these considerations in view, a certain amount of discretion must be used in estimating the values of α . The results obtained by the analysis were compared with the test results. The resulting reduction in values of α can be attributed to the warping of the surface and the deck and the edge member connections. These factors are common to both single and double decks (Figs. 2.7, 2.8).

Whether the increase in the effective relative shear rigidity for the low rise to span ratio of $1/8$, is an inherent behavior of the hypar or whether it is the shortcoming of the theory in the region of transition between flat plate and warped hypar surface is not very clear. It will be conservative to neglect any increase in the value of α obtained from flat shear test. The importance of the values of α and the recommended reductions are further discussed in Chapters IV and V.

CHAPTER III

FINITE ELEMENT METHOD FOR STIFFNESS AND STRESS ANALYSIS

III.1. INTRODUCTION

As discussed in Chapter I, the solution of the shallow shell equation for realistic boundary conditions is an extremely complicated mathematical proposition. This necessitates the use of numerical methods. The finite element method was chosen because of its versatility in handling realistic boundary conditions, different structural configurations, orthotropic deck materials and any forms of loading, with ease. The method has also demonstrated good convergence characteristics.

The finite element method based on the stiffness analysis uses the principle of minimum potential energy. The total potential energy of an elastic system, for a geometrically admissible state can be represented by,

$$\Phi = U + V \quad 3-1$$

where U is the strain energy stored in the system and V is the potential energy of the applied loads. Both U and V are expressed in terms of displacements at the joints of an idealized structure. U is a quadratic function of the nodal displacement. The principle of the minimum potential energy states that, "The total potential energy is minimum, when an elastic body is in equilibrium".

$$\frac{\partial \Phi}{\partial \Delta_i} = \frac{\partial}{\partial \Delta_i} (U+V) = 0 \quad 3-2$$

$$P_i = \frac{-\partial V}{\partial \Delta_i} \quad 3-3$$

For the linear elastic analysis, these expressions can be put in matrix form,

$$[P] = [K] [\Delta] \quad 3-4$$

The elements of the stiffness matrix can be obtained by the second differential of the strain energy,

$$K_{ij} = \frac{\partial^2 U}{\partial \Delta_i \partial \Delta_j} \quad 3-5$$

In the case of a framework composed of linear members such as beams, struts, etc., the individual elements are connected to each other at their nodal points. Well-defined boundary conditions at these joints enables one to solve the physical problem without any difficulty. In this case, there is one to one correspondence between the mathematical and the physical model. However, in the case of a two-dimensional structural medium such as a plate or a shell surface, the discrete element approach does not give a one to one correspondence between the element used in the matrix analysis and the forces in the actual surface. Here the entire structure is idealized into discrete elements, curved or flat, connected to each other at the nodal points. The displacements of the nodal points are interpreted as those occurring at the corresponding points in the structure. The state of stress and strain inside an element is defined completely in terms of its nodal point deformations. The success of determining the elastic properties of an idealized structural element lies in the equivalence established between the actual model and its equivalent discrete

model.

The linear elastic stiffness analysis consists of four important steps:

- (1) The formulation of the element stiffness matrix.
- (2) The formulation of the master stiffness matrix for the entire structure by assembling individual elements.
- (3) The solution of Eq. 3-4 for the given boundary conditions and loading.
- (4) The interpretation of the deflected shape and the computation of stresses and forces.

Two alternative stiffness formulation methods are studied here:

Method 'a': The use of rectangular curved elements, based on shallow shell theory.

Method 'b': The actual curved shell surface is approximated by the assemblage of flat rectangular elements.

III.2. ELEMENT STIFFNESS

The elements rectangular in plan are selected. These elements are very simple to formulate and for the structure under consideration, their limitation of application to the rectilinear rectangular boundaries, is not considered to be of any serious consequence.

As shown in Eq. 3-1c, the element stiffness matrix can be derived from the strain energy U of an element, expressed in terms of an assumed displacement field.

A. DISPLACEMENT FUNCTIONS

The displacement fields assumed for the analysis are

as follows:

$$u = \frac{1}{ab} [(x-a)(y-b)u_1 - x(y-b)u_2 + xyu_3 - (x-a)yu_4] \quad 3-6a$$

$$v = \frac{1}{ab} [(x-a)(y-b)v_1 - x(y-b)v_2 + xyv_3 - (x-a)yv_4] \quad 3-6b$$

$$\begin{aligned} w = & \frac{1}{a^3b^3} [(a^3+2x^3-3ax^2)(b^3+2y^3-3by^2)w_1 + (3ax^2-2x^3)(b^3+2y^3-3by^2)w_2 \\ & + (3ax^2-2x^3)(3ay^2-2y^3)w_3 + (a^3+2x^3-3ax^2)(3by^2-2y^3)w_4 \\ & - ax(x-a)^3(b^3+2y^2-3by^2)\theta_{y1} - a(x^3-ax^2)(b^3+2y^3-3by^2)\theta_{y2} \\ & - a(x^3-ax^2)(3by^2-2y^3)\theta_{y3} - a(x-a)^2x(3by^2-2y^3)\theta_{y4} \\ & + b(a^3+2x^3-3ax^2)y(y-b)^2\theta_{x1} + b(3ax^2-2x^3)y(y-b)^2\theta_{x2} \\ & + b(3ax^2-2x^3)(y^3-by^2)\theta_{x3} + b(a^3+2x^3-3ax^2)(y^3-by^2)\theta_{x4} \\ & + abxy(x-a)^2(y-b)^2\theta_{xy1} + abxy(x^2-ax)(y-b)^2\theta_{xy2} \\ & + abxy(x^2-ax)(y^2-by)\theta_{xy3} + abxy(x-a)^2(y^2-by)\theta_{xy4}] \quad 3-6c \end{aligned}$$

The same functions were used by Gallagher⁵⁰ and Yang⁵¹, but in their studies the x,y cartesian co-ordinates were replaced by the more general curvilinear co-ordinates α_1 and α_2 . As seen here, the displacement field inside an element is directly expressed as the function of its nodal displacements rather than in terms of undetermined parameters. An element, as shown in Fig. 3.1, has six degrees of freedom per nodal point and a total of 24 degrees per element. The displacements u,v,w, θ_x , and θ_y have a physical meaning at each node. The term θ_{xy} represents the twist curvature $\frac{\partial^2 w}{\partial x \partial y}$. Using the right cork-screw notation,

$$\theta_x = \frac{\partial w}{\partial y} ; \theta_y = - \frac{\partial w}{\partial x} ; \theta_{xy} = \frac{\partial^2 w}{\partial x \partial y} \quad 3-7$$

One may also note that the inplane rotation about the z-axis is being omitted in this formulation.

The function for w , normal bending displacement, is of the cubic order. The terms corresponding to the degrees of freedom w , θ_x and θ_y are obtained by the cross product of the corresponding terms for the beam function in x and y -directions. In order to represent the constant strain corresponding to the twisting term $\frac{\partial^2 w}{\partial x \partial y}$ i.e., the term 'xy', the additional degree of freedom in the form of θ_{xy} is added to the displacement.

The displacement functions are geometrically symmetrical and include the constant strain and rigid body modes for the flat plate. It is obvious that the assumed displacement fields for u , v and w are not of the same order. Whereas those for u and v are linear, as stated before, w displacement is cubic. If the displacement fields of u and v were of the same order as that of w , each node would have 12 degrees of freedom thereby having a total of 48 degrees per element. Besides this, the linear edge member elements would have to be given the same order of stiffness matrix. The additional degrees of freedom would involve more computational work and this effort could only be justified if good results, without sacrificing the required degree of accuracy, could be attained with a fewer number of elements.

Any combination of displacements which can be accomplished without straining the structure are called rigid body displacement modes. These displacement modes can be easily

recognized in the case of linear members or flat plates whereas their role is not easily recognized in the displacement field for the curved shells. The assumed displacement field does not include rigid body motion for the curved element. Cantin and Clough⁵² used the displacement field for a cylindrical shell element and added the appropriate rigid body motion terms in the form of trigonometric functions. It was shown that with the inclusion of the rigid body motion terms, there was an improvement in the rate of convergence. Haisler and Stricklin⁵³ and Connor and Brebbia¹⁷, have shown that inspite of omitting the rigid body motion terms with the refinement of the grid size, the convergence is still insured.

Pecknold and Schnobrich²⁰ proposed the most logical method for the inclusion of the rigid body motion terms. It was suggested that these terms should satisfy the homogeneous part of the strain displacement relationship used for the curved element (Eq. 3-9,3-10). The inclusion of these terms involves more computational effort but they seem to have certain advantages, which are further discussed in Chapter IV.

B. CURVED ELEMENT

Strain Displacement Relationship

The strain displacement relationships used in the curved element formulation are simplified according to the shallow shell theory. The following assumptions are made:

(1) For a given surface defined by the equation, $z=F(x,y)$, the slopes of the surface $z_{,x}$ and $z_{,y}$ are considered negligible in comparison with unity. In general, the shallow shell theory

will be quite accurate as long as $z_{,x}, z_{,y} \leq 1/8$, and often accurate enough for practical purposes as long as $z_{,x}, z_{,y} \leq 1/2^5$; though the second limit could be considered as too liberal.

(2) The sides of a differential shell element, which are orthogonal in the projected co-ordinate plane, are assumed to be orthogonal in the plane of the middle surface of the shell. In other words, the geometry of the surface is approximated by that of its projection on the co-ordinate plane.

(3) If the equation of the middle surface is of the second order as is the case for a hyperparabola, the assumption (1), leads to the approximation that the curvatures of the surface are constant.

The errors resulting from these assumptions increase as the depth of the shell increases. For the shallow hyperparabola surface defined by the equation,

$$z = \frac{C}{AB} xy \quad 3-8$$

the linear strain displacement relationships for the thin shells assume the following form^{20,17}:

The membrane strain displacement relationships:

$$\epsilon_x = u_{,x} \quad 3-9a$$

$$\epsilon_y = v_{,y} \quad 3-9b$$

$$\gamma_{xy} = u_{,y} + v_{,x} - \frac{2C}{AB} w \quad 3-9c$$

The bending strain displacement relationships:

$$K_x = -w_{,xx} \quad 3-10a$$

$$K_y = -w_{,yy} \quad 3-10b$$

$$2K_{xy} = -2w_{,xy} \quad 3-10c$$

Strain Energy

The strain energy for a typical element consists of two parts: the membrane and the bending strain energy.

$$U = U_b + U_m \quad 3-11$$

The membrane strain energy for an element is given by⁵⁴,

$$U_m = \frac{1}{2} \int_0^b \int_0^a (N_x \epsilon_x + N_y \epsilon_y + N_{xy} \gamma_{xy}) dx dy \quad 3-12$$

The stress-strain relationship for an orthotropic material (Fig. 3.2) can be represented by

$$\begin{bmatrix} N_x \\ N_y \\ N_{xy} \end{bmatrix} = \begin{bmatrix} E_{xt} & E_{lt} & 0 \\ E_{lt} & E_{yt} & 0 \\ 0 & 0 & E_{xyt} \end{bmatrix} \begin{bmatrix} \epsilon_x \\ \epsilon_y \\ \gamma_{xy} \end{bmatrix} \quad 3-13$$

The method of computation for the above mentioned elastic constants is discussed in Chapter II.

Using the strain displacement (Eq. 3-9, 3-10) and the stress-strain relationship (Eq. 3-13), the membrane strain energy (Fig. 3.2) of an element can be expressed as follows:

$$\begin{aligned} U_m = \frac{1}{2} \int_0^b \int_0^a \{ & \overset{1}{E_{xt}} u^2_{,x} + \overset{2}{E_{yt}} v^2_{,y} + \overset{3}{2E_{lt}} u_{,x} v_{,y} \\ & + \overset{4}{E_{xyt}} [u^2_{,y} + \overset{5}{v^2_{,x}} + \overset{6}{2u_{,y} v_{,x}}] \\ & - \overset{7}{4E_{xyt} \left(\frac{C}{AB}\right)} w [u_{,y} + \overset{8}{v_{,x}}] \\ & + \overset{9}{4E_{xyt} \left(\frac{C}{AB}\right)^2} w^2 \} dx dy \quad 3-14 \end{aligned}$$

The same strain energy expression is also reported in Ref. 19.

The bending strain energy is given by the expression⁵⁴,

$$U_b = \frac{1}{2} \int_0^b \int_0^a [M_x(-w,_{xx}) + M_y(-w,_{yy}) + 2M_{xy}(-w,_{xy})] dx dy \quad 3-15$$

The moment strain relationships (Fig. 3.3) are:

$$\begin{bmatrix} M_x \\ M_y \\ M_{xy} \end{bmatrix} = \begin{bmatrix} D_x & D_1 & 0 \\ D_1 & D_y & 0 \\ 0 & 0 & D_{xy} \end{bmatrix} \begin{bmatrix} -w,_{xx} \\ -w,_{yy} \\ -2w,_{xy} \end{bmatrix} \quad 3-16$$

The bending strain energy is given by³⁸,

$$U_b = \frac{1}{2} \int_0^b \int_0^a [D_x w,_{xx}^2 + D_y w,_{yy}^2 + 2D_1 w,_{xx} w,_{yy} + 4D_{xy} (w,_{xy})^2] dx dy \quad 3-17$$

This energy expression assumes that $M_{xy} = M_{yx}$. However, as pointed out in the Chapter II, for an open orthotropic deck, $M_{xy} \neq M_{yx}$ and therefore the value of M_{xy} given in Eq. 3-16, is to be interpreted as the average value. The energy expression 3-17 neglects any energy stored in the deck due to the restrained warping. As pointed out by Smith³⁵, in an open form deck, the twisting moment M_{yx} consists of two parts:

$$M_{yx} = -(2D_{yx} w,_{xy} - E\Gamma w,_{xyy}) \quad 3-18$$

The warping strain energy is given as,

$$U_{warp} = \frac{1}{2} E\Gamma \int_0^b \int_0^a (w,_{xyy})^2 dx dy \quad 3-19$$

The omission of this energy term is not considered to be of any serious consequence. The stiffness matrix for the curved element is obtained by using Eq. 3-5. The complete stiffness matrix is given in Appendix B.

C. FLAT ELEMENT

The stiffness matrix for the flat elements can be obtained directly by putting $c = 0$ in the curved element stiffness matrix. The strain displacement relationships for the flat elements are the same as those for the curved elements, except for the shear strain given by the Eq. 3-9c. For the flat plate, the last term in Eq. 3-9c, due to the twist curvature of the hyper surface disappears. The difference between the curved and the flat element stiffness matrix can be shown schematically as follows:

$$[K]_{\text{curved}} = \begin{bmatrix} [K]_m & [K]_{bm} \\ \text{-----} & \text{-----} \\ [K]_{bm}^T & [K]_{bb} \\ & + [K]_{bbm} \end{bmatrix} \begin{bmatrix} u \\ v \\ w \end{bmatrix} \quad 3-20$$

$$[K]_{\text{flat}} = \begin{bmatrix} [K]_m & 0 \\ \text{-----} & \text{-----} \\ 0 & [K]_{bb} \end{bmatrix} \begin{bmatrix} u \\ v \\ w \end{bmatrix} \quad 3-21$$

The membrane stiffness matrix $[K]_m$, is obtained from terms 1 - 6 of the membrane energy expression Eq. 3-14. This stiffness matrix is common to both curved and flat elements. The coupling matrix terms $[K]_{bm}$ and $[K]_{bbm}$ are obtained from terms 7, 8 and 9 respectively, of Eq. 3-14. These terms are zero in the case of the flat elements. The stiffness matrix $[K]_{bb}$, common to both types of elements, is obtained from the bending strain energy given by Eq. 3-17.

The stiffness matrix derived for the orthotropic flat plate was checked term by term, with the stiffness matrix for

an isotropic plate reported in Ref. 51. To establish the validity of the stiffness matrix further, the results for the plates shown in Fig. 3.4a,b,c were checked with available classical solutions. For the isotropic plates shown in Fig. 3.4a and b, the comparison between the classical solution and the stiffness analysis for the center deflection δ_B was excellent. The error was less than 1% in both cases and the geometrical symmetry in the nodal displacements was satisfied.

The third example (Fig. 3.4c) is of particular interest. The 28-G standard corrugated deck can be considered as an extreme case of orthotropy. Here the bending rigidity D_y is 1678 times D_x . The bending rigidity constants were used as given in Ref. 54. It is reported in Ref. 19, that the rectangular elements proportioned in the ratio of their bending rigidities, in two directions, would give better results than the square elements. A quadrant of the plate was analyzed by using square (6x6) elements and elongated rectangular (2 x 12) elements. The results for (1x30) size elements were also computed but are not reported since there is practically no difference between these results and those with a 2x12 element grid. The deflection profile across the corrugation is plotted in Fig. 3.5. There is practically no difference (see Table III-1) between the rectangular and the square element solutions, a dip in the deflection profile near the support is seen in both the solutions. Similar deflection profiles are also reported in Ref. 19. The solutions obtained by the stiffness analysis are compared with the classical solutions given by

Timoshenko⁵⁴ in the form of a double sine series, for the uniformly loaded, simply supported orthotropic plate.

$$w = \sum_{m=1,3,5,\dots}^{\infty} \sum_{n=1,3,5,\dots}^{\infty} a_{mn} \sin \frac{m\pi x}{a} \sin \frac{n\pi y}{b} \quad 3-22$$

where,

$$a_{mn} = \frac{16q_0}{\pi^6} \frac{1}{\left(\frac{m^4}{a^4}D_x + \frac{2m^2n^2}{a^2b^2}H + \frac{n^4}{b^4}D_y\right)} \quad 3-23$$

where,

$$H = 2D_{xy} + D_1 \quad 3-24$$

The first few significant terms in the sine series were computed. The comparison of the results is shown in Table III-1. Both the classical and the stiffness analysis solutions are well within the limits of practical accuracy.

A strongly orthotropic plate such as the one under consideration, primarily behaves as a plate on an elastic foundation. The stiffer beam strip near the support attracts more load because of the presence of the plate action. In other words, the deflected profile of the plate is the function of the assumed bending rigidities and does not appear to be dependent upon the shape of the element (rectangular or square).

The non-monotonic convergence characteristic of this problem, observed in the Ref. 19, is probably the function of the deck properties. This analysis indicates that elements which are square in plan can be used for the single deck hyper structure.

D. EDGE MEMBER

The conventional beam stiffness matrix⁵⁵ is primarily based on two assumptions:

- (1) The shear center and the centroid coincide, (Fig. 3.6a).
- (2) The bending of the section takes place about the axis of symmetry (Fig. 3.6a).

In the case of a symmetrical channel (Fig. 3.6b), the shear center (S.C.) and the centroid (C.G.) of the section do not coincide. When the section is subjected to a vertical load P (Fig. 3.6c), acting at a distance e from the shear center, it not only deflects in the plane $y-z$ but also twists through an angle θ about the x -axis, passing through the shear center. In other words, the bending displacements v and w need to be expressed at the shear center of the section. This observed fact was elegantly expressed by Bleich⁵⁶ and Hoff⁵⁷, in the strain energy of a beam of arbitrary cross-section. The total strain energy of a beam (Fig. 3.7) is given as,

$$U_{bb} = \frac{1}{2} \int_0^a [EI_y w',_{xx}{}^2 + EI_z v',_{xx}{}^2 + GJ \theta',_x{}^2 + E\Gamma_b \theta',_{xx}{}^2 + EA_b u',_x{}^2] dx \quad 3-25$$

where, w and v are the displacements of the shear center (S.C.) measured along the axes y and z parallel to the principal centroidal axes of the section and u is the average longitudinal displacement of the section along the axis x measured at the centroid (C.G.) of the section. θ is the angular rotation of the section about the x -axis.

Neglecting the warping of the section, the conventional beam stiffness matrix can be obtained by assuming the

following displacement fields:

$$u = \frac{x}{a} u_2 + (1 - \frac{x}{a}) u_1 \quad 3-26a$$

$$v = \frac{1}{a^3} [(a^3+2x^3-3ax^2)v_1+(3ax^2-2x^3)v_2+ax(x-a)^2\theta_{z1} \\ + a(x^3-ax^2)\theta_{z2}] \quad 3-26b$$

$$w = \frac{1}{a^3} [(a^3+2x^3-3ax^2)w_1+(3ax^2-2x^3)w_2-ax(x-a)^2\theta_{y1} \\ - a(x^3-ax^2)\theta_{y2}] \quad 3-26c$$

$$\theta = [\frac{x}{a} \theta_2 + (1 - \frac{x}{a})\theta_1] \quad 3-26d$$

Using Eqs. 3-25 and 3-5, one can obtain the conventional beam stiffness matrix.

However, the warping restraint is of practical importance, particularly for thin-walled open sections. To include the warping effect, the displacement field for θ is assumed to be of the same form as that of v and w ⁵⁸.

$$\theta = \frac{1}{a^3} [(a^3+2x^3-3ax^2)\theta_1+(3ax^2-2x^3)\theta_2+ax(x-a)^2\theta'_{x1} \\ + a(x^3-ax^2)\theta'_{x2}] \quad 3-27a$$

$$\theta'_x = \frac{\partial \theta}{\partial x} \quad 3-27b$$

The stiffness matrix (14x14) for this member can be directly obtained from Table III-3 by substituting $Y_c = Z_c = Y_s = Z_s = 0$. The additional degree of freedom (θ_{xy}) introduced, does not present any problem. If the beam shown in Fig. 3.8 is attached to a shell surface or a plate along the line passing through the shear center, one can easily find the correlation between the degree of freedom for the plate and the

beam.

$$\theta = \theta_x = \frac{\partial v}{\partial y} \quad \text{and} \quad \theta'_x = \theta_{xy} = \frac{\partial^2 w}{\partial x \partial y} \quad 3-28$$

Omitting the rotation about the z-axis (θ_z), the plate and the beam element can be connected to each other with a one to one correspondence in the nodal degree of freedom.

E. ECCENTRICALLY CONNECTED NON-COMPATIBLE SUPPORTING EDGE MEMBER

The above mentioned matrices can be used only in the case of non-eccentric loads or concentric connections of the edge members to a shell or a plate surface. In practice, concentric connections between the supporting edge members and a shell or a plate are seldom possible (Fig. 3.9). The eccentric connections modify the effective stiffness of the supporting members. The modified stiffness for the non-compatible edge member can be obtained by the use of simple linear congruent transformations similar to the one suggested in Ref. 59. The difference between the compatible and the non-compatible eccentric members is discussed in Appendix E and the relevant stiffness and incremental matrices for the compatible element are given in Table E-I and E-II. The linear transformation assumes that the beam bends about its own neutral axis (Fig. 3.10).

$$[\lambda]_s = \begin{bmatrix} 1 & 0 & 0 & 0 & Z_c & -Y_c & 0 \\ & 1 & 0 & Z_s & 0 & 0 & 0 \\ & & 1 & Y_s & 0 & 0 & 0 \\ & & & 1 & 0 & 0 & 0 \\ & & & & 1 & 0 & 0 \\ & & & & & 1 & 0 \\ & & & & & & 1 \end{bmatrix} \begin{bmatrix} u \\ v \\ w \\ \theta_x \\ \theta_y \\ \theta_z \\ e \end{bmatrix} \quad 3-29$$

$$[T]_s = \begin{bmatrix} [\lambda]_s & 0 \\ 0 & [\lambda]_s \end{bmatrix} \quad 3-30$$

The effective stiffness of the edge member can be given as,

$$[K]_{eb} = [T]_s^T [K] [T]_s \quad 3-31$$

Similar stiffness matrices were independently derived in Ref. 21. The stiffness matrices, with the linear variation and the non-linear variation of the twist angle are given in Table III-2 and III-3 respectively. The convergence characteristics and the accuracy of the stiffness matrices, was checked by solving three cantilever beams (Fig. 3.11). Only axial (Fig. 3.11a) and bending (Fig. 3.11b) loads were applied eccentrically to the beam. All displacements were computed along the line PQ (Fig. 3.11). The deflections and the twist angle at the free end Q, were compared with classical solutions. As it can be seen, the convergence in all cases is insured and the results for the case of six elements are within 0.2% of the classical solutions. The loading II was applied to two cases: IIa) Free torsion with a linear variation of twist. IIb) Including the warping restraints at the fixed end. The classical solutions for the case IIb, were obtained from the Ref. 60. The convergence in case of the restrained warping is slightly slower than in the case of free torsion. The influence of including the warping degree of restraint can be seen from Fig. 3.13a. The free end deflection δ_Q in the case IIb, is about 63.5% of the deflection obtained in the case IIa.

F. ELASTIC SPRINGS

In order to simplify the mathematical solution without undue loss of generality, certain structural elements are idealized in the form of concentrated spring stiffnesses. For example, the central column in the case of an umbrella shell, if idealized as a physical member with its end points, will not only create an additional node point for the master stiffness matrix but will also disrupt the regularly arranged grid pattern and will warrant a modification in the entire assembly routine. In order to avoid this, the stiffness of the column can be idealized into six discrete springs accounting for its axial, shear, bending and twisting stiffnesses (Fig. 3.14). These stiffnesses are given as,

$$\begin{aligned} S_A &= \frac{AE}{a} ; S_{BY} = \frac{4EI}{a} \frac{y}{z} ; S_{BZ} = \frac{4EI}{a} \frac{z}{y} \\ S_{SY} &= \frac{12EI}{a} \frac{y}{z} , S_{SZ} = \frac{12EI}{a} \frac{z}{y} ; S_T = \frac{GJ}{a} \end{aligned} \quad 3-32$$

These spring constants are added along the main diagonal elements of the master stiffness matrix. This idealization is not always satisfactory. In Fig. 4.1, a tension bar connecting the lower corners of the saddle shaped hypars are replaced by four springs in the u and v directions, two at each corners f and b. This idealization eliminates the interaction between the nodes f and b. The validity of this approximation can only be assessed by engineering judgement.

III.3 MASTER STIFFNESS MATRIX

The stiffness formulation presented so far is for an individual element. The total stiffness of the structure is

developed by the assemblage of these individual elements. The two different methods ('a' and 'b'), mentioned in Section III.1, differ in the formulation of the stiffness matrices.

a) Curved Element

The element stiffness is formulated by using an element of the same shape as the shell middle surface (Refs. 17, 19,20). However, the fact that the shallow shell assumptions are made in this formulation, should not be overlooked (a point which is discussed at length in Chapter IV). The assumed shallowness of the shell does not warrant any form of co-ordinate transformation. The strain displacement relationships given in Eqs. 3-9 and 3-10 are based upon the displacements u , v , and w which are measured along the tangent and normal to the surface.

b) Flat Element

The middle surface of the shell is approximated by a series of flat plates. The geometrical approximation of the actual surface needs three important steps:

(1) Definition of Surface -

As pointed out in Chapter I, different hyper structures can be built with various combinations of the basic units (Fig. 1.2). It is necessary to express the equation of the generated surface with reference to the chosen global axis. The general equation of a structure using the hyper units can be expressed as,

$$z = \frac{C_i}{A_i B_i} (x - \bar{x}_i) (y - \bar{y}_i) \quad 3-33$$

Figs. 3.15a and 3.15b show two structures and also give the

values of the constant, defining the surface equation for each quadrant. In Fig. 3.15b, points P,Q,R,S are the local origins of the quadrant surface. x' and y' , are the local co-ordinate axes passing through the local origins.

(2) Element Size -

For shallow shells, the size of the element can be approximated with the size of a rectangle projected on the co-ordinate plane xy (Fig. 3.16). For example, the size of the curved element PQRS is approximated by the projected element P'Q'R'S'.

A better approximation for the size of the element PQRS can be made by calculating the actual lengths PQ, QR, etc., and using a rectangle P'Q'R'S', of an equal area. For the low rise to span ratio ($\leq 1/5$), the error introduced by using the projected element is very small (2-3%). To take advantage of this fact, a provision is made in the computer program to choose between the above mentioned approaches. The difference in results when using these two methods was about 10% for the structure shown in Fig. 4.3. The computation of the exact lengths gives different stiffness matrices for each element.

(3) Co-ordinate Transformation -

It is not possible to generate a smooth curved surface by using flat elements with rectilinear boundaries. This results in gaps and non-compatibilities between the adjacent elements forming an idealized uneven surface (the picture of the idealized surface is left to the imagination of the readers). Such gaps and discontinuities occurring at the boundaries of

adjacent elements, have been known to produce undesirable and non-existing nodal forces, for shells of revolution⁶¹, which had significant effects on the solutions. However, no such noticeable difficulty was encountered in the solution of shallow hyper shells. The solutions obtained for these shallow shells did not show any necessity of placing local tangential orthogonal axes at each nodal point.

In writing the master stiffness matrix and the overall equilibrium equations, local nodal axes can be chosen. Instead of these, a simple and approximate approach is used. A plane tangent to the surface is drawn at a point O (Fig. 3.17). The most logical point for the tangential plane is the center of the element. In the case of umbrella shells, the flat portion near the free corner shows a pronounced bending action. To estimate this bending action conservatively, the tangent planes were drawn along the horizontal lines PQ and PS instead of at the center point O (Fig. 3.17a). When using the corner point transformation, one has to exercise proper care to retain the symmetry of the solution. For a large number of elements, both methods should give about the same results but the corner point transformation is more cumbersome and therefore it is not used in the analysis.

In Fig. 3.17a, the line OZ' is normal to the surface whereas OX' and OY' are generators of the surface. The direction cosines for the lines OX' , OY' and OZ' are given as,

$$\begin{bmatrix} OX' \\ OY' \\ OZ' \end{bmatrix} = \begin{bmatrix} \frac{1}{\sqrt{1+z_x^2}} & 0 & \frac{z_x}{\sqrt{1+z_x^2}} \\ 0 & \frac{1}{\sqrt{1+z_y^2}} & \frac{z_y}{\sqrt{1+z_y^2}} \\ \frac{-z_x}{\sqrt{1+z_x^2+z_y^2}} & \frac{-z_y}{\sqrt{1+z_x^2+z_y^2}} & \frac{1}{\sqrt{1+z_x^2+z_y^2}} \end{bmatrix} \quad 3-34$$

where

$$z_x = \frac{C}{AB} y_o \quad \text{and} \quad z_y = \frac{C}{AB} x_o.$$

As discussed in connection with the shallow shell assumptions, the angle between the generators OX' and OY' is not equal to 90° . Hence a new set of mutually orthogonal axes $O\bar{Z}$, $O\bar{X}$, and $O\bar{Y}$ are obtained, where $O\bar{Z}$ coincides with OZ' . The procedure for obtaining the direction cosines of $O\bar{X}$, $O\bar{Y}$ and $O\bar{Z}$ is a simple application of the three dimensional solid geometry (Fig. 3.17b).

The transformation matrix for each node can be represented as

$$[T]_{e\ell} = \begin{bmatrix} [\lambda]_1 & 0 \\ 0 & [\lambda]_2 \end{bmatrix}_{6 \times 6} \quad 3-35$$

$$[\lambda]_1 = \begin{bmatrix} \ell_x & \ell_y & \ell_z \\ m_x & m_y & m_z \\ n_x & n_y & n_z \end{bmatrix} \quad [\lambda]_2 = \begin{bmatrix} \ell_x & \ell_y & 0 \\ m_x & m_y & 0 \\ 0 & 0 & n_z \end{bmatrix} \quad 3-36$$

The in-plane rotation θ_z is omitted. From the matrix $[\lambda]_2$ it can be seen that θ_{xy} the additional degree of freedom, is transformed from the local to the global axis in the same way as w

except for the assumption that there is no coupling between the rotation θ_{xy} and the rotation θ_x, θ_y . This transformation can be viewed as an approximation.

The master stiffness matrix for the shell surface, using method 'b' (see Section III.1) is completed by transforming each and every element stiffness from its local axes ($O\bar{X}, O\bar{Y}, O\bar{Z}$) to the respective global axes (OX, OY, OZ). Depending upon the direction cosines of the local axes of the individual elements, every coefficient of the transformed element stiffness matrix can have a non-zero value, i.e., there is a coupling between $u, v,$ and w displacements, expressed in terms of the global co-ordinate.

Beam Element

The co-ordinate transformation given by Weaver⁵⁵, to transform the stiffness of the beam element from the local to the global axis is used. The transformation matrix with a minor modification to suit the problem at hand is given in Table III-4. After orienting the axis x of the member, it is also necessary to define the orientation of the principal axes \bar{y} and \bar{z} , since the stiffness of the beam element is expressed in reference to its principal axes. The angle β defines the orientation of the principal axes. The definition of the angle β is given in Ref. 63. (Fig. 3.18).

For the method 'a', using the curved element, the stiffness of the edge members is added without any co-ordinate transformation. For method 'b', using the flat elements, the edge member stiffness is added with a proper co-ordinate trans-

formation as given in the Table III-4.

III.4 LOADING

A uniformly distributed load acting on a rectangular element can be replaced by statically equivalent loads of equal intensity acting at each nodal point. This procedure is acceptable if the size of the element is small.

The alternative approach known as the work equivalent load is based on the equivalence of energy. The nodal forces are so assigned that during any virtual displacement the work done by these forces is equal to the corresponding work done by the actual distributed load.

The work equivalent nodal loads for the rectangular element, with unit normal load, are given below:

$$\begin{bmatrix} w_1 \\ w_2 \\ w_3 \\ w_4 \\ \theta_{y1} \\ \theta_{y2} \\ \theta_{y3} \\ \theta_{y4} \end{bmatrix} = \begin{bmatrix} ab/4 \\ ab/4 \\ ab/4 \\ ab/4 \\ a^2b/24 \\ a^2b/24 \\ a^2b/24 \\ -a^2b/24 \end{bmatrix} \begin{bmatrix} \theta_{x1} \\ \theta_{x2} \\ \theta_{x3} \\ \theta_{x4} \\ \theta_{xy1} \\ \theta_{xy2} \\ \theta_{xy3} \\ \theta_{xy4} \end{bmatrix} = \begin{bmatrix} ab^2/24 \\ ab^2/24 \\ -ab^2/24 \\ -ab^2/24 \\ a^2b^2/144 \\ -a^2b^2/144 \\ a^2b^2/144 \\ -a^2b^2/144 \end{bmatrix}$$

3-38

The nodal loads associated with θ_{xy} degree of freedom do not have any physical significance. The moment M_x is associated with θ_y degree of freedom whereas the moment M_y is associated with θ_x . For an interior point, the work equivalent load reduces the static load for uniformly sized elements. The effects of the nodal moments cancel out along the boundaries

whereas they add up in the direction normal to the boundaries. All throughout this work, work equivalent loads are used for uniformly distributed loading.

In the case of a uniform load acting normal to the surface, statically equivalent projected uniform load is calculated. The work equivalent nodal loads then calculated for the modified load intensity are directly applied to the structure, in terms of the global co-ordinate axis without any transformation. This is again an approximation. A more accurate method of determining the nodal load would involve a co-ordinate transformation from the local to the global axis.

Besides the uniformly distributed load, a concentrated force or moment can be applied to the structure by specifying the magnitude of the load at the corresponding degree of freedom in the load vector.

III.5 BOUNDARY CONDITIONS

The boundary conditions for a structure can be broadly classified into two categories:

- (1) Force boundary conditions.
- (2) Displacement boundary conditions.

In the conventional stiffness analysis, the latter can be easily satisfied whereas the former can be satisfied only in the variational sense. A detailed discussion of this point is reported in Ref. 21.

The typical boundary conditions for the edge where x is constant, are:

Boundary Conditions	u	v	w	θ_x	θ_y	τ_{xy}
Hinge	0	0	0	0	-	-
Knife-edge	0	-	0	0	-	-
Fixed	0	0	0	0	0	0
Free	-	-	-	-	-	-
Symmetric	0	-	-	-	0	0

For the free edge, no displacement boundary conditions are specified. All the boundary conditions are applied with respect to the global axes. The boundary conditions for the member PQ (Fig. 3.19), which was supported vertically but allowed to slide along its length, should be specified in terms of the local axes \bar{x} , \bar{y} and \bar{z} but instead they are specified in terms of the axes x , y and z . This is an approximation and the error due to this will increase with the increase in depth of the shell. The procedure to express the boundary conditions in the local axes \bar{x} , \bar{y} , \bar{z} is given in Ref. 62.

The connections of the edge members to the deck present a problem in expressing the correct boundary conditions. Two non-compatible boundary conditions are shown in Fig. 3.20. In Fig. 3.20a, the deck bends freely without twisting the edge member. This moment-free deck to edge member connection is quite common in practice. The open-form decks are discretely connected to the edge members whereas the close form decks are connected only along their bottom plates (Fig. 2.2). In both cases there is no transfer of moments between the edge member and deck.

The other type of discontinuity can result in the rela-

tive displacement between the deck and the edge member, normal to the boundary (Fig. 3.20b). This type of a connection can result because of an oversized hole, loosely connected screws, or due to tearing of the deck. Depending upon the continuity achieved between the deck and the edge members, different values of fixity coefficients are used. T_F and T_H represent the torsional and the horizontal fixity coefficients, respectively.

In the case of the moment-free deck to edge member connection, $T_F = 0$. The edge member stiffness matrix is modified by multiplying the columns and rows corresponding to the twisting degree of freedoms (θ_x and θ_{xy}) by T_F .

The problem is further complicated by the eccentric connections. As shown in Fig. 3.21a, even with a discontinuity of the rotational degree of freedom, twisting can still be introduced in the edge member because of eccentrically transferred vertical or horizontal load. This problem is not solved satisfactorily. By the method of fixity coefficients, the twisting action introduced by these eccentric forces is eliminated. There is no moment transfer when two elements are interconnected by means of hinges and this results in the local release of the member forces. This formulation does not include the effects of these releases. The details for the incorporation of these local member releases are given in Refs. 62 and 63.

III.6 SOLUTIONS OF EQUATIONS

The equation 3-4, relating the applied nodal loads and

the generalized nodal displacement can be solved. To obtain the displacement vector,

$$[\Delta] = [k]^{-1} [P] \quad 3-39$$

The inversion of the large matrix $[k]$ not only requires a very long time but also needs a large storage space in the computer. The structural matrices are usually well banded about their main diagonals and are also symmetrical. Banavalkar wrote a subroutine which stores only the half band of the matrix in a vertical fashion (Fig. 3.22). The equations are solved by the Gauss-elimination scheme⁶⁴. With the limitation of the available core size and the computational cost, a total of 486 equations with a maximum half band width of 66, were solved for a normal problem (64 square elements). The rectangular matrix of 486x66 was formed and stored in the computer.

However, there are problems where the structural configuration destroys the close-bandedness of the matrix. For example, the tension-tie connecting the lower corners b and f of the hyper (Fig. 4.1), creates sparse entries in the stiffness matrix (Fig. 3.22c). In such cases, instead of revising the entire solution procedure, the structural element is idealized in the form of discrete springs (see Section III.2F).

III.7 STRESS ANALYSIS

Since the main aim of the project is to establish the behavior of the hyper shells, the physical interpretation of the computer results is very important. The deflections, as well as the stresses in the different structural components

such as deck, edge members, etc., represent the physical behavior.

In the finite element analysis, the generalized nodal forces are related to the stresses. But because of an error of discretization and applied joint loads, the resulting nodal forces for the adjoining elements show deviations. In order to obtain some form of average stresses, the element forces are calculated at the mid-point of an individual element.

A. DECK STRESSES

The deck stresses are calculated at the center point of an individual element. Depending upon the choice of method of analysis, method 'a' (curved elements) and method 'b' (flat elements), corresponding strain displacement relationships are used at the center point (see Eqs. 3-9, 3-10). The forces N_x , N_y and N_{xy} and the moments M_x and M_y are calculated per unit length. For the complete derivation of these forces, see Appendix C. The major difference between the computation of stresses for a curved and a flat element is that in the case of the former, consistent with the shallow shell assumption (see Section III.2B) displacements tangential and normal to the surface can be used directly. But in the case of flat elements, the displacements obtained in the global co-ordinates are transformed into the local co-ordinate axes (see Section III.3) and the relevant displacements in the local co-ordinate axes are used. The difference between the strain-displacement relationships for the curved and the flat elements was already shown in Section III.2B.

It must be realized that the forces are calculated on

the basis of orthotropic plate theory which can be considered as an approximate mathematical idealization. The forces calculated per unit length are multiplied by the lengths of the basic units (Fig. 2.2). In the case of a uniformly loaded structure, this method can be considered to be fairly accurate. For the light gage sections with high width to thickness ratio of the individual components, the effective I_{ed} of the section and the location of the neutral axis need modification in accordance with the level of the load (Ref. 38).

The stresses calculated do not include the local bending behavior. For example, the bottom deck plate AB bends locally between the vertical web plates of the hat (Fig. C2 of Appendix C). The problem of deviation between the mathematical and the physical behavior of the orthotropic deck is discussed in detail in Refs. 46,47.

B. BEAM STRESSES

The nodal forces calculated in the local axis of the beam can be directly used to calculate the beam stresses. The method of calculation of stresses for the concentrically connected beam member is well known.

The imaginary forces calculated along the line PQ (Fig. 3.11), are to be transferred to the shear center and centroid to calculate the relevant stresses. The beam forces $[P]_b$ can be calculated by,

$$[P]_b = [T]_s^T [K] [T]_p [\Delta] \quad 3-40$$

The pre-multiplication of the global displacement $[\Delta]$, by $[T]_p$ (Table III-4), transforms the global nodal displacements to the local axes whereas the pre-multiplication of

$[K] [T]_R [\Delta]$ by $[T]_S^T$ transforms the forces to the shear center or the centroid of the beam.

Because of the mathematical idealization, certain difficulties are encountered. A beam with an eccentricity in the z-direction is shown in Fig. 3.23. The variation of the axial forces is shown in Fig. 3.23b and 3.23c. Since the forces are balanced at point O, the axial force also contributes to the equilibrium of the moments at point O. This results in the inequality of the moments along the axis of the beam PQ. The problem becomes particularly critical in the case of rapidly changing axial force and a deck with strong bending rigidity (e.g., concrete hypars). No suitable solution is found for this problem as of this moment. In the absence of definite guidelines, the deflected shape of the structure should be used to decide the sign of the moment.

Experience shows that the bigger of the two moments (M_{OP} or M_{OQ}) is always in conformity with the correct deflected shape of the beam. The difficulty experienced in computing the stresses of an eccentric edge member is one of the shortcomings of using the nodal points only along the shell surface.

The results obtained by this stiffness analysis are compared with experimental and the available solutions in the literature in Chapter IV.

CHAPTER IV
A GENERAL COMPARATIVE STUDY

IV.1 INTRODUCTION

As discussed in Chapter III, two methods were used to analyze hypar shells: method 'a', uses rectangular curved elements based on the shallow shell theory; whereas method 'b' approximates the actual shell surface by using a series of flat rectangular elements. The solutions of selected problems are presented here with three purposes:

(1) To substantiate the use of the finite element method, by method 'a' only, by comparing the solutions for problems for which analytical or other numerical solutions are available in the literature. The comparison for flat plates and linear beams are already presented in Chapter III.

(2) To compare the solutions obtained by methods 'a' and 'b', for typical hypar structures. The comparison is done primarily with a view of assessing their suitability in application to the practical problems and also to find out their shortcomings and limitations.

(3) To compare the analytical solutions with the experimental results obtained by earlier workers. The details of the structures analyzed are given in Table IV-1.

All the analytical results are further used to study, to a limited degree, the effects of different structural parameters on the behavior of hypar shells, such as relative shear

rigidity factor α , rise to span ratio, etc. The effects of these parameters are further discussed in length in Chapter V.

IV.2 COMPARISON OF METHOD 'a' WITH OTHER NUMERICAL SOLUTIONS

Connor and Brebbia¹⁷ presented the centerline deflection profile for a saddle shaped hyper structure (Struc. '1', Table IV-1), with clamped boundaries all around. Their results were based on exactly the same procedure as used in this study. The only difference is that they used a 12-term polynomial for the normal displacement w , whereas this approach used the 16-term displacement function as given in Eq. 3-6c. Fig. 4.6 shows the results obtained by the author. For the grid size of 8x8, the deflection profile along the line oa is similar with the one reported by Connor and Brebbia¹⁷. The deflection profile along the diagonal ob is also plotted to check the symmetry of the solution.

The convergence characteristics of the solutions are checked by refining the grid size for the above mentioned structure. As seen in Fig. 4.7, the convergence for the center deflection at point o (Fig. 4.1) is monotonic and rapid. By refining the grid size from 6x6 to 8x8, an improvement of only 2.3% is obtained in the result.

Pecknold and Schnobrich²⁰ presented the centerline deflection profile for the same type of a structure, with the perimeter knife-edge supported (Struc. '2'). As pointed out earlier, they used the Birkhoff and Garabedian interpolation formula for w displacements. Besides that, the complete rigid body modes of displacements were included by solving the homo-

geneous part of the strain displacement relationships given in Eq. 3-9. The inclusion of the rigid body motion terms destroyed the interelement compatibility and put additional restraints on the in-plane displacement fields of u and v .

$$u = F(u_i) + F_1(w) \quad 4-1a$$

$$v = F(v_i) + F_2(w) \quad 4-1b$$

The displacement functions $F_1(w)$ and $F_2(w)$ are the results of the solution of the homogeneous part of the Eq. 3-9c. Pecknold and Schnobrich compared their solution with a Navier-type (double sine series) solution, for which 50 terms in each direction were included²⁰. The deflection profiles along the center line oa and the diagonal ob , obtained in this study (grid size 8×8), are shown in Fig. 4.8. The central deflection obtained in this manner differs by +0.2% from that obtained by the series solution (9.18×10^{-3} inch.); whereas it differs by approximately -1% from the finite element solution of Pecknold and Schnobrich.

The solutions obtained by method 'a' for both Struct. '1' and '2' mentioned above, are considered to be quite good.

IV.3 COMPARISON OF METHOD 'a' AND METHOD 'b'

Both structures solved by method 'a', were solved again by using method 'b'. The deflections obtained by the two methods using the grid size of 8×8 , are shown in Table IV-3. Methods 'a' and 'b' show similar deflection profiles along both the center and the diagonal lines oa and ob respectively. The central deflection obtained by method 'b' for both structures is on the higher side, as compared with the one obtained by

method 'a'. For Struc. '1', the difference in the central deflection is about 0.8% whereas for Struc. '2', the difference is about 1.30%. The central deflection for Struc. '2' is only 0.5% on the higher side of the deflection obtained by Pecknold and Schnobrich.

The correlation obtained by methods 'a' and 'b' is excellent for these two structures. However, it must be pointed out that both of these structures, taken from Refs. 17 and 20, are supported all-around. From the practical point of view, these structures are only of academic interest. The boundary conditions such as free edges, encountered in an umbrella shell (Fig. 4.2), provides a more critical test for the comparison of the different methods.

It was not practical to compare methods 'a' and 'b' for all the examples, therefore only a selected number of structures were chosen for comparison (Struc. '6' and '9' were used). Struc. '6' is a small scale concrete model. In this structure, the stiffening edge members are located eccentrically, on top of the shell. The idealized edge members are considered eccentric only in the z-direction (see Figs. 4.2 and 4.5).

Struc. '9' is also an umbrella shell hyper with 28-G double layered standard corrugated decks placed perpendicular to each other. Here the edge member is connected eccentrically to the deck with the deck on top. In the case of Struc. '6' there is full fixity between the edge member and the shell, whereas in the case of Struc. '9', the connection between the

deck and the edge member is moment-free.

The comparison of the deflected profile obtained by methods 'a' and 'b' and the corresponding deflected shapes are presented in Figs. 4.13 and 4.23. Comparing the solutions obtained by methods 'a' and 'b' for Struc. '9', it is obvious that the method 'a' underestimates the free corner deflection δ_b . Method 'a' gives a good correlation between the theory and experiment for the deflection δ_a .

The deflection profile obtained by method 'b' for the edge member ab, where a major portion of the load is carried by the bending action, is very good when compared with the experimental results. The relative deflection between the points a and b according to experiments is 1.2 inches, method 'b' giving a relative deflection of 1.0 inches; whereas that predicted by the method 'a' is 0.73 inches.

A distortion in the deflected profile for the member ab and the underestimation of the relative deflection between the points a and b, results in the underestimation of the bending and the total stresses at the point a. The bending stress at point a by method 'a' is 8.44 ksi, whereas that by method 'b' is 17.14 ksi. The total stress at the point a by method 'a' is 12.50 ksi, whereas by method 'b' it is 19.90 ksi. The corner deflection δ_b and the stresses at a (Fig. 4.2) are of a great practical significance for a designer, from both the choice of edge member sizes and the overall behavior of the hyper structure.

Another important shortcoming noted of the method 'a' is that the statical check for the total vertical load is not

satisfied at the column. Because a very flexible deck was used for the shell surface, the deck could not transfer a substantial amount of load near the column and the resultant axial component and the vertical shear in the edge member oa should sum up to the total applied vertical load; only 73% of the total vertical load is accounted for by method 'a' whereas 98% of the applied load is accounted for by method 'b'. This discrepancy of the statical check was also noted when working with the computer program formulated by Parker¹⁹.

In the case of Struc. '6', the deflection profiles obtained by methods 'a' and 'b' along the compression member are reasonably close. However, these two methods give entirely different deflected shapes along the tension member ab. According to method 'a', the point b (free corner) instead of deflecting downwards relative to point a, it deflects upwards. The same difficulty was also encountered regarding the corner deflection when using the computer program of Ref. 19. Because a part of the load near the column is also carried by the concrete shell, the thickness of which is quite comparable to the depth of the edge members oa and oc, it is difficult to figure out the statical check for the total vertical load.

The corner deflection of Struc. '8', which is identical to Struc. '6' except for the fact that the edge members are downturned, was found to be quite low when analyzed by the method of Ref. 19, as compared with the experimental results.

Briefly, the shortcomings of method 'a' can be summarized as:

(1) The method underestimates the deflection of the free corner of an umbrella shell where the shell surface degenerates almost to a flat plate.

(2) The prediction of the deflection profile along the eccentrically connected tension members ab and bc is not consistent and leads to the underestimation of the bending and total stresses in the edge members, which are of practical importance.

(3) A discrepancy for the statical check of total vertical load is noted (Struc. '9').

Because of these shortcomings, it was decided to use method 'b' in the analysis of all structures. It must be emphasized that method 'b' does have certain shortcomings, though none as serious as the ones associated with method 'a'. Method 'b' is discussed later in Chapter V.

IV.4 DISCUSSION OF METHOD 'a'

The umbrella shells with flexible edge members show a pronounced bending action near the free corner b (Fig. 4.2). This bending action was observed in tests conducted on concrete shells (Refs. 31,65) and Struc. '9' (using hypar with a corrugated deck) tested at Cornell. The shell in this region acts almost like a flat plate. In Ref. 1, this observed bending behavior of the shell was termed as secondary bending and, based on the non-dimensionalized parameter of $\frac{Ct}{AB}$, the bending moment coefficients for this region were given. Method 'a' based on the use of the shallow shell theory fails to predict

this localized bending behavior at the free corner.

Before discussing this shortcoming of method 'a', it is necessary to point out that in the formulation of the curved element, the nodal displacements (u,v,w) are measured along the tangents and normal to the surface, rather than along the cartesian axes. In other words, the strain displacement relationships given in Eq. 3-9 are all expressed along the lines of generators of the surface. The element stiffness matrix based on these displacements eliminates the co-ordinate transformation. In the solution of the master stiffness matrix, method 'a' gives the displacements along the generators and normal to the surface whereas the method 'b' using flat elements gives these displacements along the global cartesian co-ordinates.

However, because of the shallowness of the shells, (see Section III.2B) the surface co-ordinates along the generators are approximated by the Cartesian co-ordinates defining the surface. Because of this approximation, a constant shearing strain term $\frac{-2WC}{AB}$ is added to the shearing strain of a flat plate (Eq. 3-9c). This term does not reduce to zero near the flat corner b (Fig. 4.2). It is believed that this term adds extra stiffness to the free corner where the structure behaves almost like a flat plate. This addition is probably the cause of the underestimation of the corner deflection. The deficiency of method 'a' in predicting the deflection of the free corner needs further investigation. The solution could possibly be improved by refining the grid size or by the use of higher order strain terms¹¹. But this will definitely entail additional

computational work.

The strain-displacement relationships for the curved element are dependent only on the twist curvature $\frac{C}{AB}$ irrespective of the shape of the actual structure. To explain this further, consider only the quadrant *oabc* of a structure of Type I, Fig. 4.1. One could build two cantilever hypars from this quadrant. The first structure would have edges *oa* and *oc* fixed whereas edges *ab* and *bc* would be free. In the second structure, the fixed and the free edges would be interchanged. If both these structures are subjected to the same loading conditions, method 'a' would give identical deflections and absolute values of the stresses.

The solutions by method 'a' for Strucs. '1' and '2' did not show any advantage of using a 16-term displacement function for *w*-displacement, which ensures the slope compatibility normal to the boundaries of the adjoining element as against the non-compatible 12-term polynomial used in Ref. 19.

The solution obtained for Struc. '2' with the inclusion of complete rigid body modes²⁰ and that obtained in this study, without the inclusion, did not show much of a difference (Fig. 4.6). To study the effects of inclusion of rigid body modes further and also to evaluate the differences in the solution using 16 or 12-term polynomials for *w* displacement, Struc. '15' was analyzed. The results are plotted in Figs. 4.37 and 4.38. It may be worthwhile to note that in this structure the rise to span ratio is rather high for it to be considered as a shallow shell (see Section V.2). The deflection profile

across the diagonal ob shows that there is practically no difference between the solution obtained by the use of a 12-term polynomial for the normal displacement w , and the function used by Banavalkar. The maximum difference of 2% is seen in the corner deflection δ_b (0.090 inches by the present method and 0.092 inches in Ref. 19). Even the u - v displacements all over the shell, obtained by the two methods were within 0.5% of each other. The striking similarity in the results tends to confirm the conclusion that both methods give the same results for the uniformly loaded hypars. This view is also shared by Pecknold and Schnobrich²¹. The comparison may not be as accurate for unsymmetrically loaded hypars where the 16-term displacement function for the normal displacement w would possibly give better results.

However, the comparison with results reported in Ref. 21 shows a difference both in the deflections and stresses (Figs. 4.37, 4.38). Though the deflection profile and the stress variation are alike, the added flexibility of the curved element with the inclusion of rigid body modes is apparent in Fig. 4.37, where the corner deflection is nearly 60% larger than the one obtained in this study as well as by the method used in Ref. 19. Though the solution obtained in Ref. 21 used a 12 x 12 grid size as against a 8 x 8 grid size used in this investigation, it is not believed that the difference in results is due to refining of the grid size.

Analysis of the same structure by method 'b' using flat elements, results in the corner deflection δ_b (0.123 inch) being nearly 33% larger than that given by the method 'a'. As

pointed out earlier, the deflections by method 'a' are given normal to the surface whereas for the method 'b' they are in the global axes. However, this does not affect the corner deflection δ_b . Moreover, the deflection profiles along the compression member oa and the tension member ab, are different for the two methods. It is quite interesting to note that both of these methods, which give close results for edge-supported hypars (see Table IV-3), could differ in the case of this structure (Fig. 4.37). The inclusion of the rigid body modes in the solution seems to account for the correct behavior of the flat corner but since no comparative results - with experiments - are presented²¹, it is not possible to comment on the validity of the method in Ref. 21.

IV.5 THE COMPARISON OF ANALYTICAL AND EXPERIMENTAL WORK

Because of the shortcomings encountered in method 'a', the analysis reported hereafter is carried out by method 'b'. The experimental results used for the comparison can be basically categorized into three types:

(1) Hypars supported vertically along the line of generators all around the perimeters. Strucs. '3', '4' and '5' come under this category (see Table IV-1).

(2) Small scale concrete models of umbrella shells⁶⁵ (Strucs. '6', '7' and '8').

(3) Umbrella shells having standard corrugated open decks for the shell surface (Strucs. '9' - '13').

All the above mentioned experimental tests were conducted at Cornell, except Struc. '5' (Ref. 33). The testing of

the concrete hypars was conducted as a part of a research project currently in progress at the Cornell University⁶⁵.

The comparison between the analytical and experimental results for the deflections, edge member stresses and the deck stresses is given in Figs. 4.9-4.36. In all the analytical solutions, the surface of the hypar is approximated by the tangent planes drawn at the center of the element except in Strucs. '6' and '8' where these planes are drawn at points along the free boundaries ab and bc (Fig. 4.5). However, these two structures were not reanalyzed because of minor differences (<10%) in the results of other similar cases using both methods of transformation.

A. EDGE-SUPPORTED HYPARS

The saddle shaped hypars (Strucs. '3' and '4') were analyzed mainly to find the effect of rise on the value of shear rigidity factor ' α '. The values of the central deflections are given in Tables II-1, II-2. In the experiments, only the central deflection δ_c (Key sketch Table II-1, II-2.) was measured. The results obtained in the analysis of these structures are used in Chapter V, to study the effects of the variation in the structural parameters.

Struc. '5' was a large scale model with the plan dimensions of 50'x30'³³. A single layer of a cellular deck (see Table IV-2) was welded to the edge members using a warped plate connection. The hat section was welded to the base plate with spot welds 1" o.c. The adjoining deck panels were butt welded so as to develop the full strength of the flat plate.

The edge members were free to move in the plane tangential to the shell boundaries but were supported vertically. A $3\frac{1}{2}$ " diameter, high-strength steel tie bar connected the points a and b (Fig. 4.3). A uniform load normal to the surface was applied by vacuuming the enclosed chamber. A predetermined tension force was applied to the tie by means of a 500 ton jack which prevented the relative displacement between the points a and c. However, the details of the connections of members oa and oc were such that there was no force on the member at the ends a and c. The members ba and bc were free to move at the end b. The stresses and the deflections were measured at various locations. The complete details of this test with the instrumentation are given in Ref. 33.

In calculating the membrane constants for the deck, the stiffening effect of the hat is neglected. The membrane stiffness calculated only on the basis of the properties of the base plate, is on the conservative side. Since no seam-slip was noticed during the tests, the shear rigidity factor α is taken equal to unity. The deck is highly orthotropic as is apparent from the bending rigidities ($D_y = 29,300 D_x$). The bending constants calculated on the basis of the geometrical shape are used in the analysis without modifications. As given in Ref. 33, the equivalent projected load is calculated on the basis of equating the shear force at the point o on the actual surface and that given by the membrane theory for an equivalent projected load. The load intensity used in this analysis is 5% on the conservative side of the criteria given in Chapter

III, Section III.4.

The experimental deflection profile along the lines de and fg (Fig. 4.3) are corrected by subtracting the vertical displacements at points d, e, f, and g. The center deflection calculated analytically is 5% on the higher side of the experimental deflection 2.30 inches (Fig. 4.9). As shown in Fig. 4.10, the axial stresses in the edge members are very close to half the values given by the membrane stresses. The reported³³ strain measurements on the edge members tend to confirm this observation. It is quite logical to expect the forces in the edge members to be lower than those given by the membrane theory because a part of the load is carried by the flexural action of the deck.

As shown in Fig. 4.11, the difference between the analytical and experimental results for the shear stresses measured by the rosettes 1 and 2, is even less than 5%. The variation of the shear force all over the hypar surface is shown in Fig. 4.12. As expected, the value of the shear force over a major portion of the shell surface is less than that given by the membrane theory. The increase in the shearing force noted at the corners a and c is due to the restraint offered by the tie; whereas the value of the shearing force in the fixed corner o is almost twice as that given by the membrane theory.

The connection between the edge members and the deck should be adequate enough to carry this high value of shear. The bending stresses calculated at the center of the span on the top of the hat, do not show good correlation with the exper-

imental results. The bending stresses calculated using the effective inertia I_{ed} (Chapter II, Section II.2.B) is 6.70 ksi, whereas the measured total stress in the y-direction at the same location is 12.50 ksi. One reason for this underestimation is that the measured stress is total whereas the calculated stress is only due to bending. Since in calculation of the membrane stiffness only the flat plate was considered, it is not known as to what extent the hat portion participated at the center of the deck in resisting the membrane stresses.

The reduction in the moment of inertia calculated on the basis of the full cross-section, is not affected by the calculated compression stress in the top hat plate (the variation is less than 5%). The change in the bending rigidity D_y does not warrant a new analysis.

B. CONCRETE UMBRELLA SHELLS

The concrete hypars differ from the hypars using corrugated orthotropic decks mainly in two aspects. For the loads used in the elastic analysis of this study, the shell can be considered as made of an isotropic material. Secondly the bending and axial stiffness of the shell is quite comparable with that of the edge member.

The experimental work on Strucs. '6', '7' and '8' was conducted at Cornell⁶⁵. Strucs. '6' and '7' were identical except for different eccentricity of the edge members (Fig. 4.5). In Struc. '6' the beams were located on the top of the shell surface whereas they were located below the deck in Struc. '7'. These structures were loaded uniformly using concentrated

loads applied discretely over the surface, whereas only half of the structure was loaded in the case of Struc. '8'.

The elastic properties of the concrete used in the model were determined experimentally. In calculating the properties of the shell only the concrete section is considered. The classical beam theory which assumes the linear variation of the angle of twist is used in the analysis. The beams are considered eccentric only in the z-direction. The beam properties calculated are based only on the ribs projecting above the deck.

For Strucs. '6' and '7', the comparison between the experimental and the analytical results are shown in Figs. 4.13-4.19. As shown in Fig. 4.13, for Struc. '6' the compression rib deflection δ_a is about 10% smaller than the experimental results whereas the free corner deflection δ_b is about 5% larger than the experimental value. For Struc. '7' (Fig. 4.17), the deflection δ_b is about 60% and δ_a is about 80% of the experimental values. Though percentage-wise the error in δ_a , in Struc. '7' is about 40%, the magnitudes of the deflections are very small. Except for the deflection profile along the diagonal ob near the column support, the general shapes of the profile agree fairly well with the experimental values. The deflection profiles of the tension members ab in both the structures, where the bending action in the shell dominates over the membrane action, is very good and almost parallel to the one observed experimentally.

To verify the idealization of the edge member, Struc. '6' was reanalyzed, but a certain portion of the deck was in-

cluded as the effective width in recalculating the beam properties. The modified eccentricity of the beam with respect to the deck and properties were recalculated. It is obvious that in doing so a certain portion of the deck is duplicated, with the result that the properties of the edge members are overestimated. For the same structure it was found that the free corner deflection δ_b remained almost unaltered (0.022 instead of 0.023) whereas the deflection δ_a reduced from 0.016 to 0.012 inches. This observation shows that important deflections are insensitive to the edge member properties for this particular structure. However, there is a redistribution of the bending and axial stresses in the shell, which are of a relatively small magnitude. The upturned beams used in Struc. '6' seem to have a pronounced effect in reducing the corner deflection δ_b as seen from the analysis as well as experiments. The free corner deflection δ_b for Struc. '6' is nearly half that of Struc. '7' whereas the compression rib deflection δ_a for Struc. '6' is larger than that for Struc. '7'. These points are further discussed in Chapter V.

Because of the varying size of the edge members, the axial forces are plotted instead of axial stresses. The ratio of the calculated axial forces to that given by the membrane theory is 70-80% for the compression members oa and oc and 50-60% for the tension members ab and bc. The analytical and experimental values of the stresses for the tension member are in close agreement, whereas the analytically calculated results for the compression members are on the conservative side.

Even though part of the vertical load near the column is carried by the concrete shell, in order to satisfy the static equilibrium for the vertical load it appears that the experimentally measured forces in the compression rib are quite low.

The axial and the bending stresses are measured along the diagonal ob at an angle of 45° with the x and y axes (Fig. 4.15). The measured axial stresses show excellent agreement with the analytically calculated value of 72 psi. An important point to note is that the calculated and the experimental values are about 34% higher than those given by the membrane theory at a load of 40.9 psi, the reasons for which are not readily apparent. The values of bending stresses are very low and are not compared here. The variation of the shearing force is plotted all over the shell for both the structures. Though there are minor differences in the shape of variation of shearing forces, two important observations can be made. The values of the shearing forces over a substantial portion of the shell, are larger than those given by the membrane theory. The shearing force near the column is nearly twice as large as that given by the membrane theory. This sudden increase in the shearing force clearly indicates that the shell participates in transmitting a certain portion of the vertical load. The same behavior is also noted in Struc. '5'.

Struc. '8' is the same as Struc. '6' but it is subjected to an unsymmetrical load (Fig. 4.20), where half of the structure is loaded uniformly. Only half the structure along the line cf (Fig. 4.20) is analyzed using 16 elements in each

quadrant. The statically equivalent load is used in one quadrant. The central column is idealized by means of concentrated elastic springs as given in Chapter III, Section III.2.F. The comparison between the theoretical and the experimental results is shown in Fig. 4.20. The deflection profiles appear to be quite reasonable though the magnitudes of the deflections δ_b and δ_e are 30-40% on the lower side of the values obtained experimentally. A static check for the vertical load is satisfied at the center column though a discrepancy in the overturning moment is noted.

A highly irregular pattern of axial forces and moments is obtained which unfortunately could not be verified properly because of the difficulties encountered during the experiment. A better solution can be obtained by using a finer grid (64 elements in a quadrant) and also by using work equivalent loads. It was not possible to check the improvement in the solution because of a limited computer core capacity. The example however, clearly showed that the theory can solve unsymmetrical loading conditions such as wind load, etc., and can satisfactorily predict the overall behavior of the shell.

The corner deflection δ_b in Struc. '8' is nearly three times as large as that obtained for the uniformly loaded Struc. '6'. The increase in deflections in the loaded quadrant is mainly due to the twisting of the shell about the line ah.

C. UMBRELLA SHELLS WITH STANDARD CORRUGATED DECKS

Four medium scale umbrella shell models (Strucs. '9', '11', '12' and '13'; Table IV-1), 12x12' in plan and with a

rise of 14.4 inches, were tested at Cornell. Struc. '10' is a hypothetical structure analyzed to study the effects of change of shape in Struc. '9' due to the excessive deformations.

Self-tapping screws were used to connect the adjoining deck panels and also to connect the deck panels to the edge members. The main supporting edge member frame consisted of circular pipes (for sizes see Table IV-1) connected eccentrically below the deck.

For the structure having two decks placed in a mutually perpendicular manner, the decks were not only connected along the peripheral edges but were also connected intermittently all over the surface. In the case of the two deck system, the bottom deck was directly connected to the edge member whereas the top deck was connected to the bottom deck (Fig. 2.6). All structures were supported at the center column and a uniform load was applied using pressurized canvas rubber bags with one bag placed under each quadrant (see Chapter VII).

The properties of the decks used in the analyses are given in Table IV-1. The gage thickness of the deck was checked by the micrometer screw and the properties corresponding to the uncoated decks are used in the analyses. To account for the effect of rise, the shear rigidity factors used in the analyses are modified from the values obtained by the flat shear tests (Figs. 2.7 and 2.8). The reduction in these values of α is roughly 25% for the single deck whereas it is about 15% for the double decks. Zero torsional fixity between the deck and the edge members is assumed for all the structures analyzed.

In order to have a better understanding of the behavior of these structures, they are classified into two categories. This classification is based on the ratio of the relative stiffnesses of the deck and the supporting edge members. Strucs. '9' and '10' are considered to have flexible edge members whereas Strucs. '11', '12' and '13' are considered to have very stiff edge members. The edge members used in Strucs. '11', '12' and '13' are 4.37 times stiffer axially and 236 times stiffer flexurally as compared with the edge members used in Strucs. '9' and '10'. This large difference particularly in the bending stiffness alters the behavior of the umbrella shells.

C.1. INVERTED UMBRELLA SHELL WITH FLEXIBLE EDGE MEMBERS

Strucs. '9' and '10' were analyzed using the boundary condition V (Table IV-2) which assumes full horizontal fixity between the edge members and the deck. The convergence characteristics for the corner deflection δ_b for Struc. '9' are shown in Fig. 4.22. By refining the grid size, the free corner deflection increases. This is because of the effect of eccentrically connected edge members (Fig. 3-12). The difference in the corner deflection δ_b between 6x6 grid size and that of 8x8 grid size is less than 2%.

The deflections and the edge member stresses obtained for Struc. '9' are compared with the experimental results in Figs. 4.24-4.28. The analysis underestimates the deflection δ_a by 32% whereas the deflection δ_e is overestimated by 40%. The difference between the analytical and experimental results for

the corner deflection δ_b is 10%. Comparing the relative magnitudes of these deflections (δ_a , δ_b and δ_e), it is apparent that in the case of a flexible edge member the free corner deflection δ_b is of utmost importance. The shape of the deflected profile for the member ab and the relative deflections between points a and b, by theory and experiments are in close agreement (error $\hat{=}$ 1%). The reasons for the underestimation of the compression rib deflections are discussed later in this section.

The corner deflection δ_b is greater than 10% of the rise of the hypar shell, which is 14.4 inches. In other words, the change in the shape of the structure is quite important. To estimate the effect of the change of shape, a very approximate method was used whereby the same structure (Struc. '9') was reanalyzed by only modifying its rise from 14.4 inches to 13.8 inches. The reduction of 0.6 inches in the rise was calculated by taking half the difference between the relative deflections of the points a and b. The analysis of Struc. '10' using the modified rise, shows an increase in deflections. The error in the deflection δ_b in particular is reduced further to 4%.

A comparison between the experimental and the analytical results for the axial and bending stresses, and the absolute value of the total stresses for the edge members is given in the Figs. 4.25 and 4.26. The bending and the total stresses show very good correlation with a maximum error of -15% for the tension members. Comparing the analytical and experimental results for the axial stresses, it is noted that the calculated

compression stresses for members oa and oc are on the high side whereas in case of the tension members ab and bc are on the low side. The measured axial stresses are only about $\frac{1}{4}$ th in magnitude of the total stresses and therefore the deviation (-55% for the member ab) between the theory and experiment is not considered to be a serious handicap.

To examine the validity of the solution and also to help to understand the behavior of hypars, the variation of the bending moment M_y and the in-plane shearing force N_{xy} are plotted over the shell surface (Figs. 4.27 and 4.28). Along the column line 1 (Fig. 4.27), the deck bends with the tension member like a cantilever (negative moment) whereas in the interior of the span, it acts as a simply supported span between the opposite edge members. Along the column line 8, the deck has a region of negative bending moments near the supporting column. The variation in the shearing force (Fig. 4.28) is similar to that indicated for the concrete hypars (Strucs. '6' and '7'). Near the center of the quadrant, the shearing force N_{xy} is larger (by 10%) than the values given by the membrane stresses. However, one major difference noted between the concrete and corrugated deck hypars is that near the column the deck does not carry a substantial portion of the vertical load as is seen in the case of Figs. 4.16 and 4.19. The comparison of the axial, bending and total stresses calculated by theory and measured experimentally at point e is given in Table IV-4.

The calculated stresses are compared with the average measured values obtained for the top and bottom deck. Be-

cause of the very small magnitude of the stresses, the variation in their measured value was extreme. The variation in the measured axial stress ranges from 210 psi to 1780 psi whereas that in the bending stresses ranges from 140 psi to 2840 psi. Though the calculated values appear to be in the vicinity of these measured values, a direct comparison would not be fruitful.

In the analytical solution of Struc. '9', it is noted that the deflection δ_a is underestimated. Fig. 4.29 shows a typical connection between the tension member ab and the compression member oa. Because of the eccentric connection between the deck and edge members, all the node points are along the top of the edge members ab and oa. The in-plane forces on the member ab are transferred eccentrically to the member oa at the node a, resulting in its upward deflection as shown in Fig. 4.29. In order to illustrate the effect of this eccentric transfer of the in-plane forces, Strucs. '9' and '11' are analyzed for the two boundary conditions V and VI (see Table IV-2).

For Struc. '9', in spite of certain redistribution of forces due to the change in the boundary conditions, there is practically no change in the deflections δ_e and δ_b . The release of the in-plane shear of 328 lbs. acting eccentrically at point a, results in an increase in the deflection δ_a by 0.17 inches (Fig. 4.30). This shear, if resisted entirely by the compression member oa acting as a cantilever supported at point o, produces a deflection of 0.22 inches. Except for the

bending stresses in the tension members ab and bc, the changes in the stresses for both the edge members and shells are insignificant. As shown in Fig. 4.31, the decrease in the vertical shearing force due to the release of the in-plane forces results in the reduction of bending stress at point a in member ab.

From the consideration of the magnitude of the in-plane shear and its eccentric transfer, Struc. '11' represents an extreme case. As shown in Fig. 4.32, the deflection profile along the diagonal ob remains practically unaltered for both boundary conditions for Struc. '11'. Because of the very high in-plane rigidity of the 3" diameter pipe, the value of the in-plane shear developed at the junction a (Fig. 4.29) is quite large (742 lbs.). Though small in magnitude, the increase in the compression rib deflection δ_c and δ_a is almost 200%. The increase in deflection exceeded that which would have been obtained by considering the edge members oa and oc as cantilevers, acted upon by the eccentric shears at points a and c respectively. A small increase in the deflection δ_b is noted and it must be pointed out that the transfer of the eccentric force also exists at the junction of the tension members but it is of minor importance.

In the case of concrete hypars where full fixity between the edge member and the shell exists, this transfer of eccentric forces in two mutually perpendicular directions does not present a problem. To get an exact solution for the discontinuities between the edge member and the steel deck, equa-

tions of compatibility will have to be satisfied at the additional nodal points thereby increasing the complexity and the storage requirement for the computer program. Both cases presented here, particularly Struc. '11', represents an extreme class of problems which will be hardly encountered in practice. Besides the eccentric connection, the in-plane stiffness of circular pipes is equal to the vertical bending rigidity. On the assumption of full horizontal fixity between the edge members and the deck, the horizontal stiffness attracts high in-plane shears, the magnitudes of which raise the question of its validity.

In practice, the rolled sections such as channels and I-sections have very small in-plane stiffnesses as compared with their bending stiffnesses. Secondly, these members will be usually connected along their shear centers by means of warped plate connections (Fig. 3.10). One way to correct the deflection δ_a is by applying the moments, equal in magnitudes but opposite in directions, to those produced by the eccentric shears at the junction of two eccentric members (Fig. 4.29) and recalculate the deflections of only the supporting frame.

Since the exact amount of horizontal fixity is not known, the other alternative is to reanalyze the structure with a complete release of the in-plane forces (boundary condition VI) and use the conservative results for the design.

C.2. INVERTED UMBRELLA SHELL WITH STIFF EDGE MEMBERS

Strucs. '11' and '12' used single corrugated decks whereas Struc. '13' used two perpendicularly placed intercon-

nected decks. The structures are analyzed using the boundary condition VI. This boundary condition is on the conservative side as far as the computation of deflections are concerned.

Fig. 4.33 shows the comparison of the experimental and analytical deflection profiles along the diagonal ob, for all the three structures. Besides this, the comparison between the measured and calculated deflections at points a, b, c and e is given in Table IV-5. During the experiments, difficulty was encountered in obtaining the symmetry of deflections. The unequal rate of leakage from each canvas bag, placed under the quadrant resulted in an unequal pressure loading being applied to different quadrants. In order to show this resulting unsymmetry in the solution, Table IV-5 shows the average, maximum and minimum measured values for the deflections. A comparison between the results is based on the average value. In general, the shape of the deflection profile along the diagonal ob shows a reasonably good correlation between theory and experiment. The deflection δ_e at the center of the quadrant for a single deck hypar (Strucs. '11' and '12') is overestimated by the theory whereas the deflection for a double deck (Struc. '13') shows a difference of only 10% from the measured value. Except for the minor scatter of the deflections δ_a , δ_b and δ_c , the analytical results are within 15% of the average experimental values.

The axial and bending stresses are measured at five locations (Table IV-6). For the bending stresses greater than 2000 psi, the experimental and analytical values show a devia-

tion of less than 20%. For very small magnitudes of stresses (such as less than 2000 psi) the calculation of the error based on the measured stresses will be misleading. The accuracy of measurement for the small magnitudes of stresses is always less. The measured total stresses also show a fair amount of agreement with the analytical solutions.

The major discrepancy arises in the comparison between the measured and the calculated axial stresses. Based purely on the membrane theory, the maximum axial stress should be 1570 psi; as against this, the measured value of stresses reaches as high as 2440 psi (Struc. '11') which is nearly 55% larger than that given by the membrane theory. This appears inconsistent with the expected behavior, since a part of the load is also carried by the bending action.

In order to understand the difference in behavior between the single layer and double layer decks, Figs. 4.34 and 4.35 show the variation of the axial stresses and the vertical shearing forces carried by the edge members. For Struc. '11' (which has a 28-G single layer deck), both the compression member oa and the tension member bc placed across the corrugations (along the weak axis), carry high axial loads as compared to the members ab and oc, placed perpendicular to the direction of the corrugations. This trend is also observed experimentally. Because of very low in-plane stiffness across the corrugations, the effective area of the deck resisting the in-plane shear along with the edge members oa and bc is very small and therefore the entire shearing forces are resisted by the

edge members alone. As against this, in a direction along the corrugations a part of the deck shares the in-plane shear and subsequently results in the reduction of the axial stresses in the edge members.

Fig. 4.35 shows the transfer of the vertical load to the edge members. With the strong axis of bending placed parallel to the lines oa and bc (Fig. 4.2) the deck basically bends between the supporting lines oa and bc . With $D_y = 1845 D_x$, practically no load is transferred directly to the edge members oc and ab . However, from the conditions of compatibility at points b and c , the member bc is supported at its end by members ab and oc . The negative shearing force at the point b on the member bc and the constant shearing forces along the members oc and ab confirm this expected behavior. This manner of transfer of load for a single deck is also reflected in the bending stresses at points a and e (Table IV-6) which are higher than those for double decks (Struc. '13').

The measured axial and bending stresses at the center of the quadrant were highly erratic and did not show any consistent behavior. The minimum measured bending stress was half the value of the maximum measured value at the same location. This wide range of scatter is due to two reasons, first the magnitudes of stresses are too small to be measured reliably and secondly there was an unsymmetry due to unequal pressure loading. For completeness, the comparisons between analytical and experimental values for the deck stresses are given in Table IV-4. The bending stresses for Strucs. '11' and

'12' are overestimated by the analytical method whereas they are underestimated for Struc. '13'.

Fig. 4.36 shows the variation of the in-plane shear force N_{xy} over the entire shell surface for Struc. '11'. An almost identical variation in the in-plane shearing force is also obtained in Struc. '12' (24-G single deck) which has 61% larger shear and bending rigidities than those of Struc. '11' (28-G single deck). For Struc. '13' with a 28-G double layered deck, the shear force distribution is very similar to that obtained for Struc. '9' with 1' diameter flexible edge members. However, the maximum values of the shear force are about 5-10% lower for Struc. '13'. The only noticeable difference for the variation of the shear force for single and double deck structures is that, in the case of the former structure, the maximum value of the shearing force does not exceed the shearing force given by the membrane theory whereas it exceeds the membrane shear force in the latter case. It may be of interest to note that the results for the deflections of the deck are quite close to those reported in Chapter VII. With the stiff members, as those used in Strucs. '11', '12' and '13', the deflections along the free boundaries are small and therefore the behavior of the shell is quite close to that of an edge-supported hypar for which, as pointed out earlier, methods 'a' and 'b' give the same results.

The salient features differentiating the behavior of the hypar with very stiff edge members (Strucs. '11', '12' and '13') and the behavior of the hypars with very flexible edge

members (Strucs. '9' and '10') are further discussed in detail in Chapter V. The effect of the edge member weight on the behavior of hypars is also discussed in Chapter V.

IV.6 SUMMARY

The validity and the accuracy of the finite element methods were assessed. Both approaches were found to converge satisfactorily. A grid of 6 by 6 gave essentially the same results as a grid of 8 by 8.

For hypars with fully supported edges, both the flat-element and the curved-element methods yielded deflected shapes that are identical with those given in the literature. Satisfactory agreement was also found with experimental results even when the effects of eccentric edge members were included. However, the deflections of flat corners, such as those at the outside corners of umbrella-type hypars, are underestimated by the curved-element method. The flat element approach predicts the experimental deflections and stresses of various types of hypar structures with satisfactory accuracy.

CHAPTER V

QUALITATIVE EFFECTS OF PRINCIPAL VARIABLES ON BEHAVIOR OF HYPARS

V.1 INTRODUCTION

Based on the analysis of some selected structures (Table IV-1) it is possible to show qualitatively the effects of different parameters on the behavior of a hypar shell. Since the number of parameters affecting the behavior of the shell is quite large and their interaction is very complex, attempts to show their effects on the structural behavior by means of formulae would involve extensive computational work. During the following discussion some of the parameters which were not investigated are mentioned.

The structural variables affecting the behavior of the shell can be broadly classified into four categories:

- (1) Geometric shape of the hypar shell.
- (2) Properties of the deck used as a hypar surface.
- (3) Boundary conditions.
- (4) Loading.

V.2 GEOMETRICAL SHAPE

All hypar surfaces have a constant twist curvature $\frac{C}{AB}$. The effect of rise to span ratio on the central deflections of the saddle shaped hypars (Strucs. '3', '4', Table IV.1) is illustrated by plotting the deflections against the non-dimensional parameter of $\frac{AB}{C^2}$ (Fig. 5.1). With the increase of

rise to span ratio, the curvature of the surface increases. This increase in curvature reduces the bending action of the shell whereas the membrane action is increased and this eventually leads to the decrease in the central deflection.

The effect of the rise can be shown by comparing the central deflections of a simply supported 28-G square plate (60"x60" in plan) with those of a hypar having a rise of 7.5 inches (rise to span ratio = 1/8) (Fig. 5.1). The deflections in the latter case are nearly 40% of those obtained in the former case.

The sensitivity of the structural behavior to the change of rise is well demonstrated by comparing the deflections and the stresses for Strucs. '9' and '10' (Table V.1) where the rise of Struc. '10' is only 4.3% smaller than that of Struc. '9'. The increase in the bending action with the reduction in rise is evidenced by the increase in the deflections δ_a , δ_b , δ_c , and δ_e and also in the bending stresses.

The bending stress in the center of the deck increases from 1870 psi to 2130 psi. According to the membrane theory, the in-plane shear force is inversely proportional to the rise to span ratio ($N_{xy} = \frac{q \cdot AB}{2C}$). The same trend is also observed in the increase of the in-plane shear and the axial edge member stresses (Table V-1).

For larger values of $\frac{AB}{C}$ ($\frac{C}{A} < \frac{1}{8}$), the membrane action is reduced to a minimum and the entire load is practically carried by bending action. The calculation of the in-plane shear on the basis of the membrane theory, as C approaches zero,

is meaningless. The theory given here is primarily good for rise to span ratio of $\leq \frac{1}{4}$ ($AB/C^2 \approx 15$) but it can be used for greater rise with loss of accuracy. From the construction point of view, the choice of rise to span ratio will be also governed by the warping of the deck.

V.3 DECK PROPERTIES

In the case of an open form deck, the membrane elastic constants E_{xt} , E_{lt} and the bending constants D_x , D_1 and D_{xy} (Fig. 2.1) are very small and their influence on the behavior of the shell is insignificant (for the stiffness coefficients see Appendix B). However, in the case of the closed cellular decks, though the magnitudes of D_x and D_1 are small and insignificant, E_{xt} , E_{lt} and D_{xy} are comparable in magnitudes to the properties E_{yt} , D_y and E_{xyt} and therefore their influence on the structural behavior cannot be overlooked. Since only one structure was analyzed for the cellular deck (Struc. '5'), the discussion given below primarily concerns the open form (standard sinusoidal) decks.

A. SHEAR RIGIDITY

According to the membrane theory, the normal loads on the hypars are carried by the in-plane shearing force N_{xy} . In reality, though a part of the load is carried by bending, the magnitude of the in-plane shear N_{xy} is quite comparable to that given by the membrane theory (Figs. 4.12, 4.16, 4.19, 4.28, and 4.36) and even exceeds it in certain regions of the shell. Therefore the in-plane shear resistance $E_{xyt} = G_{eff} \cdot nt$, is very important in the behavior of hypars. As discussed in Chapter

II, the effective shear modulus (G_{eff}) is obtained by reducing the shear modulus of the material by the factor α . In the saddle shaped hypars (Strucs. '3' and '4') for a rise to span ratio of 1/5 ($AB/C^2 = 25$) (Fig. 5.1), the reduction in the shear rigidity α from 0.06 to 0.04, shows an increase of nearly 30% in the central deflection. The behavior of the hypar shell is very sensitive to the values of $\alpha \leq 0.10$.

To illustrate the effects of α on the behavior of the shell, the results for Strucs. '13' and '13a' are compared in Table V-1. With the increase in the value of α , the deflections (δ_e, δ_b) and the edge member and deck bending stresses are reduced whereas the axial stresses in the edge members and the in-plane shear force N_{xy} are increased. Except for the axial forces in the edge members and the in-plane shear N_{xy} , the response of the structure to the variation in α is similar to that of the variation in the rise to span ratio. The optimum value of α in orthotropic hypar structures is $\alpha \approx 0.1$ since larger α does not improve the behavior much. Factors which improve the value of α were already discussed in Chapter II.

B. THICKNESS OF THE CORRUGATED DECK

In the case of an open deck the important membrane properties such as E_{yt}, E_{xyt} and the bending rigidity D_y are directly proportional to the thickness of the deck. However, it must be pointed out that the bending rigidity of the deck is small compared with the membrane stiffness. Moreover it is the change in the shear stiffness that influences the behavior

of the hypar shells and therefore the effect of increasing the thickness is analogous to that of increasing the value of α . To substantiate this observation the comparison between the deflection and stresses for Struc. '11' (28-G single deck) and Struc. '12' (24-G single deck) is given in Table V-1.

The variation of the in-plane shear rigidity, which is directly proportional to the thickness and the shear rigidity factor α , also affects the manner in which the vertical load is transferred to the supports by the membrane action. Because of the high shear rigidities for the concrete structures ('6' and '7') and Struc. '5' using the cellular deck with the full effectiveness of the bottom plate, the values of the in-plane shearing forces show a substantial increase near the supports (Figs. 4.12, 4.16, 4.19). The increase in the shearing force indicates the participation of the deck in carrying a part of the vertical load. As against this, Strucs. '9'-'13' with low shear rigidity do not show any increase in the in-plane shearing force (N_{xy}) near the supporting columns (Figs. 4.28, 4.36). In other words, in these structures the entire vertical load is primarily carried by the edge members.

C. NUMBER OF DECKS

As far as deflections and stresses in a hypar are concerned increasing the number of decks has the same effect on the behavior of the shells as that of increasing the shear rigidity factor α and the thickness. However, this observation does not apply for buckling (see Chapter VI). As discussed in Chapter II, the effectiveness of the deck in resisting the

loads depends upon the manner in which two or more decks are interconnected and connected to the supporting edge members. However, it must be pointed out that in order to avoid chatter and get a better structural performance, it is desirable to interconnect the decks all over the surface of the shell.

When two decks are used, they are placed in a mutually perpendicular manner and this gives an equal bending rigidity to the structure in both directions, thereby distributing the applied loads more evenly to the supporting edge members. The comparison of the results for Struc. '11' using a single deck (28-G) and those for Struc. '13a' using the double deck, all other constants being the same, shows that the uniformity of the stiffness in Struc. '13a' has more even distribution in the edge member axial stresses (Table V-1). Though the corner deflection shows practically no change, the center deflection δ_e for Struc. '13a' is nearly half that of Struc. '11'. The change in the bending stresses of the edge member is very small but because of the increased membrane action the bending stresses in the center of the quadrant are reduced by nearly three times.

In practice, the use of a double deck with two decks placed mutually perpendicular is more desirable than a single orthotropic deck.

V.4. BOUNDARY CONDITIONS

From the practical point of view, boundaries such as simply supported, knife-edge supported or fixed all around, are not realistic. Boundary conditions which consider the proper-

ties of edge members and the manner in which they are connected to the deck are realistic from the practical point of view.

A. EDGE MEMBER PROPERTIES

The edge member properties A_b , I_y , I_z , J and Γ_b for available rolled sections show variations over a wide range. A sufficient number of analyses could not be carried out to formulate any definite rules by which the effect of the variation of these individual properties on the behavior of the shell can be assessed. Except for the concrete hypars, the analysis was carried out for zero torsional fixity and therefore the influence of the torsional constants J and Γ is not clearly known.

To get the general idea of the effect of the stiffness of the edge members, one can compare the results of Struc. '13' with very stiff edge members and Struc. '9' with very flexible edge members. The difference in the behavior of these two extreme structures is obvious from the deflection profile along the diagonal ob (Figs. 4.24 and 4.33). In the case of Struc. '13' because of very high bending rigidity of the edge members, the deflections along the periphery are quite small and the deck bends freely between the opposite supporting edges. The simply supported plate bending action is quite dominant in this case. Because of the small bending rigidities of the edge members in Struc. '9', it appears from the deflection profile along the diagonal ob that it is the deck that supports the edge members near the free corner and therefore the deck stiffnesses (both bending and membrane) are quite

important for this structure.

The fact that the corner deflection δ_b for Struc. '13' is not very different than that of Strucs. '11' and '12', where single layer decks with different shear rigidities and thicknesses are used, clearly indicates that the deflections along the periphery of these structures primarily depend upon the properties of the edge members. In order to optimize the interaction between the deck and the edge members to give a satisfactory structural performance, the ratio of the bending rigidities of the deck and the edge members would have an optimum value between the two extreme cases (Struc. '9' and Strucs. '11'-'13').

B. EDGE MEMBER AND DECK CONNECTION

As shown for Strucs. '6' and '7' (Table IV-1), the eccentric location of the edge members affects the deflection of the structures (Figs. 4.13 and 4.17). The difference in behavior of the edge members is shown in Fig. 5.2. For umbrella shells to reduce the vertical deflection for the compression member, it is beneficial to connect the deck on top of the edge member whereas in the case of the tension members, it is beneficial to connect the edge member on the top of the deck. The experimental as well as the analytical results for Strucs. '6' and '7' seem to confirm this conclusion.

No comparative results are presented for the zero and full torsional fixity, though results are presented for the full and zero in-plane fixity (T_H) between the edge members and the deck (Figs. 4.30-4.32). Though the results are very

limited, it is believed that providing fixity along the peripheral edge members tends to attract more vertical load on the edge members (Fig. 4.31).

In the case of saddle shaped hypars, the increase in area of the tension tie bar connecting the lower corners (Key sketch, Table II-1) of the shell and the in-plane bending rigidity of the peripheral edge members have beneficial effects in reducing the bending action of the shell¹⁹. The effects of these variables may need further investigation.

V.5. LOADING

All the conclusions given above on the behavior of the hypars are based on the analysis for the uniformly distributed vertical loading. In reality the structures are also subjected to unsymmetrical loads such as wind or drifting snow. The strength of the structure under these kinds of loads is tested more severely than under the conditions of uniform loads. The unsymmetrically loaded Struc. '8' shows the corner deflection δ_b nearly three times as large as that obtained for the uniform loading condition.

A. EDGE MEMBER WEIGHT

In case of some shells, such as umbrella shells, the edge member weight is distributed along the periphery of the shell. The customary procedure of smearing this load uniformly over the whole surface and analyzing the structure can lead to a gross underestimation of both the deflections and the stresses. To demonstrate this, an umbrella shell with each quadrant of 20'x20' in plan having a rise of 4', (Table IV-1)

is analyzed. The edge member sizes and the deflection tolerances used for this structure represent the values which are encountered in practice. The deflection profiles and the bending stresses for the edge members, with and without the inclusion of edge member weights, are shown in Figs. 5.3 and 5.4. The weight of the edge member is 20% of the total uniform load of 40 psf over the whole surface. A simple frame analysis considering only the edge member weight and edge members, would have given an increase of 0.74 inches in the deflection of point a (as against 0.33 inches) and 0.202 inches in the deflection of point b relative to point a (as against 0.15 inch). This shows the effectiveness of the shell in carrying the weight of the edge members. The cable and the arch action along the diagonals ac and ob is evident in Figs. 5.3 and 5.4. The increase in the deflections δ_a and δ_c produces an upward deflection at the center of the span.

The axial stresses for both the tension and the compression members show an increase of nearly 20%. This is equal to the increase in the total load of the structure by the inclusion of the edge member weight. The bending stresses for both the tension and the compression edge members show an increase of nearly 50% in the maximum stresses (Points o and a, Fig. 5.4). The increase in the bending stresses clearly indicates the unconservative assumption of smearing the edge member weight over the whole surface.

The effectiveness of the shell in carrying the weights of the edge members raises an important question as to the

method of construction. The situation is analogous to that encountered in a composite construction using steel beams and concrete slab. There are three alternatives for the construction. Depending upon the size and shape of the shell, with the decks in position, a hyper can be built on the ground and erected in position; or it can be built in place by using an adequate shoring for the edge members. In these methods of construction, the effectiveness of the shell in carrying the weight of the edge member will be utilized. The third way of construction will eliminate the shoring and depend entirely upon the strengths of the edge members. The economics will obviously decide the method of construction.

From the analysis of the different structures, it is found that the axial stresses in the edge members derived on the basis of the membrane theory are always overestimated (Table V-2). Because of the relatively small magnitude of the edge member stresses in comparison with the bending stresses and with the uncertainty in the calculation of the exact bending stresses, the design of the edge members for the axial stresses based on the membrane theory cannot be considered to be on a very conservative side.

From the analysis of different structures it appears that the non-dimensional parameter $\frac{\alpha C n t}{\Delta B}$ provides a good index for the behavior of the shells. The higher the value of this constant, the more dominant is the membrane action. As dis-

cussed earlier, the beneficial membrane action reduces both the bending stresses and the deflections of the shell. A second good non-dimensional parameter would be the relative stiffness of the deck and the edge members. This however would need further study.

CHAPTER VI

INSTABILITY ANALYSIS OF HYPARS

VI.1. INTRODUCTION

The linear stiffness analysis given in Chapter III does not include the effects of middle-surface forces N_x , N_y and N_{xy} on the behavior of hypar shells. The omission of these effects precludes the possibility of the analysis of instability of the individual finite elements. The accumulation of the instabilities of the individual elements eventually leads to the general instability of the structure.

In the case of a hypar with light gage steel deck used as a shell surface, the effect of the in-plane forces is manifested in three different types of instabilities:

(1) Local Buckling - In the case of a N-type open deck or a cellular deck (Fig. 2.2b and c) the deck is composed of flat plates. These individual plate components, depending upon the thickness to width ratio and the boundary restraint offered by the adjoining plates, may buckle locally when subjected to in-plane compressive and shearing forces. In spite of the uncertainty in the degree of restraint offered by the adjoining plates, this local buckling can be approximated on the basis of the stress level in each component plate³⁶. The effect of the local buckling on the behavior of light gage beam section is discussed in detail in Refs. 38, 39.

The local buckling of the individual plate components

results in the redistribution of the total stiffness of the shell. The theory used in this chapter does not account for the local buckling and therefore the effect of local buckling on the shell stiffness cannot be predicted. The local buckling can be prevented by choosing proper thickness to width ratio for each individual plate element.

(2) Deck Buckling - In this mode of buckling, the edge beams remain stable whereas the deck, used as a shell, buckles as a unit. To understand the deck buckling, consider the umbrella shell in Fig. 4.2. The deck acts primarily as a compression arch between the points o and b, and therefore it can buckle along the diagonal ob; but the shell edge members remain stable.

(3) Overall Buckling - The shell and the edge members buckle as a whole unit. One can imagine an umbrella shell, folding down as an umbrella turned inside out. Overall buckling could occur either simultaneously with the deck buckling or it can happen after the deck has buckled.

According to a simplified analysis by Parker¹⁹, the possibility of overall buckling for the practical size of edge members is very remote. Very high values of deflections and stresses for both edge members and the deck will indicate the possibility of overall buckling. The conclusion that overall buckling is very unlikely is further verified by Struc. '9' (Table IV-1) tested at Cornell, where 1" diameter standard pipes were used as edge members. The resulting structure was too flexible to be used in practice. In spite of excessive

deformations (nearly one half the rise of 14.4"), the structure did not show any tendency of overall buckling though the deck buckled.

The present study was primarily concerned with deck buckling. However, the overall instability due to the buckling of the edge members can also be predicted from the load deflection curve. The assumptions used during the analysis and the limitations of the theory are as follows:

(1) A linearized stability analysis was carried out to predict the bifurcation point of buckling^{51,66}. The prebuckling deformations were within the limits of small deflection theory.

(2) No attempt was made to predict post-buckling behavior or the post-buckling strength. To be able to predict the post-buckling behavior, one needs to retain the higher order strain terms in the strain displacement relationships and have higher order matrices⁶⁷. It is extremely difficult to formulate these matrices explicitly and one has to resort to numerical integration. The non-linear equations can be solved by the use of methods such as Newton-Raphson scheme²⁵, energy search technique⁶⁷, etc.

(3) The possibility of local buckling was totally neglected.

(4) The material was assumed to be linearly elastic.

(5) Buckling was assumed to be conservative³⁶.

Both curved and flat element approaches were used.

VI.2. INCREMENTAL MATRIX FOR THE DECK AND EDGE MEMBERS

In order to represent the instability effect in the finite element analysis, the change in the potential energy due to the middle-surface forces N_x , N_y and N_{xy} , which occurs during the flexural action is to be included⁶⁶. For the constant values of N_x , N_y and N_{xy} at any prescribed load level, the potential energy due to in-plane forces assumes the form of,

$$V_N = \frac{1}{2} \int_0^b \int_0^a [N_x \left(\frac{\partial w}{\partial x}\right)^2 + N_y \left(\frac{\partial w}{\partial y}\right)^2 + 2N_{xy} \left(\frac{\partial w}{\partial x}\right) \left(\frac{\partial w}{\partial y}\right)] dx dy \quad 6-1$$

With the inclusion of the work done by the in-plane forces, the total potential energy can be written as,

$$\phi = \frac{[\Delta]}{2} [K] \{\Delta\} + \frac{[\Delta]}{2} [N] \{\Delta\} - [\Delta] \{P\} \quad 6-2$$

For stable equilibrium, the first variation of the total potential energy is zero.

$$\{P\} = [[K] + [N]] \{\Delta\} \quad 6-3$$

$$\{P\} = [K]_{\text{eff}} \{\Delta\} \quad 6-4$$

The matrix [N] is called the incremental matrix and it is obtained by the second differential of the potential energy (Eq. 6-1) with respect to nodal displacements.

$$[N]_{ij} = \frac{\partial^2 V_N}{\partial \Delta_i \partial \Delta_j} \quad 6-5$$

The coefficients of the incremental matrix [N], depend only upon the geometrical parameters of an element, such as its length. The incremental matrix is identical for both orthotropic and isotropic cases.

For constant values of N_x , N_y and N_{xy} the incremental

matrix for a shallow shell hyper element and that for flat plate elements are identical. The only difference is the manner in which the in-plane forces are determined (see Chapter III). The incremental matrix [N] for the deck is given in Appendix D, Tables D-I to D-IV.

Due to the presence of the axial force N_x , the effective stiffness of a beam element is also modified. Neglecting the torsional mode of buckling, the potential energy due to the axial force N_x can be obtained by putting the values of N_y and N_{xy} equal to zero, in Eq. 6-1. The procedure for determining the incremental matrix for the beam is identical with that for the deck. The incremental matrix for a beam element is given in Appendix E. The incremental matrix for the whole structure is obtained by the same procedure as described for the formulation of the master stiffness matrix in Chapter III.

VI.3. CHECKING OF THE INCREMENTAL MATRICES

Before analyzing hyper structures, it is necessary to establish the validity of the incremental matrix given in Appendix D. The determination of the in-plane buckling loads (N_x , N_y , N_{xy}) for flat plates provides a good check. At a critical load, absolute magnitudes of the deformations are indeterminate and the determinant of the effective stiffness matrix $[K]_{\text{eff}}$ must vanish.

$$|[[K] + \lambda [N]]| = 0 \quad 6-6$$

where λ is the eigenvalue which depends upon the applied state of membrane stress e.g. for an uniaxially compressed plate, along the x-direction it will give eigenvalues corresponding

to the in-plane force N_x (see Table VI-1). From the structural point of view, one is only interested in the minimum critical load. To achieve this, it is necessary to rearrange Eq. 6-6 to get the first eigenvalue corresponding to the critical load⁶⁸.

$$|[\frac{1}{\lambda} [I] + [K]^{-1}[N]]| = 0 \quad 6-7$$

The negative reciprocal of the first eigenvalue of the matrix [Q]; where,

$$[Q] = [[K]^{-1}[N]] \quad 6-8$$

will give the critical value of the membrane force. A subroutine named "NROOT" available in the IBM system/360 Scientific Subroutine Package⁶⁹, calculates eigenvalues and eigenvectors of a real, square, non-symmetric matrix given in Eq. 6-8, where both [K] and [N] are real symmetric matrices and [K] is real positive definite. In order to avoid underflow and overflow in the computer program, it is necessary to divide both [N] and [K] matrices by some large number, like 1000.

The first three problems solved were uniaxially compressed simply-supported plates with or without stiffeners (Table VI-1). In general, the buckling in-plane force N_x (lbs/inch) is given by,

$$N_x = \frac{K\pi^2 D}{b^2} \quad 6-9$$

where K is a constant depending upon the aspect ratio a/b and also on the relative stiffness of the plate and the stiffener. The ratio of the stiffnesses of the plate and the stiffener are given by non-dimensional parameters γ and δ ³⁶.

$$\gamma = \frac{EI}{Db} \quad \delta = \frac{A}{bt} \quad 6-10$$

I is the moment of inertia of the eccentrically connected stiffener calculated about the junction of the stiffener and the plate. For these problems, the torsional mode of buckling of the stiffener is neglected. The error for the values of K for these three cases is less than 0.2% as compared to the classical solutions. One of the interesting observations for these problems was that the plate with the aspect ratio of $a/b = 2$, buckles in a double sine wave with zero deflection at the center line. However, with the attached stiffener it buckles in a single sine wave. While analyzing only a quadrant of a plate, proper boundary conditions are to be applied to account for this behavior.

Since the shearing action is of primary importance in the case of hypars, the shear buckling loads for a square isotropic and for a 24-G standard corrugated flat deck were also calculated. The value obtained for the critical shearing force N_{xy} in the isotropic square is compared with Timoshenko³⁶ and that obtained for the corrugated deck is compared with McFarland⁴⁸. The error between the classical solutions and that obtained in this study for the shear buckling (N_{xy}) is more than that for the uniaxial compression (N_x). One reason for the greater error is that the assumed displacement field for the displacement w (Hermitian Interpolation) closely approximates the buckled surface for an axial compression. To approximate the buckled wave form due to shearing load, a greater number of elements is required to achieve equal accuracy. The error for the critical shearing force for the

orthotropic deck is 7.46% on the high side compared with a simplified formula⁴⁸. However, according to the authors⁴⁸ their formula underestimates the critical load by as much as by 5%. Therefore the actual error may be considerably less than 7.46%. The error for the isotropic plate with only 6 elements is 4.65% (Table VI-1).

The correlation between the classical solutions and the solutions obtained here is considered adequate to substantiate the incremental matrices for the beam and the plate. A further check will be presented in the Section VI-6, for the case of an isotropic hypar for which a classical solution is available⁵.

VI.4. INSTABILITY OF HYPARS

The incremental matrix [N] is a function of the in-plane forces N_x , N_y and N_{xy} . In the case of plate buckling problems there is a complete uncoupling between the flexural and membrane action. This enables one to formulate the [N] matrix from a given distribution of the in-plane forces which are predetermined, independent of the flexural action. In the case of a hypar, or for that matter any curved shell surface, the values of N_x , N_y and N_{xy} are dependent on the deflections. With the change in the applied loading, the magnitudes of the in-plane forces also change. In other words, there is a coupling between the membrane and flexural behavior. The increase in the in-plane forces resulting from the corresponding increase in the load causes some of the elements to undergo a marked decrease in the effective stiffness. This reduction in

the effective stiffness of an element will adjust the incremental force distribution. The accumulation of these local element instabilities will eventually lead to buckling. The discussion of this membrane and flexural behavior for the shell structures is given in detail in Refs. 51, 66.

The incremental $[N]$ matrix used for both curved and flat elements is identical and can be represented by,

$$[N] = \begin{bmatrix} 0 & 0 \\ \text{-----} \\ 0 & [N]_e \end{bmatrix} \begin{bmatrix} u \\ v \\ w \end{bmatrix} \quad 6-11$$

The only difference is that u , v , and w for the flat elements are measured along local axes whereas those in the case of the curved elements are measured along the tangent and normal to the surface. As pointed out in Chapter III, the transformation from the local to the global system for the flat elements can result in non-zero entries in all elements of the $[N]$ matrix and the matrix assumes a general form of,

$$[N]_{\text{global}} = \begin{bmatrix} \eta_{11} & \eta_{12} \\ \text{-----} \\ \eta_{21} & \eta_{22} \end{bmatrix} \begin{bmatrix} u \\ v \\ w \end{bmatrix} \quad 6-12$$

whereas its basic form remains unaltered in the case of the curved element.

VI.5. DETERMINATION OF THE BUCKLING LOAD

The linear eigenvalue formulation for the determination of the eigenvalue and thereby the lowest buckling load is well documented in the Refs. 51, 66 and therefore it is not repeated here. Because of the lack of a reliable eigenvalue subroutine for the large-order systems and sufficient computer

storage, Banavalkar could not use the direct eigenvalue approach. Instead, a linearized load incrementation method had to be used.

In the load incrementation method, as used by the author, the assumption is made that the in-plane forces N_x , N_y and N_{xy} are constant during an incremental step and are equal in magnitude to the value at the end of each step. The procedure of the solution can be demonstrated by the use of Fig. 6.1.

In the incremental step I, only linear analysis is carried out by solving the linear part of the equation assuming $[N]$ as a null matrix.

$$[\Delta] = [K]^{-1} [P] \quad 6-13$$

From the known values of displacement vector $[\Delta]$, corresponding in-plane forces N_x , N_y and N_{xy} are calculated and the incremental matrix $[N]$ is formed. The effective stiffness matrix $[K]_{\text{eff}}$ is used in iterative cycle II.

The iterative cycles are continued till convergence is obtained for the nodal displacements and consequently the incremental matrix $[N]$ is consistent with the deformations. It is found that for small incremental loads, convergence of displacements is obtained within three or four cycles. An incremental load δp is applied on the modified effective stiffness matrix and the increase in the displacements δ and Δ is calculated by finding new values of the in-plane forces at the end of the step II by the iteration as described before. The analysis is continued by applying the increment of the load δp on the previously determined effective stiffness matrix.

Any sudden change in the load deflection curve be-

tween any two load levels indicates the occurrence of buckling. In this method it is possible to predict only the range within which the buckling occurs. Since the solution near the unstable configuration is very sensitive, it is not possible to determine the exact point of buckling.

VI.6. NUMERICAL RESULTS AND THEIR DISCUSSION

Reissner⁵ analyzed the case of a simply supported isotropic hypar with edge members having infinite rigidity along their axes but having zero stiffness in a plane tangent to the shell surface. The saddle-shaped hypar, Struc. '1' (Table IV-1) was analyzed for these boundary conditions. The deflection profiles at three points along the compression diagonal bf are plotted for the load level of 0.20-0.50 kgms/cm² increased by the interval of 0.1 kgm/cm². The deflection profiles along the tension and the compression diagonals are shown in Figs. 6.2, 6.3. The sudden change of deflection profiles (Figs. 6.2, 6.3) between the loads 0.40 and 0.50 kgms/cm² clearly indicates that the buckling occurs between these two limits of loads and moreover close to 0.40 kgms/cm². The analysis based on the curved element for the same structure, also predicts the load between the same range though some differences in the deflection profiles are noted.

The load thus predicted is slightly higher than that given by Reissner (0.38 kgms/cm²) but this is because of the fact that Reissner used linearized membrane analysis. To verify this fact, analysis was carried out where predetermined membrane shearing force $N_{xy} = \frac{q AP}{2C}$ was used to establish the

incremental matrix. From the deflection profiles not shown herein, the buckling of the shell occurred between uniform loads of 0.35-0.4 kgms/cm² which is in the range of the loads predicted by Reissner. One of the interesting points is that for the linear elastic analysis, the normal deflections w were symmetrical about the lines bf , dh , ce and ag (Fig. 4.1). Similar observations were also made by Deak¹⁸. However, after the inclusion of the instability effects the symmetry of the normal displacement is still retained about the diagonals bf and dh but there is no symmetry about the lines ce and ag . This is because of the readjustment of the effective stiffness due to the in-plane tension and compression forces.

In order to assess the effect of edge deflection and the stiffness of the edge members on the buckling of the hypar deck, an umbrella shell with $\frac{C}{AB}$ ratio equivalent to that of Struc. '1' (Table IV-1) was analyzed for two different sizes of edge members. For all edge members of size 6x3 cms. (18 sq.cm. cross-section area), it appears (Fig. 6.4) that buckling occurred between the loads 0.20 to 0.30 kgms/cm², which is nearly one half that of the all-supported case discussed before. According to Leet²⁸, the buckling of the hypar shell primarily depends upon the axial stiffness of the edge members and not on the edge deflections. The boundary conditions used in Reissner's solution correspond to the infinite axial stiffness of the edge member. To verify Leet's conclusions, the same hypar was analyzed with the edge beams having the same properties as those of the 6x3 size beam except for the cross-sec-

tional area, which was increased from 18 sq.cm. to 108 sq.cm. Though the deflection profiles did not show the buckling very clearly up to 0.50 kgms/cm^2 , there was a small deviation in the deflection profile at about 0.40 kgms/cm^2 (Fig. 6.5). It appears that the buckling depends upon the cross-sectional area of the edge member and not so much on the edge deflection. It is believed that for the stiff edge members used in Strucs. '11'- '13' the deck buckling load can be predicted by calculating the buckling of a single quadrant of the umbrella shell with all-supported edges.

Two hypars, Struc. '13' with double 28-G corrugated decks and Struc. '12' with a single 24-G corrugated deck were analyzed to determine the buckling load. In the case of a double deck structure, the deck buckling load is between the range 200 to 243 psf. (Fig. 6.6). Experimentally the structure was tested up to 145 psf and no deck buckling was observed, though deck tearing along the lines of connection was noticed.

Struc. '12' with a 24-G single deck was analyzed using both curved and flat elements. The experimentally observed deck buckling load for this structure was in the vicinity of 75 psf, but from Figs. 6.7-6.9 both curved and flat elements analyses predict a lower buckling load. One of the possible reasons for this is that the pressurized canvas bags used as loading devices, tend to offer some restraint to the buckling of the shell. It is known that even a small external restraint to the shell surface is adequate enough to raise the

buckling load substantially. Comparing the deflection profiles in Figs. 6.7-6.9 it appears that the flat elements predict the load in the vicinity of about 46 psf whereas the curved elements predict the load in the vicinity of 60 psf. As pointed out in Chapter IV, the curved and flat elements, for hypars with all edges supported give very close results for the linear elastic analysis. It appears that the flat elements give very conservative results for the buckling of single decks. As pointed out in connection with Eq. 6-12 for the flat elements, the transformation of the incremental matrix from local to the global axes results in the modification of the flexural as well as membrane stiffnesses. Since the in-plane membrane stiffness for a corrugated deck is very small in the weak direction, a premature buckling could possibly be triggered by the reduction in the membrane stiffness. As against this, in the curved element formulation because of the assumptions used in the analysis, the membrane stiffness is not modified.

For a double deck or an isotropic deck, because of high in-plane rigidity in both directions, both methods predict the buckling loads in the same range. As pointed out in Chapter IV, the bending action is very dominant in the flat portion of the shell. But in the buckling analysis, the curvature of the hypar in the center of the quadrant may be more critical. This fact occurs even more in the case of a single deck and therefore the curved element, which accounts better for this curvature effect, probably predicts a higher load.

Reissner⁵ in his analysis of buckling of isotropic hypar shell, has indicated that except for a difference in numerical coefficients, the critical in-plane shearing force for the shell differs from that of a flat plate by the fact that a thickness square factor is replaced by the product of shell thickness and shell rise. However, in the case of an orthotropic shell, the increase in the critical shearing force does not appear to be as high as in the case of an isotropic shell. Because of equal bending rigidities in both directions, the buckling load for a double deck hypar shell appears to be three or four times larger than that of a single deck. This is also observed in the case of the critical shearing stress for a flat plate.

Struc. '12' was also analyzed using the identical boundary conditions as the structure analyzed in Fig. 6.7, but allowing the edges to deflect. As pointed out previously, though the exact point of deck buckling is not known, the deck buckling occurs between the loads of 43.0-50.0 psf. The interesting point to note here is that even though the deck buckled (Figs. 6.10, 6.11), the deflection of the edge members was still quite linear. The same trend was also observed during the experiment. The buckling also showed a similar trend as observed in the case of an all-supported hypar. The deflection profile along the tension diagonal did not show any buckling (Fig. 6.10).

It may not be convenient to analyze every structure in practice by this load incrementation method. According to

Reissner⁵, the buckling load for an isotropic hypar shell is given as,

$$q_{cr} = 4(C/AB)^2 \sqrt{D Et} \quad 6-14$$

where D is the bending rigidity and Et is the membrane stiffness. In the case of a double deck, the bending rigidities of the shell are equal in both the directions, however, the membrane stiffness is affected by the shear rigidity factor α . If the equivalent thickness in the formula 6-14 is replaced by αt , the estimated buckling load will be very conservative because of the fact that it will also underestimate the in-plane axial stiffness. In order to eliminate this underestimation of the axial stiffness the shear rigidity factor α is arbitrarily multiplied by $2(1+\nu)$ (the ratio of E/G for the parent material).

$$q_{cr \text{ Double Deck}} = 4\left(\frac{C}{AB}\right)^2 \sqrt{2 D_y E(1+\nu)\alpha t} \quad 6-15$$

This formula is a conservative approximation of the buckling load of hypars with double decks.

VI.7. DECK BUCKLING BY THE ENERGY METHOD

The buckling of isotropic hyperbolic paraboloid shells was investigated in a classical paper by Reissner⁵. He developed the general shallow shell theory and reduced it to two differential equations in the displacement w and a stress function F . From these equations he studied the buckling of simply-supported isotropic hypars under uniform loading. The assumed displacement was a double sine series and the form for the stress function F was assumed to be a double sine series with an additional term containing xy . The substitution of these series into the two equations result in homogeneous algebraic equations because the sine terms drop out. The condition of non-trivial solution yields the buckling load:

$$P_{cr} = \frac{2E}{\sqrt{3(1-\nu^2)}} \cdot \frac{h^2 C^2}{A^2 B^2} \quad 6-16$$

This solution was possible because each of the two differential equations contained only one elastic constant: E in one equation and D in the other. Thus the sine terms could drop out.

In the case of orthotropic shells these equations contain several elastic constants and therefore the sine terms would not drop out. This means that one cannot use these shallow shell equations to obtain reasonable buckling load. It may be possible to find very simple assumed functions for w and F but the accuracy of such a solution would probably be very poor.

Another alternative approach uses energy principles. The potential energy of an orthotropic hypar shell is¹⁹:

$$\begin{aligned}
 V = \frac{1}{2} \int_0^b \int_0^a [D_x w_{xx}^2 + 2D_1 w_{xx} w_{yy} + D_y w_{yy}^2 + 4D_{xy} w_{xy}^2 \\
 + 4 G_{eff} h (C/AB)^2 w^2 + 2N_{xy} w_x w_y] dx dy \quad 6-17
 \end{aligned}$$

The selection of an assumed buckling shape requires very careful attention. A double sine series is very difficult to use because of the complexity of the resulting arithmetic. Furthermore, the direction of the buckles is at an angle with the coordinate axes in the case of orthotropic shells and the deflection function must contain a factor which accounts for this fact. Several types of deflected shapes were tried. By far the best results were obtained using the following shape:

$$w = \sin \frac{\pi y}{B} \sin \left[\frac{n\pi}{A} (x - sy) \right] \quad 6-18$$

where the factor s represents the tangent of the angle of the buckles measured from the y axis and n is the number of buckled waves. This function was used by Timoshenko and Gere³⁶ and by Easley and McFarland⁴⁸ for the buckling of shear diaphragms.

This deflection assumption corresponds to a simply supported shell (or diaphragm) where B (and the y axis) is measured along the deformations (corrugations). Actually this expression does not satisfy $w = 0$ along the y axis, but comparisons with more exact analyses for the buckling of diaphragms showed⁴⁸ that this discrepancy is not serious.

Substitution of the assumed w into the potential energy expression and integration yields:

$$V = \frac{AB}{8} (Q_1 + Q_2 + Q_3)$$

$$\text{where } Q_1 = D_x a^4 + 2D_1 a^2 b^2 + 2D_1 a^4 s^2 + D_y b^4 + D_y a^4 s^4 \\ + 2D_y a^2 b^2 s^2 + 4D_{xy} a^4 s^2 + C'$$

$$Q_2 = 4D_y a^2 b^2 s^2 + 4D_{xy} a^2 b^2$$

$$Q_3 = -2N_{xy} a^2 s \quad a = n\pi/A, \quad b = \pi/B, \quad C' = 4G_{\text{eff}} h \left(\frac{C}{AB}\right)^2$$

Since V represents the change of potential energy under a deflection w, the condition V = 0 corresponds to the buckling load. Thus

$$Q_1 + Q_2 + Q_3 = 0$$

From the membrane theory $N_{xy} = pAB/2C$, thus

$$p_{\text{cr}} = \frac{C}{ABs} \left(\frac{\pi}{B}\right)^2 [D_x u^2 + 2D_1(1+u^2 s^2) + D_y(1/u^2 + u^2 s^4 + 6s^2) \\ + 4D_{xy}(1+s^2 u^2) + c/u^2] \quad 6-19$$

where

$$u = a/b = nB/A \quad \text{and} \quad c = C'b^4 = 4G_{\text{eff}} h(BC/A)^2/\pi^4$$

This expression has to be minimized with respect to the direction of the buckles (s) and the number of buckles (n). This can easily be done by trial and error, using a computer.

The analysis of the single-layer 24-Gage structure (No. 12) gave 50 psf for the buckling load as compared with the experimental value of about 75 psf and the finite element analysis of about 60 psf using curved elements. Minimum occurs for n = 8 and the buckles form at an angle of 8.0 degrees with

the y axis (Fig. 6.12). The buckling load was not very sensitive to n and therefore the prediction of the number of buckles may not be accurate.

For structure No. 13 (double-layers, 28 Gage) the above analysis resulted in a buckling load of 192 psf at $n = 2$ and at an angle of 35.8 degrees. The finite element analysis gave about 200 psf and the test structure did not buckle up to a load of 145 psf when loading was discontinued.

The main advantage of this energy analysis of the buckling load is that it is very fast as compared with the finite element analysis. Simple supports are assumed and therefore the actual buckling load may be somewhat higher if some bending or in-plane fixity is present. The deflection of the edge members is not considered, but the finite element analysis showed (Section VI.6) that edge member deflections do not affect the deck buckling load appreciably. The deck buckling load is influenced by the area of the edge members. If the edge members are very slender then deflections will control; on the other hand, the above analysis should give conservative results for structures with heavy edge members.

VI.7 STABILITY OF ISOLATED EDGE MEMBERS

The edge members of a hypar structure receive uniform axial loads along their lengths from the deck. Some or all the edge members are in compression. The loading remains axial during the deformation of the edge members and therefore it constitutes a non-conservative force field. To obtain an approximate value of the buckling of the compression edge members, the membrane

shear force was applied to isolated edge members with various idealized boundary conditions. The buckling loads determined in this manner are conservative since the stiffening effect of the deck is neglected.

The marginal member was analyzed both as a fixed free and a fixed pinned member. The equation used to solve the non-conservative force field problem was:

$$EI_y y^{IV} + S(L-x)y'' + My' = 0 \quad 6-20$$

where S = the shear force, L = the column length, M = mass per unit length, y = deflection, and (\cdot) means differentiation with respect to time.

The solution of the differential equation was obtained by using Galerkin's Method for solving differential equations with non-constant coefficients. The numerical solution for the fixed free case was found in an article by V. H. Leipholz; "Die Knicklast des Einseitig Eingespannten Stabes mit Gleichmassig Verteilter, Tangentialer Längsbelastung", published in ZAMP, 13, 6, 1962.

The solution for the fixed pinned case was determined using the same method as described above, but a computer program was written to facilitate the trigonometric integrations and the mathematical solution.

The numerical solutions are:

$$(q1)_{cr} = 40.7 EI/l^2 \quad \text{for the fixed free case}$$

$$(q1)_{cr} = 122.6 EI/l^2 \quad \text{for the fixed pinned case}$$

where q = shear per unit length transferred from shell to marginal member. These values and some comparison values are given in Fig. 6.13.

The results show that the buckling load of members loaded by tangential shear forces is very much greater than that of members under gravity load of constant direction parallel to the original, undeflected axis of the member.

Thus, if case IV is compared with V, with loading and end conditions the same except for the direction of the load, it is seen that in the elastic range the edge member of a hypar will buckle at a load $(1.12/0.49)^2 = 5.2$ times that which the same member would carry under uniform gravity load. Similarly, comparing cases VI and VII, it is seen that the corresponding ratio is $(0.436/0.284)^2 = 2.4$.

If the total load which will make the edge member of a hypar buckle, is compared with that which the same member, loaded as a hinged-hinged Euler column (basic case) would carry, it is seen that the edge member in the fixed-free condition (case V) will carry $(1/0.49)^2 = 4.1$ times the buckling load of the basic Euler column, or, for the fixed-hinged condition (case VII) $(1/0.284)^2 = 12.4$ times the basic Euler load.

The above results do not represent a complete analysis of the problem, which is really one of buckling interaction between the edge member and the shell. However, if the shell action is close to that of a membrane, as in the case of light-gage steel hypars, the approximation should be reasonably good. This approximation shows that, while a buckling possibility exists, these edge members are very much more stable than they would be if they were part of ordinary framing subject to gravity loads.

CHAPTER VII

EXPERIMENTAL INVESTIGATION

VII.1 INTRODUCTION

An extensive experimental investigation was carried out. The purpose of the testing program was twofold: (1) to study the behavior of light gage steel hypar roofs subjected to vertical loads and (2) to provide a comparison with analytical approaches.

The following tests were carried out:

a) Sixteen flat shear tests - Properties and dimensions of all the specimens are presented in Table VII-1 and a picture of one is shown in Fig. 7.1. It was necessary to carry out these tests to determine the shear rigidity G' of the decking used for the hypar models. Twelve specimens were 6' x 6' in plan, three were 5' x 5' in plan (all referred to as "medium scale tests"), and one was 1' x 1' in plan ("small scale test").

b) Twelve saddle shaped hypar specimens - All of them were 5' x 5' in plan with various rises (Table VII-2-VII-3). A picture of one is shown in Fig. 7.2. The specimens are designated by three numbers: the first one indicating the rise/span ratio, the second the number of layers of decking, and the third whether it is an original or duplicate. For example, for test no. 512, "5" indicates a 1/5 rise/span ratio, "1" indicates one layer of decking, and "2" indicates that it is a duplicate test (each specimen was duplicated).

c) Three inverted umbrellas with very stiff edge beams - Numbers 11, 12, 13 in Table IV-1. All were 12' x 12' in plan

with a 14.4" rise. A picture of one is shown in Figure 7.3. They are referred to as "medium scale inverted umbrellas with very stiff edge beams".

d) One small-scale inverted umbrella with very flexible edge beams. The model was 2' by 2' in plan with a 3" rise. The edge members were made of 3/16" O.D. and 0.014" thick brass tubes, two were used for the interior compression beams. Two layers of corrugated decking of 2 mil thickness formed the shell. The deck was soldered at every valley to the edge members. A picture of the model is shown in Figure 7.4.

e) One medium scale inverted umbrella with very flexible edge beams - The model was 12' x 12' in plan with a 14.4" rise, structure number 9, Table IV-1. A picture of it is shown in Figure 7.5.

The tests are described in the following sections.

VII.2 FLAT SHEAR TESTS

1. Introduction

A series of flat shear tests were conducted in order to determine the shear rigidity G' of corrugated steel decking. Luttrell⁴⁵ investigated the shear behavior of light gage steel diaphragms. Based on the results of numerous tests he concluded that the primary variables influencing the shear rigidity are length of diaphragm parallel to the corrugations and spacing of connectors to the edge members in the direction perpendicular to the corrugations. It was also determined by Luttrell that the only reliable means of determining the shear rigidity of a given diaphragm with framw was by experiment.

The formula for G' developed by Luttrell accounts for the deflection due to shear alone by subtracting from the measured deflection the bending deflection of the cantilevered structure due to axial deformation of the edge members. The value of G' obtained from a given test can be applied to the following case: Any set-up with exactly the same spacing of diaphragm to edge member connections perpendicular to the corrugations, and the same diaphragm. The size of the edge members should have little or no effect.

It may be applied with simple modifications to the following cases: (1) everything the same except diaphragm has different thickness - G' is (approximately) directly proportional to the thickness; (2) everything the same except length of frame parallel to the corrugations is different - new G' may be obtained from Figures 4-23 and 4-24 in Reference 45 for box-rib and standard corrugated diaphragms, respectively.

2. Edge Member Frame

For all tests except two the edge members were light gage channels. Two different size channels were used. One, designated as "heavy frame", consisted of 6" x 1 1/2" x .1046" channels and the other, designated "light frame", consisted of 6" x 3/4" x .1046" channels. For the other two tests, the frame was made up of tubing.

3. Decking

All the medium scale tests employed standard corrugated decking; including 24, 26, and 28 gage. Either one layer or two layers, with the second layer placed with the corrugations

perpendicular to those of the first layer, were used.

The small scale test had 2 mil corrugated steel foil. This material was produced by United States Steel Corp. as a reinforcing center for cardboard cartons. Two layers, running transverse to each other, were used.

4. Connections

For the medium scale tests, #8 x 1/2" self-tapping screws were used to connect adjacent sheets to each other along the seams. #14 self-tapping screws with aluminum-backed neoprene washers were used to connect the decking to the edge members. For double layered decking, the second layer was attached to the first layer around the perimeter only with #8 x 1/2" self-tapping screws. The spacing of connections for each test is given in Table VII.1.

In test no. 14, the effect of the relative positions of the screws connecting the top layer to the bottom layer and the screws connecting the bottom layer to the edge members was noted. Referring to Figure 7.6, one possibility is shown in (a) where the shear flow causes a region of compression between screws 1 and 2 and the bottom layer distorts considerably between screws 2 and 3. The other possibility is shown in (b) where the shear flow now causes a region of tension between screws 1 and 2 and very little distortion of the bottom layer occurs. However, in this case, because of the tendency of the tensile region between screws 1 and 2 to flatten out, eventually screw #1 tears out of the bottom layer.

For the small scale test, the top layer was soldered to the bottom layer at every point of contact around the perimeter

and the bottom layer was soldered to the edge members at every point of contact. One full panel was used for each layer.

5. Loading Apparatus

The medium scale frames were placed in a horizontal plane and load was applied by means of a 50 ton hydraulic jack. Vertical support along the loaded edge was provided by rollers on beams. Reactions were provided by a fixed wall beam to which the frame was pinned. Steel bricks were placed on the loaded edge to prevent out-of-plane warping.

The small scale frame was attached to a wooden frame with metal guides to prevent the specimen from warping out-of-plane. The entire set-up was placed in the vertical position in a Tinius-Olsen hydraulic testing machine and load was applied by the machine.

6. Deflection Measurement

For each test, deflections were measured by .001" dial gages. At first, .0001" gages were tried but it was discovered that they are too sensitive because the readings obtained from them were erratic. Sufficient accuracy was obtained with the .001" gages. If possible the stem of the gage was placed in contact with the specimen, otherwise a thread was used to attach the stem of the gage to the specimen.

7. Determination of Shear Rigidity G'

G' was determined by the use of the expression given by Luttrell⁴⁵. The initial linear portion of the load-deflection curve was used to obtain the slope. The customary testing procedure was to initially load the specimen to a predetermined value so as to seat all connections and then to conduct as many

loading cycles as necessary to get good agreement between the load-deflection curves of successive cycles. Usually, only two or three cycles were required. The dimensions, properties, and the values of G' and of $\alpha = G'/Gnt$ for each test are presented in Table VII.1. The load-deflection curve for test #14 is shown in Fig. 7.7.

VII.3 SADDLE SHAPED HYPAR TESTS

1. Introduction

A series of light gage steel hypar models, 5' x 5' in plan, with various curvatures were tested in an effort to determine if the shear rigidity as determined by a flat shear test is valid for the plate on elastic foundation approach. If an exact analysis of light gage steel hypars were possible, then it would appear that the experimental shear rigidity could be used with validity in the analysis. However, the assumptions which were introduced into the approximate plate on elastic foundation approach may lead to errors in the results if the shear rigidity as determined by a flat shear test is used in the analysis. Better results may be obtained if a "fictitious" shear rigidity were calculated backwards from experimental deflections. Thus, it might be possible to determine the fictitious shear rigidity as a function of the curvature.

For the above reasons, the only variable in this series of tests was the rise, i.e. curvature. Three different rise/span ratios were employed, 1/8, 1/5, and 1/3; one set for single layer decking and the other for double layer. Two tests, one a duplicate of the other, were carried out for each rise/span ratio and number of layers of decking. The tests were

designated according to the rise/span ratio, number of layers, and first test or duplicate as explained in Section VII-1

2. Details of Test Specimens

The edge beam frames with supports were the same for all the tests. They consisted of 3" O.D. x 1/4" wall thickness cold rolled steel tubular members welded together to give the correct rise/span ratio for each specimen. The diagonally opposite corners, two low and two high, along with the midpoints of each side were rigidly supported in the vertical direction by steel bricks (Fig. 7.2). This support system together with the fact that the tubes have a large bending rigidity was considered to offer continuous rigid support in the vertical direction.

A tie bar, 2 1/2" x 1/4" in cross-section, was used to limit the spreading of the two low corners due to the vertical load.

The decking was made up of 28 gage standard corrugated steel sheets with 2' cover. Three sheets were used for each layer, with the middle sheet cut to fit the 5' width. Single layered decking was connected to the edge beams by #14 self-tapping screws with aluminum-backed neoprene washers at 8" spacing while the two seams were fastened together with #8 x 1/2" self-tapping screws at 2 2/3" spacing. For the double layered decks, the top layer was fastened to the bottom layer, around the perimeter only, with #8 x 1/2" self-tapping screws at 8" spacing. The two seams of the top layer were fastened together exactly the same as those of the bottom layer.

Uniform vertical loading was achieved with sand held in place by wooden sides and screeded to a uniform depth for each 400 lb. (about 15 psf) load increment.

For each one of the models, subsequent to the uniform load test, a partial load covering an 8" x 12" area was applied at the center of the same decking. These tests were designated with a "C". In addition, for each one of the two duplicate models with double layered decking and subsequent to the tests with unconnected decks, the two layers were fastened together with #8 x 1/2" self-tapping screws on an 8" square grid and subjected to uniform loading first and then the partial loading on an 8" x 12" area. These tests were designated with an "I".

Deflections were measured with .001" dial gages. Strains were measured at the center of the decking with SR-4 strain gages with 1" gage length. The strain gages were placed in a valley on the top side and on the adjacent crest on the bottom side, and in the direction parallel to the corrugations. They were also located at mid-length of the tie bar, top and bottom, on some of the models. The purpose of the gages on the decking was to determine the axial and bending stresses at the center of the deck and on the tie bar was to determine the axial force in it.

The experimental deflections and stresses at 40 psf for the saddle shaped hypar tests are presented in Tables VII-2 and VII-3. The method of determining the shear rigidity versus curvature (or rise/span ratio) by using the experimental

deflections in the plate on elastic foundation approximation is presented in Section VII.6.

VII.4 MEDIUM SCALE INVERTED UMBRELLAS WITH VERY STIFF EDGE BEAMS

1. Introduction

Three medium scale models (Structures 11, 12, 13, Table IV-1) were designed and tested with the main purpose being to check the theory for the buckling of orthotropic hypar shells. Therefore, edge beams with a large bending rigidity were chosen so as to remain stable when the decking buckled. Vertical deflections as well as strains were measured for the decking and the edge beams.

The same edge beam frame was used for all three tests. It consisted of 3" O.D. x 1/4" wall thickness cold rolled steel tubular members welded together. The dimensions of the full inverted umbrella were 12' x 12' in plan, centerline to centerline of the edge beams, with a 14.4" rise (1/5 rise/span ratio). Each interior edge beam consisted of two tubular members side by side (spot welded together at 1 1/2' intervals) so that decking could be fastened to one of the members in a given quadrant and decking in an adjacent quadrant could be fastened to the adjacent member. Therefore, the plan dimensions of each quadrant were 70.5" x 70.5", centerline to centerline of the edge beams.

2. Details of Test Specimens and Procedure

Two of the models had one layer of standard corrugated steel decking, 28 gage for one model and 24 gage for the other. The third model had two layers of 28 gage standard corrugated steel decking.

For both of the models with one layer of decking, #14 self-tapping screws at 8" spacing fastened the decking to the edge beams and #8 x 5/8" self-tapping screws at 2 2/3" spacing fastened the seams together. Three panels, each with 2' cover, were used per quadrant. For the model with two layers of decking, the bottom layer was attached to the edge beams exactly as described above. The top layer was fastened to the bottom layer, around the perimeter only, with #8 x 1/2" self-tapping screws at 8" spacing. The seams for the top layer were fastened together exactly the same as those in the bottom layer as described above.

For all three models, uniform normal air pressure was applied to the inverted umbrella shape by four rubberized canvas bags placed between the floor and the hypar in the inverted position. A water manometer was used to measure the pressure.

Vertical deflections were measured by level sightings on meter sticks held at each location. Strains in the decking were measured with SR-4 gages with 1" gage length and those on the edge beams with SR-4 gages with 1/2" gage length. The vertical deflections, experimental axial stresses, and experimental bending stresses at 40 psf normal pressure are presented in Figs. 7.8-7.10.

VII.5 INVERTED UMBRELLAS WITH VERY FLEXIBLE EDGE BEAMS

1. Introduction

Two models were tested with extremely flexible edge beams. The purpose of these tests was to determine the mode of failure as well as to check how closely the failure could be predicted

by theory.

2. Small Scale Model

One of the inverted umbrellas with very flexible edge beams (Fig. 7.4) had overall plan dimensions of 2' x 2', centerline to centerline of the perimeter edge beams, with a 3" rise (1/4 rise/span ratio).

The edge beam frame was made up of 3/16" O.D. x .014" wall thickness brass tubes brazed together. The decking consisted of two layers of 2 mil corrugated steel sheets soldered together at each point of contact around the perimeter. The decking was soldered to the brass tubes at each point of contact.

Uniform vertical loading was simulated by 64 discrete weights (16 per quadrant) hung from strings passing through very small holes in the decking and attached to 1" square pads.

Vertical deflections were measured with .001" dial gages. The dial gages were positioned such that the stems did not touch the shell. To take a deflection reading, the stem of the gage was pressed until contact with the deck was made; avoiding the application of any force by the stem as much as possible.

Experimental deflections at 40 psf load are presented in Fig. 7.11.

Collapse of this model occurred at 73 psf. It was initiated by splitting of the decking along a row of holes through which the weights were suspended. This splitting caused the brass tubes to fail in bending very close to the central supporting column.

3. Medium Scale Model

The test set-up and procedure for this model were almost the same as for the 12' x 12' inverted umbrella with two layers of 28 gage decking described in Section VII.4 except for the size of the edge beams.

The edge beams were 1" nominal diameter standard weight black steel pipe with a 50 ksi yield point.

The vertical deflections were measured with .001" dial gages. The stems of the gages were attached to the shell by means of thread which was glued to the structure.

Experimental deflections and stresses at 40 psf load are presented in Fig. 7.12.

VII.6 DISCUSSION OF EXPERIMENTAL RESULTS

1. Shear Rigidity G' of Standard Corrugated Decks

Comparison of the results for the flat shear tests, which are presented in Table VII-1, reveals that the variable having the largest effect on G' is the spacing of the connections to the edge members. In particular, the spacing transverse to the corrugations has the predominant effect whereas the spacing along the corrugations has little or no effect on G' . For example, screws at every third valley as in test no. 3 produce a G' approximately one-third that for screws at every valley (one-third the spacing) as in tests no. 1 and 2.

According to Luttrell⁴⁵, another variable which affects the shear rigidity is the dimension along the corrugations; the larger this dimension the larger the shear rigidity. From the results presented in Table 3.1, it is not possible to verify Luttrell's finding conclusively. For test no. 8, with plan

dimensions of 5' x 5', G' is less than that for 6' x 6' test no. 5 but slightly more than that for 6' x 6' test no. 6. Thus, it appears that scatter in the test results masks any effect of the small variation in size.

The spacing of seam connections and number of seams have no discernable effect on G' based on the results presented in Table VII-1. Also, it appears, at least for a limited range of thicknesses of panels, that the shear rigidity increases linearly with the thickness. For example, compare the results for tests no. 5 and 7.

Tests numbered 10 - 16 had two layers of decking running transverse to each other. In each case the top layer was connected to the bottom layer along the edges, rather than being connected directly to the edge members. The effect of this arrangement of connections is to make the top layer less effective in shear than the bottom layer, which is attached directly to the edge members. The reason for this is that any shear deformation which occurs in the bottom layer along the edge members occurs also in connections for the top layer which in turn reduces the effective shear stiffness of the top layer below that obtained by connecting the top layer directly to the edge beams. From Table VII-1, tests no. 10 and 11 versus 1 and 2; 12 and 13 versus 4, 5, and 6; and 15 versus 8 and 9 show that the shear rigidity for the double layer tests is less than twice that for the corresponding single layer tests. It appears that connecting the second layer in this manner results in only a 33% increase in G' over that of the single layer, although as mentioned previously the relative positions of the screws appear to

affect the shear rigidity. If all the connections between the two layers were such as to create the condition shown in Fig. 7.6(b) then the shear rigidity should be larger than for the case shown in Fig. 7.6(a).

Fig. 7.7 shows the load-deflection curve for test no. 14. The linear portion extends to about 1800 lbs. load which corresponds to a shear $N_{xy} = 25$ lbs. per inch. Beyond this point, the curve indicates that the shear rigidity decreases with increasing load.

Figs. 7.8 and 7.9 indicate that the shear rigidity of standard corrugated steel decked hypars with a rise/span ratio $\geq 1/5$ is somewhat (20 - 30%) less than that of the same flat deck. However, as mentioned briefly in Section VII.2, this information may be misleading because of the approximate plate on elastic foundation approach used in conjunction with the experimental deflections to obtain these curves. Two factors were omitted in the theory used to obtain Figs 7.8 and 7.9, the inclusion of which indicate that the shear rigidity obtained from a flat shear test may be valid for the hypar shell. One of the factors omitted was the middle-surface deformations u and v . The other was the spreading of the low corners of the saddle shaped models. Even though a tie bar connected the low corners, tension in the tie bar caused by the shear forces resulted in its elongation. Duplicate tests no. 521 and 522 were chosen to illustrate the effect of these two factors. If the u , v displacements are included then the resulting α is .046 instead of .042 as shown in Fig. 7.9 for the 12" rise. If, in addition,

the spreading of the low corners is included by introducing the stiffness of the tie bar into the analysis then the resulting α is approximately .05 which is the same as that obtained from the flat shear test. These results for only one example are not meant to be conclusive but the indication is that the shear rigidity in a warped element is not much different from that determined from a flat shear test.

2. Hypar Deflections

a) Saddle Shape Supported All Around

Table VII-2 presents the maximum deflections at 40 psf for the models tested in this investigation. The results reveal the decrease in maximum deflection with increasing rise as well as the fact that the maximum deflection of a given model with two layers of decking is more than half that of the corresponding model with one layer of decking; the reason being, as mentioned previously, that since the top layer is connected only to the bottom layer it is not as effective in shear as the bottom layer and thus the rigidity of the single layered deck is more than half that of the double layered deck.

Table VII-2(b) shows the effect of interconnecting two layers all over and not just around the perimeter. Test numbers with an "I" indicate interconnected layers. The reduction in maximum deflection due to interconnecting is seen to be only 10 - 20%. However, it appears that interconnecting would be necessary in practice to prevent chatter.

Table VII-3 presents the maximum deflection due to a partial load covering an 8" x 12" area in the center. A comparison of the maximum deflection due to a 100 lb. load on a single layered

deck with that due to a 200 lb. load on a double layered deck reveals that a double layered deck is more than twice as rigid as a single layered deck for carrying a concentrated load; the reason being that a concentrated load on a single layer is carried mainly by a few beam strips whereas on the double layer it is spread out and thus carried by more beam strips in each layer. For all the models tested, the maximum deflection due to a 100 lb. load on a double layered deck is approximately one-third that for a single layered deck.

b) Inverted Umbrellas With Very Stiff Edge Beams

Figs. 7.10(a), 7.11(a), and 7.12(a) show the measured vertical deflection at 40 psf normal pressure for three inverted umbrellas tested at Cornell. It is seen that difficulty in obtaining symmetry was experienced. The lack of symmetry was probably due to unequal air pressures in the rubberized canvas bags. The bags were not entirely air tight so that unequal rates of leakage from the bags could have caused relatively large percentage variations in the pressures.

c) Inverted Umbrellas with Very Flexible Edge Beams

Figs. 7.13 and 7.14(a) show the measured deflections at 40 psf for the 2 ft by 2 ft small-scale test and test No. 9, respectively. Fig. 7.13 reveals that rotation about one diagonal apparently occurred during testing of the small scale model. Fig. 7.14(a) shows that a reasonably good condition of symmetry was obtained for the medium scale model. For both models, it is apparent that the deflection at the free corners is much larger than that at the center of each quadrant.

3. Hypar Stresses

a) Saddle Shape Supported all Around

The experimental stresses presented in Table VII-2 reveal the difference in structural action between a very flat hypar (rise/span = 1.8) and one with a much larger curvature (rise/span = 1/3). The bending stresses in the models with a 1/8 rise/span ratio are much greater than those in the models with a 1/3 rise/span ratio. The decrease in bending with increasing rise/span ratio is accompanied by an increase in membrane action as seen in the last column of Table VII-2. The experimental force in the tie bar for the models with a 1/8 rise/span ratio is much less than that given by membrane theory whereas the force in the tie bar for the models with a 1/3 rise/span ratio is almost as large as that given by the membrane theory. Thus, it is demonstrated experimentally that for very flat hypars, shear stresses are much smaller than predicted by the membrane theory and that bending constitutes the major part of the structural action whereas for deep hypars (rise/span \geq 1/3) membrane stresses predominate with values close to those given by membrane theory and bending stresses are insignificant. The axial stresses in the deck, for all models, are seen to be insignificant.

Table VII-3 shows that a concentrated load produces significant bending stresses, especially in the flat hypars, but very little membrane action.

b) Inverted Umbrellas with Very Stiff Edge Beams

Figs. 7.10(b), 7.11(b), and 7.12(b) show the axial and bending stresses obtained from strain measurements at 40 psf load

for the three models tested at Cornell. The axial stresses in the strong direction of the corrugated decking are seen to be quite erratic and do not indicate any consistent behavior. It appears that their magnitudes are too small to give reliable results.

The bending stresses in the decking at the quadrant centers vary from 6200 to 10200 psi for the 28 gage single layer, from 4800 to 5700 psi for the 24 gage single layer, and from 5100 to 10200 psi in the bottom layer of the 28 gage double layer decking. The wide range of these values for each model indicates a considerable departure from symmetry which was probably caused by unequal pressures applied to each quadrant.

Experimental edge beam axial and bending stresses as well as edge beam axial stresses from the membrane theory are also shown in Figs. 7.10(b), 7.11(b), and 7.12(b). It is difficult to observe consistent trends in the experimental axial stresses in the edge beams. In some locations they are very close to those values given by the membrane theory while at other locations the difference is quite large. It is to be expected that the experimental axial stresses would be less than those given by the membrane theory because of the fact that part of the load is carried by bending. However, the results for the three models do not give any indication as to whether or not this is the case.

Again, referring to Figs. 7.10(b), 7.11(b), and 7.12(b), the bending stresses at the mid-lengths of the perimeter beams for the two models with one layer of decking are larger in the

beams parallel to the weak direction of the decking. This is to be expected because the bending which occurs in the decking transmits a vertical shear loading to these edge beams. The bending stresses in the interior edge beams for all three models are small although the strains in these beams at points of maximum stress near the column were not measured.

CHAPTER VIII

SUMMARY, CONCLUSIONS AND RECOMMENDATIONS

The behavior of thin steel hypars was studied experimentally and analytically to determine the stresses, deflections, and buckling loads of such structures under various conditions.

The experimental program consisted of tests on: a) Five inverted umbrella type hypar structures, b) Sixteen flat shear tests which were made to determine the shear rigidity of corrugated steel decks used on the hypar models, c) Twelve saddle-shaped hypars with different rises and with rigid edge supports which were tested in order to evaluate the effect of rise or warping on the shear rigidity of decks.

Several small-scale and single-quadrant exploratory tests preceded the above tests. The results are not included in this report because of experimental difficulties or uncertainties experienced with those models.

Two different approaches based on the finite element method were used in the analysis of hypars. These approaches basically differ in the stiffness formulation for individual elements. In the first, a curved element rectangular in plan was developed on the basis of shallow shell theory. The displacements u , v , and w used in the formulation of this element are measured along the tangents and normal to the surface. In the second approach, the actual shell surface was approximated by a series of flat plates assembled in the global coordinate system. The stiffness matrices for the eccentrically connected edge members were developed. The effect of a tension tie rod and a column support

was incorporated in the analysis by replacing the physical structural members by idealized equivalent springs (see Section III-2F). Computer programs were developed for the analysis of thin-steel hypar structures.

The linear elastic analysis is applicable for various types of hypar structures (e.g. umbrella shell, saddle-shape, etc.) and also for different loading conditions such as uniformly distributed load, unsymmetrical load and the load due to edge member weight. Deflections and stresses for both deck and edge members were calculated.

The linear elastic analysis was further extended to include the instability effect introduced due to the in-plane forces N_x , N_y and N_{xy} . The load incrementation method was used to predict the deck buckling and the overall (edge member) buckling of the structure.

The solutions available in the literature for both the linear elastic analysis (Refs. 17, 19, 20, 21) and for the instability analysis⁵ were compared with the solutions obtained in this study (Figs. 4.6, 4.8 and 6.2). The analytical results were further compared with the experimental work conducted at Cornell and also with test results available in the literature elsewhere^{33,65}.

Based on the finite element analysis of several structures and the comparison of analyses with available experimental and analytical results, the following observations evolved:

In the case of hypars with all edges fully supported, and for hypars with very stiff edge members (Figs. 4.6, 4.8 and 4.33) the results of curved and flat elements show excellent correlation. However, in the case of hypars with flexible edges (Fig.

4.23), the curved element formulation tends to underestimate the bending in the flat portion of the shell (e.g. free corner of an umbrella shell). In the case of a uniformly loaded hypar, the fully compatible 16-term Hermitian polynomial used for the normal displacement w , does not show any improvement over a 12-term non-compatible polynomial displacement field.

The relative stiffness of the edge members to the decks is quite important from the point of view of behavior of shells. In the case of moment-free connections between the deck and the edge members, the type primarily investigated in this work, for very stiff edge members the deck tends to bend freely between the opposite sides. In the case of umbrella shells with flexible edge members, the deck supports the edge member at the free corner. The change in behavior of shells with stiff and flexible edge members is quite noticeable from the deflection profiles for Strucs. '9' and '13' (Table IV-1).

The in-plane shearing rigidity of a hypar shell is of utmost importance in its behavior. The effective value of the shear modulus of the corrugated decks is given by $G_{\text{eff}} = \alpha G$. Depending upon the rise to span ratio of the hypar surface, the value of α , determined by the flat shear test needs modification. It is recommended that α as obtained from a flat test be reduced by 25% for single deck structures whereas it should be reduced by 20% for a double deck (Figs. 2.7-2.8). Since the deflections and the stresses of the hypar shell primarily depend upon the value of α , the conservative estimation of its value will provide a significant factor of safety for the structure.

Since a part of the vertical load is carried by bending action, the value of the membrane shearing force given by the membrane theory is on the conservative side. However, the analysis of several structures (Chapter IV) tends to indicate that over a major portion of the shell the value of the in-plane shear is very close to and at places somewhat higher than the membrane shear (Figs. 4.19, 4.28). Connections between the adjoining panels designed on the basis of the membrane shear, are considered adequate.

The axial forces calculated in the edge member on the basis of the membrane theory are on the conservative side (see Table V-2). The axial stresses form a relatively small portion of the total stresses (axial + bending) in the edge members. Therefore the computation of the axial stresses in the edge member on the basis of the membrane theory neglecting the bending stresses, cannot be considered as conservative.

The eccentric connections of the edge members to the deck have a pronounced effect on the deflections of the shell (Figs. 4.13, 4.17). With a proper choice of the eccentricity, the influence of the eccentric connection can be used to advantage (see Chapter V) to reduce deflections.

As indicated in the analysis of Struc. '8' (Table IV-1) unsymmetrical loading in an umbrella roof produces considerably larger deflections and stresses (Fig. 4.20) than uniform loading. The unsymmetrical load due to wind or drifting of snow should be given due consideration in selection of decks and edge member sizes.

The weight of the edge members is partly carried by the shell action. To average it over the whole surface of the shell will underestimate the bending stresses in the edge members (Figs. 5.3, 5.4). The effect of the edge member weight on the behavior of the shell will depend upon the construction procedure.

The effect of the amount of restraint against spreading of the low corners of saddle-shaped hypars on the deflection of the center of the shell was studied by means of numerical examples. It was found that a tie bar connecting the points of support is very effective in restraining the outward movement of the supports and thus in reducing the center deflections. Edge members with large bending rigidity in a horizontal plane also restrain the spreading of the supports effectively.

Partial loading on hypars was studied to a very limited extent experimentally. Loads were applied on an 8 in. by 12 in. area in the center of the saddle-shaped models with rigid supports around the perimeter. It was found that such a loading on a single layer of corrugated decking produces a maximum deflection three times that for two layers of corrugated decking. Therefore, two layers of decking are recommended for hypars which will be subjected to significant loads on small areas.

The linear elastic analysis adequately represents the behavior of the shell for low levels of loads. However, as the load level increases it is necessary to incorporate the effects of instability in the analysis.

The buckling in hypar shells using a light gage corrugated open deck is manifested in three different forms. The individual plate elements composing the deck may show local buckling when

subjected to in-plane shearing or axial forces. This however, can be prevented by a proper choice of thickness to width ratio for each plate element. Deck buckling takes place when the deck acting as a unit buckles along the compression arch (Chapter VI) while the edge members are still stable. Overall buckling of the shell is defined as the one when the edge members along with the deck buckle simultaneously. For practical sizes of edge members there is only a very remote possibility of overall buckling¹⁹.

Though the magnitude of the deck stresses is quite low, the possibility of the deck buckling must not be overlooked. Two decks placed perpendicular to each other for the same geometric configuration of the shell will increase the deck buckling load roughly three to four times compared with that for a single deck. From the analysis it appears that the axial stiffness of the edge members is more important than the deflections of the edges as far as deck buckling is concerned. It also appears that the deck buckling load is roughly proportional to the area of the edge members.

The membrane action in the shell increases and the bending action decreases with increase in the rise to span ratio, thickness t , and shear rigidity factor α . A non-dimensionalized parameter $\frac{\alpha n t C}{AB}$ can be used as a good index for the behavior of the shell. A higher value of this non-dimensionalized parameter indicates reduction in the vertical deflection as well as in the bending stresses for both the deck and the edge members. Furthermore, it will increase the buckling load.

Though this investigation resulted in acceptable and reliable methods of analysis, the following recommendations can be made for future analytical work:

The computer program using flat elements for the stiffness analysis gave consistent results. It is not clearly established as to whether the deficiency of the curved elements in predicting deflections and bending stresses near the flat free corner of an umbrella shell is due to element stiffness formulation or whether its due to the use of stiffening eccentric edge members. As for the response of the structure, for the variations of different parameters (rise to span ratio, α , etc.) both curved and flat elements in general give the same pattern.

The assumption of shallowness of the shell surface is used in applying boundary conditions. This limitation can be eliminated by a suitable choice of local coordinate axes along the boundaries. This will need additional computer programming.

The computer program can incorporate the beams built along the lines of generators. However, their influence on improving the shear rigidity and reducing the deflection of the shell is not studied. The local release of forces such as hinge connection (moment-free) was not incorporated in the solution.

BIBLIOGRAPHY

1. Anon., "Elementary Analysis of Hyperbolic Paraboloid Shells," Portland Cement Association, 1960.
2. Sondhi, J. R., and Patel, M. N., "Design for Hyperbolic Paraboloid Shell Footings for a Building in Mombasa, Kenya," Indian Concrete Journal, June 1961.
3. Marguerre, K., "Zur Theorie der gekrümmten Platte grösser Formänderung," Proceedings, Fifth International Congress on Applied Mechanics, 1938.
4. Vlasov, V. Z., "General Theory of Shells and its Applications in Engineering," NASA Technical Translation F-99.
5. Reissner, E., "On Some Aspects of the Theory of Thin Elastic Shells," Journal of the Boston Society of Civil Engineers, Vol. 42, No. 2, 1955.
6. Apeland, K., and Popov, E., "Analysis of Bending Stresses in Translational Shells," Proceedings of the Colloquium on Simplified Calculation Methods, Brussels, September 4-6, 1961.
7. Bleich, H. H., and Salvadori, M. G., "Bending Moments on Shell Boundaries," Journal of the Structural Division, ASCE, October 1959.
8. Chetty, S.M.K., and Tottenham, H., "An Investigation into the Bending Analysis of Hyperbolic Paraboloid Shells," Indian Concrete Journal, July 1964.
9. Das Gupta, N. C., "Edge Disturbances in a Hyperbolic Paraboloid," Civil Engineering and Public Works Review, February 1963.
10. Mirza, J. F., "Stresses and Deformations in Umbrella Shells," Journal of Structural Division, ASCE, April 1967.
11. Russel, R. R., and Gerstle, K. H., "Bending of Hyperbolic Paraboloid Structures," Journal of the Structural Division, ASCE, June 1967.
12. Russel, R. R., and Gerstle, K. H., "Hyperbolic Paraboloid Structures on Four Supports," Journal of the Structural Division, ASCE, April 1968.

13. Schnobrich, W. C., and Gustafson, W. C., "Discussion on Reference 10," Journal of Structural Division, ASCE, January 1968.
14. Croll, James G. A., and Scrivener, J. C., "Edge Effects in Hyperbolic Paraboloid Shells," Journal of the Structural Division, ASCE, March 1969.
15. Croll, James G. A., and Scrivener, J. C., "Convergence of Hypar Finite-Difference Solutions," Journal of the Structural Division, ASCE, May 1969.
16. Brebbia, Carlos A., "A Critical Review of Bending Solutions in Hyperbolic Paraboloid Shells," University of Southampton Report (England).
17. Connor, J., and Brebbia, Carlos A., "Stiffness Matrix for Shallow Rectangular Shell Element," Journal of Engineering Mechanics Division, ASCE, October 1967.
18. Déak, Alexander L., "Analysis of Shallow Shells by the Displacement Method," Report 67-A, University of Washington, College of Engineering, Department of Aeronautics and Astronautics.
19. Parker, John E., "Behavior of Light Gage Steel Hyperbolic Paraboloid Shells," Ph.D. Dissertation, Cornell University, 1969.
20. Pecknold, David A., and Schnobrich, W. C., "Finite-Element Analysis of Skewed Shallow Shells," Journal of the Structural Division, ASCE, April 1969.
21. Pecknold, D. A., and Schnobrich, W. C., "Finite Element Analysis of Skewed Shallow Shells," A Technical Report to the Office of Naval Research, Department of the Navy.
22. Ralston, A., "On the Problem of Buckling of a Hyperbolic Paraboloid Shell Loaded by Its Own Weight," Journal of Mathematical Physics, 1956.
23. Dayaratnam, P., and Gerstle, K. H., "Buckling of Hyperbolic Paraboloids," World Conference on Shell Structures, October 1-4, 1962.
24. Muskat, Richard, "Buckling of Light Gage Steel Hyperbolic Paraboloid Roofs," Ph.D. Dissertation, Cornell University, 1968.
25. Brebbia, Carlos A., and Connor, J., "Geometrically Non-linear Finite-Element Analysis," Engineering Mechanics Division of ASCE, April 1969.

26. Rowe, R. E., and Mirza, J. F., "An Experimental Investigation of Small Scale Hyperbolic Paraboloids," Proceedings of World Conference on Shell Structures, San Francisco, October 1962.
27. Rowe, R. E., "Tests on Four Types of Hyperbolic Shells," Proceedings of the Symposium on Shell Research, Delft, August 30-September 2, 1961.
28. Leet, Kenneth M., "Study of Stability in the Hyperbolic Paraboloid," Journal of the Engineering Mechanics Division, ASCE, February 1966.
29. Bertero, V., and Choi, John, "Chemically Prestressed Concrete Hyperbolic Paraboloid Shell Model," Proceedings of World Conference on Shell Structures, San Francisco, October 1962.
30. McDermott, John F., "Single-Layer Corrugated-Steel-Sheet Hypars," Journal of the Structural Division, ASCE, June 1968.
31. Yu, C. W., and Kriz, Ladislav B., "Tests of a Hyperbolic Paraboloid Reinforced Concrete Shell," Proceedings of World Conference on Shell Structures, San Francisco, October 1962.
32. Nilson, A. H., "Testing a Light Gage Steel Hyperbolic Paraboloid Shell," Journal of the Structural Division, ASCE, October 1962.
33. "Reports of Shear Proprietary Tests of Hypar Metal Decking," (Private Communication).
34. Hutchinson, N. J., Jr., "Theoretical Determination of Rigidity Properties of Orthogonally Stiffened Plates," Journal of Applied Mechanics, March 1956.
35. Smith, Geoffrey E., "Elastic Buckling in Shear of Infinitely Long Corrugated Plates with Clamped Parallel Edges," A Thesis presented to Cornell University, for a Master of Aeronautical Engineering 1957.
36. Timoshenko, S. P., and Gere, J. N., "Theory of Elastic Stability," McGraw Hill Second Edition 1961.
37. Barés, Richard and Massonnet, Charles, "Analysis of Beam Grids and Orthotropic Plates," Crosby Lockwood and Sons, Ltd., SNTL-Publishers of Technical Literature, Prague, 1968.
38. Anon., "Light Gage Cold-Formed Steel Design Manual," Edition 1961, AISI.

39. Winter, G., "Commentary on 1968 Edition, Light Gage Cold-Formed Steel Design Manual," AISI.
40. Kinloch, H., and Harvey, J. M., "Analysis and Design of Anisotropic Plate Structures with Particular Preference to Decking Systems," An Article from "Thin-Walled Structures," Edited by Chilver, A. H., John Wiley and Sons, Inc., N.Y.
41. Lekhnitskii, S. G., "Anisotropic Plates," Translated from Second Russian Edition by S. W. Tsai and T. Cheron, Gordon and Breach Science.
42. Zienkiewicz, O. C., and Cheung, Y. K., "The Finite Element Method in Structural and Continuum Mechanics," McGraw-Hill Publication 1968.
43. Bryan, E. R., and El-Dakhakhni, W. H., "Shear Flexibility and Strength of Corrugated Decks," Journal of Structural Division, ASCE, November 1968.
44. Falkenberg, J. C., "Discussion on Reference 43," Journal of the Structural Division, ASCE, June 1969.
45. Luttrell, L. D., "Structural Performance of Light Gage Steel Diaphragms," Ph.D. Dissertation, Cornell University, 1965.
46. Troitsky, M. S., "Orthotropic Bridges Theory and Design," The James F. Lincoln Arc Welding Foundation.
47. Anon., "Design Manual for Orthotropic Steel Plate Deck Bridges," AISC Publication 1963.
48. Easky, J. T., and McFarland, D. E., "Buckling of Light Gage Corrugated Metal Shear Diaphragms," ASCE Journal of the Structural Division, July 1969.
49. Wright, R. N., et. al., "BEF Analogy for Analysis of Box Girders," Journal of Structural Division, ASCE, July 1968.
50. Gallagher, R. H., "The Development and Evaluation of Matrix Methods for Thin Shell Structural Analysis," Ph.D. Dissertation, State University of New York, Buffalo, June 1966.
51. Yang, Henry T. Y., "A Finite Element Formulation for Stability Analysis of Doubly Curved Thin Shell Structures," Ph.D. Dissertation, Cornell University, 1968.
52. Cantin, P., and Clough, R., "A Curved, Cylindrical Shell Finite Element," AIAA Journal, Vol. 6, June 1968.

53. Haisler, W., and Stricklin, J., "Rigid-Body Displacements of Curved Elements in the Analysis of Shells by Matrix Displacement Method," AIAA Journal, Vol. 5, No. 8, August 1967.
54. Timoshenko, S. P., and Woinowsky-Krieger, "Theory of Plates and Shells," McGraw-Hill Book Company, Second Edition 1959.
55. Weaver, William, Jr., "Computer Programs for Structural Analysis," D. Van Nostrand Company, Inc.
56. Bleich, Friedrich, "Buckling Strength of Metal Structures," McGraw-Hill Book Company, 1952.
57. Hoff, N. J., "The Analysis of Structures," John Wiley and Sons, Inc., 1964.
58. Gallagher, R. and Barsoum, R., "Finite Element Analysis of Torsional and Lateral Stability Problems," Int. Journal for Num. Meth. in Engrg., Vol. 2, No. 2, April-June 1970.
59. Hall, A. S. and Woodhead, P. W., "Frame Analysis," John Wiley and Sons, Inc., 1961.
60. Anon., "Torsion Analysis of Rolled Steel Section," Steel Design File Design Data from Bethlehem Steel, AIA, File No. -13A-1.
61. Jones, R. E. and Strome, P. P., "A Survey of Analysis of Shells by the Displacement Method," Matrix Methods in Structural Mechanics Proceedings of the First Wright Patterson Airfield Conference, October 1965.
62. Gere, J. M. and Weaver, W., "Analysis of Framed Structures," D. Van Nostrand Company, Inc., 1966.
63. Anon., "Stress, A User's Manual," MIT Press.
64. Brooks, D. F. and Brotton, D. N., "Formulation of a General Space Frame Program for a Large Computer," The Structural Engineer, Vol. 44, No. 11, November 1966.
65. "Behavior of Hypar Shells," National Science Foundation Grant GK-1282, A Project under progress at Cornell University.
66. Gallagher, P. H., et. al., "Discrete Element Procedure for Thin Shell Instability Analysis, AIAA Journal, January 1967.
67. Mallett, R. H. and Marcal, P. V., "Finite Element Analysis of Non-Linear Structures," Journal of Structural Division, ASCE, September 1968.

68. Kapur, K. and Harz, B. J., "Stability of Plates using the Finite Element Method," Journal of Engineering Mechanics Division, ASCE, Vol. 92, April 1966.
69. Anon., "System/360 Scientific Subroutine Package (360A-CM-03X) Version II, Programmer's Manual IBM Applications Program Manual H20-0205-2, 1967.
70. Gustafson, W. C. and Wright, R. N., "Analysis of Skewed Composite Girder Bridges," Journal of Structural Division, ASCE, April 1968.
71. Argyris, J. H. and Scharpf, D. W., "A Further Sequel to Technical Note 14 Fuga Family of Elements for Folded Plate Structures," The Aeronautical Journal of the Royal Aeronautical Society, Vol. 73, July 1969.
72. Ojalvo, I. V. and Newman, M., "Natural Vibrations of a Stiffened Pressurized Cylinder with an Attached Mass," AIAA Journal, June 1967.
73. Scniggs, P. M., "An Analytical and Experimental Study of the Vibration of Orthogonally Stiffened Cylindrical Shell," AIAA/ASME 9th Structural Dynamics and Materials Conference, Palm Springs, California, April 1-3, 1968.

APPENDIX A
DECK PROPERTIES

The elastic properties along principal directions of orthotropy are given for both closed and open decks. A detailed computation of the elastic constants for an orthotropic deck are reported in Refs. 34, 35, 36, 37, 40, 41, 46, 47, 48.

A-I CORRUGATED OPEN DECK

Fig. A₁(a) shows an arbitrary cross-section of unit length, in y-direction, for an open deck.

A-Ia Membrane Constants

E_x = The extensional elastic constant for the equivalent orthotropic plate, is obtained by equating the extension Δ_x between the physical and the idealized system.

From Fig. A₁(a),

$$M_s = Pz; \quad m_s = z; \quad I_0 = \frac{t^3}{12} \quad A-1$$

For constant thickness t of the deck,

$$\Delta_x = \frac{Pl}{EtI_0} \int_0^s \frac{z^2 t}{l} ds \quad A-2$$

$$\int_0^s \frac{z^2 t}{l} ds = I_y' \quad A-3$$

where I_y' is the moment of inertia of the cross-section, per unit length, about the line of action of load P , which coincides with the x -axis.

For the equivalent flat plate, (Fig. A₁(b)),

$$\Delta_x = \frac{P\ell}{E_x t} \quad \text{A-4}$$

Equating equations A-2, A-3 and A-4, we get

$$E_x = \frac{I_0}{I_y'} E \quad \text{A-5}$$

The other membrane constants are given in Table A-I.

A-Ib Bending Rigidities

Bending rigidities for the x and y-directions are given in Table A-I. The method of determining the constants is given in Ref. 35. For the orthotropic plate, the twisting constants D_{xy} and D_{yx} are not equal and hence the average values of these constants are used in the analysis³⁵. Minor deviations in the properties of D_x and D_{xy} are noted in Refs. 48,54, however, the small deviations in these relatively unimportant properties are considered of no consequence at all.

A-II CELLULAR CLOSED DECK

The Fig. A₃ shows a typical cellular deck where a trapezoidal hat section is connected to the base plate.

A-IIa Membrane Constants

The principle for the computation of membrane constants for the closed decks is the same as that for the open deck. However, because of the continuous base plate, certain modifications in the constants, such as E_{xy} and ν_{yx} , are required. E_x - Assuming full fixity between the base plate and the hat (Fig. A₃), for BC,

$$P_1 + P_2 = P \quad \text{A-6}$$

From Eq. A-5, E_{xh} , the elastic extensional constant, for the hat only,

$$E_{xh} = \frac{EI_{ot2}}{I_y'} \quad A-7$$

I_y' is the moment of inertia of the hat portion about the base plate. By compatibility,

$$P_2 = P_1 \left(\frac{E_{xh}}{E} \right) \left(\frac{t_2}{t_1} \right) \quad A-8$$

The equivalent orthotropic plate is assumed to be of the thickness t_1 ,

$$E_x = \frac{E}{\left(\frac{a}{\ell \left(1 + \left(\frac{E_{xh}}{E} \right) \left(\frac{t_2}{t_1} \right) \right)} + \frac{e}{\ell} \right)} \quad A-9$$

For all practical purposes, the denominator of the above equation (A-9) is equal to unity.

$$E_x = E \quad A-10$$

E_y and ν_{yx} - If the full cross-section in Fig. A₃ is effective in resisting the axial force along the y-axis then,

$$E_y = \frac{EA_y}{A_x} \quad A_x = \ell t_1 \quad A-11$$

where A_y is the cross-sectional area of the section shown in Fig. A₃. By the Maxwell-Betti reciprocal theorem,

$$\nu E_x = \nu_{yx} E_y \quad A-12$$

$$\nu_{yx} = \nu \frac{A_x}{A_y} \quad A-13$$

The shear rigidity for the closed deck can be considered equal to that of the base plate which is usually directly connected to the edge members. Even a thin plate interconnecting the free hat portions will increase the effective shear rigidity of

the section. However, the cost of construction will have to be taken into consideration in this approach.

A-IIb Bending Properties

These properties are given in the Table A-I.

A-IIc Torsional Rigidity

Here again the values of D_{xy} and D_{yx} are not equal. As shown in Fig. A₅, the value of D_{xy} is negligibly small as compared to that of D_{yx} . The value of D_{yx} can be obtained by using Brendt's formula⁴⁶.

$$D_{yx} = \frac{4A_c^2}{\left(\frac{b+2h'}{t_2}\right) + \frac{a}{t_1}} \cdot \frac{1}{l} \quad \text{A-14}$$

where A_c is equal to the area enclosed by the cellular hat portion.

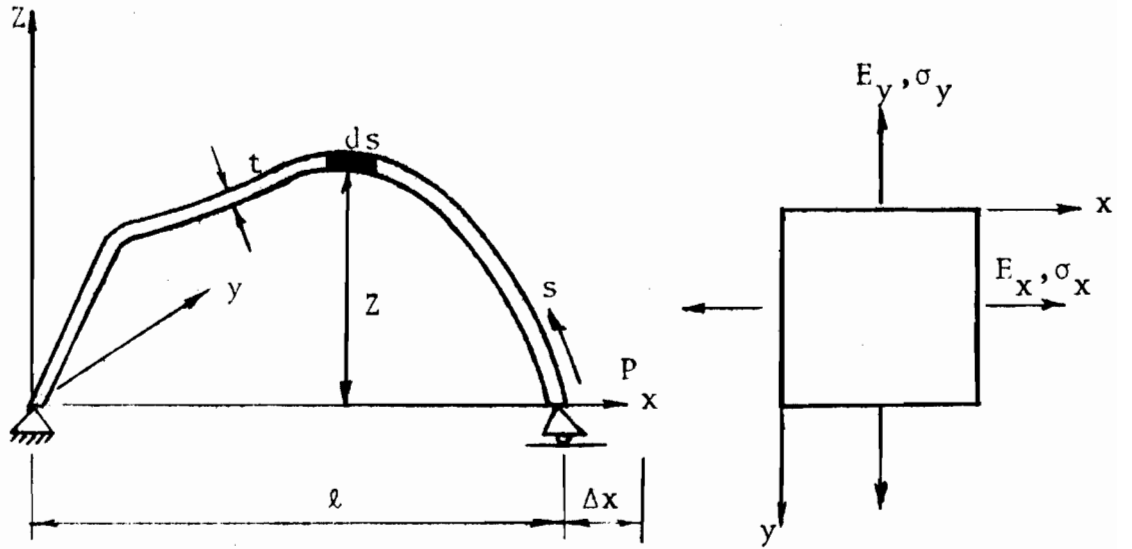
However, the magnitude of D_{yx} tacitly assumes that the shape of the deck does not deform (dotted lines in Fig. A₄)⁴⁷. The in-plane shear forces set up due to the twisting, produce secondary bending moments in the individual plates. Besides, the bending of the overhanging plate, outside the cellular portion, further adds flexibility to the cellular section.

In order to account for this reduction in torsional stiffness, an effective torsional rigidity of the cellular deck is defined as the torsional rigidity of the ideal system (shown by the dotted lines in Fig. A₄), free from individual plate flexural deformations. The work of the deformations due to the torsion of an idealized system is equated with the work due to torsion and secondary flexure. The modified twisting rigidity can be given as,

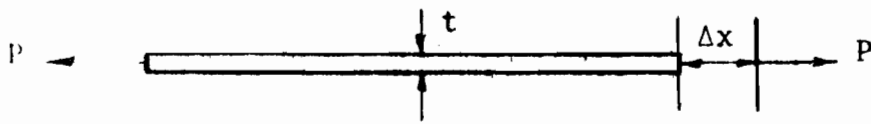
$$D_{yx} = \frac{4A_c^2}{\left\{ \frac{(b+2h')}{t_2} + \frac{a}{t_1} \right\}} \frac{1}{R_{red}} \frac{1}{l}$$

A-15

The reduction factors given in Ref. 47 were checked. The method of calculating the reduction factors is given in the Ref. 46. As pointed out in Chapter II, the warping⁴⁹ stiffness for both closed and open form decks is neglected in the analysis.



(a)



(b)

Fig. A₂

Fig. A₁ Equivalent Orthotropic Plate

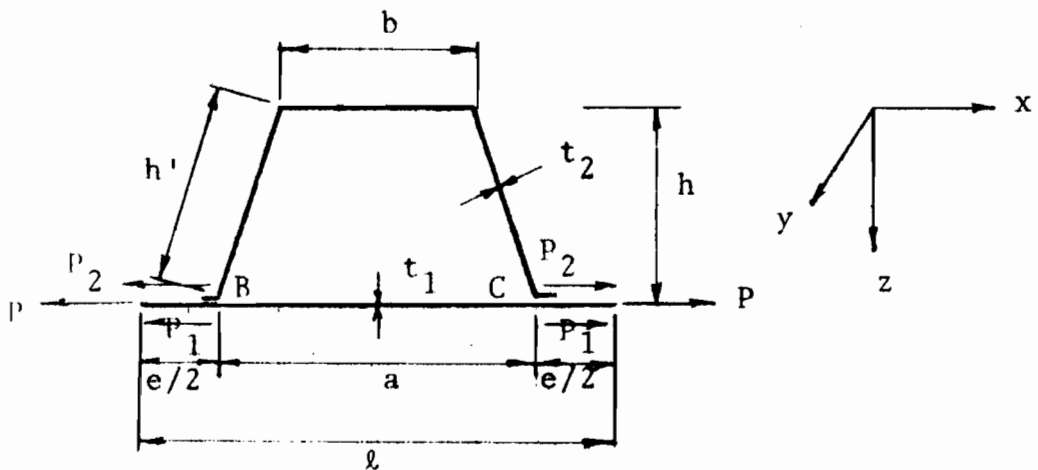


Fig. A₃ Cellular Deck

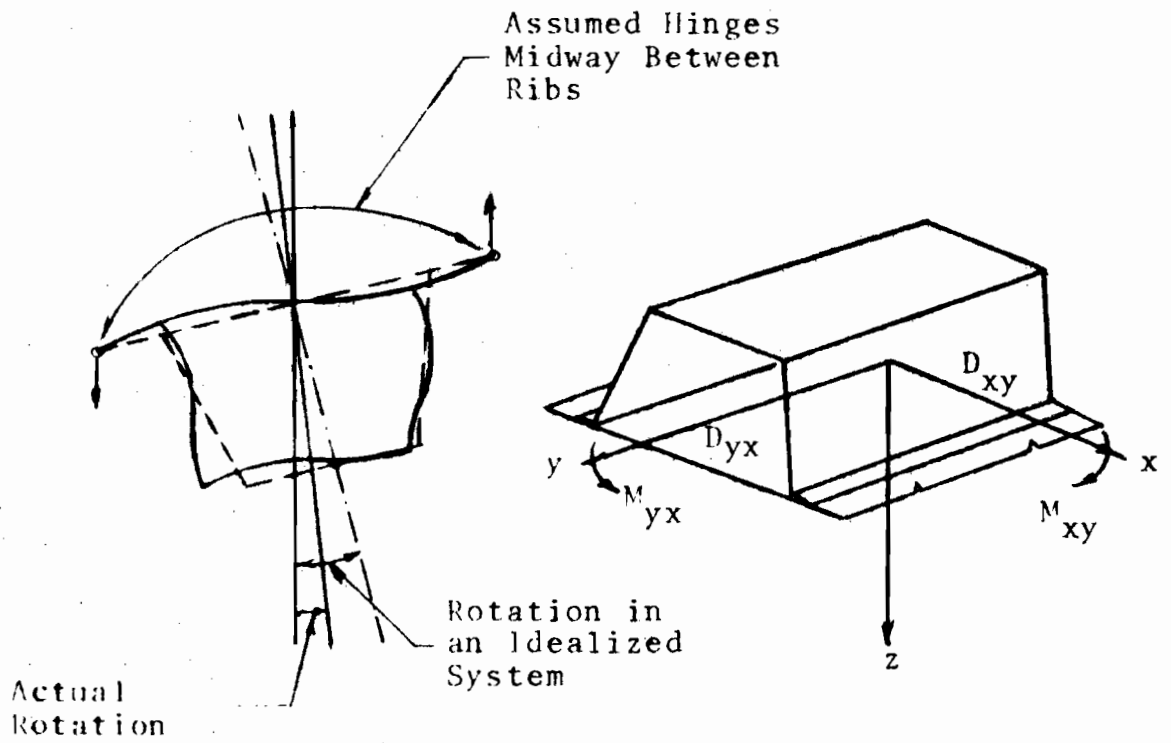


Fig. A₄ (Ref. 47)

Fig. A₅

Twisting of a Cellular Section

TABLE A-I

PROPERTY:	DECKS		
	OPEN	CELLULAR	ISOTROPIC
<u>Membrane</u>			
E_x	$E \frac{I_o}{I_y}$	E	E
E_y	$F \frac{S}{\ell}$	$F \frac{A_y}{A_x}$	E
ν_{xy}	ν	ν	ν
ν_{yx}	$\nu \frac{I_o}{I_y} \frac{\ell}{S}$	$\nu \frac{A_x}{A_y}$	ν
E_1	$\nu E \frac{I_o}{I_y}$	νE	νE
$1 - \nu_{yx} \nu_{xy}$	≈ 1.0	$1 - \nu^2 \frac{A_x}{A_y}$	$1 - \nu^2$
E_{xy}	αG	αG	G
<u>Bending</u>			
D_x	$\frac{\ell E t^3}{12S}$	$\frac{E t_1^3}{12(1 - \nu^2)}$	$\frac{E t^3}{12(1 - \nu^2)}$
D_y	$E I_{yd}$	$E I_{yd}$	$\frac{F t^3}{12(1 - \nu^2)}$
D_1	$\frac{\nu E t^3 \ell}{12S}$	0	$\frac{\nu E t^3}{12(1 - \nu^2)}$
B_{xy}	$G I_o$	0	$\frac{E t^3}{24(1 + \nu)}$
D_{yx}	$\frac{G I_o S}{\ell}$	$\frac{4 A_c^2 G}{R_{red} \left(\int \frac{ds}{t} \right) \ell}$	$\frac{E t^3}{24(1 + \nu)}$

APPENDIX B

STIFFNESS MATRICES

The stiffness of the curved element is given in three parts: I: Membrane Stiffness (u,v, displacements); II: Bending Stiffness ($w, \theta_x, \theta_y, \theta_{xy}$); III: The coupled terms of u, v and w.

I: MEMBRANE STIFFNESS MATRIX $[K]_m$

TABLE B-I

Term	E_{xt}	E_{lt}	E_{yt}	E_{xyt}
ϕ_1	$\frac{b}{3a}$	-	-	$\frac{a}{3b}$
ϕ_2	-	$\frac{1}{4}$	-	$\frac{1}{4}$
ϕ_3	-	$\frac{1}{4}$	-	$\frac{1}{4}$
ϕ_4	$-\frac{b}{3a}$	-	-	$\frac{a}{6b}$
ϕ_5	$-\frac{b}{6a}$	-	-	$-\frac{a}{6b}$
ϕ_6	$\frac{b}{6a}$	-	-	$-\frac{a}{3b}$
ϕ_7	-	-	$\frac{a}{3b}$	$\frac{b}{3a}$
ϕ_8	-	-	$\frac{a}{6b}$	$-\frac{b}{3a}$
ϕ_9	-	-	$-\frac{a}{6b}$	$\frac{b}{6a}$
ϕ_{10}	-	-	$-\frac{a}{3b}$	$\frac{b}{6a}$

e.g. $\phi_1 = \frac{b}{3a} E_{xt} + \frac{a}{3b} E_{xyt}$

II: BENDING STIFFNESS MATPIX $[K]_{bb} + [K]_{bbm}$

$$C_1 = \frac{E_{xyt}}{1225} \times \left(\frac{C}{AAxBB} \right)^2$$

All terms multiplied by C_1 are resulted because shear strain depends upon the w terms as well (see Eq. 3-9c). These terms follow the same pattern as the bending stiffness terms derived from the Eq. 3-17.

TABLE B-II

Coeff.	D_x	D_y	D_{xy}	E_1	C_1
β_1	$\frac{156}{35} \frac{b}{a^3}$	$\frac{156}{35} \frac{a}{b^3}$	$\frac{144}{25} \frac{1}{ab}$	$\frac{72}{25} \frac{1}{ab}$	676 ab
β_2	$\frac{22}{35} \frac{b^2}{a^3}$	$\frac{78}{35} \frac{a}{b^2}$	$\frac{12}{25} \frac{1}{a}$	$\frac{36}{25} \frac{1}{a}$	$\frac{286}{3} ab^2$
β_3	$-\frac{78}{35} \frac{b}{a^2}$	$-\frac{22}{35} \frac{a^2}{b^3}$	$-\frac{12}{25} \frac{1}{b}$	$-\frac{36}{25} \frac{1}{b}$	$-\frac{286}{3} a^2b$
β_4	$\frac{11}{35} \frac{b^2}{a^2}$	$\frac{11}{35} \frac{a^2}{b^2}$	$\frac{1}{25}$	$\frac{11}{50}$	$\frac{121}{9} a^2b^2$
β_5	$-\frac{156}{35} \frac{b}{a^3}$	$\frac{54}{35} \frac{a}{b^3}$	$-\frac{144}{25} \frac{1}{ab}$	$-\frac{72}{25} \frac{1}{ab}$	234 ab
β_6	$-\frac{22}{35} \frac{b^2}{a^3}$	$\frac{27}{35} \frac{a}{b^2}$	$-\frac{12}{25} \frac{1}{a}$	$-\frac{36}{25} \frac{1}{a}$	33 ab^2
β_7	$-\frac{78}{35} \frac{b}{a^2}$	$\frac{13}{35} \frac{a^2}{b^3}$	$-\frac{12}{25} \frac{1}{b}$	$-\frac{6}{25} \frac{1}{b}$	$\frac{169}{3} a^2b$
β_8	$\frac{11}{35} \frac{b^2}{a^2}$	$-\frac{13}{70} \frac{a^2}{b^2}$	$\frac{1}{25}$	$\frac{3}{25}$	$-\frac{143}{18} a^2b^2$
β_9	$-\frac{54}{35} \frac{b}{a^3}$	$-\frac{54}{35} \frac{a}{b^3}$	$\frac{144}{25} \frac{1}{ab}$	$\frac{72}{25} \frac{1}{ab}$	81 ab
β_{10}	$\frac{13}{35} \frac{b^2}{a^3}$	$\frac{27}{35} \frac{a}{b^2}$	$-\frac{12}{25} \frac{1}{a}$	$-\frac{6}{25} \frac{1}{a}$	$-\frac{217}{6} ab^2$
β_{11}	$-\frac{27}{35} \frac{b}{a^2}$	$-\frac{13}{35} \frac{a^2}{b^3}$	$\frac{12}{25} \frac{1}{b}$	$\frac{6}{25} \frac{1}{b}$	$\frac{217}{6} a^2b$

Continued

Continued

Coeff.	D_x	D_y	D_{xy}	D_1	C_1
β_{12}	$-\frac{13}{70} \frac{b^2}{a^2}$	$-\frac{13}{70} \frac{a^2}{b^2}$	$\frac{1}{25}$	$\frac{1}{50}$	$\frac{169}{36} a^2 b^2$
β_{13}	$\frac{54}{35} \frac{b}{a^3}$	$-\frac{156}{35} \frac{a}{b^3}$	$-\frac{144}{25} \frac{1}{ab}$	$-\frac{72}{25} \frac{1}{ab}$	$234 ab$
β_{14}	$-\frac{13}{35} \frac{b^2}{a^3}$	$\frac{78}{35} \frac{a}{b^2}$	$\frac{12}{25} \frac{1}{a}$	$\frac{6}{25} \frac{1}{a}$	$-\frac{169}{3} ab^2$
β_{15}	$-\frac{27}{35} \frac{b}{a^2}$	$\frac{22}{35} \frac{a^2}{b^3}$	$\frac{12}{25} \frac{1}{b}$	$\frac{36}{25} \frac{1}{b}$	$-33 a^2 b$
β_{16}	$-\frac{13}{70} \frac{b^2}{a^2}$	$\frac{11}{35} \frac{a^2}{b^2}$	$\frac{1}{25}$	$\frac{3}{25}$	$-\frac{143}{18} a^2 b^2$
β_{17}	$\frac{4}{35} \frac{b^3}{a^3}$	$\frac{52}{35} \frac{a}{b}$	$\frac{16}{25} \frac{b}{a}$	$\frac{8}{25} \frac{b}{a}$	$\frac{52}{3} ab^3$
β_{18}	$-\frac{11}{35} \frac{b^2}{a^2}$	$-\frac{11}{35} \frac{a^2}{b^2}$	$-\frac{1}{25}$	$-\frac{61}{50}$	$-\frac{121}{9} a^2 b^2$
β_{19}	$\frac{2}{35} \frac{b^3}{a^2}$	$\frac{22}{105} \frac{a^2}{b}$	$\frac{4}{75} b$	$\frac{4}{25} b$	$\frac{22}{9} a^2 b^3$
β_{20}	$-\frac{4}{35} \frac{b^3}{a^3}$	$\frac{18}{35} \frac{a}{b}$	$-\frac{16}{25} \frac{b}{a}$	$-\frac{8}{25} \frac{b}{a}$	$6 ab^3$
β_{21}	$\frac{2}{35} \frac{b^3}{a^2}$	$-\frac{13}{105} \frac{a^2}{b}$	$\frac{4}{75} b$	$\frac{2}{75} b$	$-\frac{13}{9} a^2 b^3$
β_{22}	$\frac{3}{35} \frac{b^3}{a^3}$	$\frac{9}{35} \frac{a}{b}$	$\frac{4}{25} \frac{b}{a}$	$\frac{2}{25} \frac{b}{a}$	$-\frac{9}{2} ab^3$
β_{23}	$-\frac{3}{70} \frac{b^3}{a^2}$	$-\frac{13}{210} \frac{a^2}{b}$	$-\frac{b}{75}$	$-\frac{b}{150}$	$\frac{13}{12} a^2 b^3$
β_{24}	$-\frac{3}{35} \frac{b^3}{a^3}$	$\frac{26}{35} \frac{a}{b}$	$-\frac{4}{25} \frac{b}{a}$	$-\frac{2}{25} \frac{b}{a}$	$-13 ab^3$
β_{25}	$-\frac{3}{70} \frac{b^3}{a^2}$	$\frac{11}{105} \frac{a^2}{b}$	$-\frac{b}{75}$	$-\frac{b}{25}$	$-\frac{11}{6} a^2 b^3$
β_{26}	$\frac{52}{35} \frac{b}{a}$	$\frac{4}{35} \frac{a^3}{b^3}$	$\frac{16}{25} \frac{a}{b}$	$\frac{8}{25} \frac{a}{b}$	$\frac{52}{3} a^3 b$
β_{27}	$-\frac{22}{105} \frac{b^2}{a}$	$-\frac{2}{35} \frac{a^3}{b^2}$	$-\frac{4}{75} a$	$-\frac{4}{25} a$	$-\frac{22}{9} a^3 b^2$

Continued

Continued

Coeff.	D_x	D_y	D_{xy}	D_1	C_1
β_{28}	$\frac{26}{35} \frac{b}{a}$	$-\frac{3}{35} \frac{a^3}{b^3}$	$-\frac{4}{25} \frac{a}{b}$	$-\frac{2}{25} \frac{a}{b}$	$-\frac{13}{6} a^3 b$
β_{29}	$-\frac{11}{105} \frac{b^2}{a}$	$\frac{3}{70} \frac{a^3}{b^2}$	$\frac{a}{75}$	$\frac{a}{25}$	$\frac{11}{6} a^3 b^2$
β_{30}	$\frac{9}{35} \frac{b}{a}$	$\frac{3}{35} \frac{a^3}{b^3}$	$\frac{4}{25} \frac{a}{b}$	$\frac{2}{25} \frac{a}{b}$	$-\frac{9}{2} a^3 b$
β_{31}	$\frac{13}{210} \frac{b^2}{a}$	$\frac{3}{70} \frac{a^3}{b^2}$	$\frac{a}{75}$	$\frac{a}{150}$	$-\frac{13}{12} a^3 b^2$
β_{32}	$\frac{18}{35} \frac{b}{a}$	$-\frac{4}{35} \frac{a^3}{b^3}$	$-\frac{16}{25} \frac{a}{b}$	$-\frac{8}{25} \frac{a}{b}$	$6 a^3 b$
β_{33}	$\frac{13}{105} \frac{b^2}{a}$	$-\frac{2}{35} \frac{a^3}{b^2}$	$-\frac{4}{75} a$	$-\frac{2}{75} a$	$\frac{13}{9} a^3 b^2$
β_{34}	$\frac{4}{105} \frac{b^3}{a}$	$\frac{4}{105} \frac{a^3}{b}$	$\frac{16}{225} ab$	$\frac{8}{225} ab$	$\frac{4}{9} a^3 b^3$
β_{35}	$\frac{2}{105} \frac{b^3}{a}$	$-\frac{1}{35} \frac{a^3}{b}$	$-\frac{4}{225} ab$	$-\frac{2}{225} ab$	$-\frac{a^3 b^3}{3}$
β_{36}	$-\frac{1}{70} \frac{b^3}{a}$	$-\frac{1}{70} \frac{a^3}{b}$	$\frac{1}{225} ab$	$\frac{1}{450} ab$	$\frac{1}{4} a^3 b^3$
β_{37}	$-\frac{1}{35} \frac{b^3}{a}$	$\frac{2}{105} \frac{a^3}{b}$	$-\frac{4}{225} ab$	$-\frac{2}{225} ab$	$-\frac{a^3 b^3}{3}$

III: COUPLING MATRIX $[K]_{bm}$

These terms are formed due to the coupling of u, v and w displacements (see Eq. 3-9c)

$$C_2 = E_{xyt} \left(\frac{C}{AAxBB} \right)$$

The stiffness matrix for the curved element can be reduced to that of a flat plate by putting $c=0$; whereby $C_1=0$ and $C_2=0$. The schematic representation of these two matrices is shown in Eqs. 3-20 and 3-21.

TABLE B-III

Coeff. C_2	Coeff. C_2	Coeff. C_2	Coeff. C_2
$\theta_1 \quad \frac{7}{20} a$	$\theta_5 \quad \frac{3}{20} a$	$\theta_9 \quad \frac{7}{20} b$	$\theta_{13} \quad -\frac{1}{30} b^2$
$\theta_2 \quad \frac{7}{120} ab$	$\theta_6 \quad \frac{1}{40} ab$	$\theta_{10} \quad \frac{1}{20} b^2$	$\theta_{14} \quad \frac{1}{180} ab^2$
$\theta_3 \quad -\frac{1}{20} a^2$	$\theta_7 \quad \frac{1}{30} a^2$	$\theta_{11} \quad \frac{1}{120} ab^2$	
$\theta_4 \quad \frac{1}{120} a^2 b$	$\theta_8 \quad -\frac{1}{180} a^2 b$	$\theta_{12} \quad \frac{3}{20} b$	

u_1	v_1	w_1	θ_{x1}	θ_{y1}	θ_{xy1}	u_2	v_2	w_2	θ_{x2}	θ_{y2}	θ_{xy2}	u_3	v_3	w_3	θ_{x3}	θ_{y3}	θ_{xy3}	u_4	v_4	w_4	θ_{x4}	θ_{y4}	θ_{xy4}	
Φ_1	Φ_2	θ_1	θ_2	θ_3	θ_4	Φ_4	Φ_3	θ_5	θ_6	θ_7	θ_8	Φ_5	$-\Phi_2$	θ_5	$-\theta_6$	θ_7	$-\theta_8$	Φ_6	$-\Phi_3$	θ_1	$-\theta_2$	θ_3	$-\theta_4$	u_1
	Φ_7	θ_9	θ_{10}	$-\theta_2$	θ_{11}	$-\Phi_3$	Φ_8	θ_9	θ_{10}	θ_2	$-\theta_{11}$	$-\Phi_2$	Φ_9	θ_{12}	θ_{13}	θ_6	θ_{14}	Φ_3	Φ_{10}	θ_{12}	θ_{13}	$-\theta_6$	$-\theta_{14}$	v_1
		β_1	β_2	β_3	β_4	θ_5	$-\theta_9$	β_5	β_6	β_7	β_8	$-\theta_5$	$-\theta_{12}$	β_9	β_{10}	β_{11}	β_{12}	$-\theta_1$	θ_{12}	β_{13}	β_{14}	β_{15}	β_{16}	w_1
			β_{17}	β_{18}	β_{19}	θ_6	$-\theta_{10}$	β_6	β_{20}	$-\beta_8$	β_{21}	$-\theta_6$	θ_{13}	$-\beta_{10}$	β_{22}	β_{12}	β_{23}	$-\theta_2$	$-\theta_{13}$	$-\beta_{14}$	β_{24}	β_{16}	β_{25}	θ_{x1}
				β_{26}	β_{27}	$-\theta_7$	θ_2	$-\beta_7$	β_8	β_{28}	β_{29}	θ_7	θ_6	$-\beta_{11}$	β_{12}	β_{30}	β_{31}	$-\theta_3$	$-\theta_6$	β_{15}	$-\beta_{16}$	β_{32}	β_{33}	θ_{y1}
					β_{34}	$-\theta_8$	$-\theta_{11}$	$-\beta_8$	$-\beta_{21}$	β_{29}	β_{35}	θ_8	$-\theta_{14}$	β_{12}	$-\beta_{23}$	$-\beta_{31}$	β_{36}	$-\theta_4$	θ_{14}	$-\beta_{16}$	β_{25}	$-\beta_{33}$	β_{37}	θ_{xy1}
						Φ_1	$-\Phi_2$	θ_1	θ_2	$-\theta_3$	$-\theta_4$	Φ_6	Φ_3	θ_1	$-\theta_2$	$-\theta_3$	θ_4	Φ_5	Φ_2	θ_5	$-\theta_6$	$-\theta_7$	θ_8	u_2
							Φ_7	$-\theta_9$	$-\theta_{10}$	$-\theta_2$	θ_{11}	$-\Phi_3$	Φ_{10}	$-\theta_{12}$	$-\theta_{13}$	$-\theta_6$	$-\theta_{14}$	Φ_2	Φ_9	$-\theta_{12}$	$-\theta_{13}$	θ_6	θ_{14}	v_2
								β_1	β_2	$-\beta_3$	$-\beta_4$	$-\theta_1$	$-\theta_{12}$	β_{13}	β_{14}	$-\beta_{15}$	$-\beta_{16}$	$-\theta_5$	θ_{12}	β_9	β_{10}	$-\beta_{11}$	$-\beta_{12}$	w_2
									β_{17}	$-\beta_{18}$	$-\beta_{19}$	$-\theta_2$	θ_{13}	$-\beta_{14}$	β_{24}	$-\beta_{16}$	$-\beta_{25}$	$-\theta_6$	$-\theta_{13}$	$-\beta_{10}$	β_{22}	$-\beta_{12}$	$-\beta_{23}$	θ_{x2}
										β_{26}	β_{27}	θ_3	$-\theta_6$	$-\beta_{15}$	β_{16}	β_{32}	β_{33}	$-\theta_7$	θ_6	β_{11}	$-\beta_{12}$	β_{30}	β_{31}	θ_{y2}
											β_{34}	θ_4	θ_{14}	β_{16}	$-\beta_{25}$	$-\beta_{33}$	β_{37}	$-\theta_8$	$-\theta_{14}$	$-\beta_{12}$	β_{23}	$-\beta_{31}$	β_{36}	θ_{xy2}
												Φ_1	Φ_2	$-\theta_1$	θ_2	θ_3	$-\theta_4$	Φ_4	Φ_3	$-\theta_5$	θ_6	θ_7	$-\theta_8$	u_3
													Φ_7	$-\theta_9$	θ_{10}	$-\theta_2$	$-\theta_{11}$	$-\Phi_3$	Φ_8	$-\theta_9$	θ_{10}	θ_2	θ_{11}	v_3
														β_1	$-\beta_2$	$-\beta_3$	β_4	$-\theta_5$	θ_9	β_5	$-\beta_6$	$-\beta_7$	β_8	w_3
															β_{17}	β_{18}	$-\beta_{19}$	θ_6	$-\theta_{10}$	$-\beta_6$	β_{20}	$-\beta_8$	$-\beta_{21}$	θ_{x3}
																β_{26}	$-\beta_{27}$	$-\theta_7$	θ_2	β_7	β_8	β_{28}	$-\beta_{29}$	θ_{y3}
																	β_{34}	θ_8	θ_{11}	$-\beta_8$	β_{21}	$-\beta_{29}$	β_{35}	θ_{xy3}
																		Φ_1	$-\Phi_2$	$-\theta_1$	θ_2	$-\theta_3$	θ_4	u_4
																			Φ_7	θ_9	$-\theta_{10}$	$-\theta_2$	$-\theta_{11}$	v_4
																				β_1	$-\beta_2$	β_3	$-\beta_4$	w_4
																					β_{17}	$-\beta_{18}$	β_{19}	θ_{x4}
																						β_{26}	$-\beta_{27}$	θ_{y4}
																							β_{34}	θ_{xy4}

SYMMETRIC

TABLE B-IV

CURVED ELEMENT STIFFNESS MATRIX [K]

APPENDIX C
DECK STRESSES

A typical deck element 1-2-3-4 rectangular in plan is shown in Fig. C₁. The deck forces and the deck moments with notations shown in Figs. 3.2 and 3.3 are calculated at the center point o. The deck in-plane forces and moments are calculated for a curved element using the strain displacement relationships given in Eqs. 3-9 and 3-10. The forces for the flat elements can be deduced from the expressions given below. The two major differences are: (a) c=0; (b) The local nodal displacements in the local axes for each element are to be used.

$$N_x = E_{xt} u_{,x} + E_{1t} v_{,y}$$

$$= \frac{E_{xt}}{2a} [-u_1 + u_2 + u_3 - u_4] + \frac{E_{1t}}{2b} [-v_1 - v_2 + v_3 + v_4] \quad C-1$$

$$N_y = E_{1t} u_{,x} + E_{yt} v_{,y}$$

$$= \frac{E_{1t}}{2a} [-u_1 + u_2 + u_3 - u_4] + \frac{E_{yt}}{2b} [-v_1 - v_2 + v_3 + v_4] \quad C-2$$

$$N_{xy} = (u_{,y} + v_{,x} - 2 \frac{C}{AE} w) E_{xyt}$$

$$= E_{xyt} \{ (-u_1 - u_2 + u_3 + u_4) / 2b + (-v_1 + v_2 + v_3 - v_4) / 2a$$

$$- \frac{C}{AE} [(w_1 + w_2 + w_3 + w_4) / 2 + (\theta_{x1} + \theta_{x2} - \theta_{x3} - \theta_{x4}) \frac{b}{8}$$

$$+ (-\theta_{y1} + \theta_{y2} - \theta_{y3} - \theta_{y4}) \frac{a}{8} + (\theta_{xy1} - \theta_{xy2} + \theta_{xy3} - \theta_{xy4}) \frac{ab}{32}] \} \quad C-3$$

$$w_{,xx} = [(\theta_{y1} - \theta_{y2} - \theta_{y3} + \theta_{y4}) / 2a + (-\theta_{xy1} + \theta_{xy2} - \theta_{xy3} + \theta_{xy4}) \frac{b}{8a}] \quad C-4$$

$$w_{,yy} = [(-\theta_{x1} - \theta_{x2} + \theta_{x3} + \theta_{x4}) / 2b + (-\theta_{xy1} + \theta_{xy2} - \theta_{xy3} + \theta_{xy4}) \frac{a}{8b}] \quad C-5$$

The moments per unit length can be obtained

$$M_x = -[D_x w_{,xx} + D_1 w_{,yy}] \quad \text{C-6}$$

$$M_y = -[D_1 w_{,xx} + D_y w_{,yy}] \quad \text{C-7}$$

Fig. C₂ shows the bending stresses which could be introduced due to the local bending of each individual plate elements. These stresses are not calculated here.

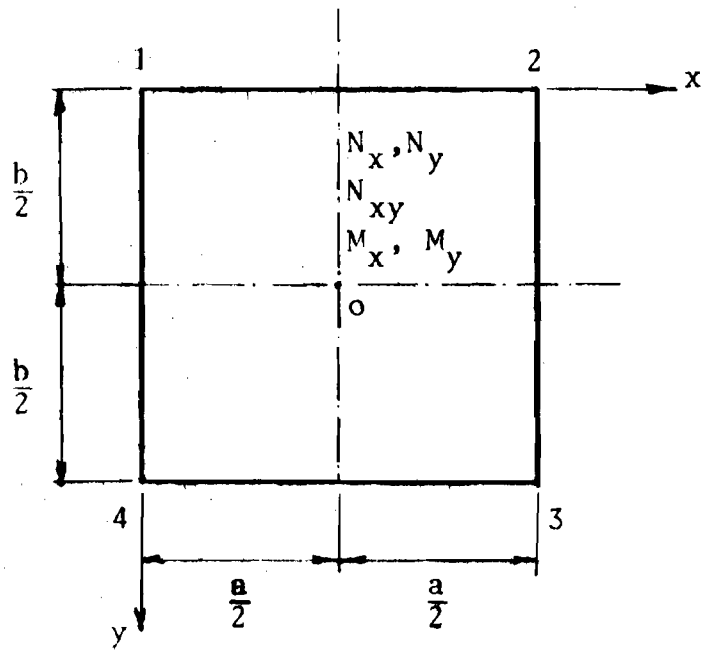


Fig. C₁ Deck Forces at Point 'o'.

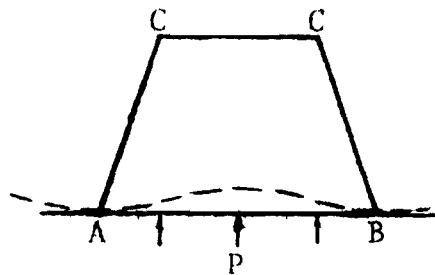


Fig. C₂ Local Bending of Plate AB

APPENDIX D

INCREMENTAL MATRIX FOR THE DECK

For simplicity, the matrix is split up into two parts. $[N]_1$ which contains the terms corresponding to the in-plane forces N_x and N_y whereas the matrix $[N]_2$ contains the terms corresponding to the shearing force N_{xy}

$$[N] = [N]_1 + [N]_2 \quad D-1$$

TABLE D-I

Coeff.	N_x	N_y	Coeff.	N_x	N_y
ϕ_1	$\frac{78}{175} \frac{b}{a}$	$\frac{78}{175} \frac{a}{b}$	ϕ_{13}	$\frac{27}{175} \frac{b}{a}$	$-\frac{78}{175} \frac{a}{b}$
ϕ_2	$\frac{11}{175} \frac{b^2}{a}$	$\frac{13}{350} a$	ϕ_{14}	$-\frac{13}{350} \frac{b^2}{a}$	$\frac{13}{350} a$
ϕ_3	$-\frac{13}{350} b$	$-\frac{11}{175} \frac{a^2}{b}$	ϕ_{15}	$-\frac{9}{700} b$	$\frac{11}{175} \frac{a^2}{b}$
ϕ_4	$\frac{11}{2100} b^2$	$\frac{11}{2100} a^2$	ϕ_{16}	$-\frac{13}{4200} b^2$	$\frac{11}{2100} a^2$
ϕ_5	$-\frac{78}{175} \frac{b}{a}$	$\frac{27}{175} \frac{a}{b}$	ϕ_{17}	$\frac{2}{175} \frac{b^3}{a}$	$\frac{26}{525} ab$
ϕ_6	$-\frac{11}{175} \frac{b^2}{a}$	$\frac{9}{700} a$	ϕ_{18}	$-\frac{11}{2100} b^2$	$-\frac{11}{2100} a^2$
ϕ_7	$-\frac{13}{350} b$	$\frac{13}{350} \frac{a^2}{b}$	ϕ_{19}	$\frac{1}{1050} b^3$	$\frac{11}{1575} a^2 b$
ϕ_8	$\frac{11}{2100} b^2$	$-\frac{13}{4200} a^2$	ϕ_{20}	$-\frac{2}{175} \frac{b^3}{a}$	$\frac{3}{175} ab$
ϕ_9	$-\frac{27}{175} \frac{b}{a}$	$-\frac{27}{175} \frac{a}{b}$	ϕ_{21}	$\frac{1}{1050} b^3$	$-\frac{13}{3150} a^2 b$
ϕ_{10}	$\frac{13}{350} \frac{b^2}{a}$	$\frac{9}{700} a$	ϕ_{22}	$\frac{3}{350} \frac{b^3}{a}$	$-\frac{3}{700} ab$
ϕ_{11}	$-\frac{9}{700} b$	$-\frac{13}{350} \frac{a^2}{b}$	ϕ_{23}	$-\frac{1}{1400} b^3$	$\frac{13}{12600} a^2 b$
ϕ_{12}	$-\frac{13}{4200} b^2$	$-\frac{13}{4200} a^2$	ϕ_{24}	$-\frac{3}{350} \frac{b^3}{a}$	$-\frac{13}{1050} ab$

Continued

Continued

Coeff.	N_x	N_y	Coeff.	N_x	N_y
ϕ_{25}	$-\frac{1}{1400} b^3$	$-\frac{11}{6300} a^2 b$	ϕ_{31}	$\frac{3}{175} ab$	$-\frac{2}{175} \frac{a^3}{b}$
ϕ_{26}	$\frac{26}{525} ab$	$\frac{2}{175} \frac{a^3}{b}$	ϕ_{33}	$\frac{13}{3150} ab^2$	$-\frac{1}{1050} a^3$
ϕ_{27}	$-\frac{11}{1575} ab^2$	$-\frac{1}{1050} a^3$	ϕ_{34}	$\frac{2}{1575} ab^3$	$\frac{2}{1575} a^3 b$
ϕ_{28}	$-\frac{13}{1050} ab$	$-\frac{3}{350} \frac{a^3}{b}$	ϕ_{35}	$-\frac{1}{3150} ab^3$	$-\frac{1}{1050} a^3 b$
ϕ_{29}	$\frac{11}{6300} ab^2$	$\frac{1}{1400} a^3$	ϕ_{36}	$\frac{1}{4200} ab^3$	$\frac{1}{4200} a^3 b$
ϕ_{30}	$-\frac{3}{700} ab$	$\frac{3}{350} \frac{a^3}{b}$	ϕ_{37}	$-\frac{1}{1050} ab^3$	$-\frac{1}{3150} a^3 b$
ϕ_{31}	$-\frac{13}{12600} ab^2$	$\frac{1}{1400} a^3$			

TABLE D-II

Coeff.	N_{xy}	Coeff.	N_{xy}	Coeff.	N_{xy}
θ_1	$\frac{1}{2}$	θ_4	$\frac{a}{10}$	θ_7	$\frac{a^2}{60}$
θ_2	$\frac{ab}{50}$	θ_5	$\frac{a^2 b}{300}$	θ_8	$\frac{b^2}{60}$
θ_3	$\frac{b}{10}$	θ_6	$\frac{ab^2}{300}$	θ_9	$\frac{a^2 b^2}{1800}$

e.g. $N(1,4) = \frac{11}{2100} N_x b^2 + \frac{11}{2100} N_y a^2 - \frac{N_{xy} ab}{50}$

w_1	θ_{x1}	θ_{y1}	θ_{xy1}	w_2	θ_{x2}	θ_{y2}	θ_{xy2}	w_3	θ_{x3}	θ_{y3}	θ_{xy3}	w_4	θ_{x4}	θ_{y4}	θ_{xy4}	
ϕ_1	ϕ_2	ϕ_3	ϕ_4	ϕ_5	ϕ_6	ϕ_7	ϕ_8	ϕ_9	ϕ_{10}	ϕ_{11}	ϕ_{12}	ϕ_{13}	ϕ_{14}	ϕ_{15}	ϕ_{16}	w_1
	ϕ_{17}	ϕ_{18}	ϕ_{19}	ϕ_6	ϕ_{20}	$-\phi_8$	ϕ_{21}	$-\phi_{10}$	ϕ_{22}	ϕ_{12}	ϕ_{23}	$-\phi_{14}$	ϕ_{24}	ϕ_{16}	ϕ_{25}	θ_{x1}
		ϕ_{26}	ϕ_{27}	$-\phi_7$	ϕ_8	ϕ_{28}	ϕ_{29}	$-\phi_{11}$	ϕ_{12}	ϕ_{30}	ϕ_{31}	ϕ_{15}	$-\phi_{16}$	ϕ_{32}	ϕ_{33}	θ_{y1}
			ϕ_{34}	$-\phi_8$	$-\phi_{21}$	ϕ_{29}	ϕ_{35}	ϕ_{12}	$-\phi_{23}$	$-\phi_{31}$	ϕ_{36}	$-\phi_{16}$	ϕ_{25}	$-\phi_{33}$	ϕ_{37}	θ_{xy1}
				ϕ_1	ϕ_2	$-\phi_3$	$-\phi_4$	ϕ_{13}	ϕ_{14}	$-\phi_{15}$	$-\phi_{16}$	ϕ_9	ϕ_{10}	$-\phi_{11}$	$-\phi_{12}$	w_2
					ϕ_{17}	$-\phi_{18}$	$-\phi_{19}$	$-\phi_{14}$	ϕ_{24}	$-\phi_{16}$	$-\phi_{25}$	$-\phi_{10}$	ϕ_{22}	$-\phi_{12}$	$-\phi_{23}$	θ_{x2}
						ϕ_{20}	ϕ_{27}	$-\phi_{15}$	ϕ_{16}	ϕ_{32}	ϕ_{33}	ϕ_{11}	$-\phi_{12}$	ϕ_{30}	ϕ_{31}	θ_{y2}
							ϕ_{34}	ϕ_{16}	$-\phi_{25}$	$-\phi_{33}$	ϕ_{37}	$-\phi_{12}$	ϕ_{23}	$-\phi_{31}$	ϕ_{36}	θ_{xy2}
								ϕ_1	$-\phi_2$	$-\phi_3$	ϕ_4	ϕ_5	$-\phi_6$	$-\phi_7$	ϕ_8	w_3
									ϕ_{17}	ϕ_{18}	$-\phi_{19}$	$-\phi_6$	ϕ_{20}	$-\phi_8$	$-\phi_{21}$	θ_{x3}
										ϕ_{26}	$-\phi_{27}$	ϕ_7	ϕ_8	ϕ_{28}	$-\phi_{29}$	θ_{y3}
											ϕ_{34}	$-\phi_8$	ϕ_{21}	$-\phi_{29}$	ϕ_{35}	θ_{xy3}
												ϕ_1	$-\phi_2$	ϕ_3	$-\phi_4$	w_4
													ϕ_{12}	ϕ_{17}	$-\phi_{18}$	θ_{x4}
														ϕ_{26}	$-\phi_{27}$	θ_{y4}
															ϕ_{34}	θ_{xy4}

SYMMETRIC

TABLE D-III

$[N]_1$ MATRIX

w_1	θ_{x1}	θ_{y1}	θ_{xy1}	w_2	θ_{x2}	θ_{y2}	θ_{xy2}	w_3	θ_{x3}	θ_{y3}	θ_{xy3}	w_4	θ_{x4}	θ_{y4}	θ_{xy4}	
θ_1	0	0	$-\theta_2$	0	$-\theta_5$	0	θ_2	$-\theta_1$	θ_3	$-\theta_4$	$-\theta_2$	0	0	θ_4	θ_2	w_1
	0	$-\theta_2$	0	θ_3	0	θ_2	0	$-\theta_3$	θ_8	$-\theta_2$	$-\theta_6$	0	0	θ_2	θ_6	θ_{x1}
		0	0	0	θ_2	0	$-\theta_5$	θ_4	$-\theta_2$	θ_7	θ_5	$-\theta_4$	θ_2	0	0	θ_{y1}
			0	θ_2	0	θ_5	0	$-\theta_2$	θ_6	$-\theta_5$	$-\theta_9$	θ_2	$-\theta_6$	0	0	θ_{xy1}
				$-\theta_1$	0	0	$-\theta_2$	0	0	θ_4	θ_2	θ_1	$-\theta_3$	$-\theta_4$	$-\theta_2$	w_2
					0	$-\theta_2$	0	0	0	θ_2	θ_6	θ_3	$-\theta_8$	$-\theta_2$	$-\theta_6$	θ_{x2}
					0	0	$-\theta_4$	θ_2	0	0	0	θ_4	$-\theta_2$	$-\theta_7$	$-\theta_5$	θ_{y2}
						0	θ_2	$-\theta_6$	0	0	$-\theta_2$	θ_6	θ_5	θ_9	0	θ_{xy2}
							θ_1	0	0	$-\theta_2$	0	θ_3	0	θ_2	0	w_3
								0	$-\theta_2$	0	$-\theta_3$	0	θ_2	0	0	θ_{x3}
									0	0	0	θ_2	0	θ_5	0	θ_{y3}
											0	θ_2	0	$-\theta_5$	0	θ_{xy3}
												$-\theta_1$	0	0	$-\theta_2$	w_4
													0	$-\theta_2$	0	θ_{x4}
														0	0	θ_{y4}
															0	θ_{xy4}

SYMMETRIC

TABLE D-IV

$[N]_2$ MATRIX

APPENDIX E

STIFFNESS AND INCREMENTAL MATRICES FOR A
FULLY COMPATIBLE ECCENTRIC STIFFENER

INTRODUCTION

In the case of light gage hypars the orthotropic deck is connected at discrete points to the supporting edge member. Because of this discrete connection, there is a certain amount of non-compatibility between the edge members and the deck. The stiffness matrix used in Chapter III was developed by the use of direct co-ordinate transformation. The co-ordinate transformation assumes that the neutral plane of bending for the original beam cross-section remains unaltered. With the type of connections used for the light-gage hypars, the assumption made above represents the true behavior.

However, in the case of stiffeners which are rigidly connected to a plate or a shell or a monolithically cast concrete beam, there is full compatibility between the strains at the junction of the deck and the beam. In this compatible case, a part of the deck also acts along with the stiffener (effective width concept). The interaction of the deck and the stiffener results in the adjustment of the neutral axis of the section. To account for this change of neutral axis, the bending property of the stiffener will have to be modified by arbitrarily assuming the effective width of the deck acting along with the beam (see discussion on Struc. '6', Section IV-5B). Depending upon

the relative stiffness of the plate, this kind of arbitrary adjustment in the stiffener property will present a problem. This arbitrariness is removed by formulating the compatible stiffener element.

STIFFNESS MATRIX

A typical eccentric member is shown in Fig. 3.10. It is assumed that the member is uniform in size and its local axes \bar{x} , \bar{y} and \bar{z} , through the shear center and the centroid, are parallel to the global axes x , y and z . Let U_c be the average axial deformation of the section measured at the centroid of the section (C.G.) and V_s and W_s be the bending deformations measured at the shear center (S.C.).

Assuming a rigid connection between the stiffener and the reference structural node points, the displacements at the shear center and the centroid can be expressed as follows:

$$U_c = u - z_c \left(\frac{\partial w}{\partial x} \right) - Y_c \left(\frac{\partial v}{\partial x} \right) \quad \text{E-1a}$$

$$V_s = v - z_s \theta \quad \text{E-1b}$$

$$W_s = w + Y_s \theta \quad \text{E-1c}$$

where $\theta = \frac{\partial w}{\partial y}$. The total strain energy of the beam element can be given as

$$U_b = \frac{EA_b}{2} \int_0^a \left(\frac{\partial U_c}{\partial x} \right)^2 dx + \frac{EI_y}{2} \int_0^a \left(\frac{\partial^2 W_s}{\partial x^2} \right)^2 dx + \frac{EI_z}{2} \int_0^a \left(\frac{\partial^2 V_s}{\partial x^2} \right)^2 dx + \frac{1}{2} GJ \int_0^a \theta^2 dx + \frac{1}{2} EI \int_0^a \theta''^2 dx \quad \text{E-2}$$

All the member properties are expressed with reference to their local principal axes. The displacement fields

for u , v , w and θ are given by Equations 3-26, 3-27. The stiffness matrix (neglecting the in-plane rotation θ_z) is given in Table E-I. Though not tested on the hypar structure, the element when checked for simple cases such as simple and cantilever beams, converged to the correct results. The element can be used for a rigidly connected eccentric member and correctly locates its own neutral axis under different types of loading.

It may be worthwhile to note that because of the coupling of the u , v and w displacements, the resulting displacements for u are no longer linear. The use of a Hermitian polynomial of the same order as used for the v and w displacements will give more rapid convergence characteristic than with a linear u displacement field. It was not possible to use u as non-linear because of the lack of a corresponding degree of freedom in the formulation for a plate or a shell element. Similar stiffness matrices are reported in Refs. 70, 71, whereas the theory of the element is developed in detail in Refs. 72, 73.

INCREMENTAL MATRIX FOR UNIFORMLY COMPRESSED ECCENTRIC STIFFENER

The load acting on a fiber whose cross-sectional area is dA , is σdA and the change in the distance between the end point of a fiber is given by Δu . The increase in the potential energy due to the change of fiber is given by

$$\delta V = - \int_A \sigma \Delta u dA \quad E-3$$

For the section which shows both modes of buckling (flexural

as well as twisting), the change in the length of a fiber is given by⁵⁷, (Fig. E₁)

$$\Delta u = \frac{1}{2} \int_0^a \left\{ \left(\frac{\partial w}{\partial x} + y\theta' \right)^2 + \left(\frac{\partial v}{\partial x} - z\theta' \right)^2 \right\} dx \quad E-4$$

For the uniformly loaded section, σ is the constant quantity and $\sigma A = P$. Therefore the change in the potential energy

$$\delta V = \frac{1}{2} P \int_0^a \left\{ \left(\frac{\partial w}{\partial x} \right)^2 + \left(\frac{\partial v}{\partial x} \right)^2 + 2Y_c \left(\frac{\partial w}{\partial x} \right) \theta' - 2Z_c \left(\frac{\partial v}{\partial x} \right) \theta' + \theta'^2 \rho^2 \right\} dx \quad E-5$$

where Z_c and Y_c are the distances of the centroid of the section (Fig. 3.10) and ρ is the radius of gyration for the polar moment of inertia of the cross section about the point o.

$$\rho^2 = \frac{1}{A} \int_A (z^2 + y^2) dA \quad E-6$$

The incremental matrix can be obtained by integrating the expression E-5 and then obtaining the second derivative of the total change in the potential energy. The incremental matrix (8x8) is given in Table E-II.

The stiffness and the incremental matrices for the eccentric stiffeners can be used to predict the buckling load for the stiffened plate. Because of the non-availability of a large-order eigenvalue solution routine, the formulation could not be checked with other available solutions. However a simple case of twist-buckling of column section about the forced shear center for a T-section and I-section was compared with the classical solution for hinged end condition given by

Bleich⁵⁶.

$$\sigma_c = \frac{\pi^2 E}{a^2} \left[\frac{z_s^2 I_y + \Gamma_b}{I_{pc}} + \frac{G}{\pi^2 E} \frac{a^2 J}{I_{pc}} \right] \quad \text{E-7}$$

I_{pc} = Polar moment of inertia about the forced shear center 0.
The only difference for both the cases is that the T-section has $\Gamma_b = 0$ whereas Γ_b for the I-section is 1590 inch⁶. In both the cases, for simply supported ends, the twist buckling load was within <<1% in error, from the values given by the classical solutions. A negligible error is observed in one element solution. The buckling stress predicted with 2 and 4 number of elements showed an almost insignificant improvement.

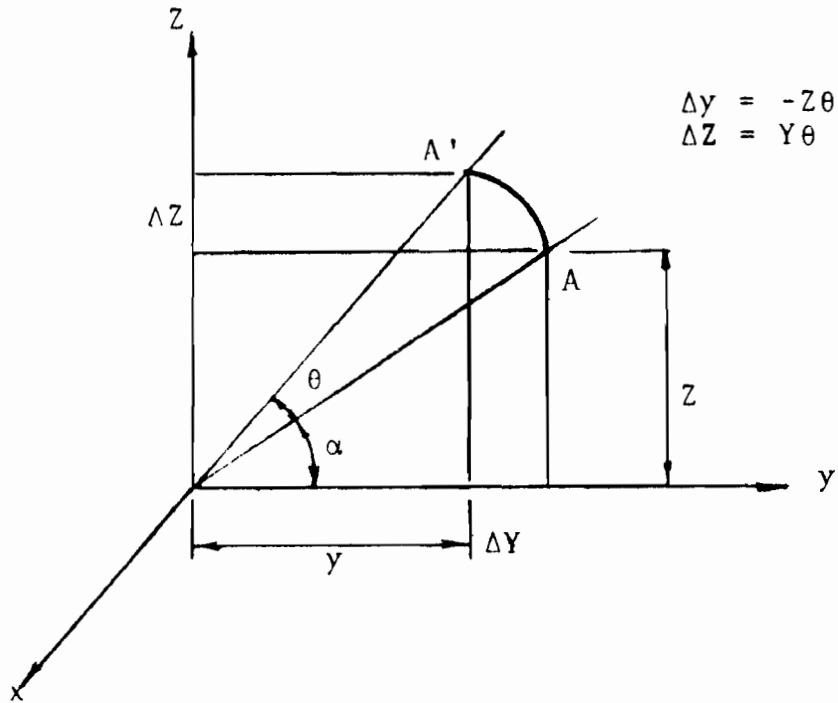


Fig. E₁ Displacement Due to Twisting of a Beam

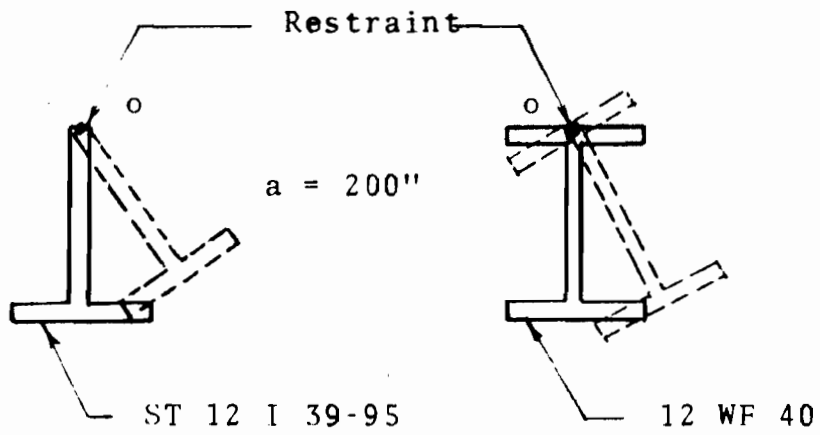


Fig. E₂ Twist Buckling

u_1	v_1	w_1	θ_{x1}	θ_{y1}	θ_{xy1}	u_2	v_2	w_2	θ_{x2}	θ_{y2}	θ_{xy2}
$\frac{A_b E}{a}$	0	0	0	$\frac{A_b E z_c}{a}$	0	$-\frac{A_b E}{a}$	0	0	0	$-\frac{A_b E z_c}{a}$	0
	$\frac{12EI_{ox}}{a^3}$	$\frac{12EA_b y_c z_c}{a^3}$	$-\frac{12EI_z z_s}{a^3}$	$-\frac{6EA_b y_c z_c}{a^2}$	$-\frac{6EI_z z_s}{a^2}$	0	$-\frac{12EI_{ox}}{a^3}$	$-\frac{12EA_b y_c z_c}{a^3}$	$\frac{12EI_z z_s}{a^3}$	$-\frac{6EA_b y_c z_c}{a^2}$	$-\frac{6EI_z z_s}{a^2}$
		$\frac{12EI_{oy}}{a^3}$	$\frac{12EI_y y_s}{a^3}$	$-\frac{6EI_{oy}}{a^2}$	$\frac{6EI_y y_s}{a^2}$	0	$-\frac{12EA_b y_c z_c}{a^3}$	$-\frac{12EI_{oy}}{a^3}$	$-\frac{12EI_y y_s}{a^3}$	$-\frac{6EI_{oy}}{a^2}$	$\frac{6EI_y y_s}{a^2}$
			$\frac{12EI_y y_s^2}{a^3}$	$-\frac{6EI_y y_s}{a^2}$	$\frac{6EI_z z_s^2}{a^2}$	0			$-\frac{12EI_y y_s^2}{a^3}$		$\frac{6EI_y y_s^2}{a^2}$
			$+\frac{12EI_z z_s^2}{a^3}$	$-\frac{6EI_y y_s}{a^2}$	$+\frac{6EI_y y_s^2}{a^2}$	0	$\frac{12EI_z z_s}{a^3}$	$-\frac{12EI_y y_s}{a^3}$	$-\frac{12EI_z z_s^2}{a^3}$	$-\frac{6EI_y y_s}{a^2}$	$+\frac{6EI_z z_s^2}{a^2}$
			$+\frac{6}{5} \frac{GJ}{a}$		$+\frac{GJ}{10}$				$-\frac{6}{5} \frac{GJ}{a}$		$+\frac{GJ}{10}$
			$+\frac{12E\Gamma_b}{a^3}$		$+\frac{6E\Gamma_b}{a^2}$				$-\frac{12E\Gamma_b}{a^3}$		$+\frac{6E\Gamma_b}{a^2}$
				$\frac{4EI_{oy}}{a}$	$-\frac{4EI_y y_s}{a}$	$-\frac{A_b E z_c}{a}$	$\frac{6EA_b y_c z_c}{a^2}$	$\frac{6EI_{oy}}{a^2}$	$\frac{6EI_y y_s}{a^2}$	$\frac{2EI_{oy}}{a}$	$-\frac{2EI_y y_s}{a}$
					$\frac{4EI_y y_s^2}{a}$				$-\frac{6EI_y y_s^2}{a^2}$		$\frac{2EI_y y_s^2}{a}$
					$+\frac{4EI_z z_s^2}{a}$	0	$\frac{6EI_z z_s}{a^2}$	$-\frac{6EI_y y_s}{a^2}$	$-\frac{6EI_z z_s^2}{a^2}$	$-\frac{2EI_y y_s}{a}$	$+\frac{2EI_z z_s^2}{a}$
					$+\frac{2}{15} \frac{GJa}{a}$				$-\frac{GJ}{10}$		$+\frac{2E\Gamma_b}{a}$
					$+\frac{4E\Gamma_b}{a}$				$-\frac{6E\Gamma_b}{a^2}$		$-\frac{1}{30} \frac{GJa}{a}$
						$\frac{A_b E}{a}$	0	0	0	$\frac{A_b E z_c}{a}$	0
							$\frac{12EI_{ox}}{a^3}$	$\frac{12EA_b y_c z_c}{a^3}$	$-\frac{12EI_z z_s}{a^3}$	$\frac{6EA_b y_c z_c}{a^2}$	$\frac{6EI_z z_s}{a^2}$
								$\frac{12EI_{oy}}{a^3}$	$\frac{12EI_y y_s}{a^3}$	$\frac{6EI_{oy}}{a^2}$	$-\frac{6EI_y y_s}{a^2}$
									$\frac{12EI_y y_s^2}{a^3}$		$-\frac{6EI_y y_s^2}{a^2}$
									$+\frac{12EI_z z_s^2}{a^3}$		$-\frac{6EI_z z_s^2}{a^2}$
									$+\frac{6}{5} \frac{GJ}{a}$		$-\frac{GJ}{10}$
									$+\frac{12E\Gamma_b}{a^3}$		$-\frac{6E\Gamma_b}{a^2}$
										$\frac{4EI_{oy}}{a}$	$-\frac{4EI_y y_s}{a}$
											$\frac{4EI_y y_s^2}{a}$
											$+\frac{4EI_z z_s^2}{a}$
											$+\frac{2}{15} \frac{GJa}{a}$
											$+\frac{4E\Gamma_b}{a}$

SYMMETRIC

$$I_{oy} = I_y + A_b z_c^2$$

$$I_{oz} = I_z + A_b y_c^2$$

TABLE E-1

STIFFNESS MATRIX FOR A COMPATIBLE
ECCENTRIC STIFFENER

w_1	θ_{x1}	θ_{y1}	θ_{xy1}	w_2	θ_{x2}	θ_{y2}	θ_{xy2}
$\frac{6}{5}$	$\frac{6}{5} G_1$	$-\frac{a}{10}$	$\frac{a}{10} G_1$	$-\frac{6}{5}$	$-\frac{6}{5} G_1$	$-\frac{a}{10}$	$\frac{a}{10} G_1$
	$\frac{6}{5} G_2$	$-\frac{a}{10} G_1$	$\frac{a}{10} G_2$	$-\frac{6}{5} G_1$	$-\frac{6}{5} G_2$	$-\frac{a}{10} G_1$	$\frac{a}{10} G_2$
		$\frac{2}{15} a^2$	$-\frac{2}{15} a^2 G_1$	$\frac{a}{10}$	$\frac{a}{10} G_1$	$-\frac{1}{30} a^2$	$-\frac{1}{30} a^2 G_1$
			$\frac{2}{15} a^2 G_2$	$-\frac{a}{10} G_1$	$-\frac{a}{10} G_2$	$\frac{a^2}{30} G_1$	$-\frac{1}{30} a^2 G_2$
				$\frac{6}{5}$	$\frac{6}{5} G_1$	$\frac{a}{10}$	$-\frac{a}{10} G_1$
					$\frac{6}{5} G_2$	$\frac{a}{10} G_1$	$-\frac{a}{10} G_2$
						$\frac{2}{15} a^2$	$-\frac{2}{15} a^2 G_1$
							$\frac{2}{15} a^2 G_2$

SYMMETRIC
 $G_1 = \frac{Y_c}{I}$
 $G_2 = \frac{p c}{A}$
 Note Common Factor $\frac{P}{a}$

TABLE E-II INCREMENTAL MATRIX FOR
 COMPATIBLE ECCENTRIC STIFFENER

APPENDIX F

COMPUTER PROGRAMS

Computer programs were written for linear stiffness and instability analysis using both curved and flat elements (Method 'a' and Method 'b'). Since the input data for both curved and flat elements is nearly the same, a general description of both stiffness and instability programs is given here. All information given in this appendix, is pertinent to IBM 360/65 model available at the Cornell University. Double precision is used in all programs.

STIFFNESS ANALYSIS

Hypars have mostly been analyzed for a uniform grid size 8x8 (64 elements). Depending upon the available core storage and required accuracy of the solution, the grid size can be varied. For the flat plate elements, the program requires a core size 365K and has a compiling time roughly of 55 secs. The computation time for one problem is roughly 70 secs. The time requirement for the curved element program is somewhat less.

The input information can be categorized as follows:

1. Properties of the Deck

Properties of decks shown in Fig. 2.2a, b and c can be calculated by a subroutine "PDEC" in which the geometrical properties such as thickness and other physical parameters can be specified. For decks other than those mentioned above,

elastic constants E_x , E_y , ... etc., are to be calculated and read in as input data. Besides the type of deck, the orientation and number of decks also need to be specified. The geometrical properties calculated on the basis of shape can be further modified by the use of coefficients determined experimentally.

2. Geometry of the Surface

The geometry of the surface is defined by specifying the number of hyper quadrants and the property of each quadrant in terms of its rise, spans, local origin (A_i , B_i , C_i , \bar{x}_i and \bar{y}_i , Chapter III). The grouping of the elements in each quadrant also needs to be specified. Structural shapes other than umbrella shell, can be handled with ease.

3. Spring Data

As pointed out in Chapter III, in order to retain the close-bandedness of the stiffness matrix, members such as a supporting column and tension tie rod are idealized by springs having equivalent stiffnesses. The number of such stiffness constants has to be specified.

4. Beam Data

Beams can be added along any lines of generators. The beam data is given in the usual way with its location specified by the start and end points and their co-ordinates. Beam properties such as area, moment of inertia, warping constant, eccentricities and distance of extreme fibers for the calculation of stresses are required.

5. Loading

The solution can be obtained for three different loading cases or any combination of the three. The three cases of loading are: a. uniformly distributed load over the whole surface; b. weight of the edge member; c. discretely applied forces at any nodal points.

OUTPUT

The output is given in the following order:

- (i) Six components of displacements at each node point ($u, v, w, \theta_x, \theta_y, \theta_{xy}$).
- (ii) Axial, bending and total stresses for beam.
- (iii) Deck forces per unit length (N_x, N_y, N_{xy}, M_x , and M_y).
- (iv) Reaction forces in each idealized spring.

INSTABILITY ANALYSIS

Instability analysis is done only for uniformly distributed loading for the grid size of 6x6 with 36 elements though results can be obtained for any general type of loading. As pointed out in the stiffness analysis, the grid size can be varied to meet the requirements. The compiling time is roughly 50 secs, whereas the time for individual iterative cycle ranges along 20 to 50 secs.

The input stream is basically the same as that for the stiffness analysis, the additional information needed here is the starting load point (First increment, see Chapter VI) subsequent incremental loads and the number of iteration

cycles required at each step.

The output gives only the load level and the corresponding displacements at all node points.

The program using the flat plates can be easily modified to solve any shallow shell problems by defining the equation of the shell surface in the global co-ordinates.

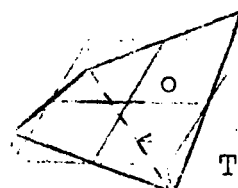
TABLE II-1

SINGLE DECK

TEST No.	EXPT. δ_o INCH	AVERAGE δ_o INCH	α	THEORETICAL	
				δ_o INCH	$\alpha_{interpolated}$
811	1.14	1.14	0.07	1.23	0.077
812	1.14		0.05	1.45	
511	0.80	0.78	0.06	0.68	0.050
512	0.77		0.04	0.87	
311	0.33	0.32	0.06	0.28	0.052
312	0.32		0.04	0.38	

TABLE II-2

DOUBLE DECK



Tie 2 1/2" x 1/4"

TEST No.	EXPT. δ_o INCH	AVERAGE δ_o INCH	α	THEORETICAL	
				δ_o INCH	$\alpha_{interpolated}$
821	0.86	0.75	0.07	0.71	0.080
822	0.65		0.06	0.77	
821(I)	0.65		0.05	0.84	
			0.04	0.93	
521	0.59	0.58	0.06	0.38	0.040
522	0.58		0.04	0.48	
521(I)	0.48				
321	0.24	0.26	0.06	0.14	0.037
322	0.32		0.040	0.20	
321(I)	0.21				

Test No. 521(I) means:

5 = The curvature of the hyper, same as that of a quadrant having rise/span ratio of 1/5.

2 = Two decks.

1 = Test No.1

(I) = Both top and bottom decks were interconnected.

TABLE III-1

COMPARISON OF CLASSICAL AND FINITE
ELEMENT SOLUTIONS FOR SIMPLY-SUPPORTED
AND UNIFORMLY LOADED 28-G
ORTHOTROPIC PLATE

LOCATION	FINITE ELEMENT SOLUTION		DOUBLE SINE SERIES SOLUTION
	GRID SIZE		
	6x6 8 INCH	12x2 8 INCH	8 INCH
A	0	0	0
1/6	6.117	6.106	6.31
1/3	7.397	7.397	7.36
1/2	7.137	7.139	7.09
2/3	6.961	6.962	6.96
5/6	6.944	6.944	6.98
B	6.952	6.952	6.97

See Figs. 3-4c and 3-5.

u_1	v_1	w_1	θ_{x1}	θ_{y1}	θ_{z1}	u_2	v_2	w_2	θ_{x2}	θ_{y2}	θ_{z2}
$\frac{A_b E}{a}$	0	0	0	$\frac{A_b E Z_c}{a}$	$\frac{A_b E Y_c}{a}$	$\frac{A_b E}{a}$	0	0	0	$\frac{A_b E Z_c}{a}$	$\frac{A_b E Y_c}{a}$
	$\frac{12 E I_z}{a^3}$	0	$\frac{-12 E I_z Z_s}{a^3}$	0	$\frac{6 E I_z}{a^2}$	0	$\frac{-12 E I_z}{a^3}$	0	$\frac{12 E I_z Z_s}{a^3}$	0	$\frac{6 E I_z}{a^2}$
		$\frac{12 E I_y}{a^3}$	$\frac{12 E I_y Y_s}{a^3}$	$\frac{-6 E I_y}{a^2}$	0	0	0	$\frac{-12 E I_y}{a^3}$	$\frac{-12 E I_y Y_s}{a^3}$	$\frac{-6 E I_y}{a^2}$	0
			$\frac{12 E I_z Z_s^2}{a^3} + \frac{12 E I_y Y_s^2}{a^3} + \frac{GJ}{a}$	$\frac{-6 E I_y Y_s}{a^2}$	$\frac{-6 E I_z Z_s}{a^2}$	0	$\frac{12 E I_z Z_s}{a^3}$	$\frac{-12 E I_y Y_s}{a^3}$	$\frac{-12 E I_z Z_s^2}{a^3} - \frac{12 E I_y Y_s^2}{a^3} - \frac{GJ}{a}$	$\frac{-6 E I_y Y_s}{a^2}$	$\frac{-6 E I_z Z_s}{a^2}$
			$\frac{A_b E Z_c^2}{a}$	$\frac{-A_b E Y_c Z_c}{a}$	$\frac{-A_b E Z_c}{a}$	0	$\frac{6 E I_y}{a^2}$	$\frac{6 E I_y Y_s}{a^2}$	$\frac{A_b E Z_c^2}{a} + \frac{4 E I_y}{a}$	$\frac{-A_b E Y_c Z_c}{a}$	$\frac{A_b E Y_c Z_c}{a}$
			$\frac{A_b E Y_c^2}{a}$	$\frac{A_b E Y_c}{a}$	$\frac{-6 E I_z}{a^2}$	0	$\frac{6 E I_z Z_s}{a^2}$	$\frac{A_b E Z_c Y_c}{a}$	$\frac{-A_b E Y_c^2}{a} + \frac{4 E I_z}{a}$	$\frac{-A_b E Y_c Z_c}{a}$	$\frac{A_b E Y_c Z_c}{a}$
						$\frac{A_b E}{a}$	0	0	0	$\frac{A_b E Z_c}{a}$	$\frac{-A_b E Y_c}{a}$
							$\frac{12 E I_z}{a^3}$	0	$\frac{-12 E I_z Z_s}{a^3}$	0	$\frac{-6 E I_z}{a^2}$
								$\frac{12 E I_y}{a^3}$	$\frac{12 E I_y Y_s}{a^3}$	$\frac{6 E I_y}{a^2}$	0
									$\frac{12 E I_z Z_s^2}{a^3} + \frac{12 E I_y Y_s^2}{a^3} + \frac{GJ}{a}$	$\frac{6 E I_y Y_s}{a^2}$	$\frac{6 E I_z Z_s}{a^2}$
									$\frac{A_b E Z_c^2}{a} + \frac{4 E I_y}{a}$	$\frac{-A_b E Y_c Z_c}{a}$	
										$\frac{A_b E Y_c^2}{a}$	
											$\frac{-A_b E Y_c Z_c}{a} + \frac{4 E I_z}{a}$

SYMMETRIC

TABLE III-2

STIFFNESS MATRIX FOR NON-COMPATIBLE ECCENTRIC BEAM ELEMENT (LINEAR VARIATION OF ANGLE OF TWIST θ)

u_1	v_1	w_1	θ_{x1}	θ_{y1}	θ_{z1}	θ_{xy1}	u_2	v_2	w_2	θ_{x2}	θ_{y2}	θ_{z2}	θ_{xy2}
$\frac{A_b E}{a}$	0	0	0	$\frac{A_b E Z_c}{a}$	$-\frac{A_b E Y_c}{a}$	0	$-\frac{A_b E}{a}$	0	0	0	$-\frac{A_b E Z_c}{a}$	$\frac{A_b E Y_c}{a}$	0
	$\frac{12EI_z}{a^3}$	0	$-\frac{12EI_z Z_s}{a^3}$	0	$\frac{6EI_z}{a^2}$	0	0	$-\frac{12EI_z}{a^3}$	0	$\frac{12EI_z Z_s}{a^3}$	0	$\frac{6EI_z}{a^2}$	0
		$\frac{12EI_y}{a^3}$	$\frac{12EI_y Y_s}{a^3}$	$-\frac{6EI_y}{a^2}$	0	0	0	0	$-\frac{12EI_y}{a^3}$	$-\frac{12EI_y Y_s}{a^3}$	$-\frac{6EI_y}{a^2}$	0	0
			$\frac{12EI_y Y_s^2}{a^3}$ $+\frac{12EI_z Z_s^2}{a^3}$ $+\frac{6GJ}{5a}$ $+\frac{12EI_b}{a^3}$	$-\frac{6EI_y Y_s}{a^2}$ $-\frac{6EI_z Z_s}{a^2}$	0	$\frac{GJ}{10}$ $+\frac{6EI_b}{a^2}$	0	$\frac{12EI_z Z_s}{a^3}$ $-\frac{12EI_y Y_s}{a^3}$ $-\frac{12EI_y Y_s^2}{a^3}$ $-\frac{6GJ}{5a}$ $-\frac{12EI_b}{a^3}$	$-\frac{12EI_z Z_s^2}{a^3}$ $-\frac{12EI_y Y_s^2}{a^3}$ $-\frac{6GJ}{5a}$	$-\frac{6EI_y Y_s}{a^2}$ $-\frac{6EI_z Z_s}{a^2}$	0	$\frac{GJ}{10}$ $+\frac{6EI_b}{a^2}$	0
			$\frac{4EI_y}{a}$ $+\frac{AEZ_c^2}{6a}$	$-\frac{AEZ_c Y_c}{a}$	0	0	$\frac{A_b E Z_c}{a}$	0	$\frac{6EI_y}{a^2}$ $\frac{6EI_y Y_s}{a^2}$	$\frac{6EI_y Y_s}{a^2}$ $\frac{6EI_z Z_s}{a^2}$	$\frac{2EI_y}{a}$ $-\frac{AEZ_c^2}{6a}$	$\frac{A_b E Y_c Z_c}{a}$ $-\frac{AEY_c^2}{6a}$	0
			$\frac{4EI_z}{a}$ $+\frac{AEY_c^2}{6a}$	0	0	0	$\frac{A_b E Y_c}{a}$	$-\frac{6EI_z}{a^2}$	0	$\frac{6EI_z Z_s}{a^2}$	$\frac{A_b E Z_c Y_c}{a}$ $+\frac{2EI_z}{a}$	0	0
						$\frac{2GJ}{15}$ $+\frac{4EI_b}{a}$	0	0	0	$-\frac{GJ}{10}$ $-\frac{6EI_b}{a^2}$	0	0	$-\frac{1}{30}GJ$ $+\frac{2EI_b}{a}$
							$\frac{A_b E}{a}$	0	0	0	$\frac{A_b E Z_c}{a}$	$-\frac{A_b E Y_c}{a}$	0
								$\frac{12EI_z}{a^3}$	0	$-\frac{12EI_z Z_s}{a^3}$	0	$-\frac{6EI_z}{a^2}$	0
									$\frac{12EI_y}{a^3}$	$\frac{12EI_y Y_s}{a^3}$	$\frac{6EI_y}{a^2}$	0	0
										$\frac{12EI_z Z_s^2}{a^3}$ $+\frac{12EI_y Y_s^2}{a^3}$ $+\frac{6GJ}{5a}$ $+\frac{12EI_b}{a^3}$	$\frac{6EI_y Y_s}{a^2}$ $\frac{6EI_z Z_s}{a^2}$	$\frac{6EI_z Z_s}{a^2}$ $-\frac{6EI_b}{a^2}$	$-\frac{GJ}{10}$ $-\frac{6EI_b}{a^2}$
											$\frac{4EI_y}{a}$ $+\frac{AEZ_c^2}{6a}$	$-\frac{AEY_c Z_c}{a}$	0
											$\frac{4EI_z}{a}$ $+\frac{AEY_c^2}{6a}$	0	0
												$\frac{2GJ}{15}$ $+\frac{4EI_b}{a}$	

SYMMETRIC

TABLE III-3

STIFFNESS MATRIX FOR
NON-COMPATIBLE ECCENTRIC

BEAM ELEMENT (CUBIC

VARIATION OF ANGLE OF TWIST, θ)

TABLE III-4
ROTATIONAL TRANSFORMATION MATRIX
FOR A BEAM ELEMENT⁵⁵

$$[T]_R = \begin{bmatrix} [\lambda] & 0 \\ 0 & [\lambda] \end{bmatrix} \quad [\lambda] = \begin{bmatrix} [\lambda]_1 & 0 \\ 0 & [\lambda]_2 \end{bmatrix}$$

$$[\lambda]_1 = \begin{bmatrix} C_x & C_y & C_z \\ \frac{-C_x C_y \cos\beta - C_z \sin\beta}{\sqrt{C_x^2 + C_z^2}} & \sqrt{C_x^2 + C_z^2} \cos\beta & \frac{-C_y C_z \cos\beta + C_x \sin\beta}{\sqrt{C_x^2 + C_z^2}} \\ \frac{C_x C_y \sin\beta - C_z \cos\beta}{\sqrt{C_x^2 + C_z^2}} & -\sqrt{C_x^2 + C_z^2} \sin\beta & \frac{C_y C_z \sin\beta + C_x \cos\beta}{\sqrt{C_x^2 + C_z^2}} \end{bmatrix}$$

$$[\lambda]_2 = \begin{bmatrix} C_x & C_y & 0 \\ \frac{-C_x C_y \cos\beta - C_z \sin\beta}{\sqrt{C_x^2 + C_z^2}} & \sqrt{C_x^2 + C_z^2} \cos\beta & 0 \\ 0 & 0 & \frac{C_y C_z \sin\beta + C_x \cos\beta}{\sqrt{C_x^2 + C_z^2}} \end{bmatrix}$$

$$C_x = \frac{x_2 - x_1}{L}$$

$$C_y = \frac{y_2 - y_1}{L}$$

$$C_z = \frac{z_2 - z_1}{L}$$

$$L = \sqrt{(x_2 - x_1)^2 + (y_2 - y_1)^2 + (z_2 - z_1)^2}$$

See Fig. 3-18.

TABLE IV-1 CONTINUED

STRUCTURE		GEOMETRY			DECK							EDGE MEMBERS		BOUNDARY CONDITIONS	LOADING
NO.	TYPE	A INCH	B INCH	C INCH	TYPE	NO. OF DECKS	THICKNESS INCH	I_{yd} INCH ⁴ /INCH	α	Ex10 ⁶ LBS/INCH ²	ν	B ₁	B ₂	TYPE	PSF
11	II	72	72	14.40	II	1	28G 0.0149	0.00047	0.06	29.5	0.3	3"O.D. ½"Thk pipe	2-3"O.D. ½"Thk pipe	V VI	40
12	"	"	"	"	"	"	24G 0.0239	0.000753	"	"	"	"	"	VI	"
13	II	"	"	"	II	2	28G 0.0149	0.00047	0.05	"	"	"	"	"	"
13a	"	"	"	"	"	"	"	"	0.06	"	"	"	"	"	"
14	"	240	240	48	"	"	16G 0.060	0.00192	"	"	"	12[40	2-12 [40	V	"
15	"	12.92	12.92	5.216	I	1	0.25	-	1.0	0.50	0.39	←NO BEAMS→		IV	14'

x Dimensions are in cms

+ gm/cm²

* Only half the structure was loaded

• Two loading conditions are analyzed:

1 With 40 psf only 2 40 psf + weight of the edge members.

For types of structures see Figs. 4.1 - 4.5.

TABLE IV-2

DECKS

- I = Isotropic deck of uniform thickness
- II = Corrugated sine-form. Fig. 2-2a.
- III = Corrugated trapezoidal. Fig. 2-2b.
- IV = Cellular trapezoidal deck. Fig. 2-2c.

BOUNDARY CONDITIONS

- I = Edges $x = \pm A$ and $y = \pm B$ are fixed.
- II = Edges $x = \pm A$ and $y = \pm B$ Knife-edge supported.
- III = $T_F = 0$ for edge members along $x = \pm A$ and $y = \pm B$.
 - (i) $w = 0$ along $x = \pm A$ and $y = \pm B$
 - (ii) a tension bar connects low corners. (f and b - Structure I and a and c = Structure IV).
- IV = $T_F = 1$ and $T_H = 1$. For all edge members. For the eccentric locations of edge member with respect to the deck, see Fig. 4-5.
 - (i) $x = y = 0$ Lines of symmetry.
 - (ii) $x = \pm A$ and $y = \pm B$ Free edges.
 - (iii) $x = y = 0$ rigid support.
- V = $T_F = 0$ $T_H = 1$ for all edge members. For the eccentric connection of edge members see Fig. 4-2. For
 - (i) $x = 0$ $u = 0$.
 - (ii) $y = 0$ $v = 0$.
 - (iii) $\theta_{ya} = \theta_{xya} = \theta_{yh} = \theta_{xyh} = \theta_{xc} = \theta_{xyc} = \theta_{xf} = \theta_{xyf} = 0$.
 - (iv) $x = y = 0$ rigid support.

- VI = Boundary conditions identical with V except $T_H = 0$
for all edge members.
- VII = $T_F = 0$ $T_H = 1$ for all edge members. Edge members are
connected concentrically. Boundary conditions (i),
(ii) and (iii) are same as in the case V.
- VIII = Boundary and fixity conditions. Same as given in IV.
The line cf ($y=0$, Fig. 4.2) is the only line of symmetry.
Also see Fig. 4.20.

TABLE IV-3

COMPARISON OF DEFLECTIONS BY
METHODS 'a' and 'b'; FOR STRUCTURES 1 and 2

LOCATION	STRUCTURE 1		STRUCTURE 2	
	Method 'a' 10^{-2} cms	Method 'b' 10^{-2} cms	Method 'a' 10^{-3} inch	Method 'b' 10^{-3} inch
C	1.228	1.235	5.50	5.552
	2.352	2.384	8.398	8.466
	2.574	2.602	9.149	9.262
0	2.531	2.551	9.196	9.322
B	-	-	-	-
	0.742	0.750	3.271	3.251
	2.218	2.248	7.526	7.561
	2.613	2.647	9.081	9.184
	0	2.531	2.551	9.196

NOTE: See Figs. 4-6 and 4-8.

TABLE IV-4

DECK STRESSES IN PSI AT THE CENTER
OF A QUADRANT (Point e in Fig. 4.2)

STRUCTURE NO.	DESCRIPTION	AXIAL STRESSES		BENDING STRESSES		TOTAL STRESSES	
		EXPERI-MENTAL	CALCU-LATED	EXPT	CALCU-LATED	EXPT	CALCU-LATED
9	28-G Double Deck	832	848	1460	1870	2292	2718
11	28-G Single Deck	890	62	6820	10700	7710	10762
12	24-G Single Deck	-	69	5600	6200	-	6269
13	28-G Double Deck	2780	22	6505	4510	9385	4532

For the Structure numbers, refer to Table IV-1.

TABLE IV-5

DEFLECTIONS IN INCHES OF INVERTED UMBRELLA
SHELL WITH STIFF EDGE MEMBERS

LOCATION	ANALYTICAL	EXPERIMENTAL		
		AVERAGE	MAXIMUM	MINIMUM
STRUCTURE 11				
δ_a	0.133	0.20	0.26	0.15
δ_b	0.29	0.29	0.48	0.18
δ_c	0.16	0.15	0.15	0.15
δ_e	0.91	0.70	0.92	0.59
STRUCTURE 12				
δ_a	0.12	0.11	0.180	0.04
δ_b	0.26	0.23	0.26	0.32
δ_c	0.13	0.095	0.150	0.040
δ_e	0.57	0.42	0.62	0.26
STRUCTURE 13				
δ_a	0.18	0.15	0.26	0.040
δ_b	0.31	0.31	0.55	0.15
δ_c	0.18	0.15	0.26	0.040
δ_e	0.56	0.54	0.92	0.26

See Fig. 4.2.

TABLE IV-6

EDGE BEAM STRESSES FOR INVERTED UMBRELLA SHELL
WITH STIFF EDGE MEMBERS (q = 40 PSF)

LOCATION	AXIAL		BENDING		TOTAL (Absolute)	
	EXPT.	ANALYTICAL	EXPT.	ANALYTICAL	EXPT.	ANALYTICAL
1 STRUCTURE 11 28-G Single Deck $\alpha=0.06$						
a	2440	1070	4850	4481	7290	5551
b	1400	456	3120	3990	4520	4446
c	- 580	- 586	1660	1167	2240	1753
d	-	- 900	2320	2496	-	3396
e	1620	856	3020	3050	4640	3906
2 STRUCTURE 12 24-G Single Deck $\alpha=0.06$						
a	1740	1093	4140	4385	5880	5478
b	530	420	3500	3801	4030	4221
c	-1060	- 609	540	955	1600	1564
d	-1070	-1075	1100	2165	2170	3240
e	1100	874	2300	2668	3400	3542
3 STRUCTURE 13 28-G Double Deck $\alpha=0.05$						
a	2250	435	4110	4228	6360	4663
b	930	435	5260	4228	6190	4663
c	- 900	- 518	2040	1650	2940	2168
d	- 560	- 734	2020	2106	2580	2840
e	1110	357	2320	2561	3430	2918

All stresses are in psi

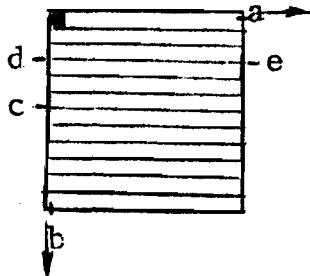


TABLE V-1

SELECTED EXAMPLES SHOWING THE EFFECTS OF CHANGE OF STRUCTURAL PARAMETERS

*Structure	VARIABLE		DEFLECTIONS IN INCHES				EDGE MEMBER STRESSES PSI MAX. AXIAL				
	Type	Value	δ_a	δ_b	δ_c	δ_e	oa	oc	ab	bc	
9 & 10	Rise 'C'	14.40"	0.38	1.57	0.38	0.69	-5329	-5329	2747	2747	
		13.80"	0.41	1.69	0.41	0.75	-5518	-5518	2752	2752	
13 & 13a	Shear Rigidity factor α	0.05	0.18	0.31	0.18	0.56	-856	-856	435	435	
		0.06	0.15	0.28	0.15	0.48	-881	-881	481	481	
11 & 12	Thick- ness	28G	0.0149	0.13	0.29	0.16	0.91	-1129	-802	456	1070
		24G	0.0239	0.116	0.26	0.13	0.57	-1150	-870	420	1093
11 & 13a	No. of Deck	Single Deck	0.13	0.29	0.16	0.91	-1129	-802	456	1070	
		Double Deck	0.15	0.28	0.15	0.48	-881	-881	481	481	
*Structure	EDGE MEMBER STRESSES PSI MAX. BENDING				DECK BENDING STRESS		Shear force at Center for N_{xy} lbs/inch				
	oa	oc	ab	bc	PSI						
9 & 10	18,357	18,357	17,144	17,144	1,870		52.75				
	19,077	19,077	18,179	18,179	2,130		54.96				
13 & 13a	6,648	6,648	4,228	4,228	4,510		50.0				
	5,899	5,899	4,095	4,095	3,780		51.28				
11 & 12	5,225	4,634	3,990	4,480	10,700		36.96				
	4,723	3,974	3,801	4,385	6,200		37.75				
11 & 13a	5,225	4,634	3,990	4,480	10,700		36.96				
	5,899	5,899	4,095	4,095	3,780		51.28				

For locations of deflections and stresses see Fig. 4-2.

* For the type of structure according to number see Table IV-1.

TABLE V-2

THE COMPARISON OF AXIAL STRESSES IN THE EDGE MEMBER AS GIVEN
BY MEMBRANE THEORY AND BY ANALYSIS

STRUCTURE NO.	α	MEMBRANE THEORY STRESS PSI	ANALYTICAL PSI				% OF MEMBRANE THEORY			
			oa	oc	ab	bc	oa	oc	ab	bc
SINGLE DECK										
5	1.0	*19660 18640	10700	9070	9440	11040	54.4	48.7	50.6	56.1
11	0.06	1570	1129	802	456	1070	71.8	51.5	29.	68.2
12	0.06	1570	1150	870	420	1093	73.2	55.5	26.7	69.6
DOUBLE DECKS										
9	0.04	7100	5329	5329	2747	2747	75.2	75.2	38.8	38.8
13	0.05	1570	856	856	435	435	54.40	54.4	27.7	27.7
13a	0.06	1570	881	881	481	481	56.2	56.2	31.30	31.3
14	0.06	3420	1673	1673	1575	1575	49.0	49.0	46.0	46.0

* Member sizes are different, see Table IV-1

TABLE VI-1

STIFFENED PLATE BUCKLING PROBLEMS

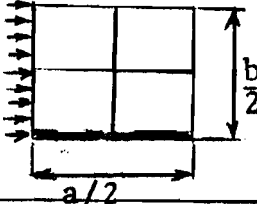
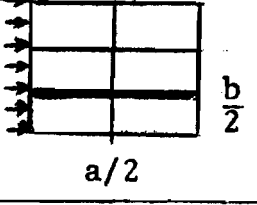
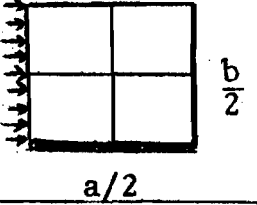
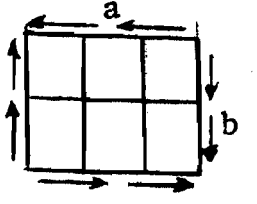
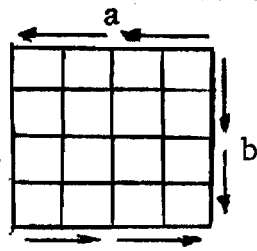
LOADING	DIMENSIONS						% Error
	a-inch	b-inch	t-inch	γ	δ	K	
	108	108	5/8	-	-	4.0	
	108	108	5/8	5	0.10	11.10	
	108	108	5/8	-	-	4.0	<0.2
	108	108	5/8	5	0.10	20.5	
	108	54	5/8	-	-	4.0	
	108	54	5/8	5	0.10	7.69	
	16	16	0.10	-	-	9.34	4.65
	70.5	70.5	24-G 0.0239	-	-	0.670	7.46

TABLE VII-1 Properties and Dimensions of Flat Shear Tests

Test No.	Dimensions (ft)	Steel Decking	Edge Members	No. of Panels	Seam Connections	Deck - Edge Connections	c	G' (lb/in)
1	6 x 6	26G S.C.* 1 layer	6"x1½"x.1046" channels	3	screws @ 8"	screws @ every valley and @ 4"	.163	33100
2	6 x 6	26G S.C. 1 layer	6"x3/4"x.1046" channels	3	screws @ 8"	screws @ every valley and @ 4"	.159	32300
3	6 x 6	26G S.C. 1 layer	6"x3/4"x.1046" channels	3	screws @ 8"	screws @ every 3rd valley and @8"	.056	11400
4	6 x 6	28G S.C. 1 layer	6"x1½"x.1046" channels	4	screws @ 8"	screws @ every 3rd valley and @8"	.071	12000
5	6 x 6	28G S.C. 1 layer	6"x1½"x.1046" channels	3	screws @ 2-2/3"	screws @ every 3rd valley and @8"	.077	13000
6	6 x 6	28G S.C. 1 layer	6"x1½"x.1046" channels	3	screws @ 2-2/3"	screws @ every 3rd valley and @8"	.066	11200
7	6 x 6	24G S.C. 1 layer	6"x1½"x.1046" channels	3	screws @ 2-2/3"	screws @ every 3rd valley and @8"	.078	21100
8	5 x 5	28G S.C. 1 layer	6"x1½"x.1046" channels	3	screws @ 2-2/3"	screws @ every 3rd valley and @8"	.068	11500

* Standard Corrugated

TABLE VII-1 Continued

Test No.	Dimensions (ft)	Steel Decking	Edge Members	No. of Panels	Seam Connections	Deck - Edge Connections	σ	G' (lb/in)
9	5 x 5	28G S.C. 1 layer	6"x1½"x.1046" channels	3	screws @ 2-2/3"	screws @ every 3rd valley and @8"	.068	11500
10	6 x 6	26G S.C. 2 layers	6"x1½"x.1046" channels	3	screws @ 8"	screws @ every valley and @ 4"	.098	39800
11	6 x 6	26G S.C. 2 layers	6"x3/4"x.1046" channels	3	screws @ 8"	screws @ every valley and @ 4"	.114	46300
12	6 x 6	28G S.C. 2 layers	6"x1½"x.1046" channels	4	screws @ 8"	screws @ every 3rd valley and @8"	.056	18900
13	6 x 6	28G S.C. 2 layers	6"x1½"x.1046" channels	3	screws @ 2-2/3"	screws @ every 3rd valley and @8"	.040	13500
14	6 x 6	28G S.C. 2 layers	1" std weight pipe	3	screws @ 2-2/3"	screws @ every 3rd valley and @8"	.045	15200
15	5 x 5	28G S.C. 2 layers	6"x1½"x.1046" channels	3	screws @ 2-2/3"	screws @ every 3rd valley and @8"	.050	15400
16	1 x 1	2 mil corr. 2 layers	3/16"ODx.014" brass tubes	1	—	soldered @ every valley and cont.	.030	1360

TABLE VII-2 Experimental Results for Saddle Shaped Hypars Supported All Around ($q = 40$ psf)

(a) One Layer of Decking

Test No.	w_{max} in inches	Stress at Center in Strong Dir.		Axial Force in Tie Bar (lbs)
		Bending (psi)	Axial (psi)	
811	1.14	20800	-640	1820 (5660)**
812	1.14	19100	-1700	1630
511	0.80	14700*	—	—
512	0.77	15900*	—	—
311	0.33	2500	1260	—
312	0.32	3560	810	1710 (2120)

(b) Two Layers of Decking

Test No.	w_{max} in inches	Stress at Center in Strong Dir.				Axial Force in Tie Bar (lbs)
		Bending (psi)		Axial (psi)		
		Bot. Layer	Top Layer	Bot. Layer	Top Layer	
321	0.86	12400	10000	-290	1810	1560
822	0.65	13000	13000	-820	740	1310
821I	0.65	10300	7600	-680	1750	1250
521	0.59	11300	7700	1660	650	—
522	0.58	11000	7800	1380	360	—
522I	0.48	10000	5200	80	2060	—
321	0.24	4000	4500	570	920	1720
322	0.32	5560	2310	-560	1220	1570
322I	0.21	3990	640	-310	1670	1570

* Based on one strain gage at extreme fiber, axial stress assumed to be zero.

** Value in () is calculated from membrane theory.

TABLE VII-3 Experimental Results for Saddle Shaped Hypars Supported All Around (8" x 12" area loaded)

(a) One Layer of Decking, Load = 100 lb.

Test No.	w_{max} in inches	Stress at Center in Strong Dir.		Axial Force in Tie Bar (lbs)
		Bending (psi)	Axial (psi)	
811C	0.63	17000	4300	150
812C	0.67	17400	2300	130
512C	0.61	—	—	—
311C	0.39	13900	1990	—
312C	0.37	12400	2050	0

(b) Two Layers of Decking, Load = 200 lb.

Test No.	w_{max} in inches	Stress at Center in Strong Dir.				Axial Force in Tie Bar (lbs)
		Bending (psi)		Axial (psi)		
		Bot. Layer	Top Layer	Bot. Layer	Top Layer	
821C	0.50	13400	20000	-160	-1380	470
822C	0.42	11300	17000	-400	210	530
8211C	0.39	13600	10900	-1650	-1300	390
521C	0.44	14000	16500	1060	-1090	—
522C	0.41	15300	11300	460	360	—
5221C	0.32	13000	9300	860	-350	—
321C	0.24	15700	10100	1220	750	140
322C	0.28	10200	9900	10	-40	180
3221C	0.17	6800	7700	1060	-340	110

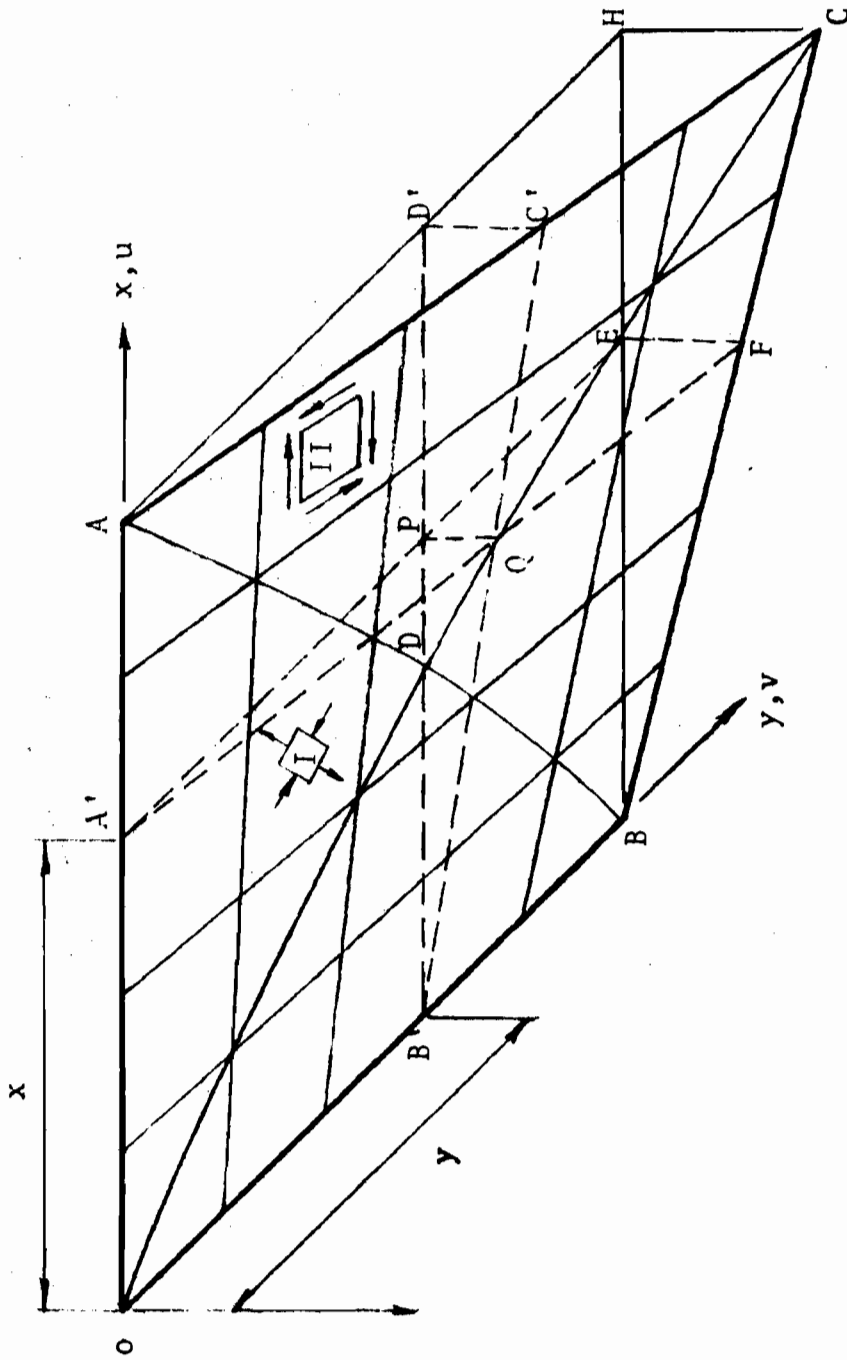


Fig. 1-1 A Basic Hyper Unit

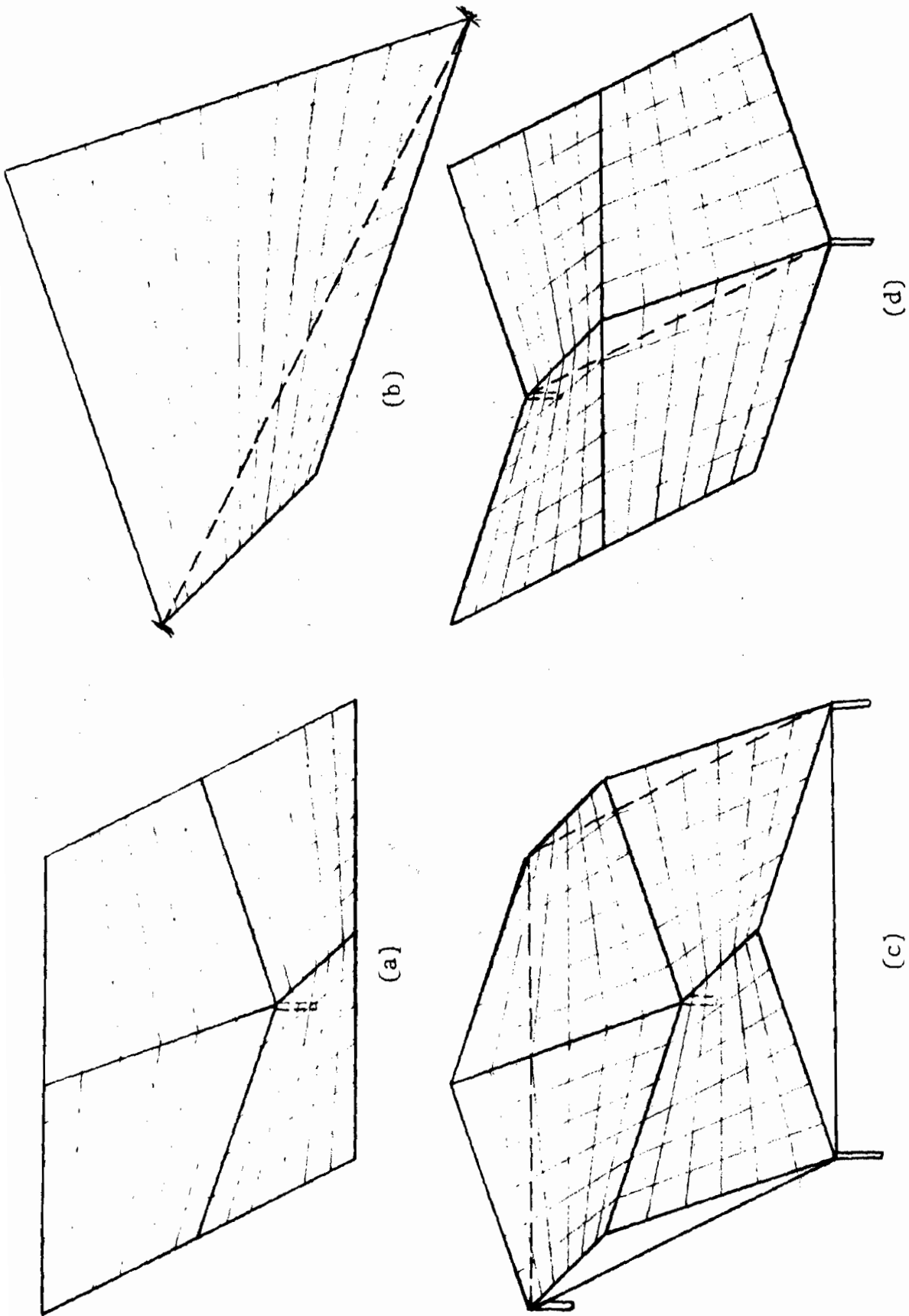


Fig. 1-2 Different Hypar Configurations

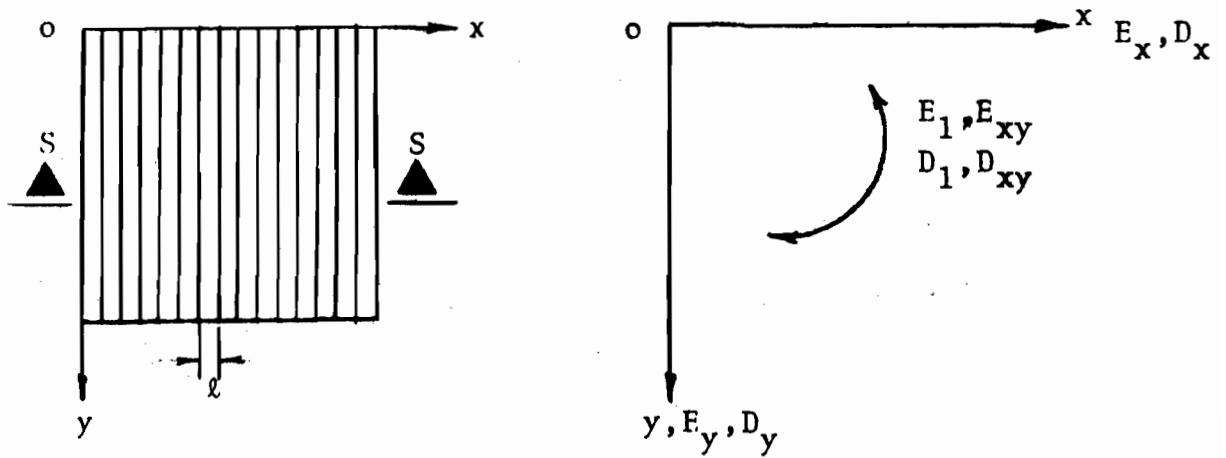


Fig. 2-1 Typical Orthotropic Deck

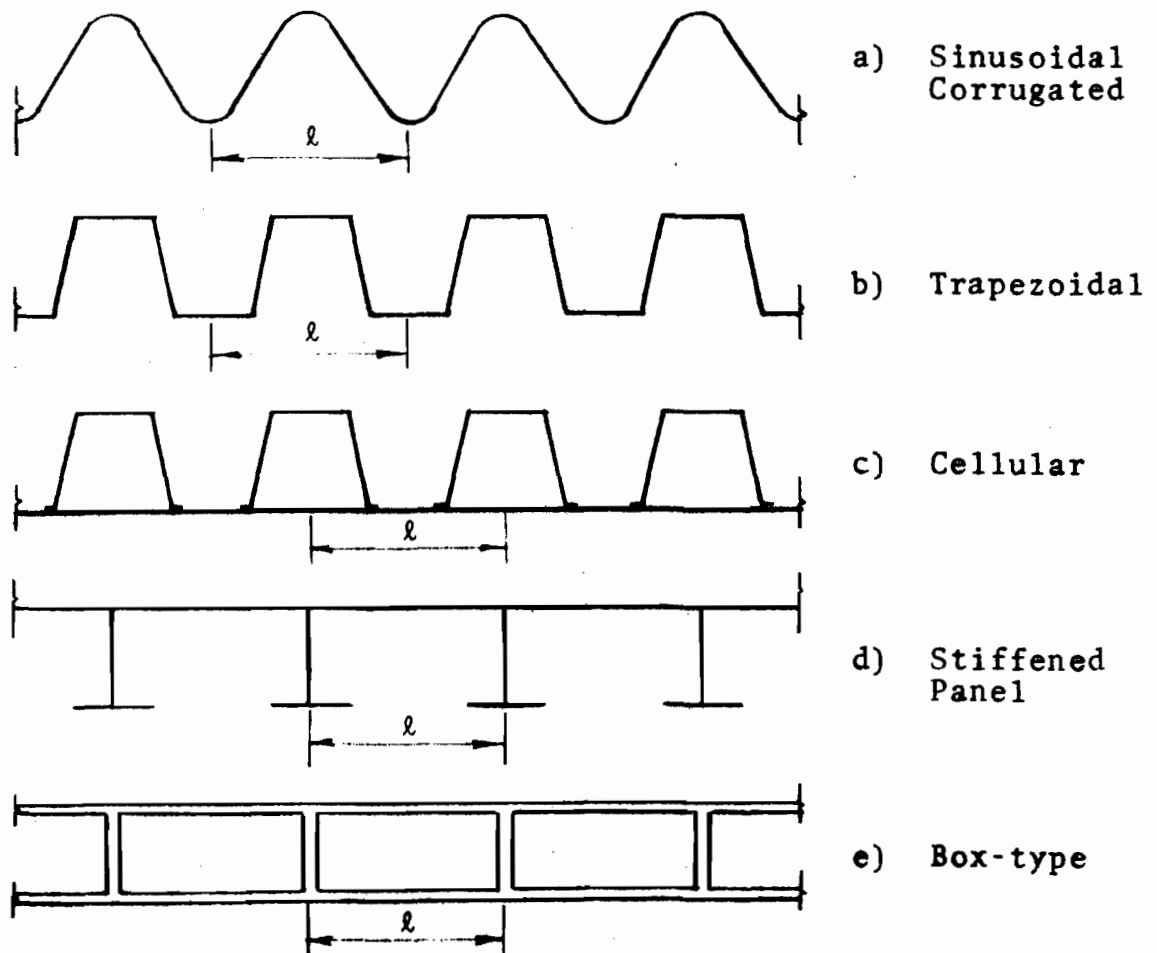


Fig. 2-2 Section S-S Showing Different Types of Decks

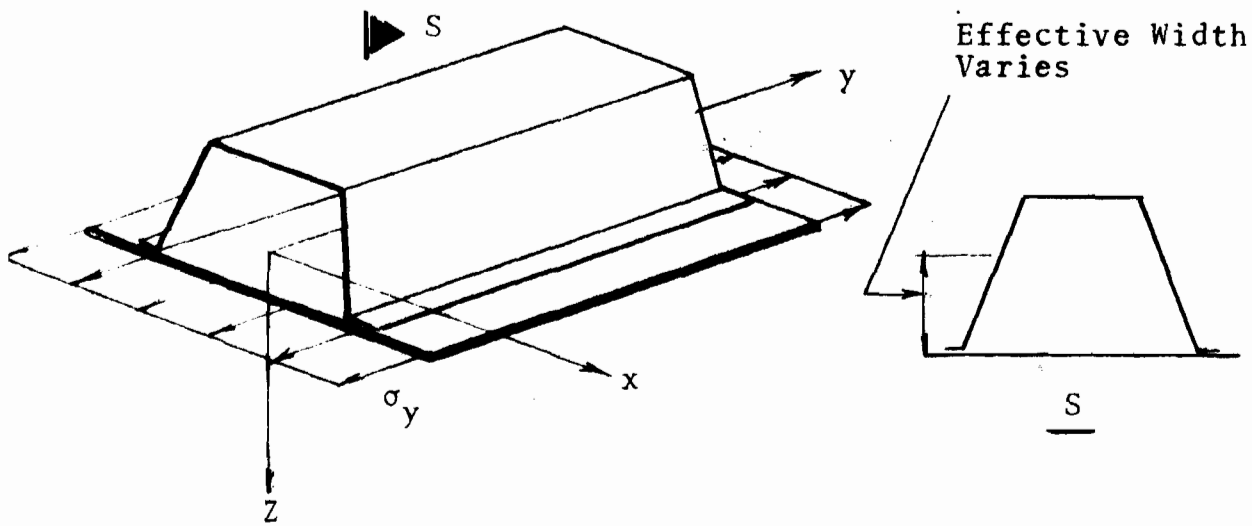


Fig. 2-3 Effective Cross-Sectional Area of a Hat for Axial Force

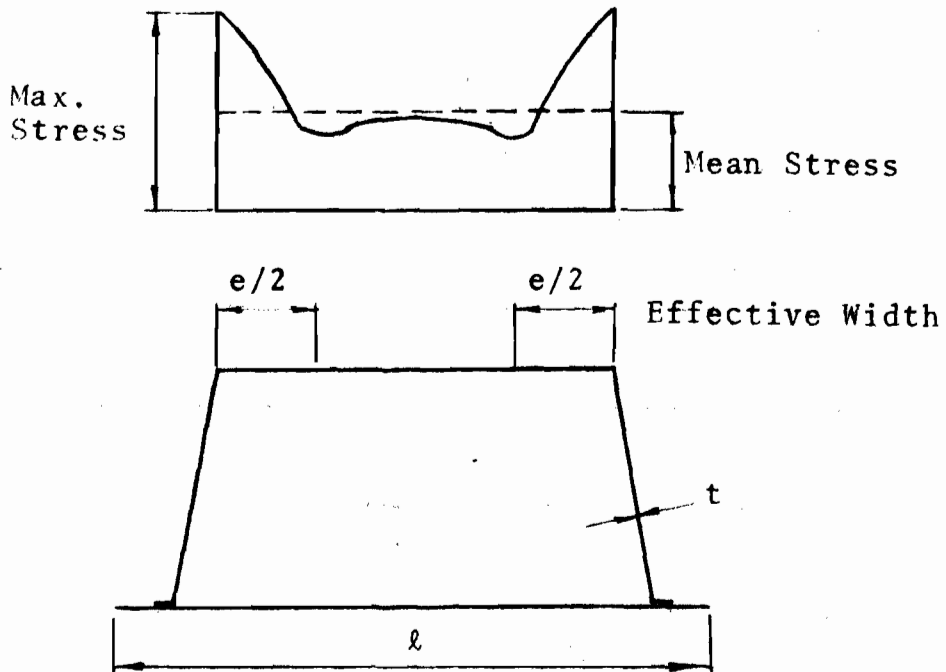


Fig. 2-4 Effective Width of Compression Flange in Bending

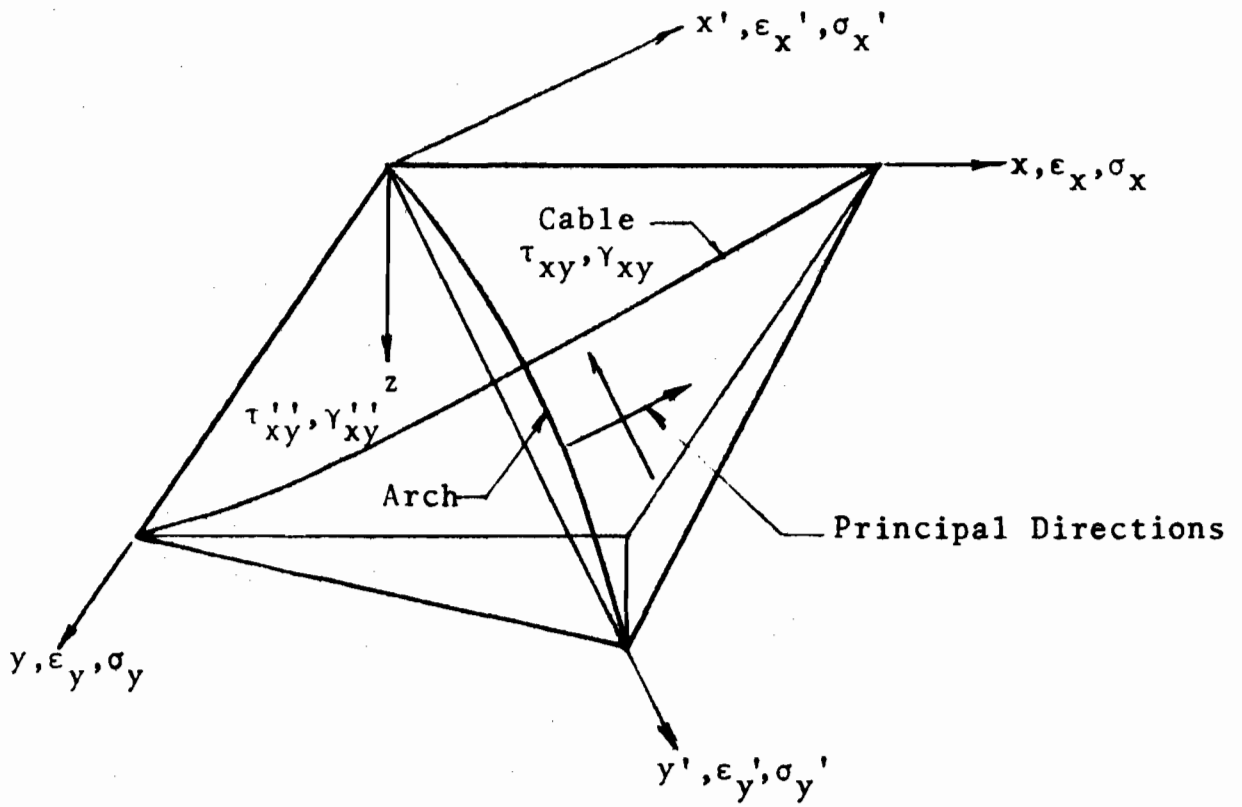


Fig. 2-5 An Arbitrarily Oriented Orthotropic Deck

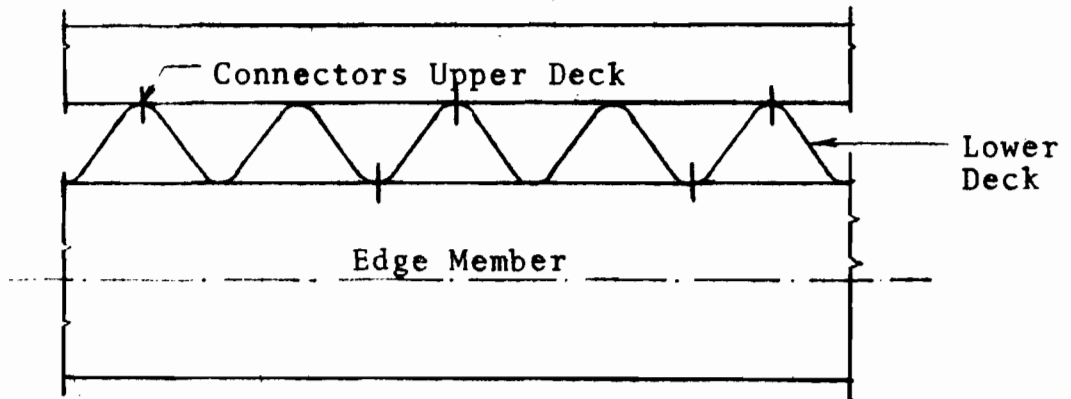


Fig. 2-6 Edge Member and Decks Connection

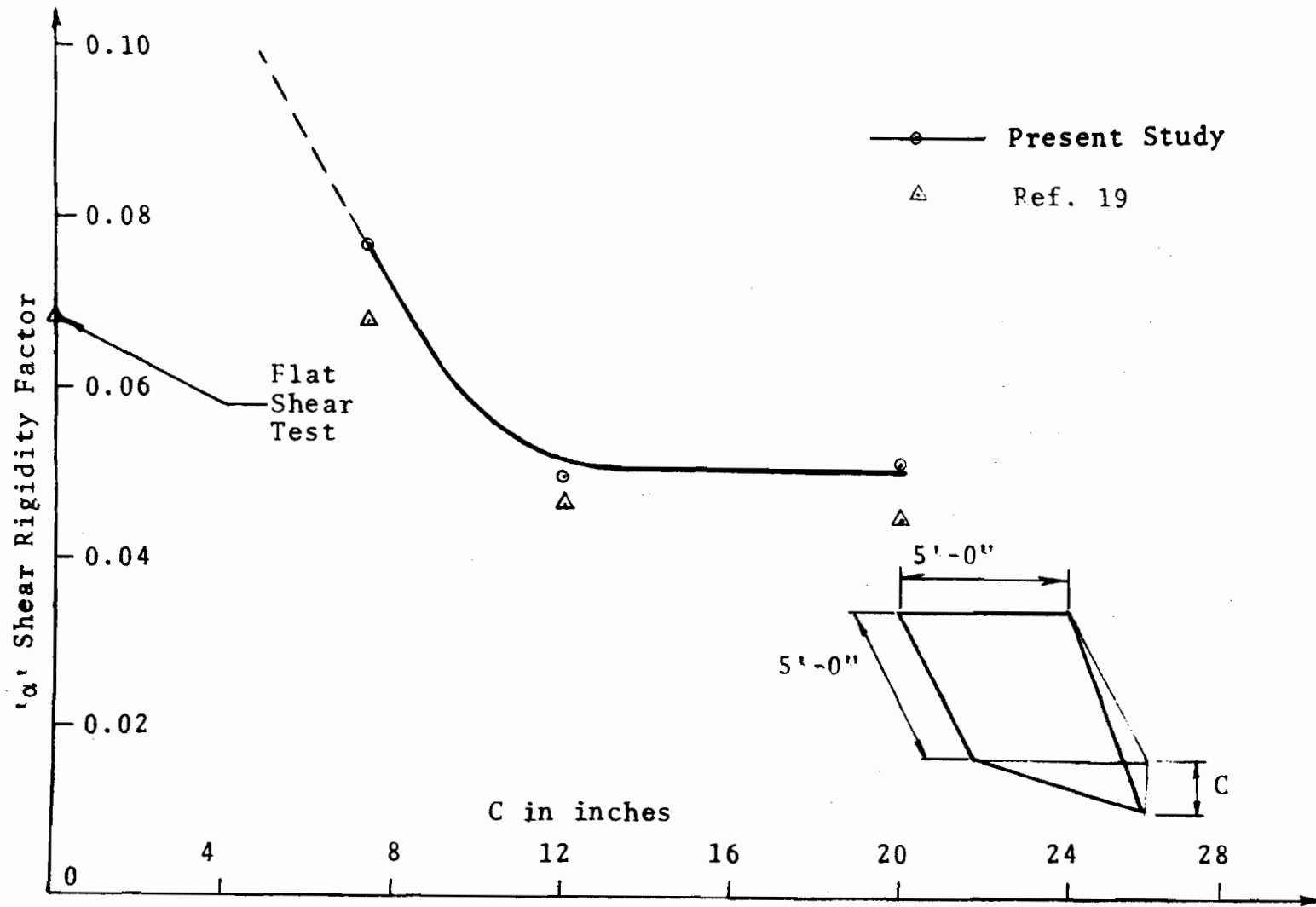


Fig. 2-7 Shear Rigidity Factor ' α ' Vs Hypar Curvature (One Layer of Decking)

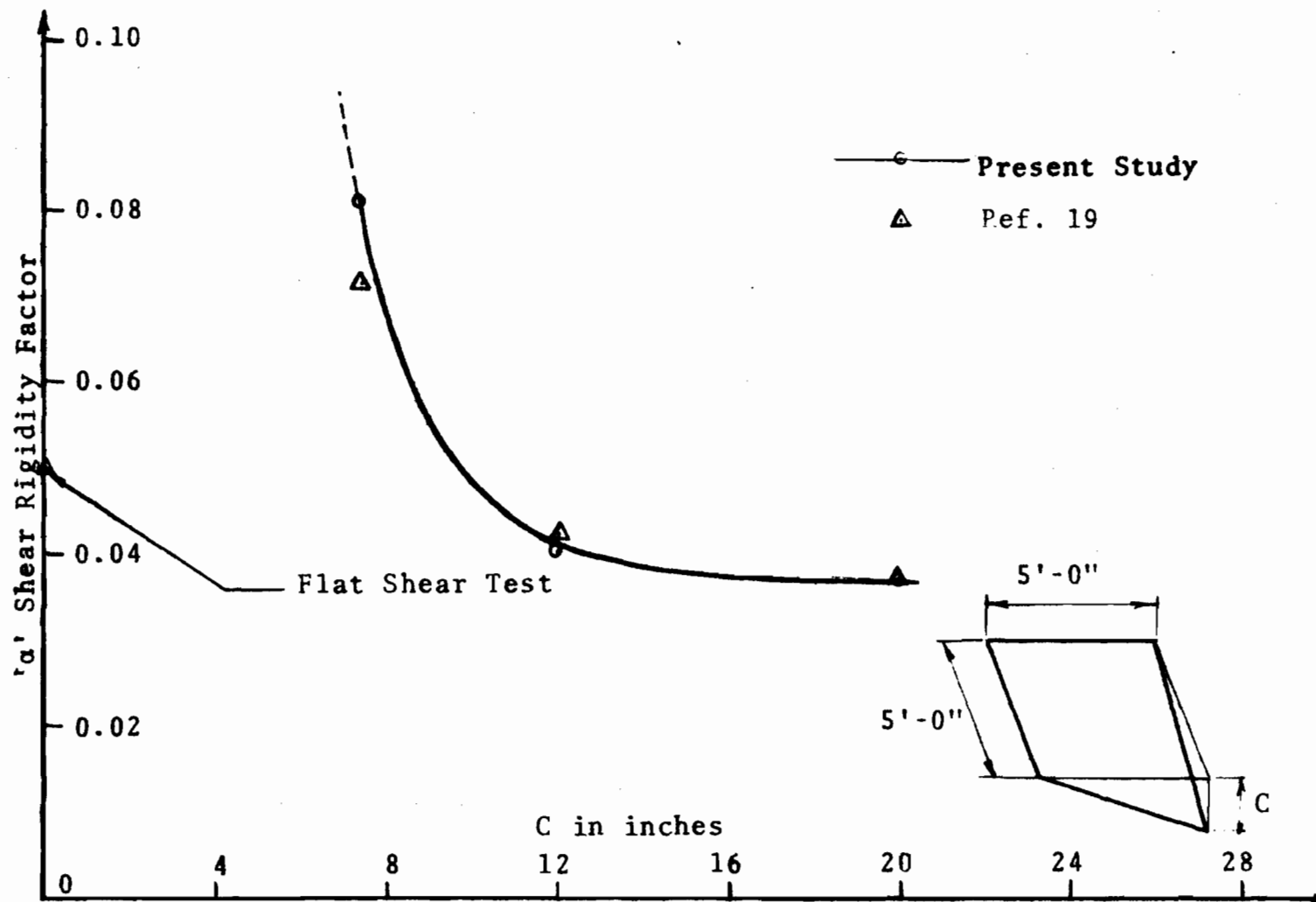


Fig. 2-8 Shear Rigidity Factor ' α ' Vs Hypar Curvature (Double Layer of Decking)

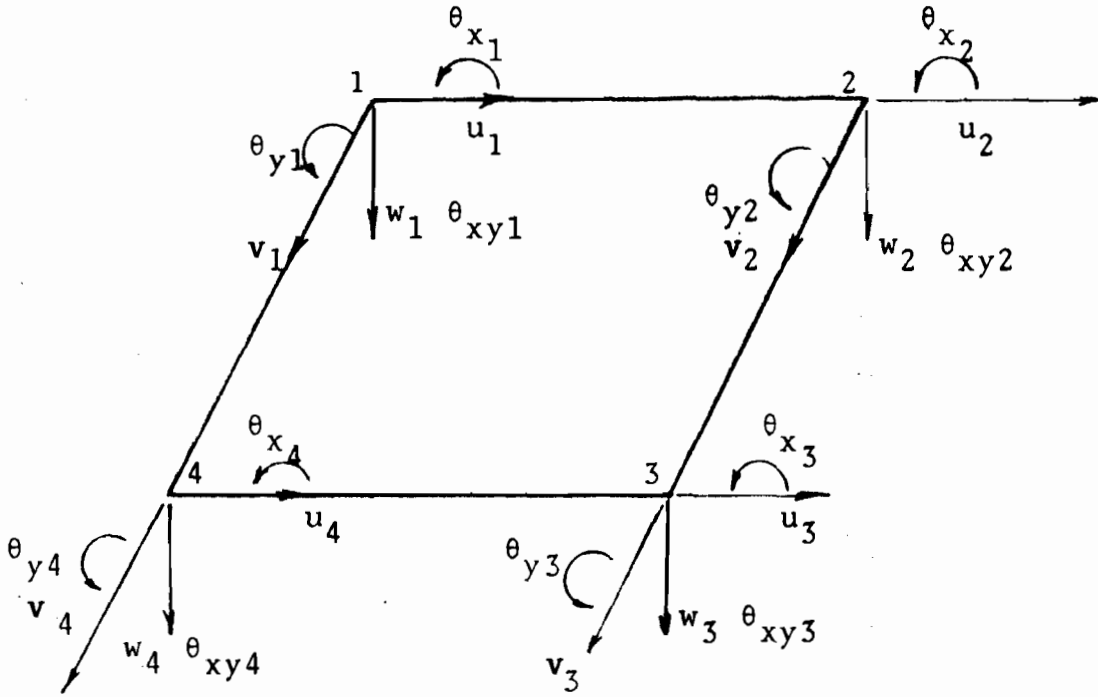


Fig. 3-1 Nodal Displacements

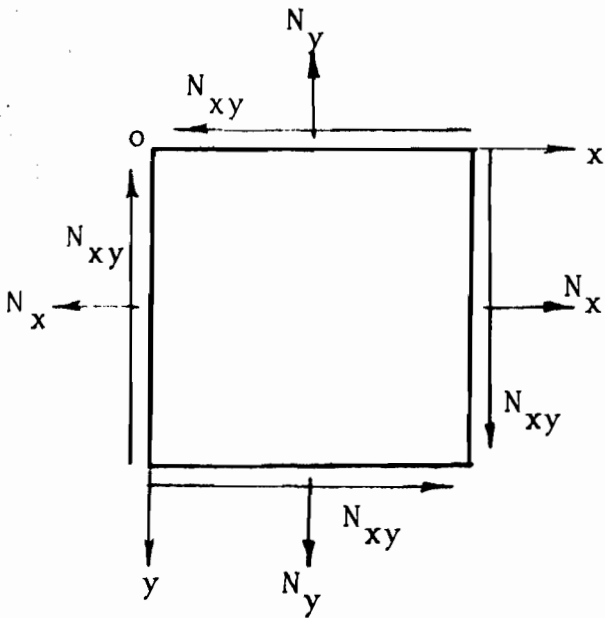


Fig. 3-2 In-plane Forces

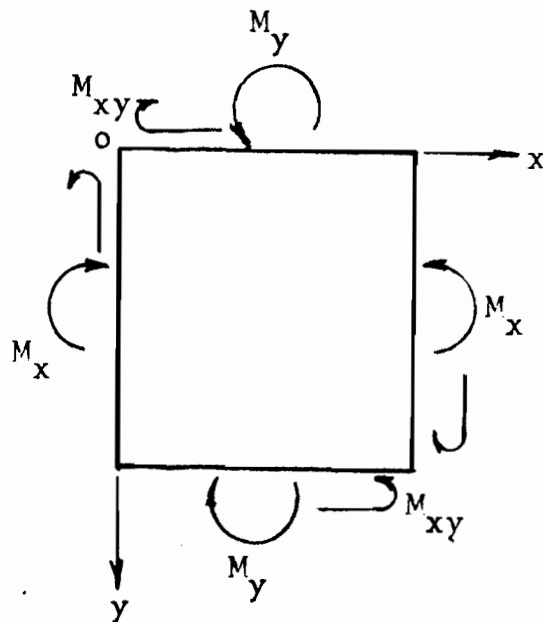
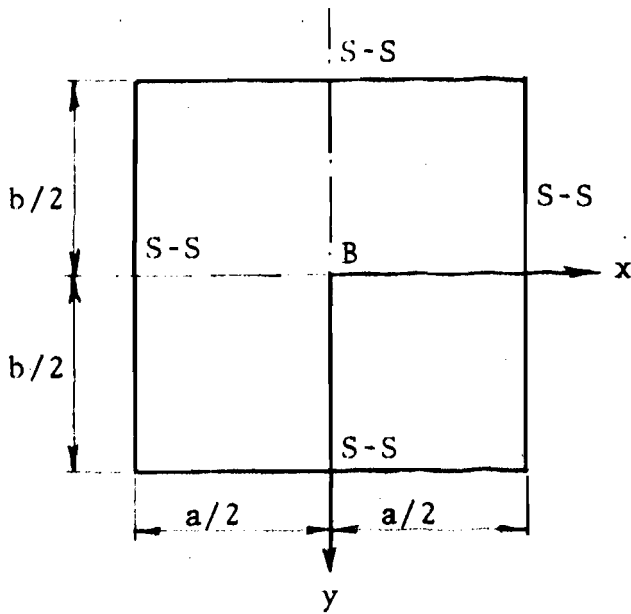
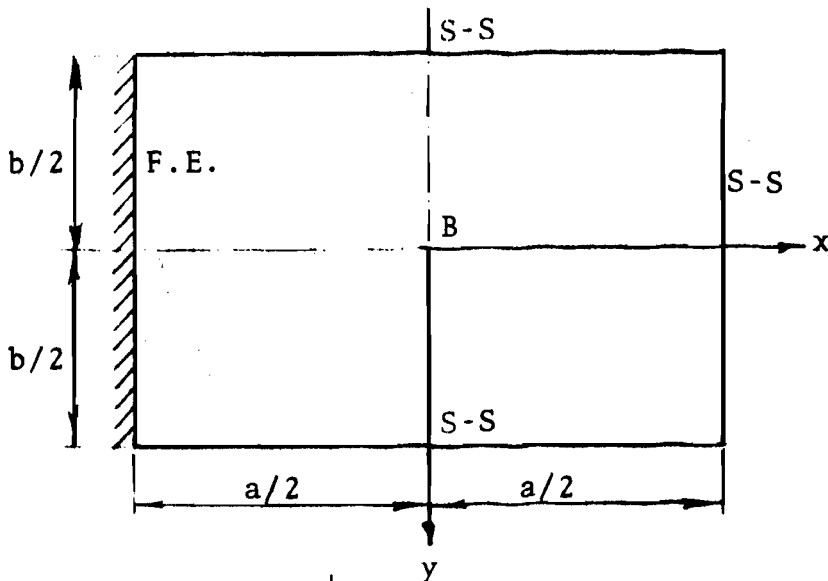


Fig. 3-3 Moments



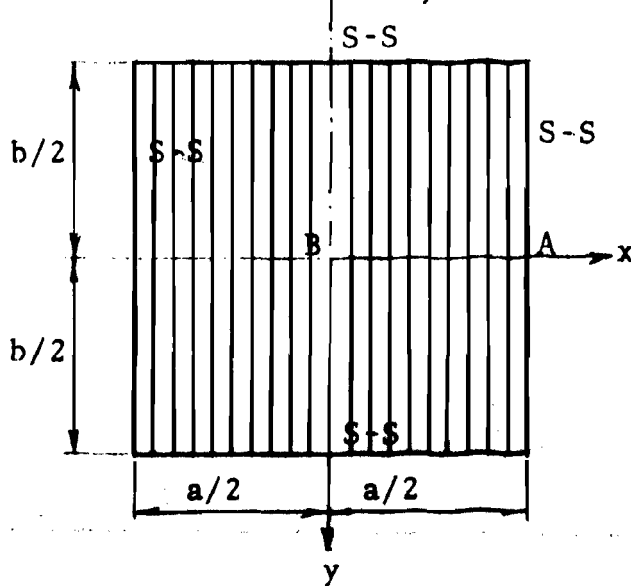
- a) $a = b = 80$ inches
 $t = 0.05$ inch
 $E = 29.5 \times 10^6$ lbs/inch²
 $\nu = 0.30$
 $q = 1$ psi
 No. of Elements = 64
 (Full Plate)

$$\delta_B = \frac{0.00406qa^4}{D}$$



- b) $a = 96$ inches
 $b = 144$ inches
 $t = 5.0$ inch
 $E = 3 \times 10^6$ lbs/inch²
 $\nu = 0.30$
 $q = 200$ lbs/ft²
 No. of Elements = 18 (Half Plate)

$$\delta_B = \frac{0.0064a^4}{D}$$

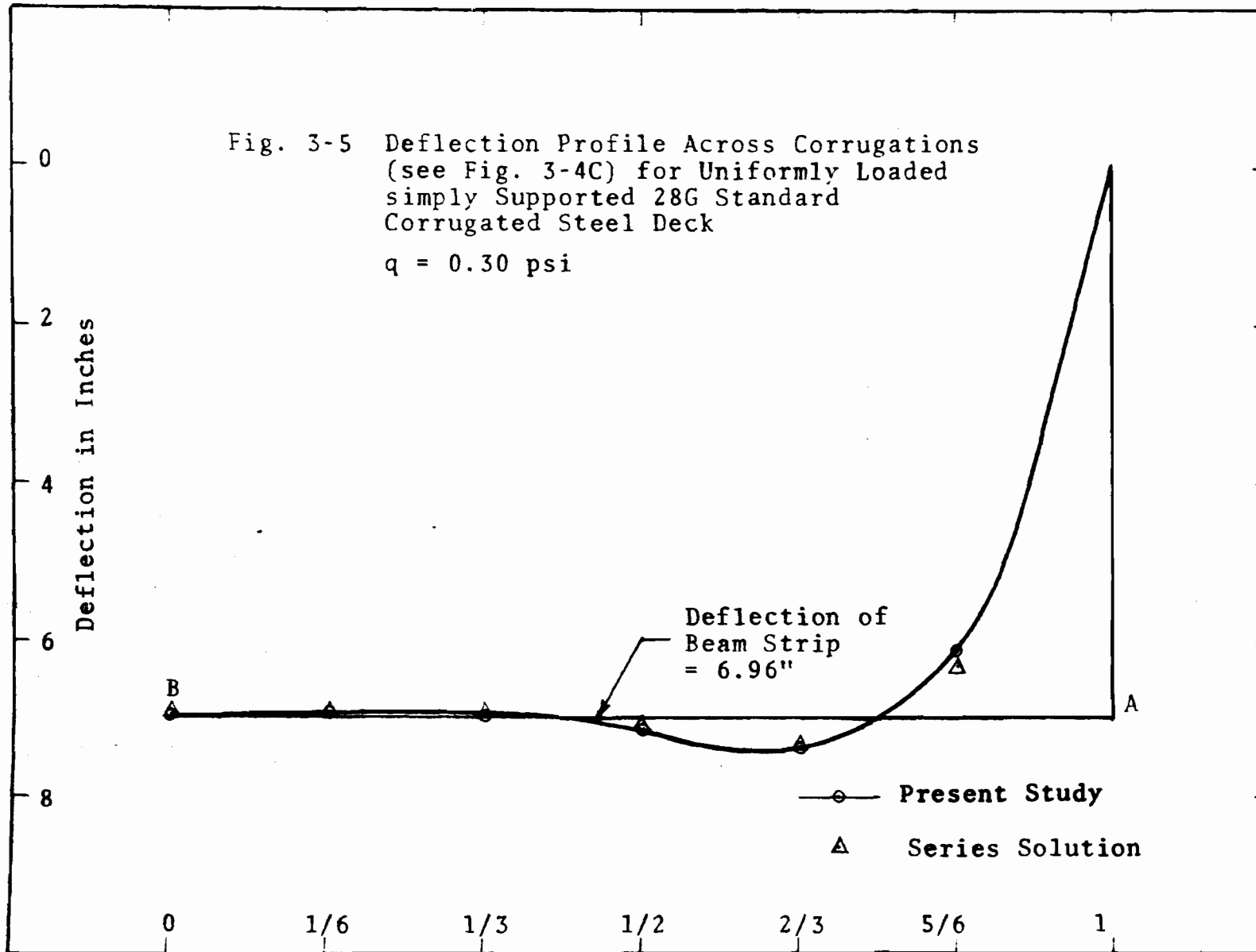


- c) $a = b = 70.50$ inches
 $t = 0.0149$ inch
 28G Std. Corrugated Deck
 $E = 29.5 \times 10^6$ lbs/inch²
 $\nu = 0.30$
 $q = 0.30$ psi
 No. of Elements = Varies (Quadrant)

$$\delta_B = \frac{5}{384} \frac{qa^4}{EI^2}$$

Fig. 3-4 Plate Bending Problems

Fig. 3-5 Deflection Profile Across Corrugations
 (see Fig. 3-4C) for Uniformly Loaded
 simply Supported 28G Standard
 Corrugated Steel Deck
 $q = 0.30 \text{ psi}$



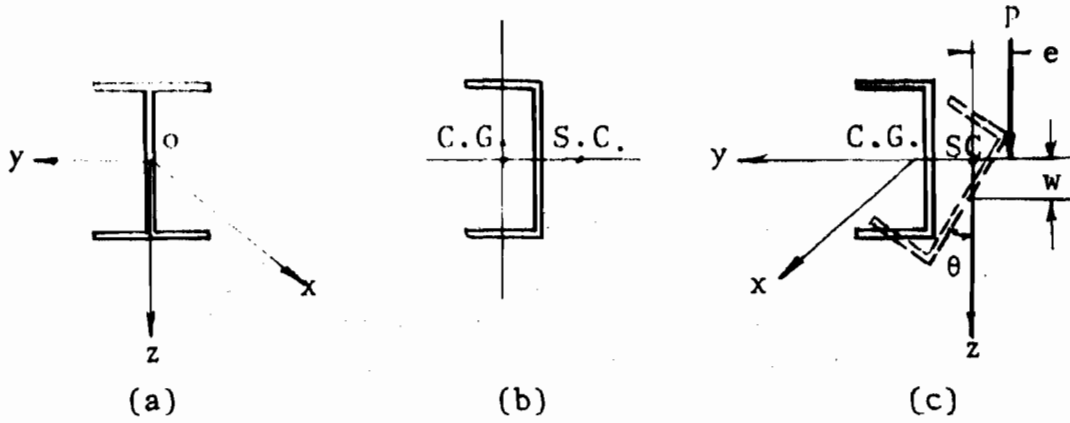


Fig. 3-6 Typical Cross-Sections of Beams

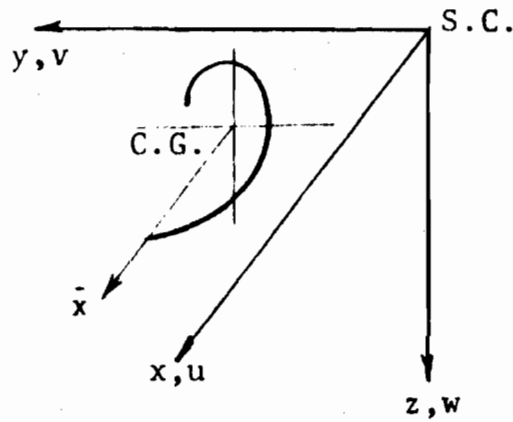


Fig. 3-7 An Arbitrary Cross-Section of a Beam

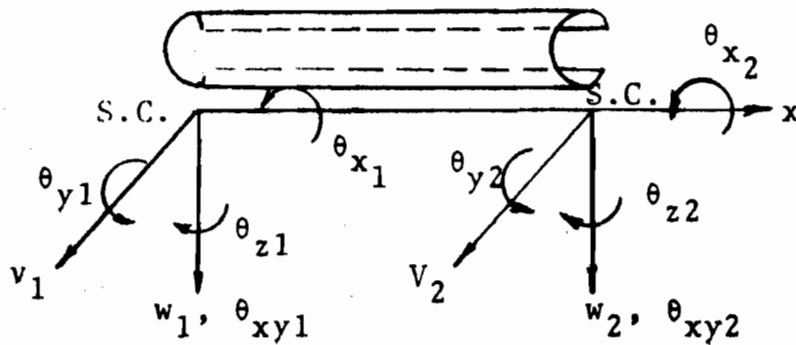


Fig. 3-8 Nodal Bending Displacements of a Typical Beam Element

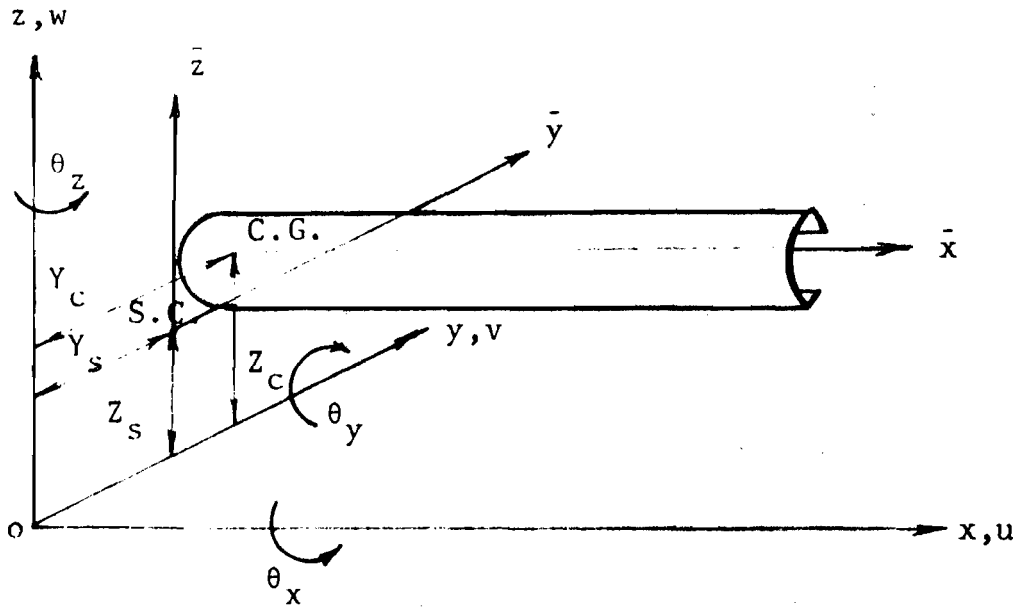


Fig. 3-9 Typical Eccentric Edge Member

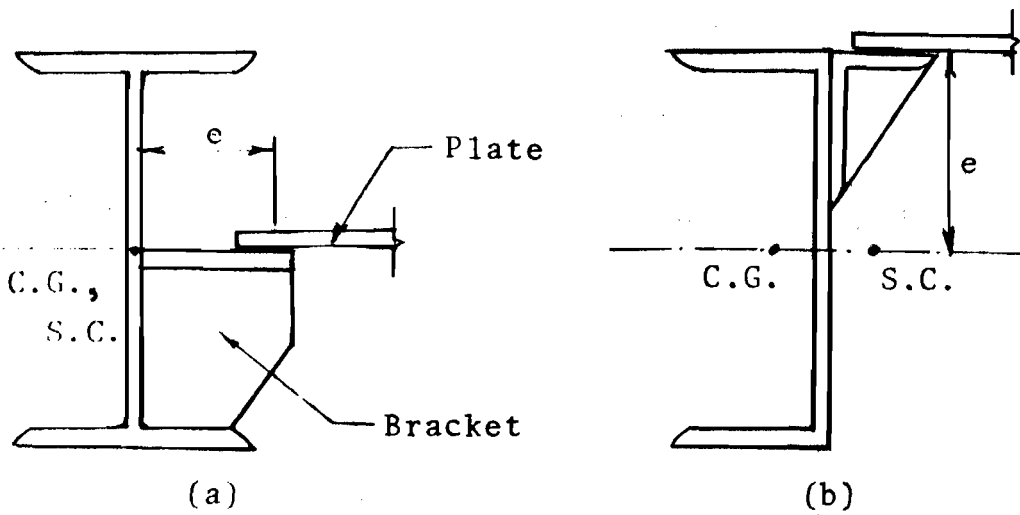


Fig. 3-10 Eccentric Connections

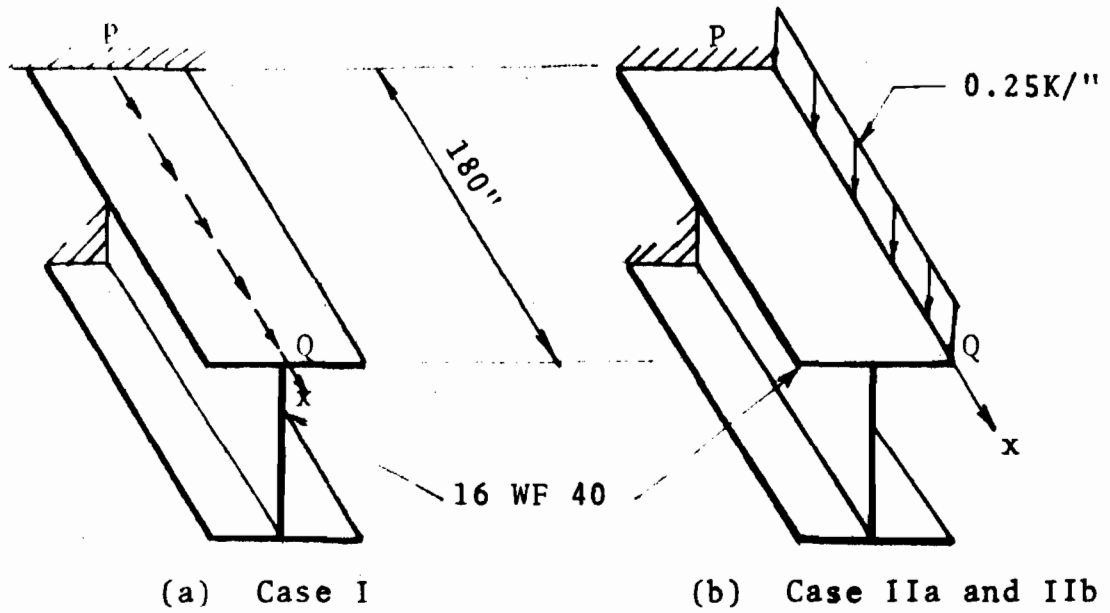


Fig. 3-11 Loading on Eccentric Edge Members

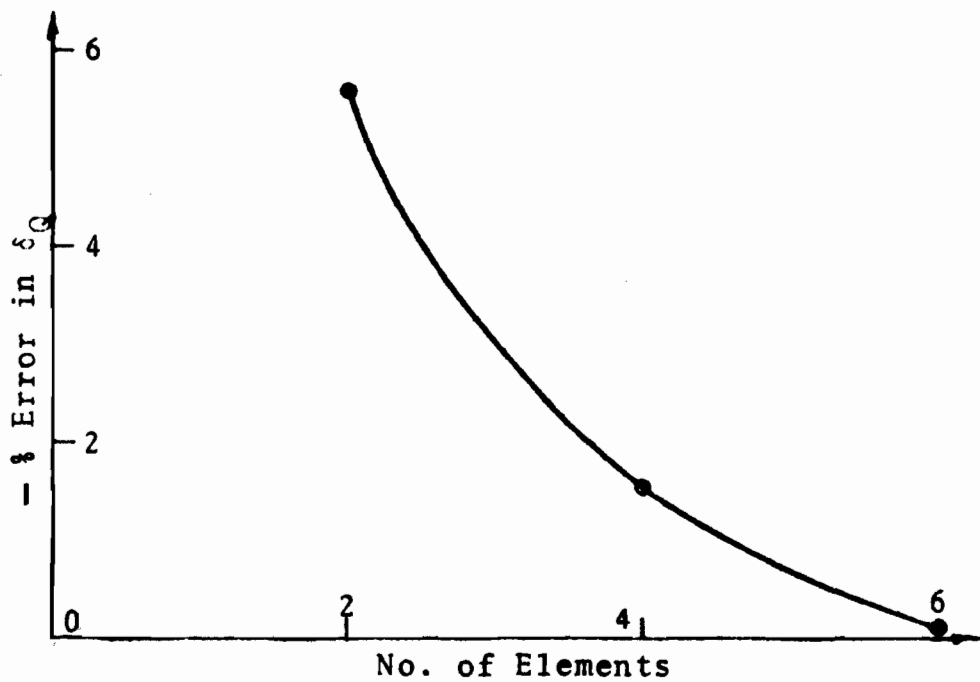


Fig. 3-12 Convergence Characteristics for Vertical Deflection ' δ_Q ' for Case I (Fig. 3-11a)

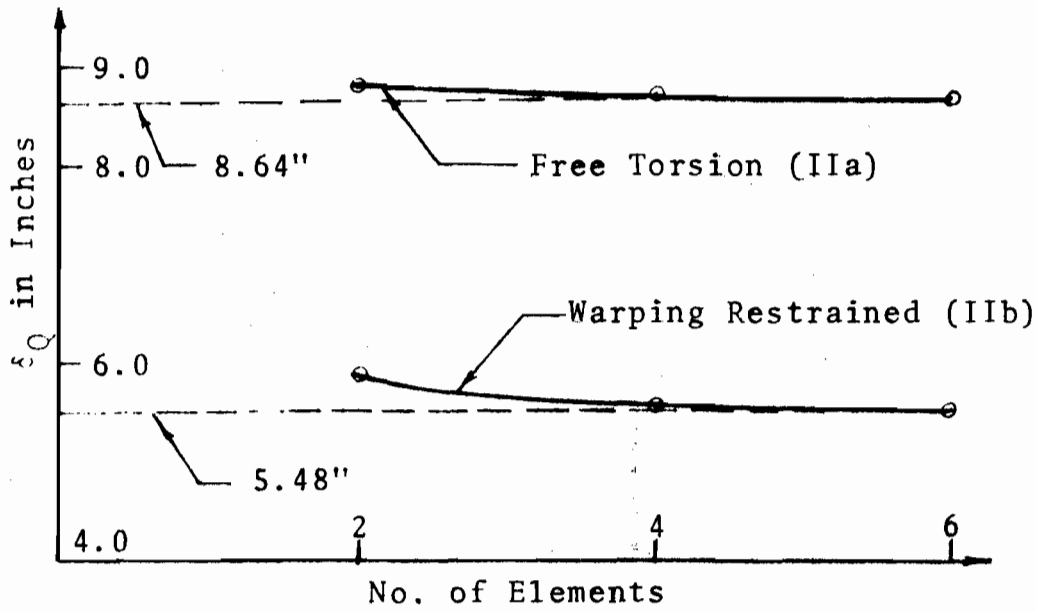


Fig. 3-13a Effect of Restrained Warping on Vertical Deflection ' δ_Q '

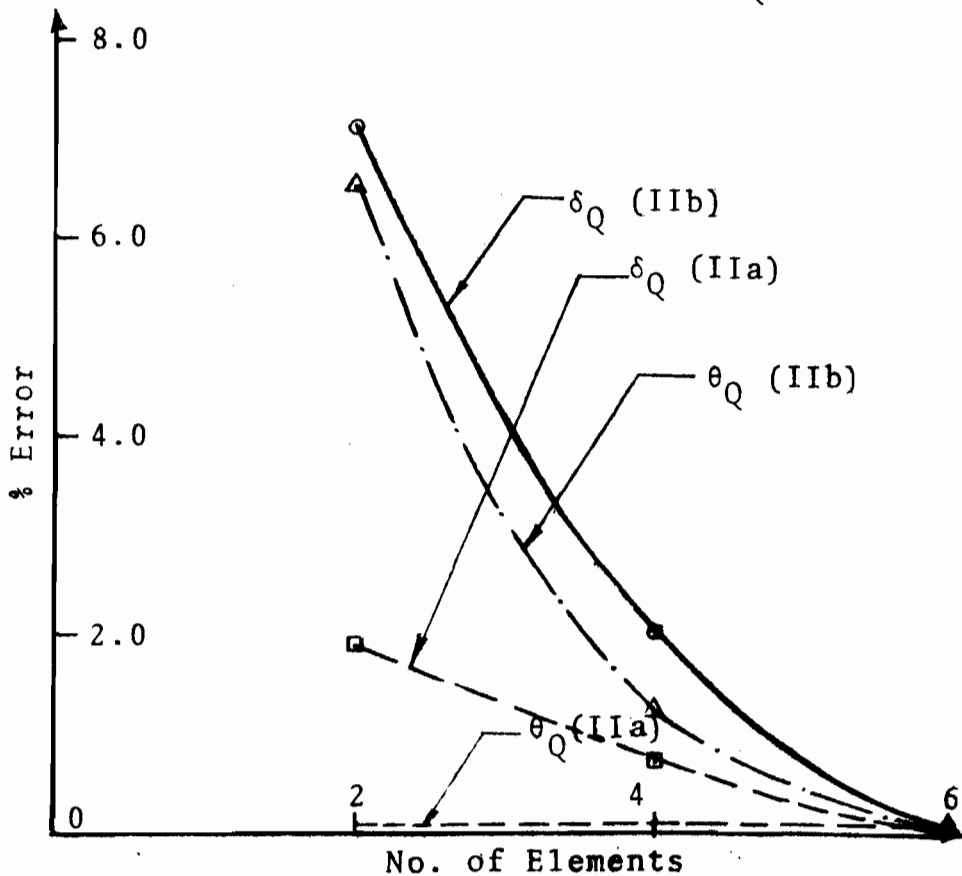


Fig. 3.13b Convergence Characteristics for ' δ_Q ' and ' θ_Q '

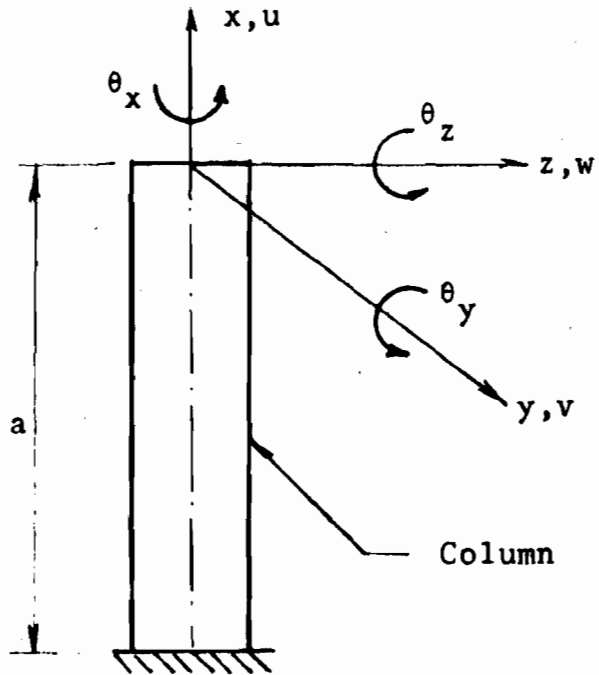


Fig. 3.14a A Cantilever Column

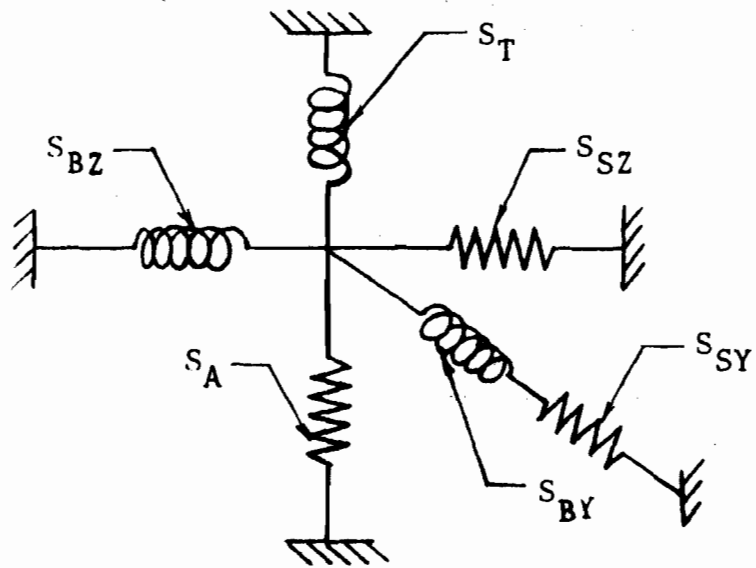
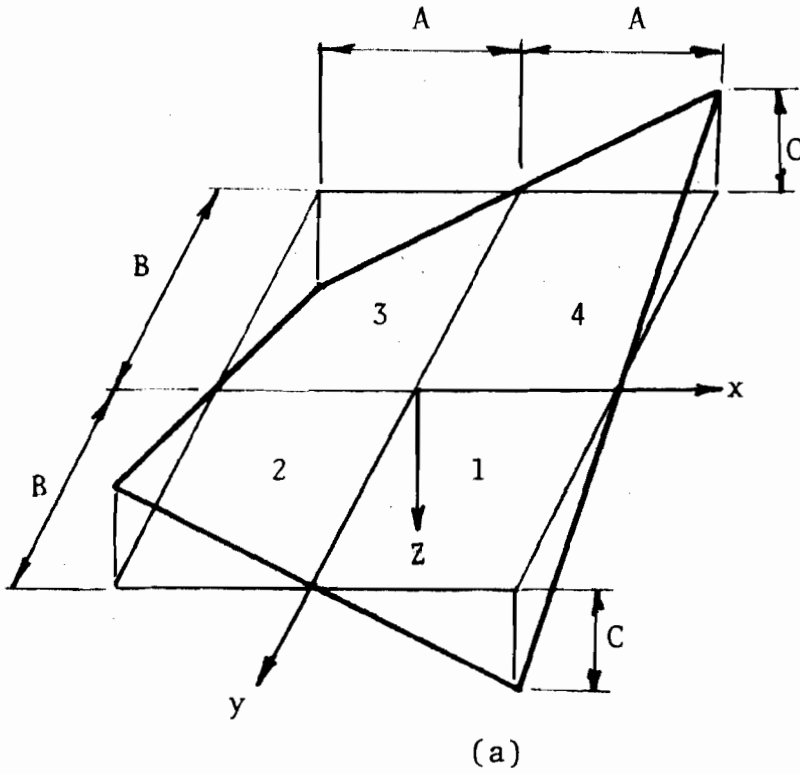
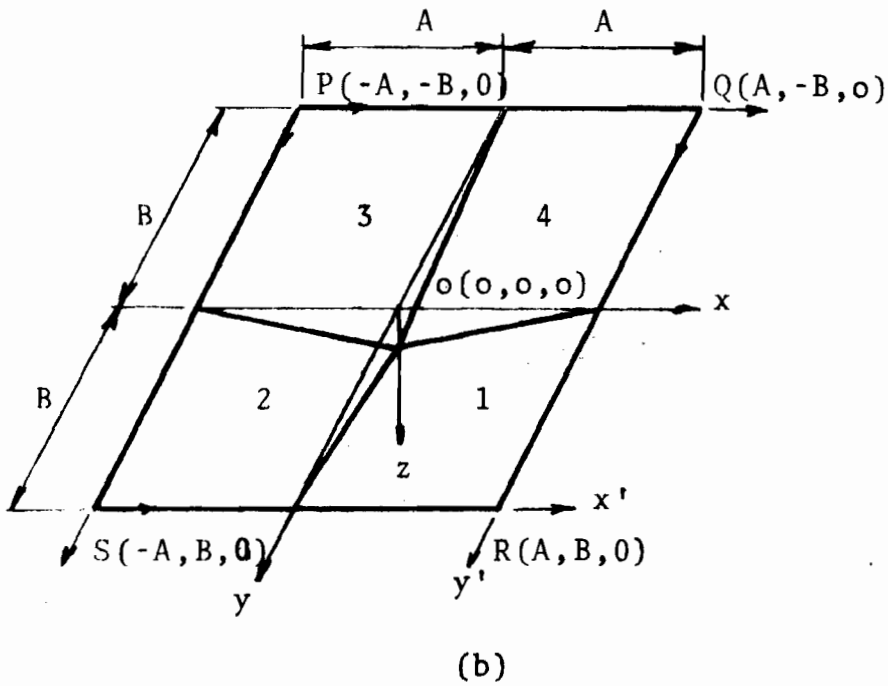


Fig. 3.14b Idealized Spring System



$$\begin{aligned}
 A_1 &= A_2 = A_3 = A_4 = A \\
 B_1 &= B_2 = B_3 = B_4 = B \\
 C_1 &= C_2 = C_3 = C_4 = C \\
 \bar{x}_1 &= \bar{x}_2 = \bar{x}_3 = \bar{x}_4 = c \\
 \bar{y}_1 &= \bar{y}_2 = \bar{y}_3 = \bar{y}_4 = 0
 \end{aligned}$$



$$\begin{aligned}
 A_1 &= A_2 = A_3 = A_4 = A \\
 B_1 &= B_2 = B_3 = B_4 = B \\
 C_1 &= C_3 = C \\
 C_2 &= C_4 = -C \\
 \bar{x}_1 &= \bar{x}_4 = A \\
 \bar{x}_2 &= \bar{x}_3 = -A \\
 \bar{y}_1 &= \bar{y}_2 = B \\
 \bar{y}_3 &= \bar{y}_4 = -B
 \end{aligned}$$

Fig. 3-15 Geometrical Definition of a Hypar Surface

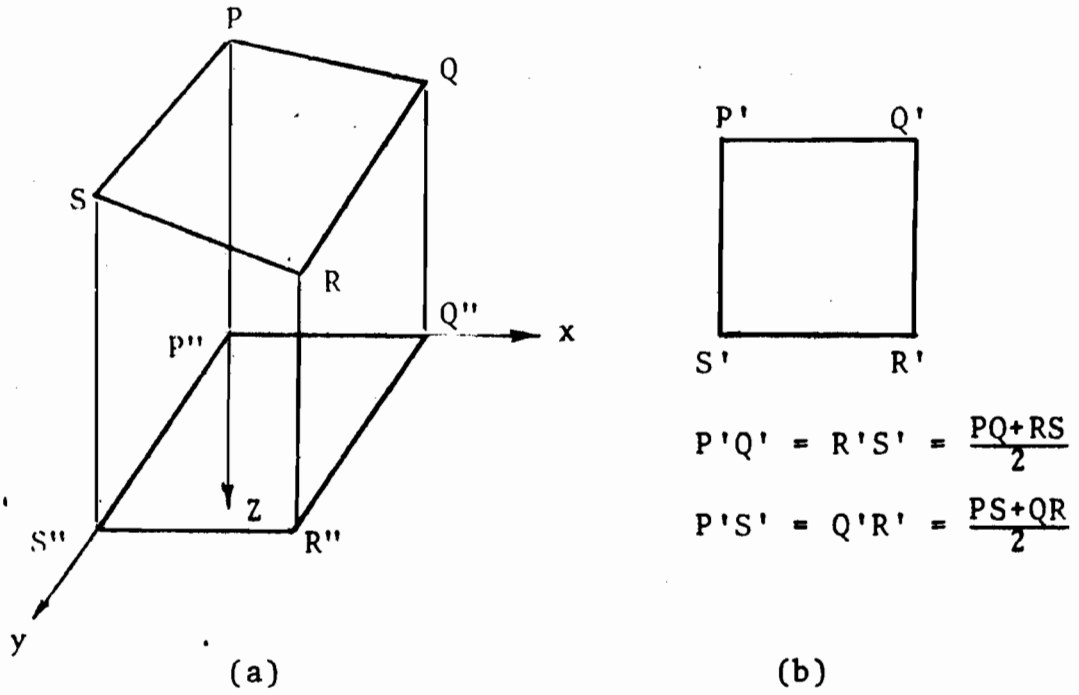


Fig. 3-16 Element Size

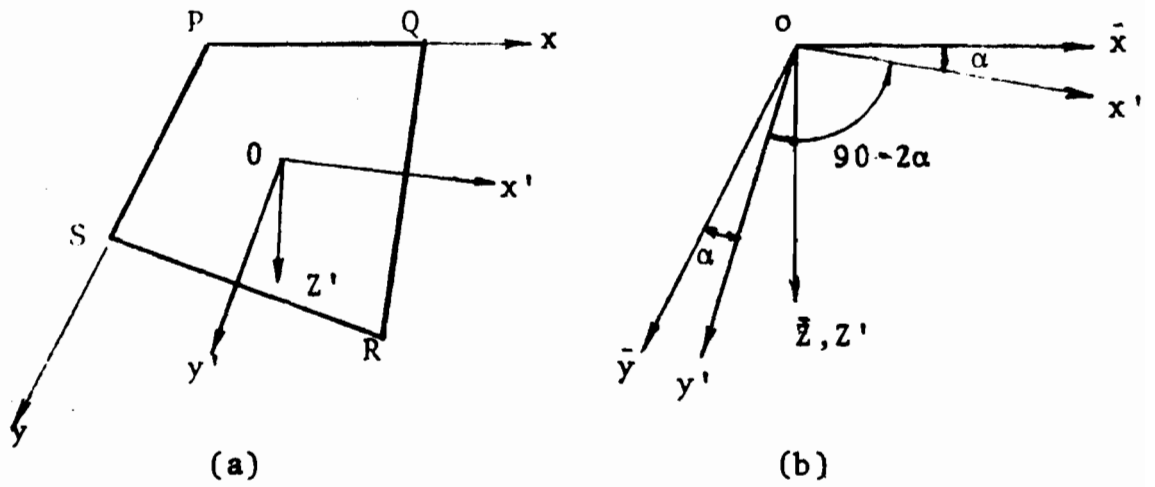


Fig. 3-17 Co-ordinate Transformation

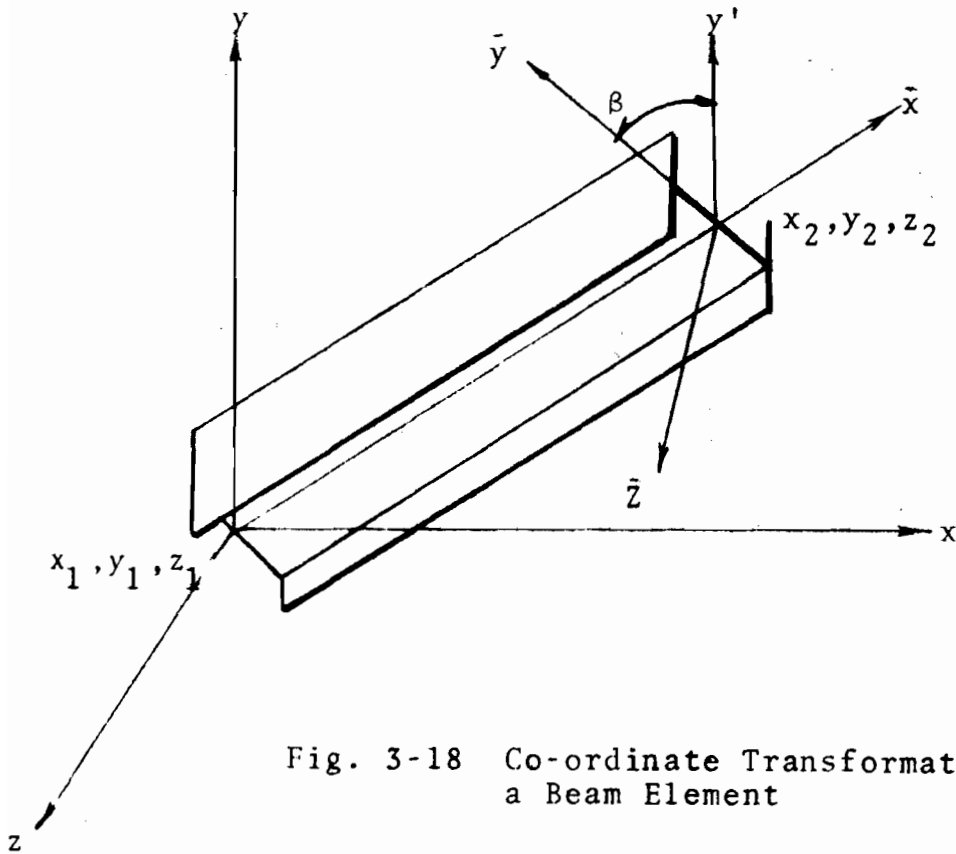


Fig. 3-18 Co-ordinate Transformation for a Beam Element

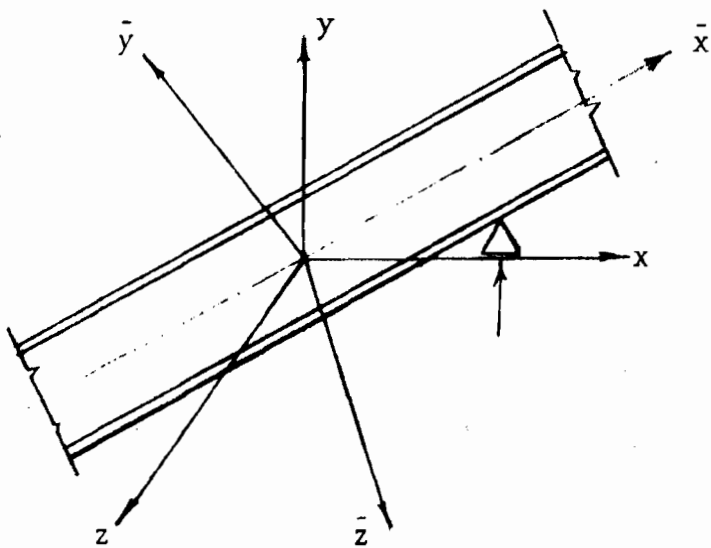


Fig. 3-19 Boundary Conditions in Global Co-ordinates

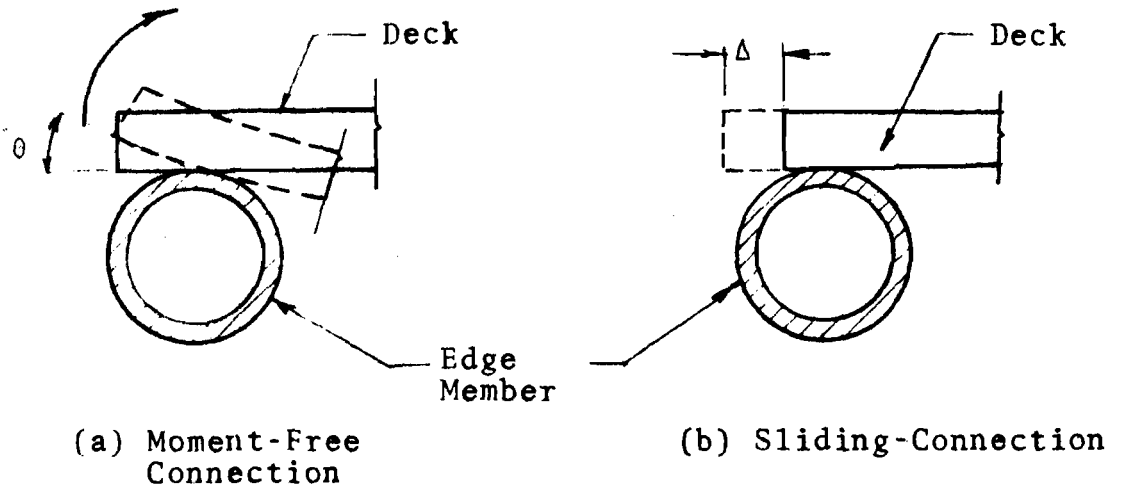


Fig. 3-20 Deck and Edge Member Connections

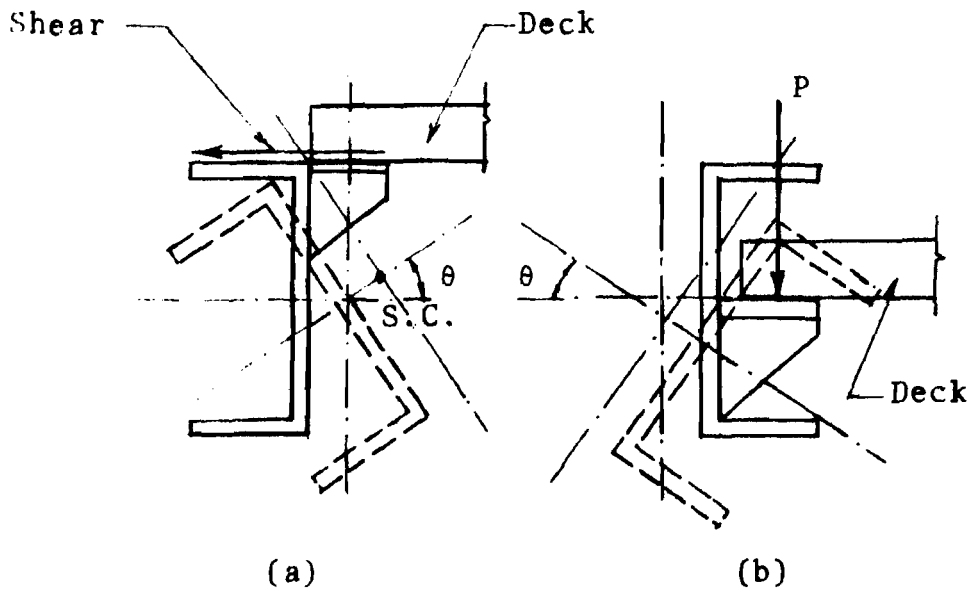
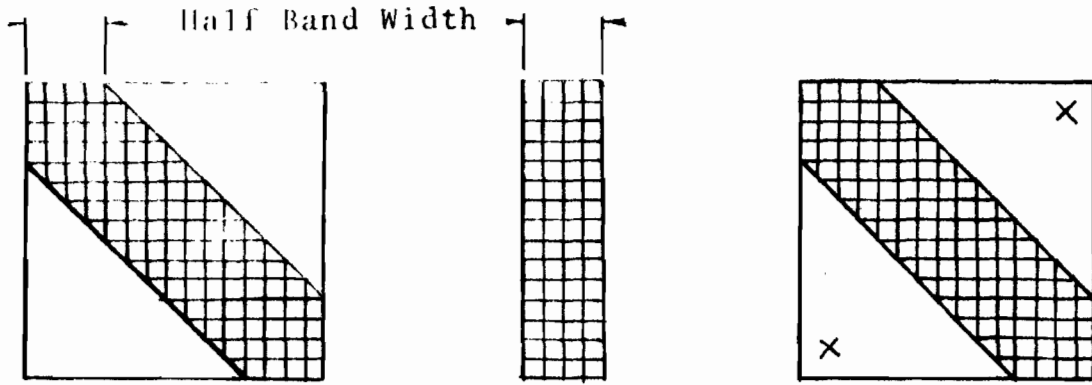


Fig. 3-21 Twisting of an Eccentric Edge Member for $T_F=0$



(a) Stiffness Matrix [K] (b) Vertically Stored Half-Band (c) Stiffness Matrix with Sparse entries

Fig. 3-22 Solutions of Equations

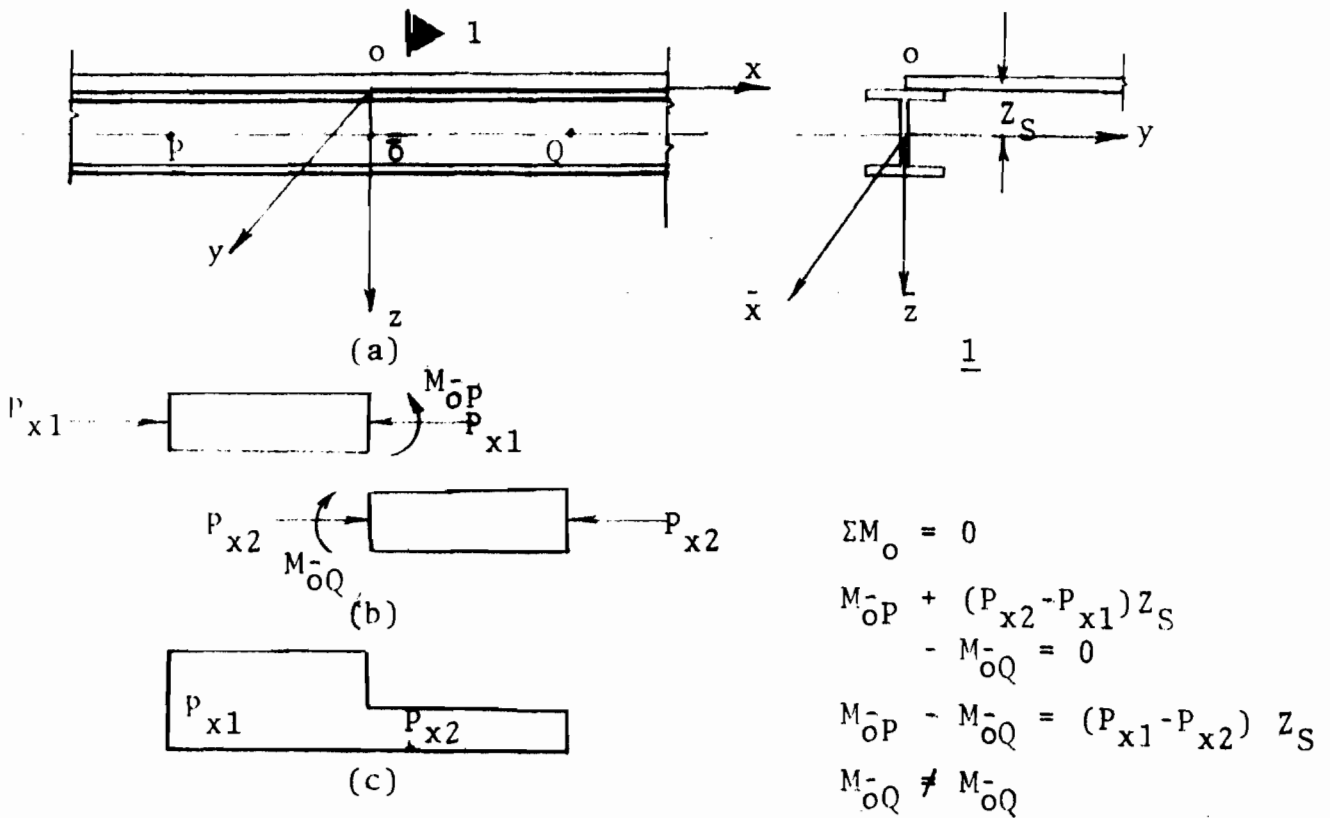


Fig. 3-23 Computation of Forces in Eccentric Edge Members

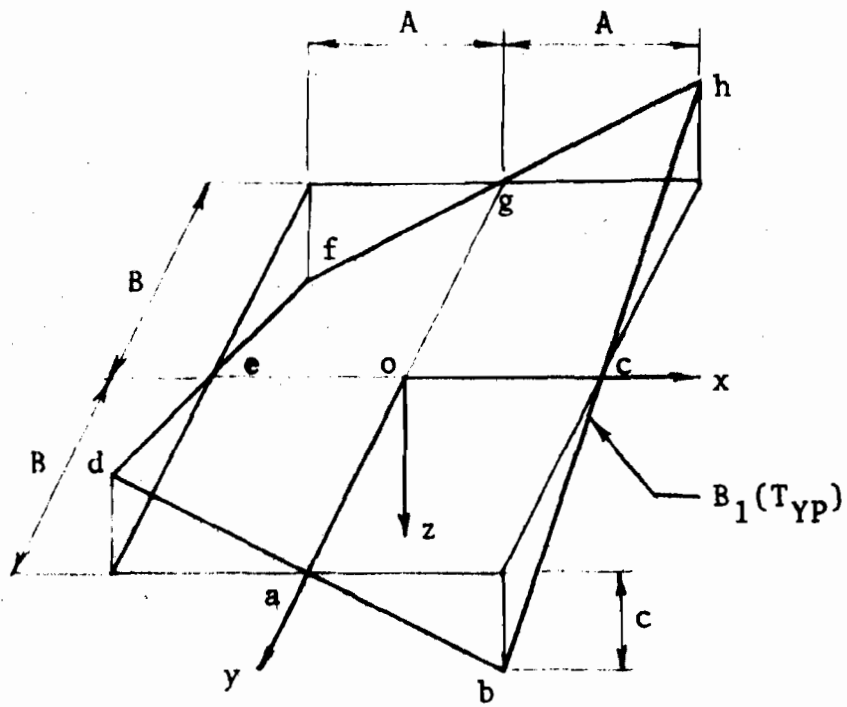


Fig. 4-1 Structure Type I

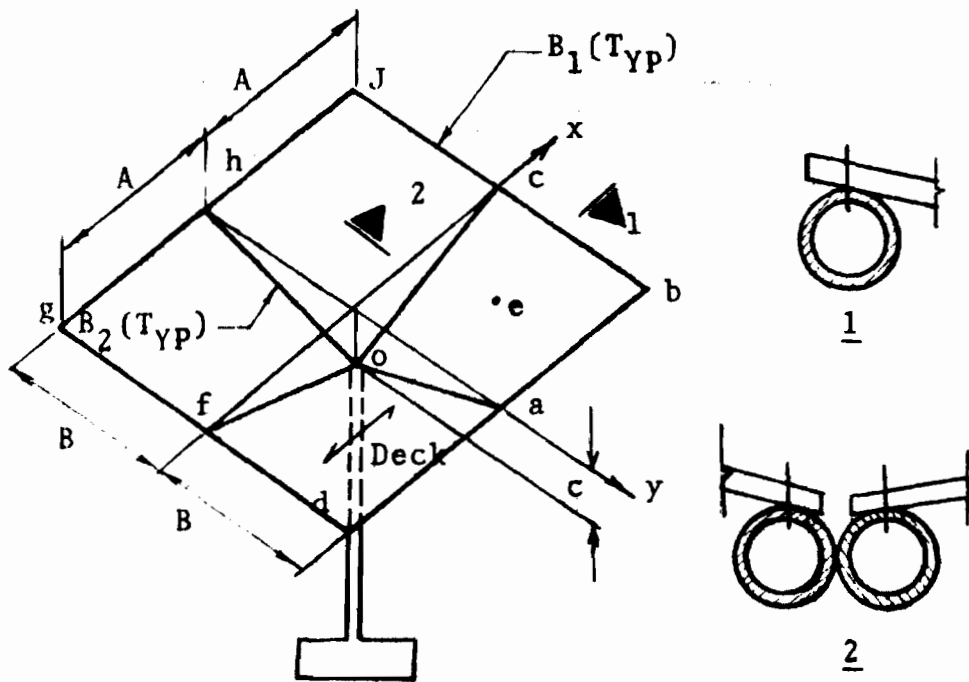


Fig. 4-2 Structure Type II

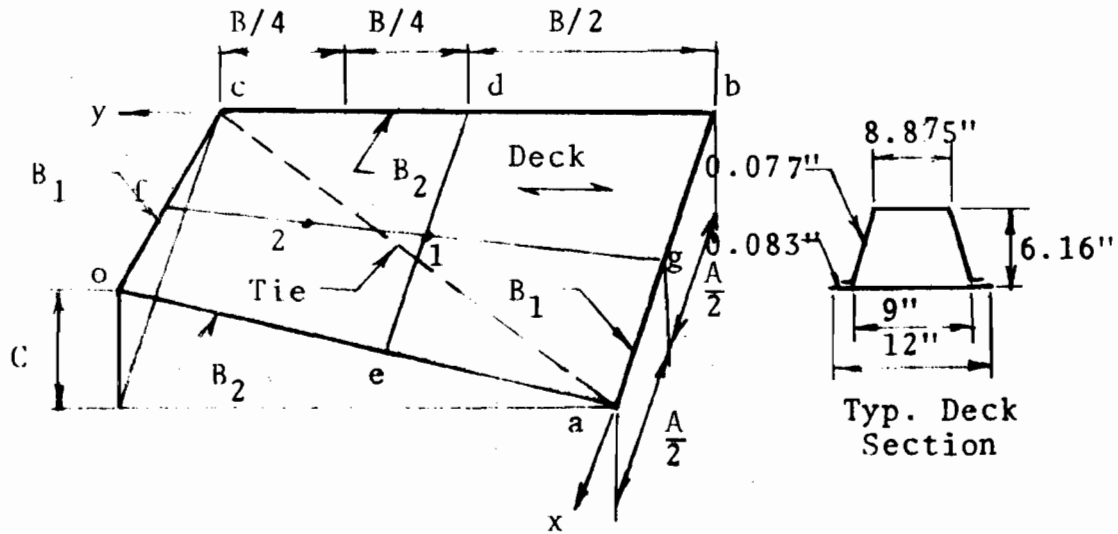


Fig. 4-3 Structure Type IV

Note: 1 & 2 Refer to the Locations of Rosettes

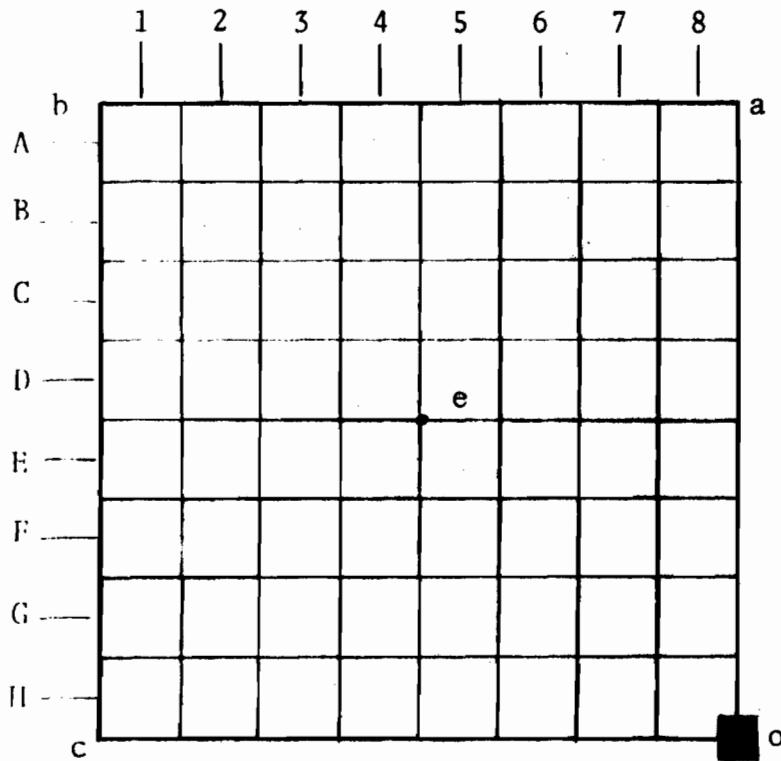


Fig. 4-4 Quadrant of a Hypar

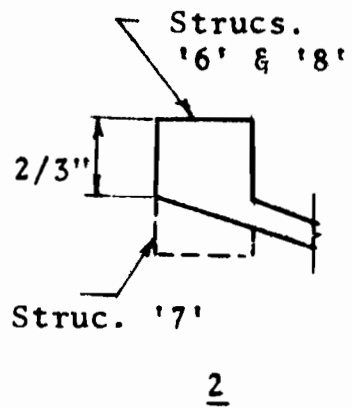
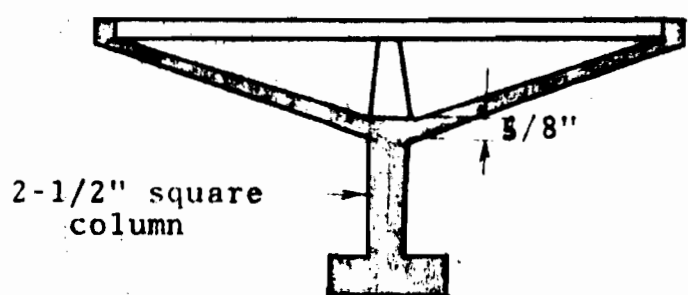
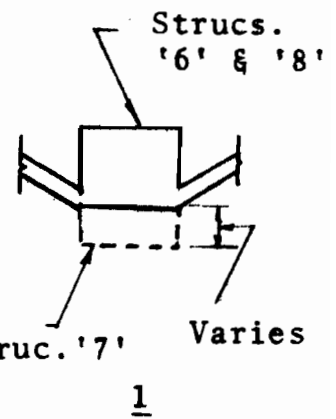
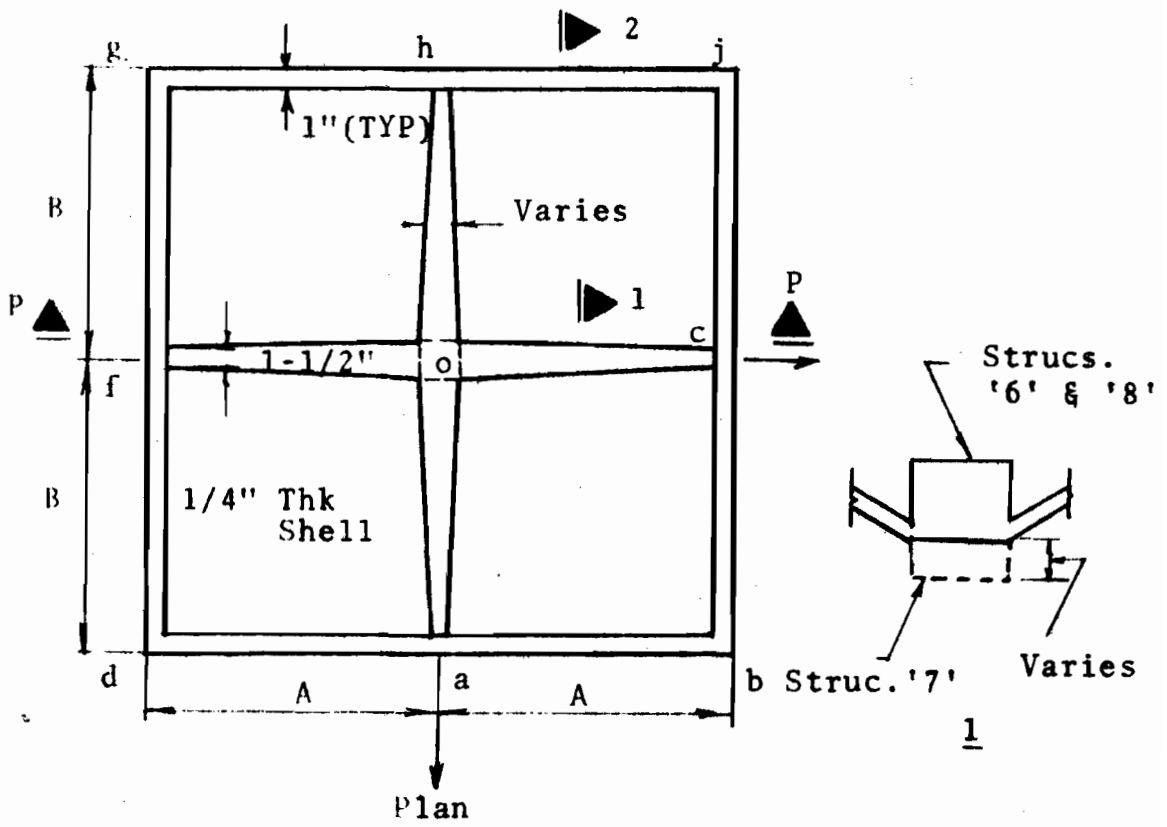


Fig. 4-5 Structure Type III

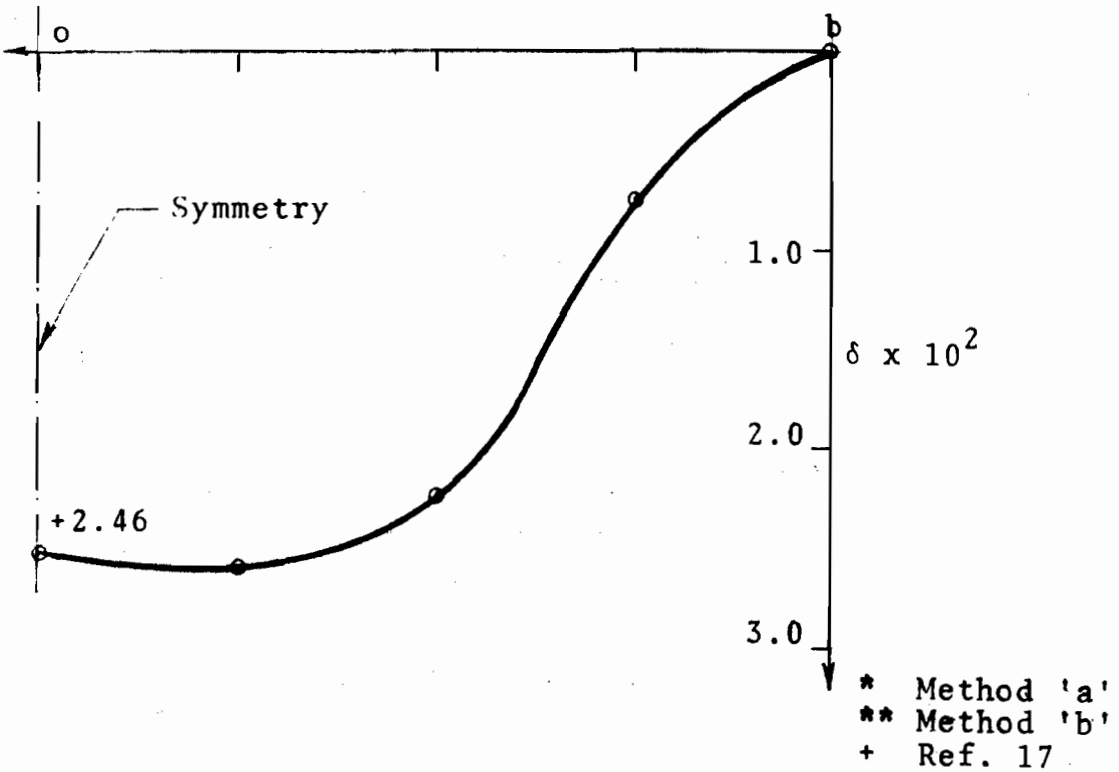
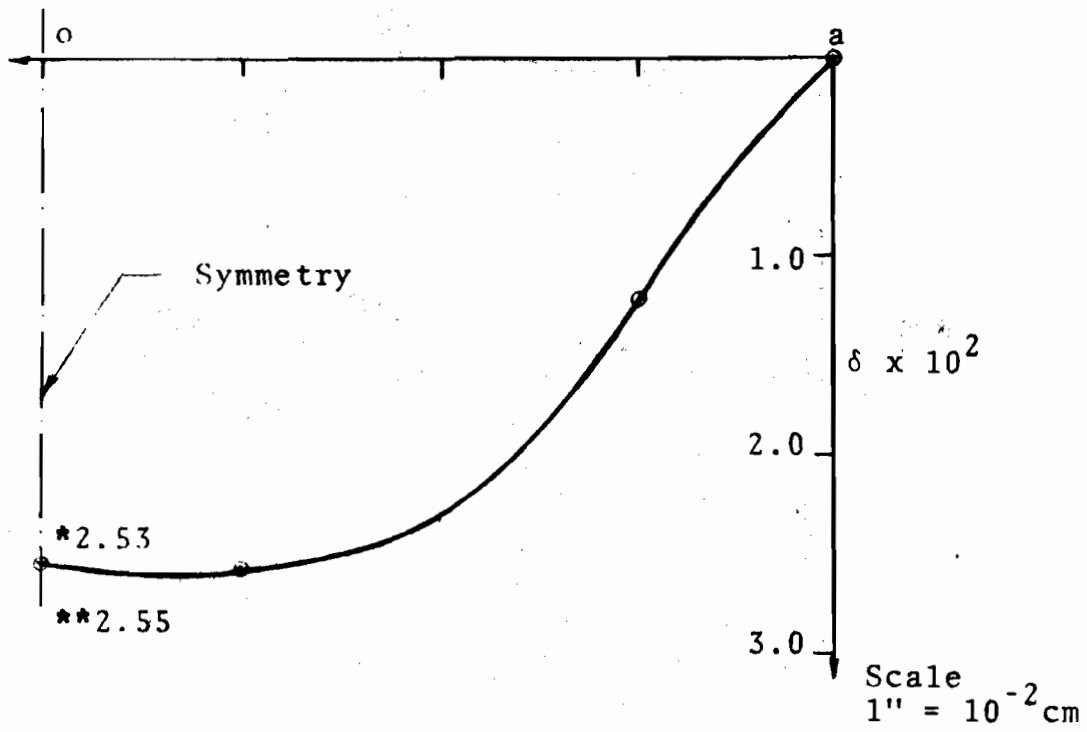


Fig. 4-6 Deflection Profiles (Structure '1')

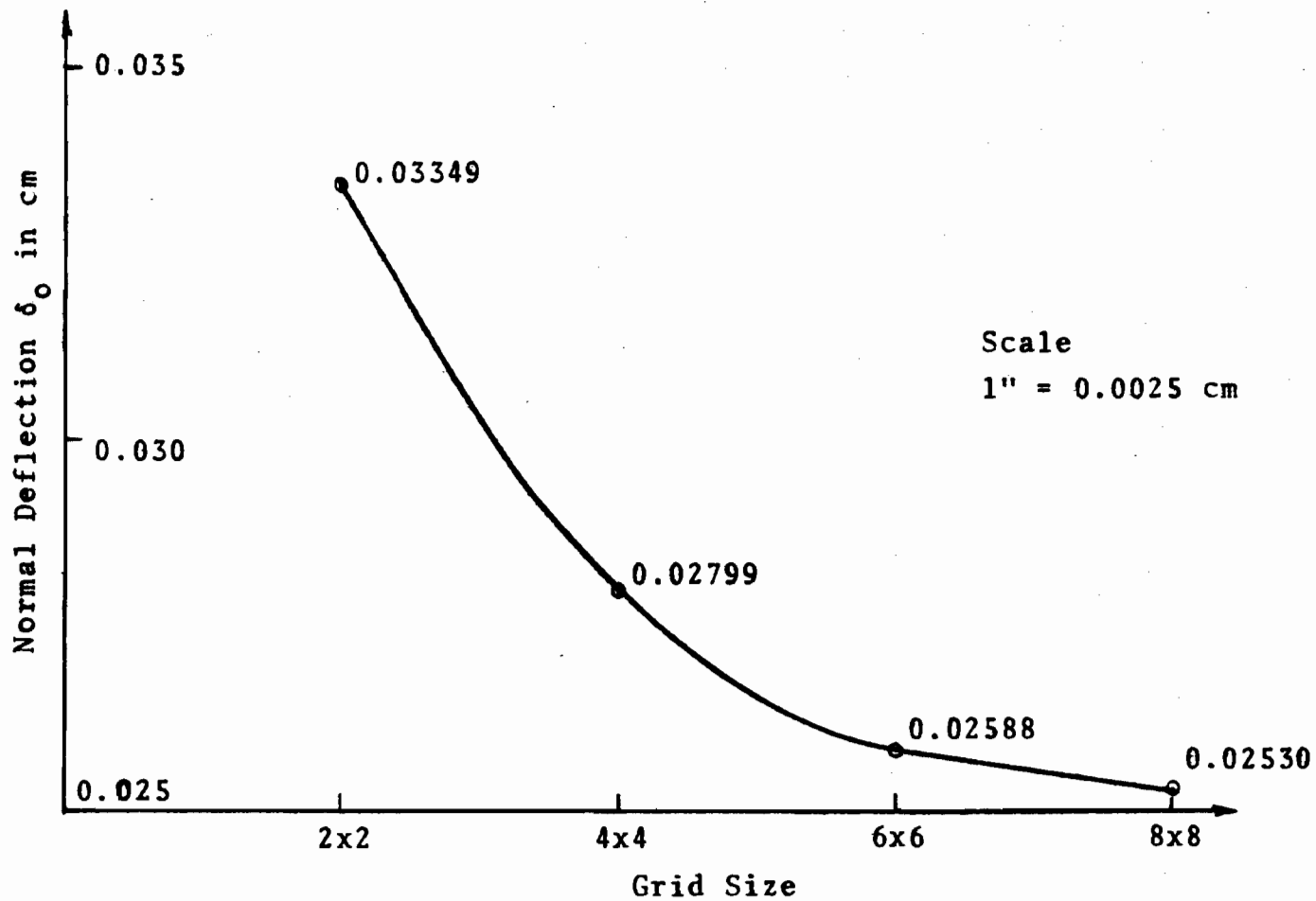


Fig. 4-7 Convergence Characteristics for Deflection ' δ_0 ' (Structure '1')

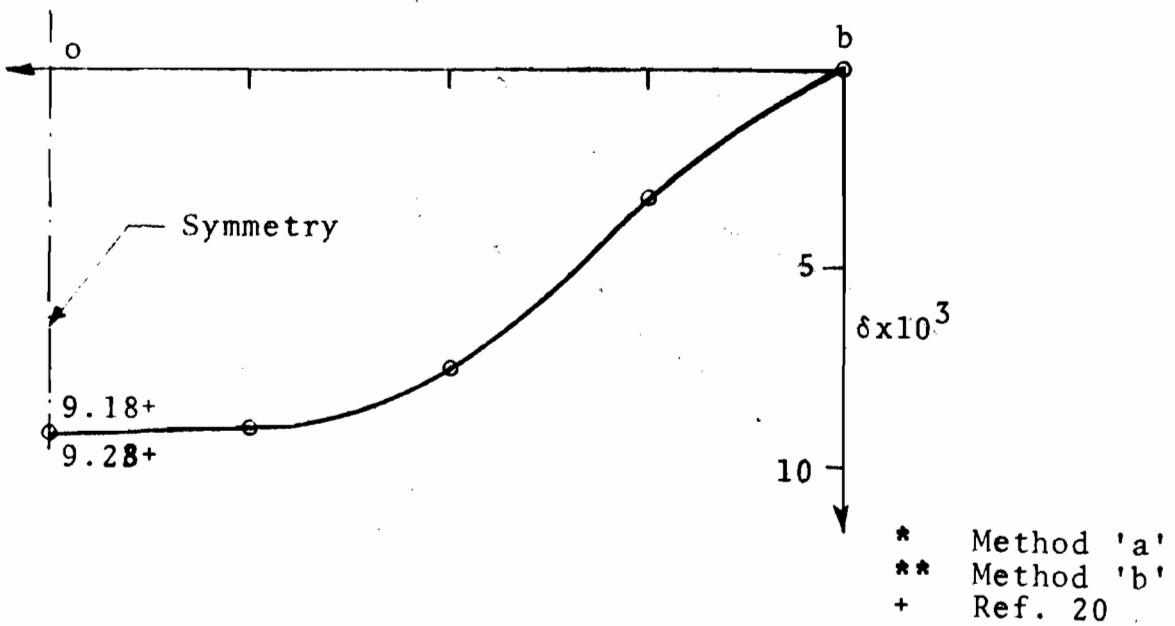
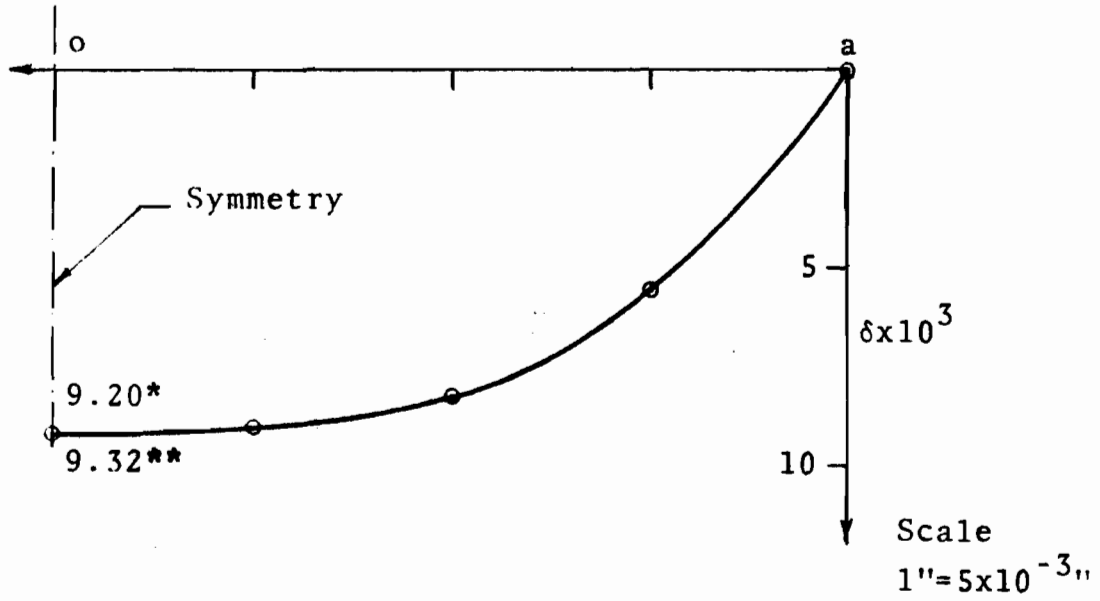


Fig. 4-8 Deflection Profiles (Structure '2')

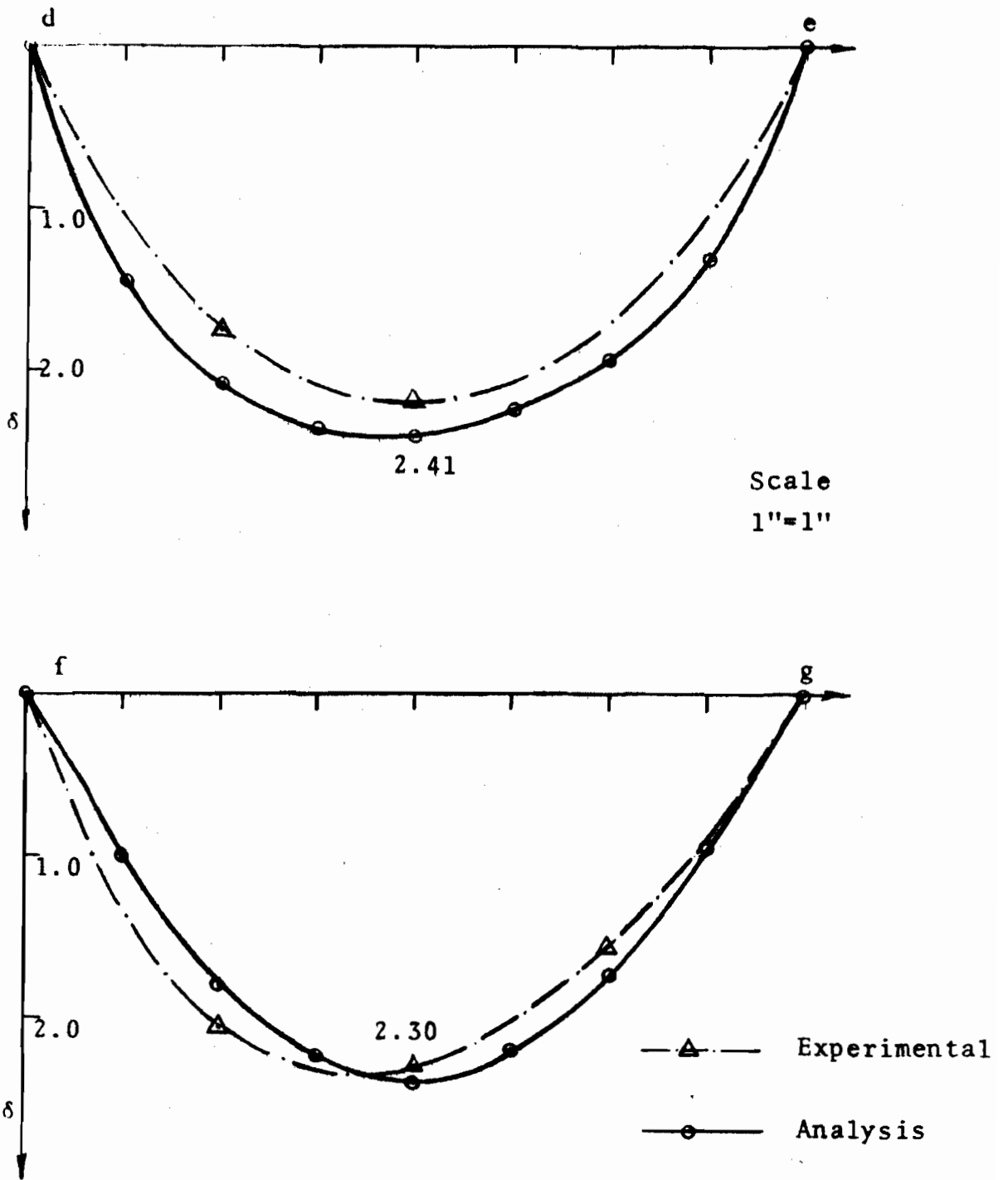


Fig. 4-9 Deflection Profiles
(Structure '5')

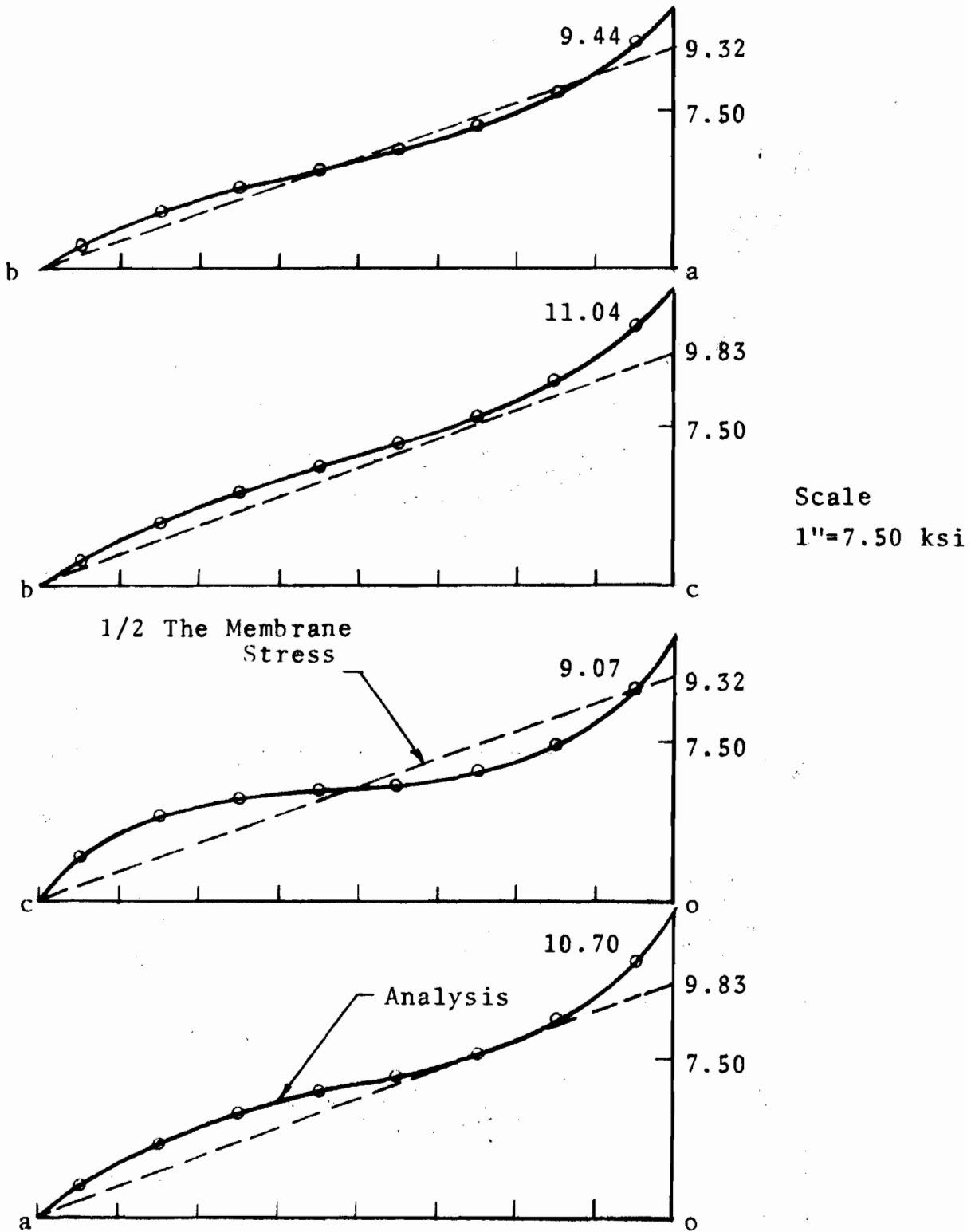


Fig. 4-10 Axial Stresses in Edge Members (Structure '5')

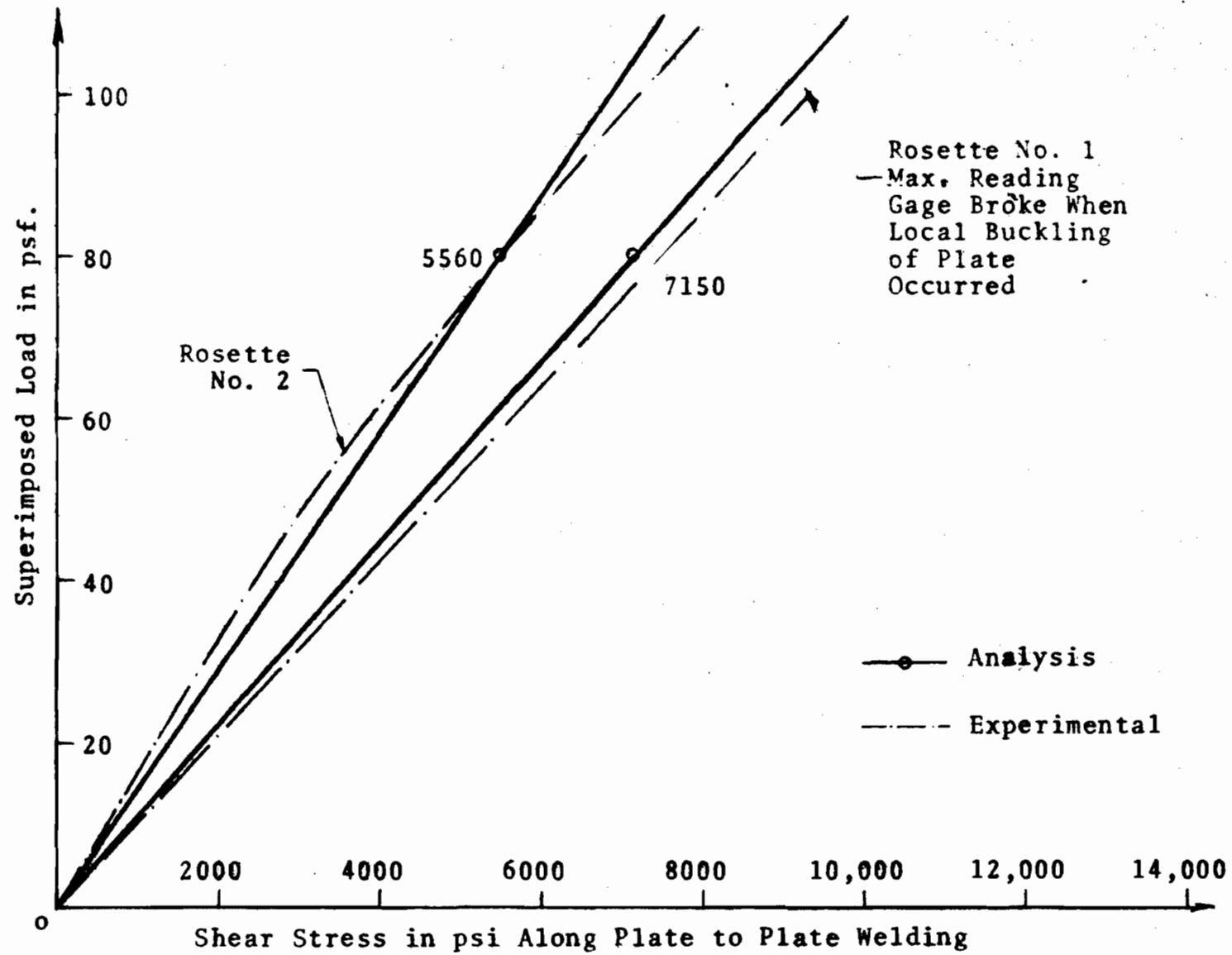


Fig. 4-11 Load vs Shear Stress (Structure '5')

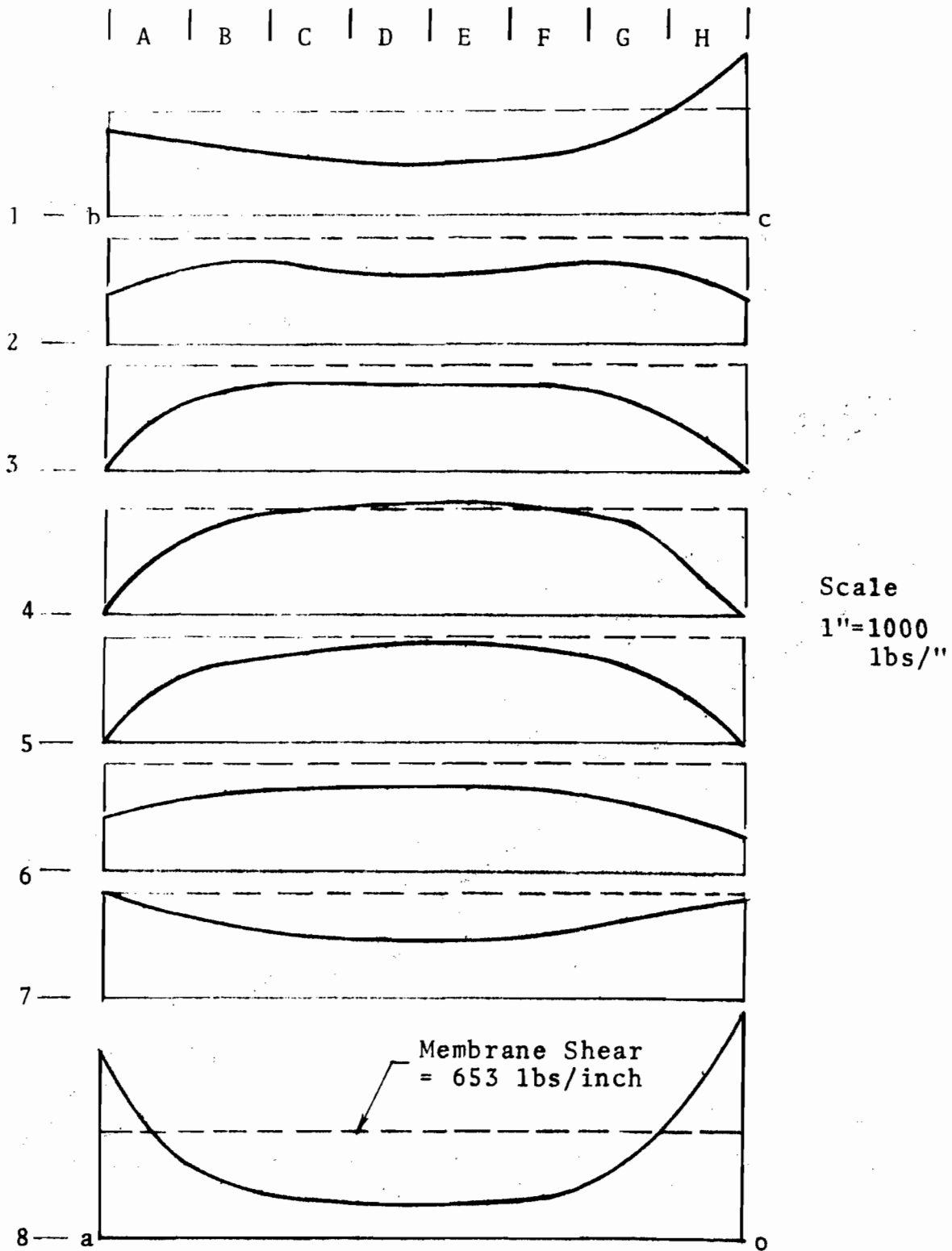


Fig. 4-12 Shear Force N_{xy} lbs/inch
(Structure '5')

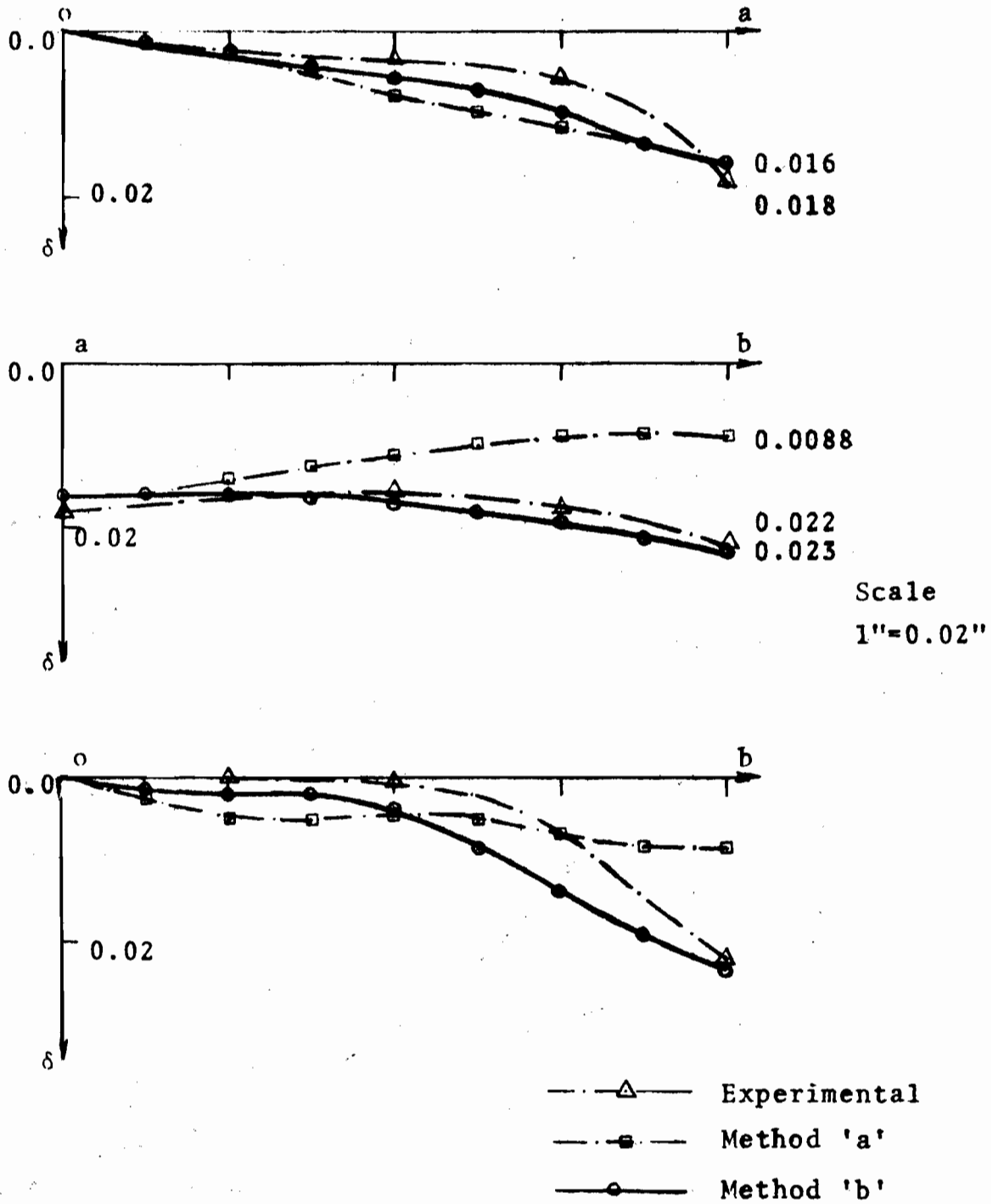


Fig. 4-13 Deflection Profiles
(Structure '6')

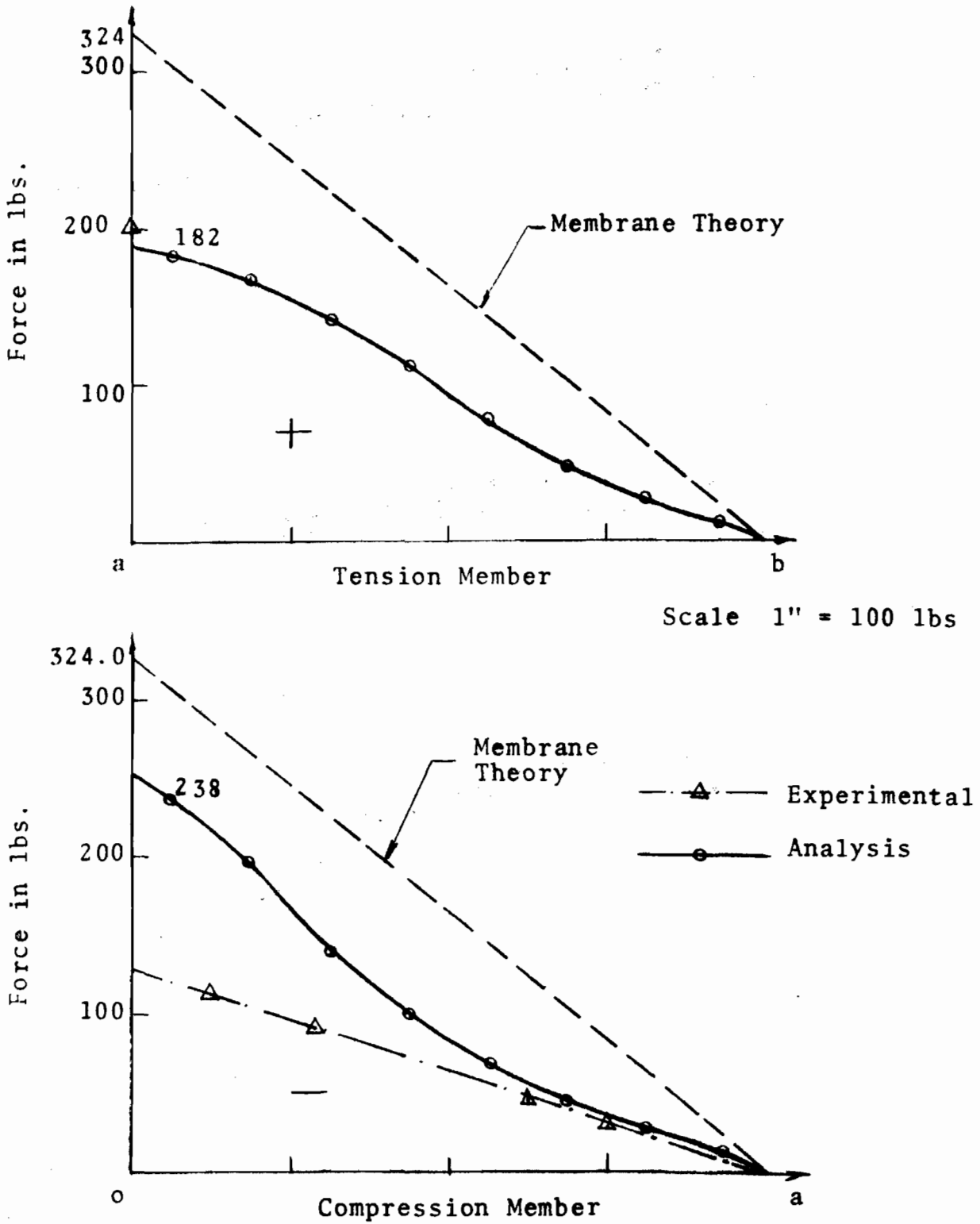


Fig. 4-14 Axial Forces in Edge Members (Structure '6')

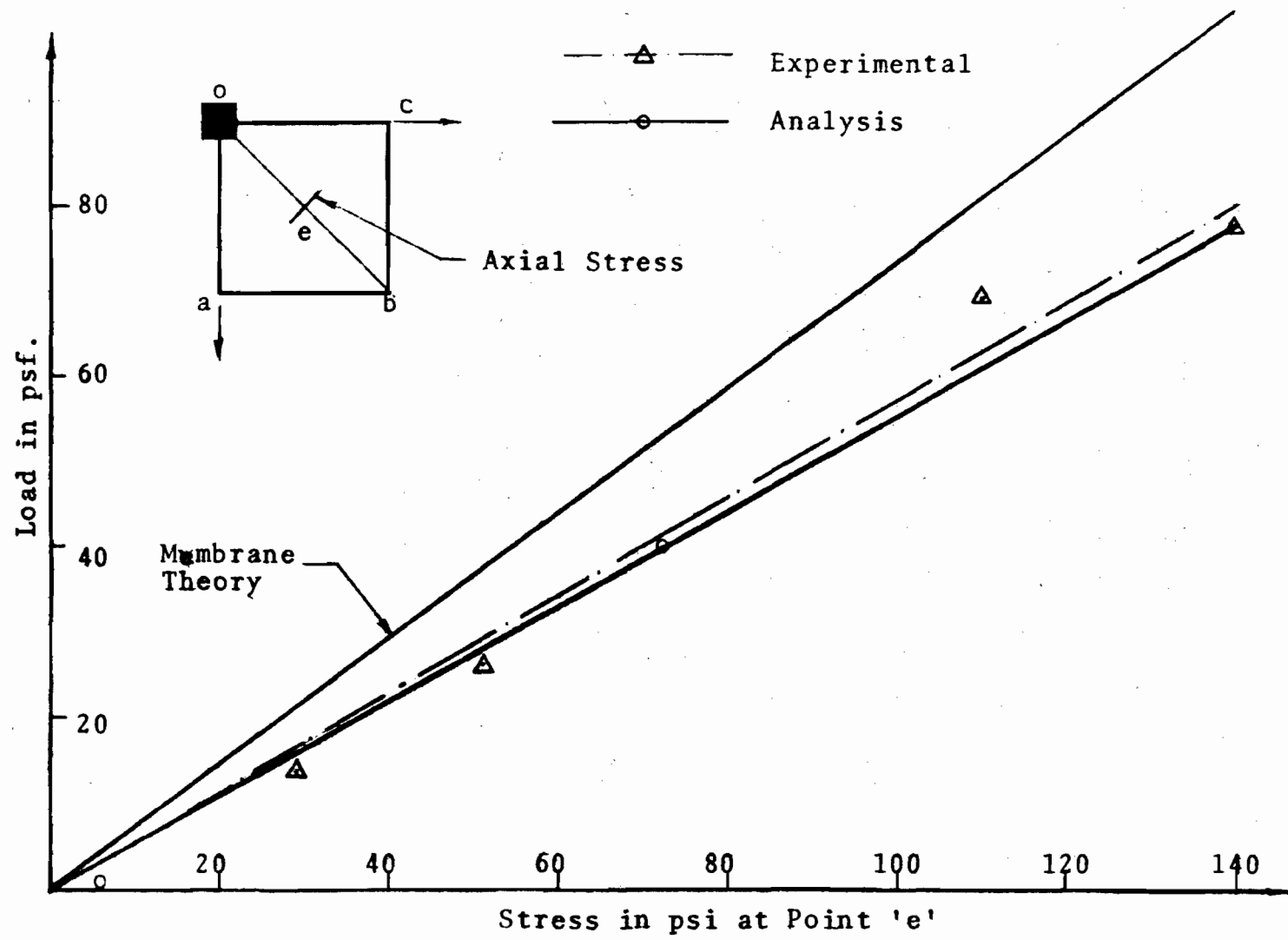


Fig. 4-15 Load vs Stress at Point 'e' (Structure '6')

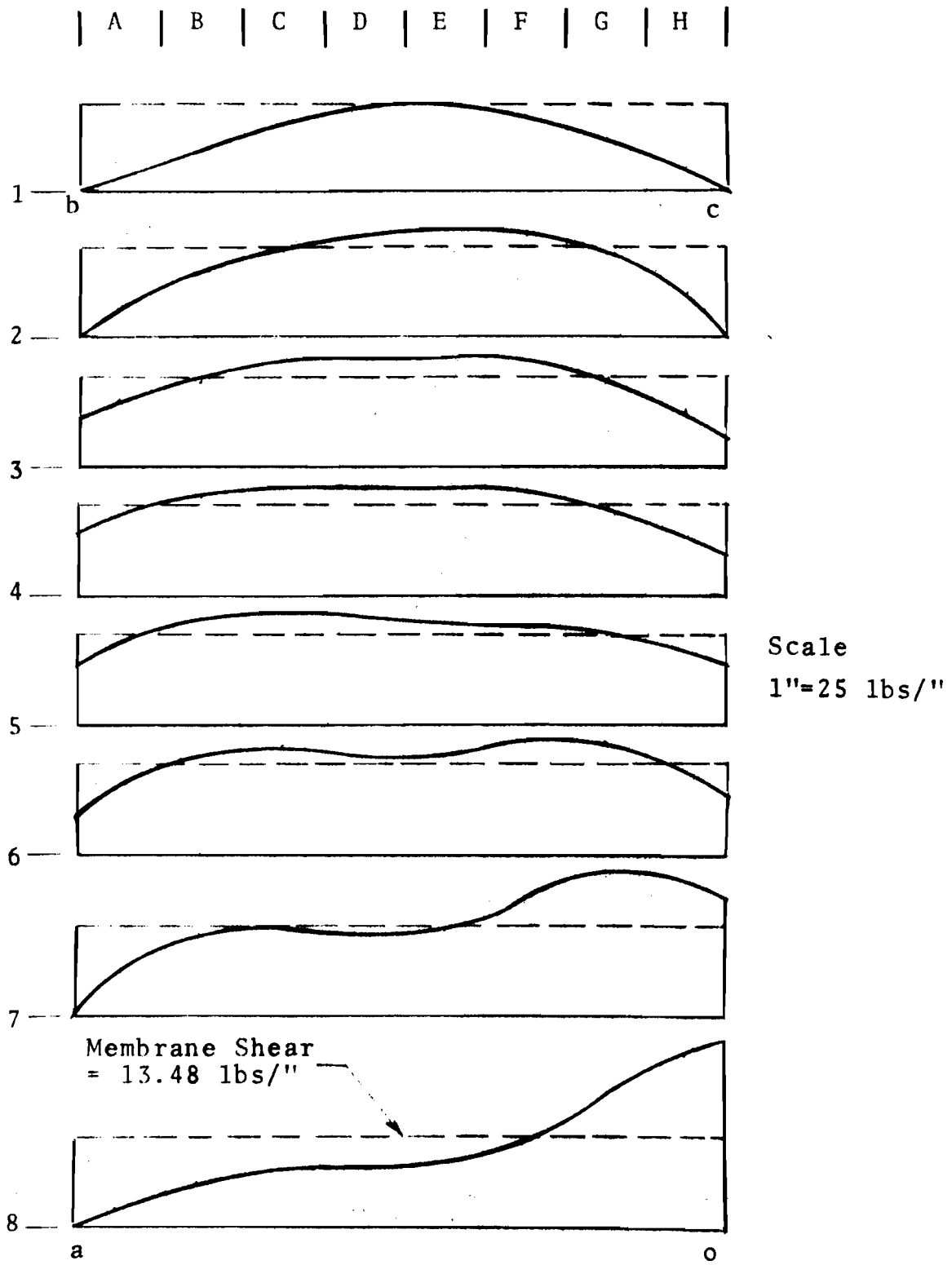


Fig. 4-16 Shear Force N_{xy} lbs/inch
(Structure '6')

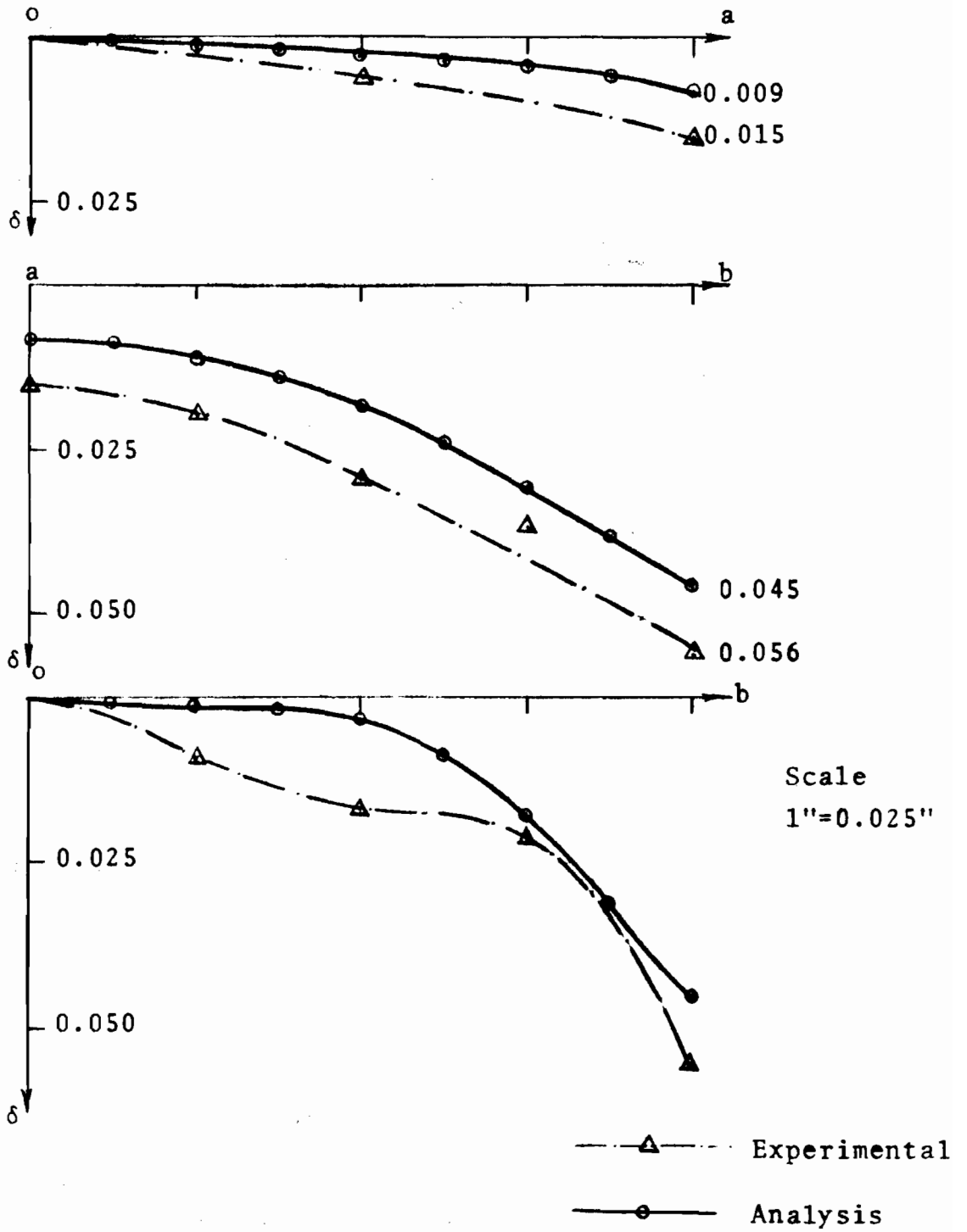
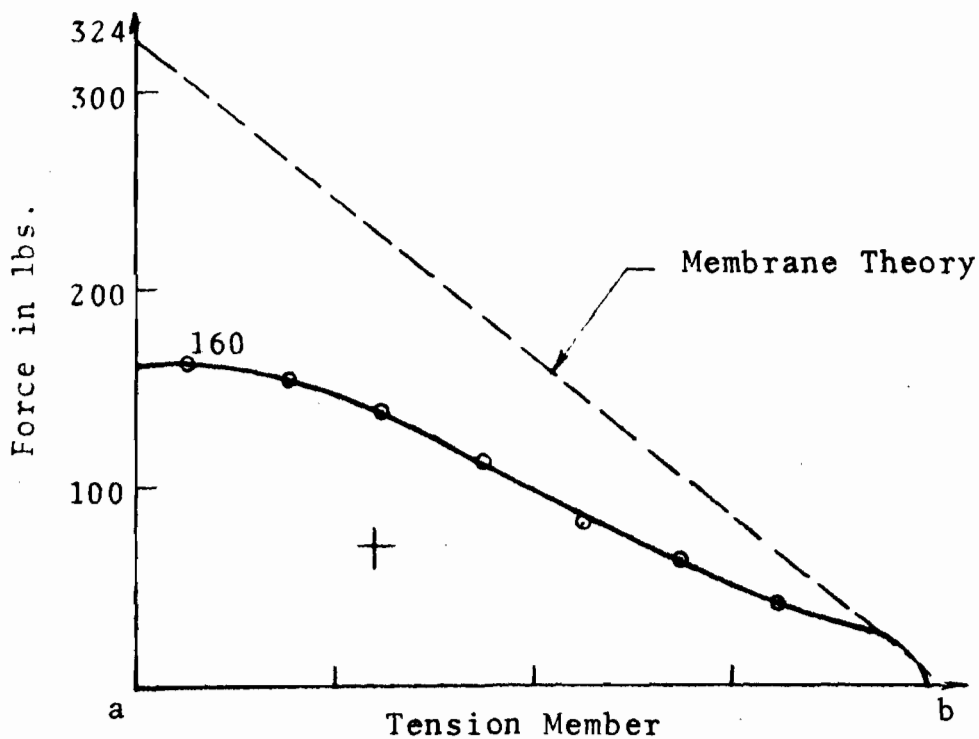


Fig. 4-17 Deflection Profiles
(Structure '7')



Scale
1"=100 lbs.

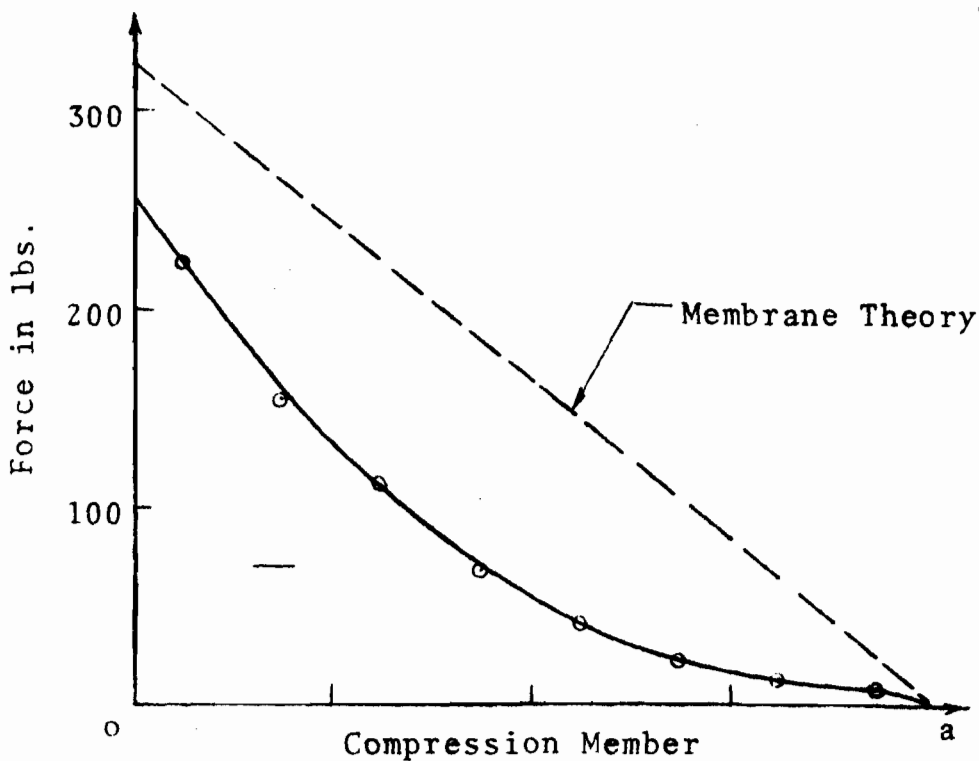
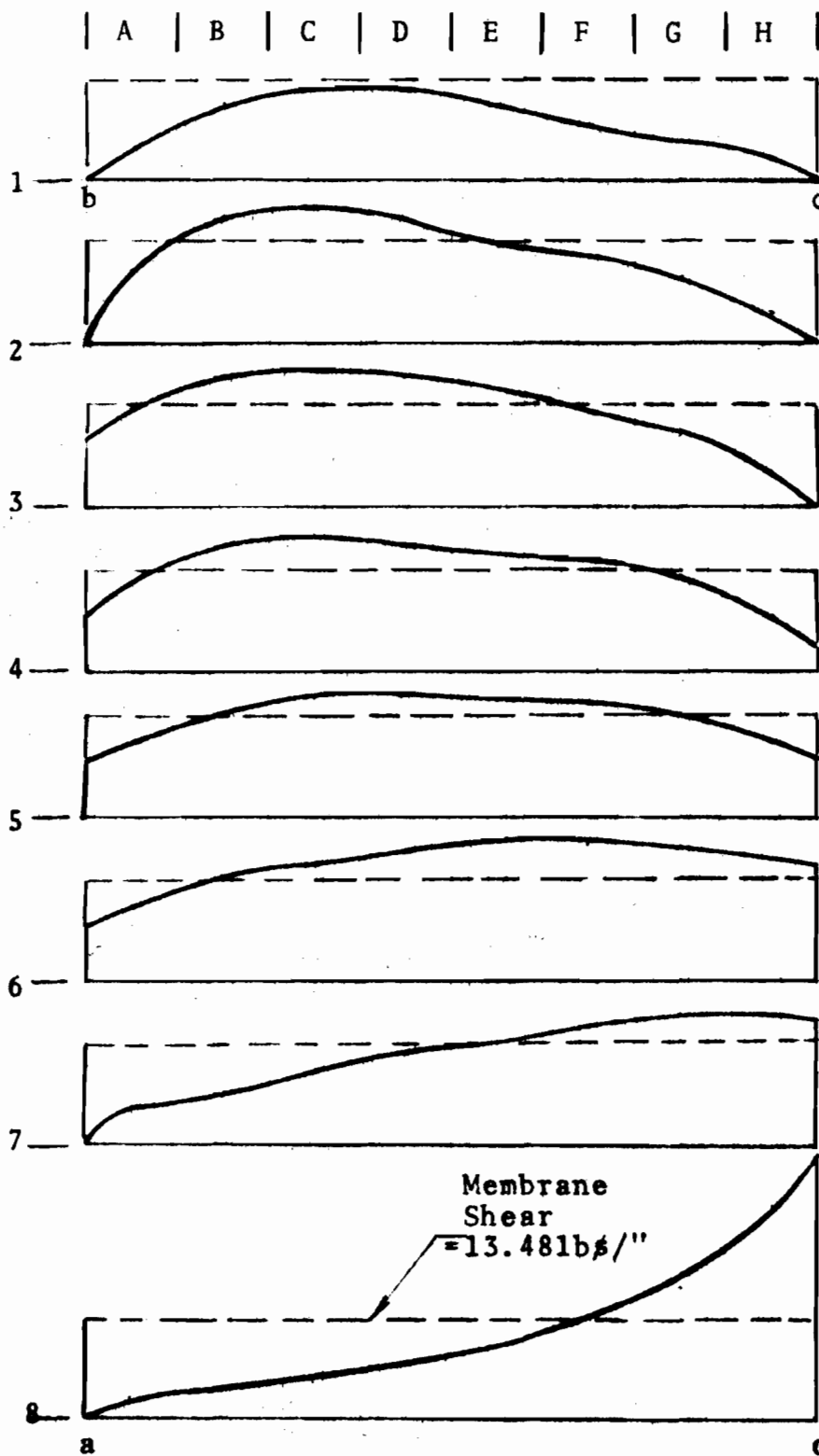


Fig. 4-18 Axial Forces in Edge Members (Structure '7')



Scale
1"=25
lbs/"

Fig. 4-19 Shear Force N_{xy} lbs/inch
(Structure '7')

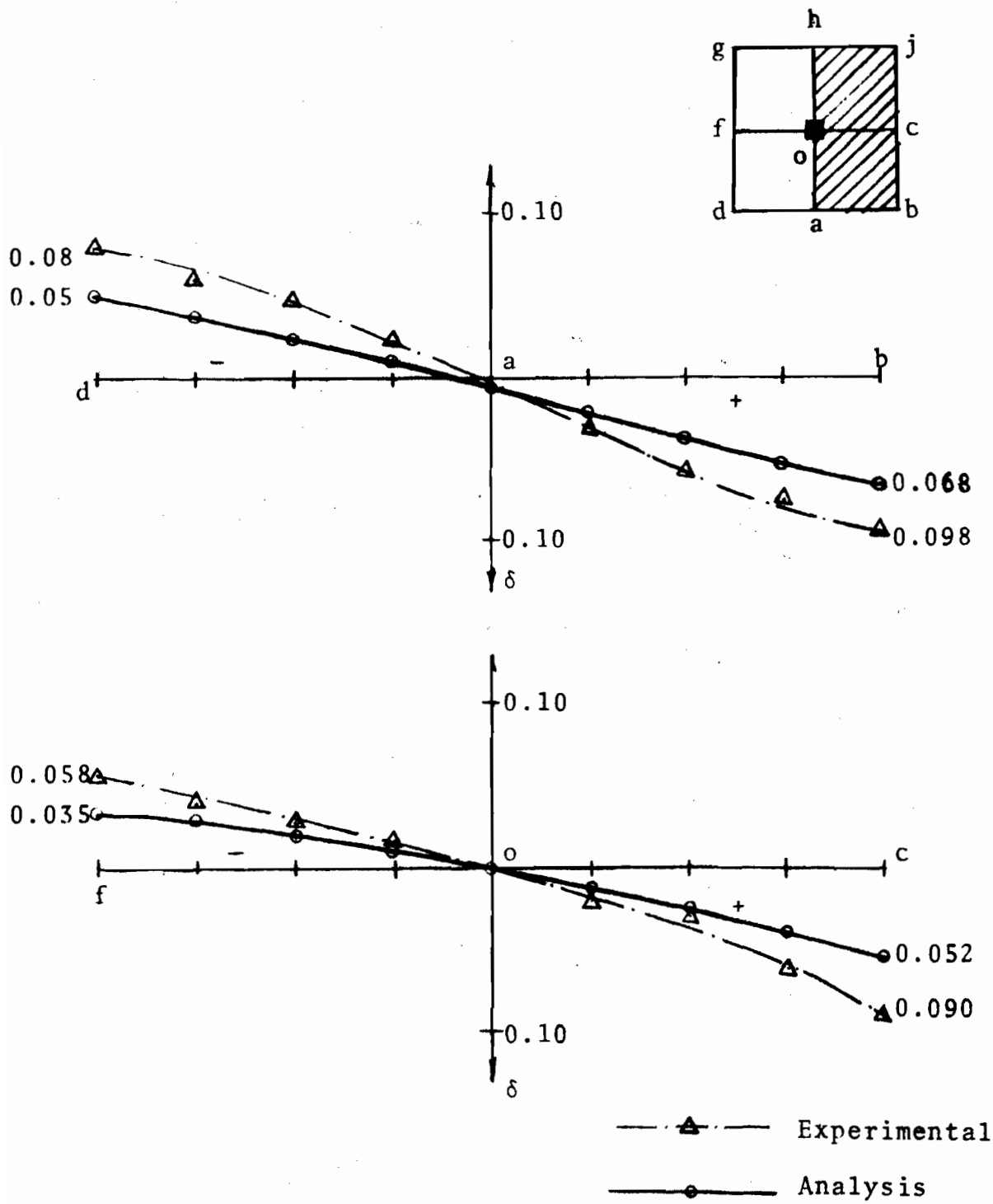


Fig. 4-20 Deflection Profiles (Structure '8')

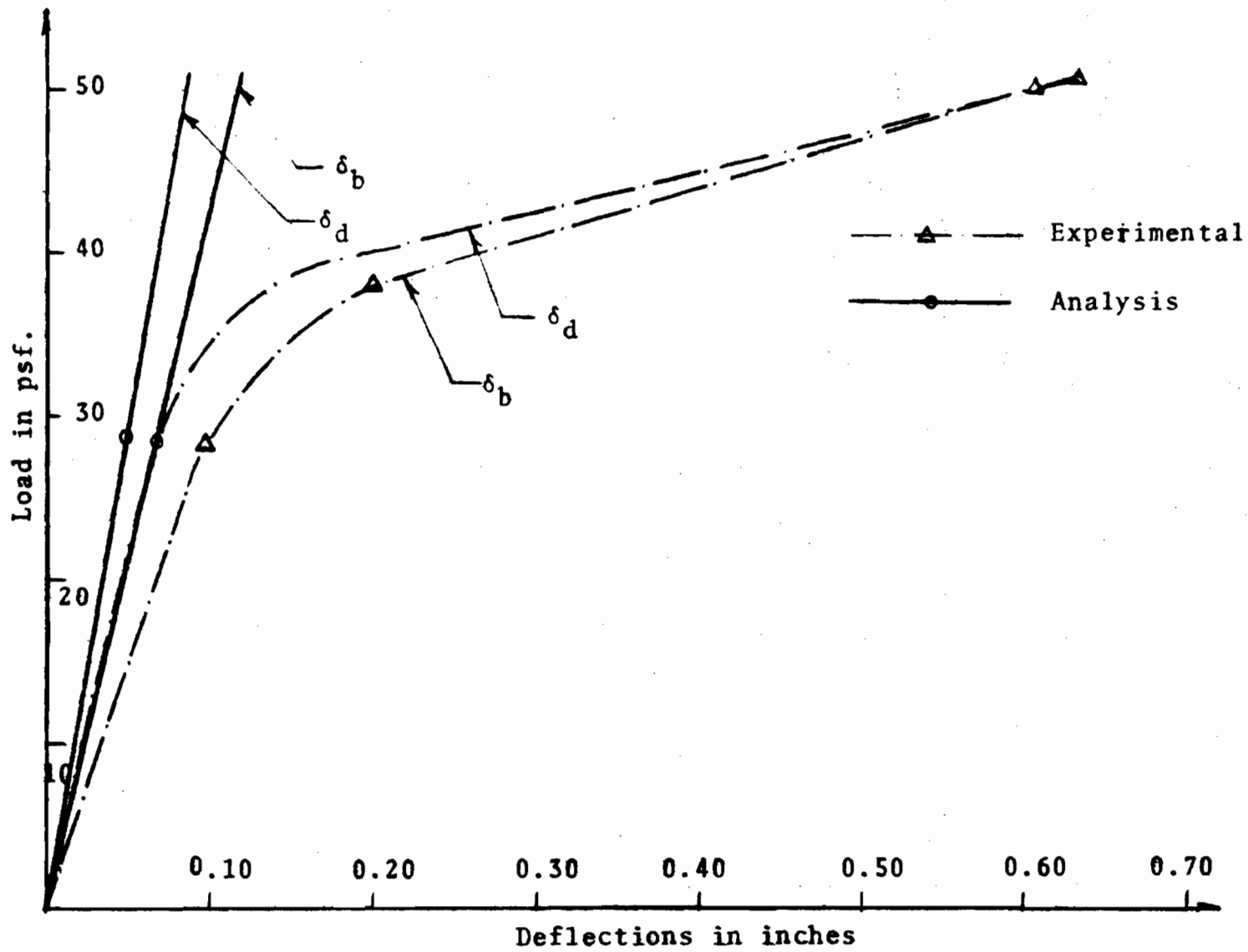


Fig. 4-21 Load vs Deflections (Structure '8')

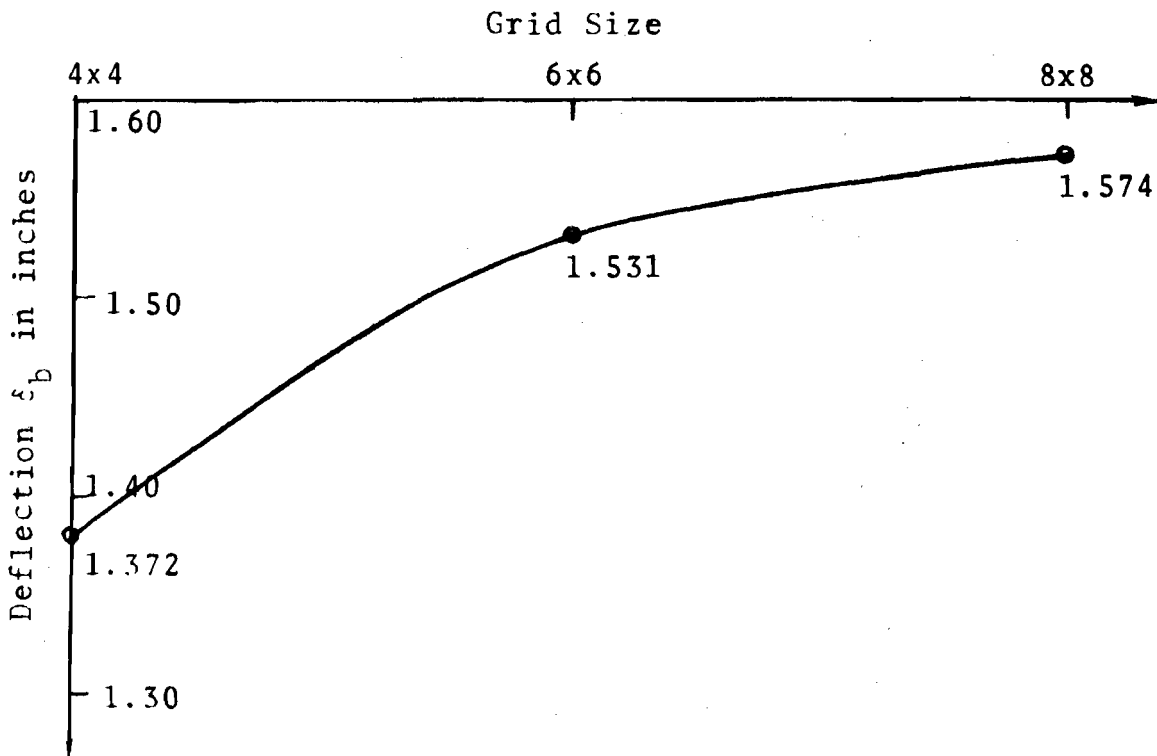
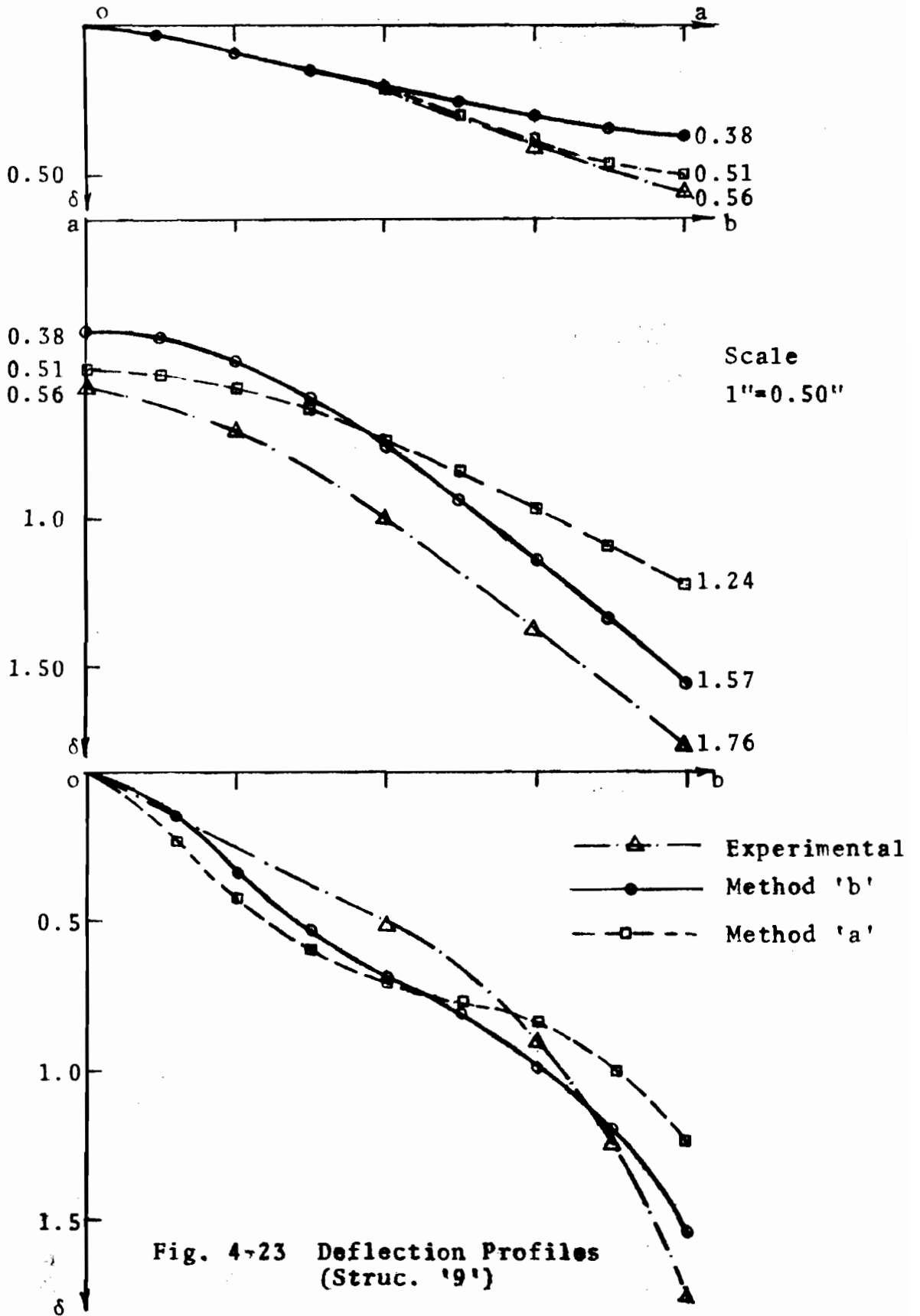
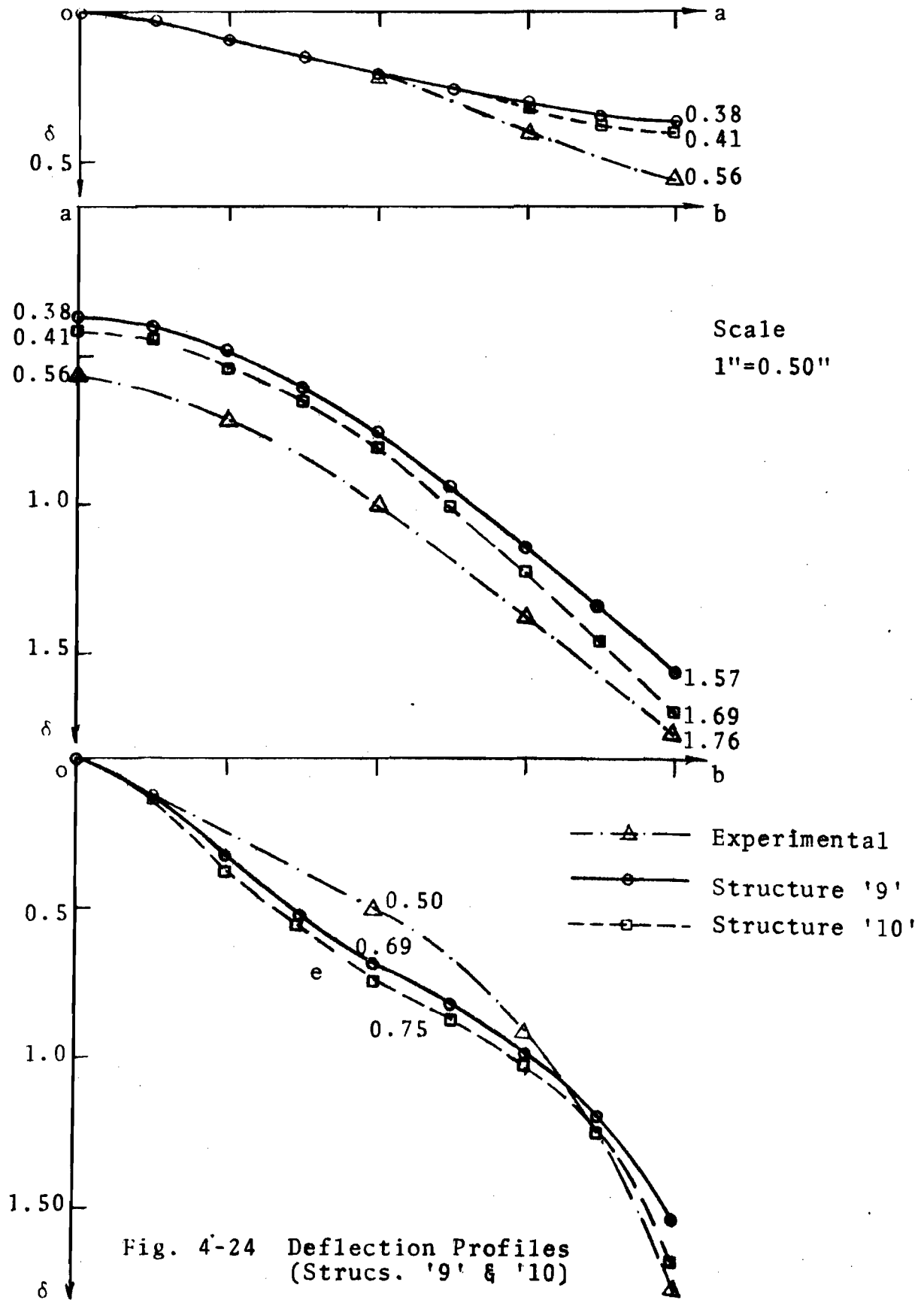


Fig. 4-22 Convergence Characteristics for Corner Deflection ' δ_b ' (Structure '9')





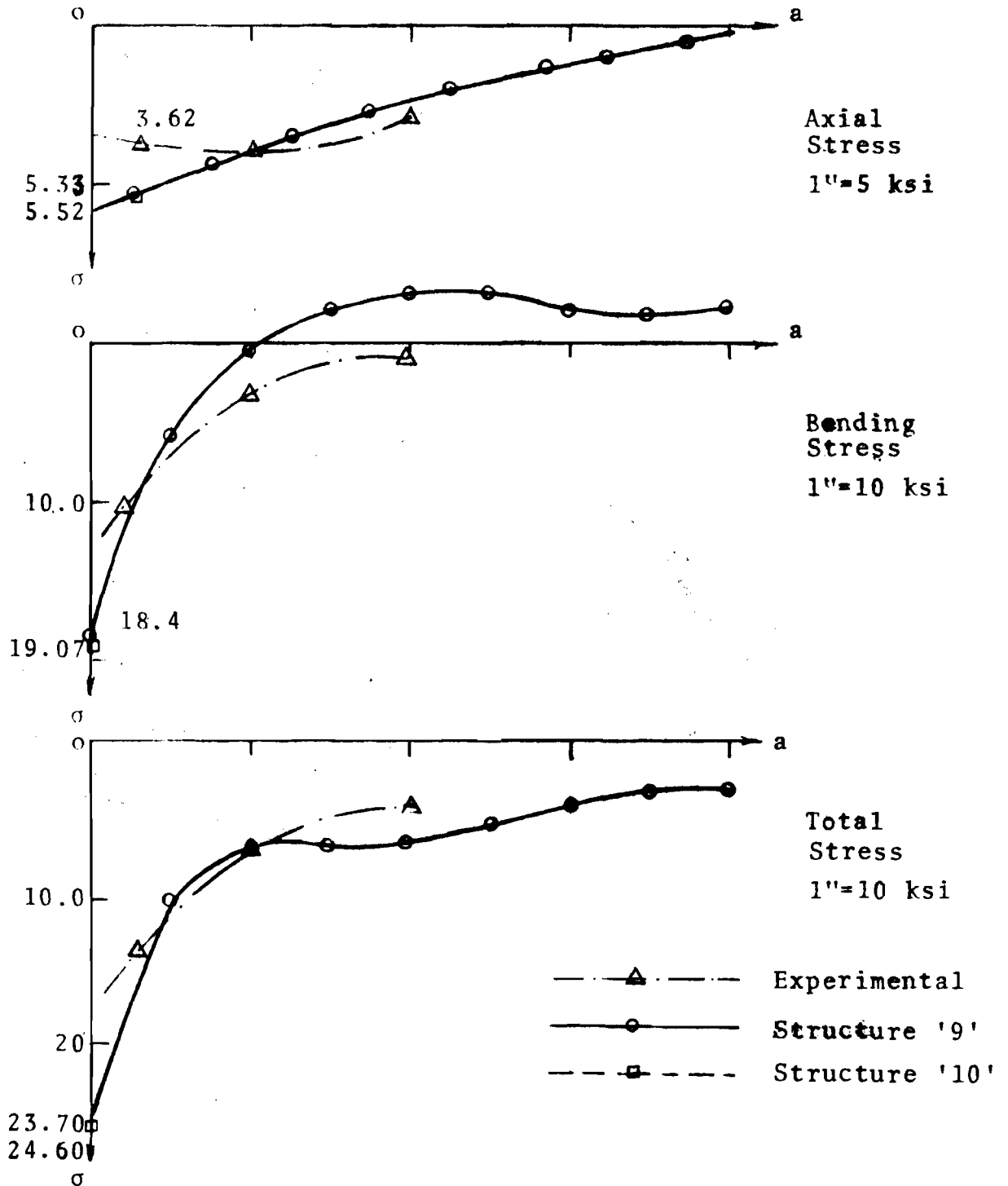


Fig. 4-25 Stresses in Compression Member (Structures '9' and '10')

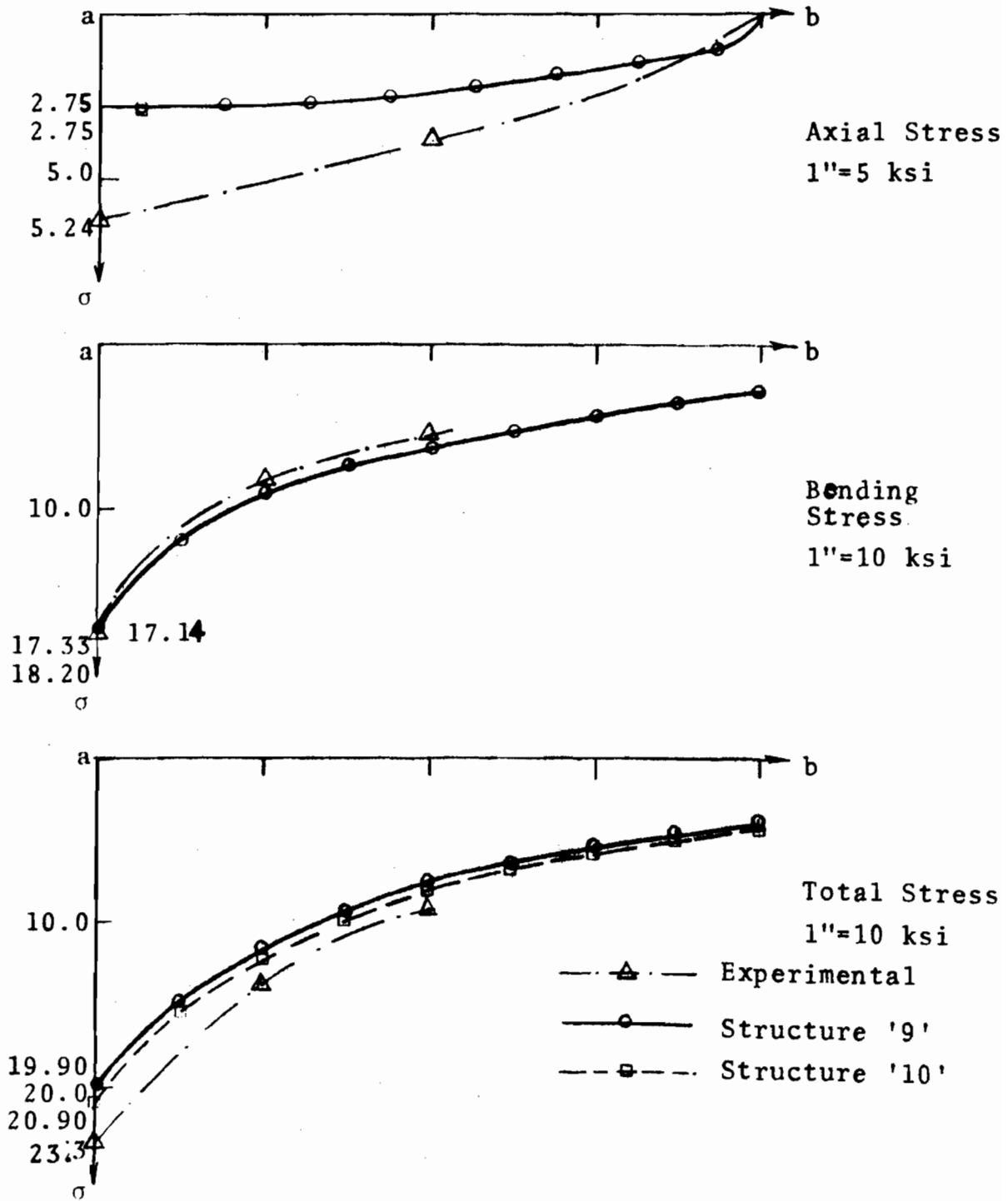


Fig. 4-26 Stresses in Tension Member (Structures '9' and '10')

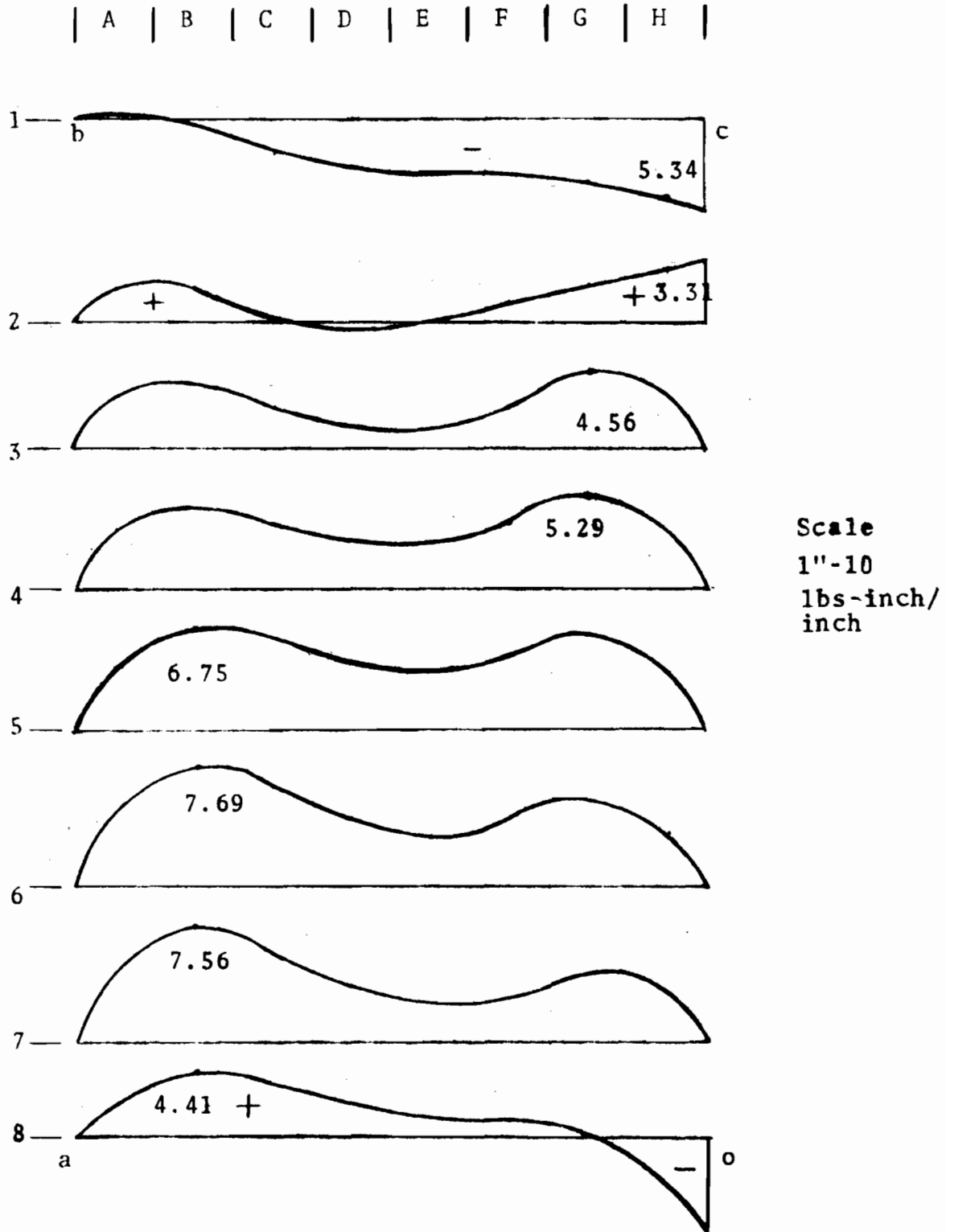


Fig. 4-27 Bending Moments M_y (Structure '9')

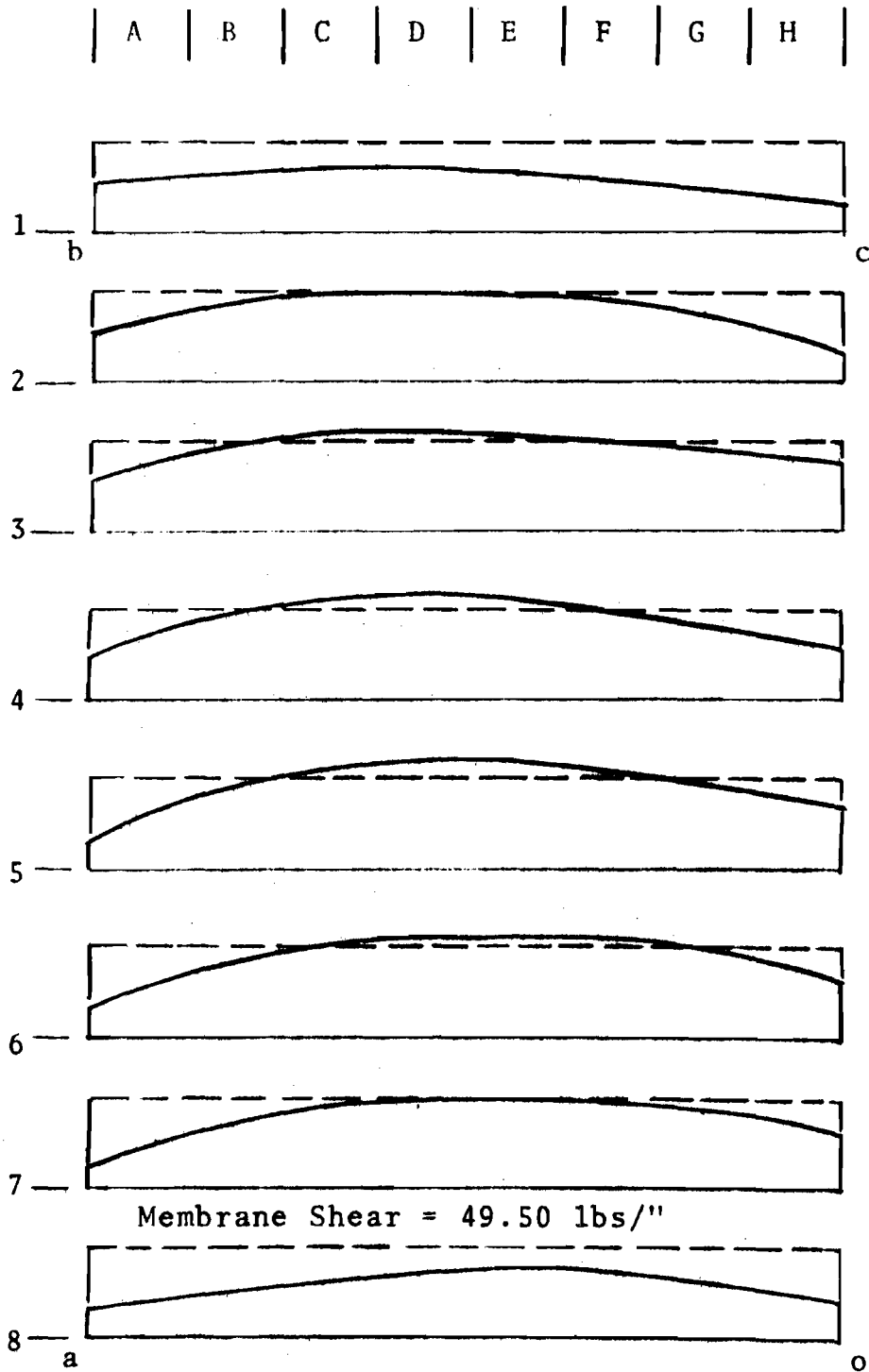
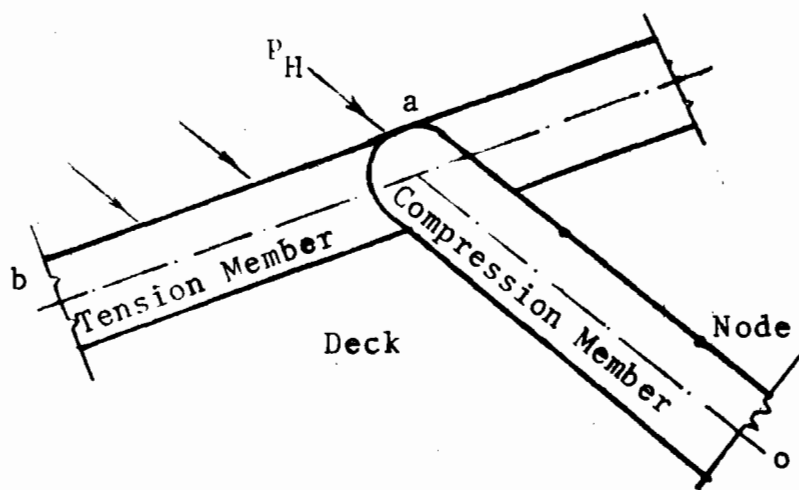
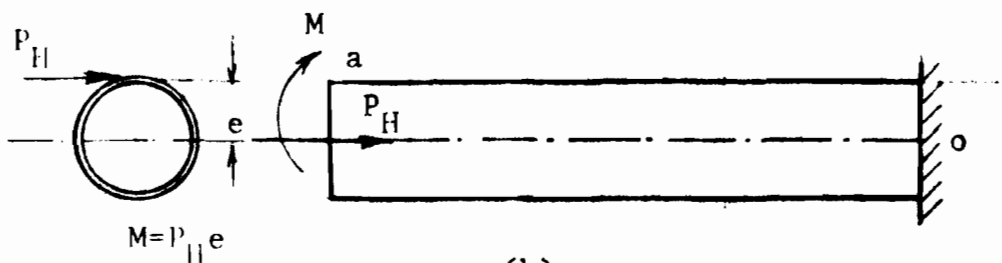


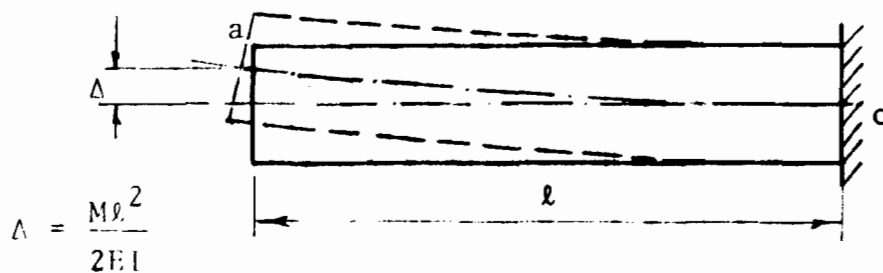
Fig. 4-28 Shear Force N_{xy} lbs/inch
(Structure '9')



(a)



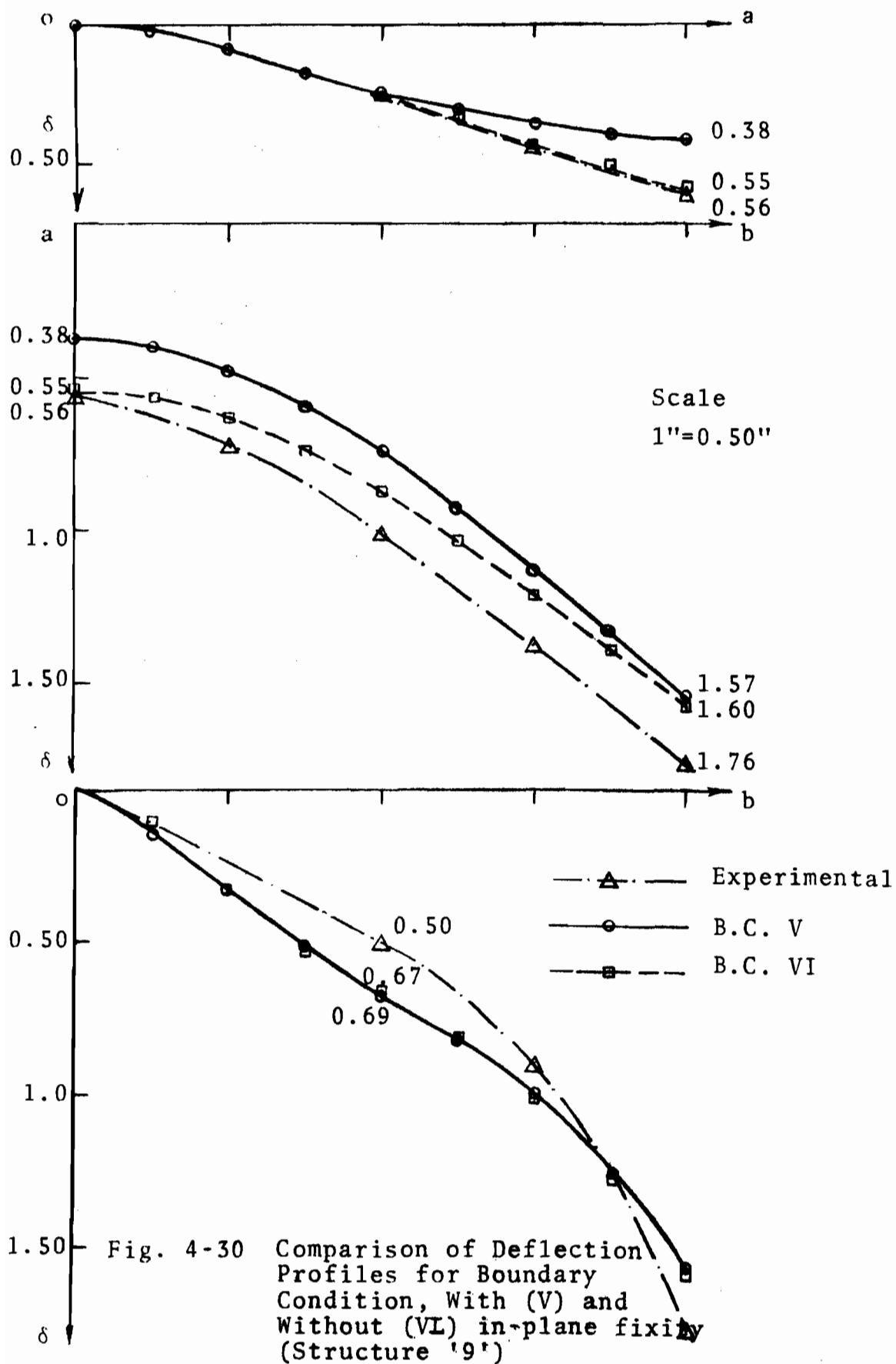
(b)



$$\Delta = \frac{Ml^2}{2EI}$$

(c)

Fig. 4-29 Effect of Eccentric Transfer of Force at a Junction of Tension and Compression Edge Members



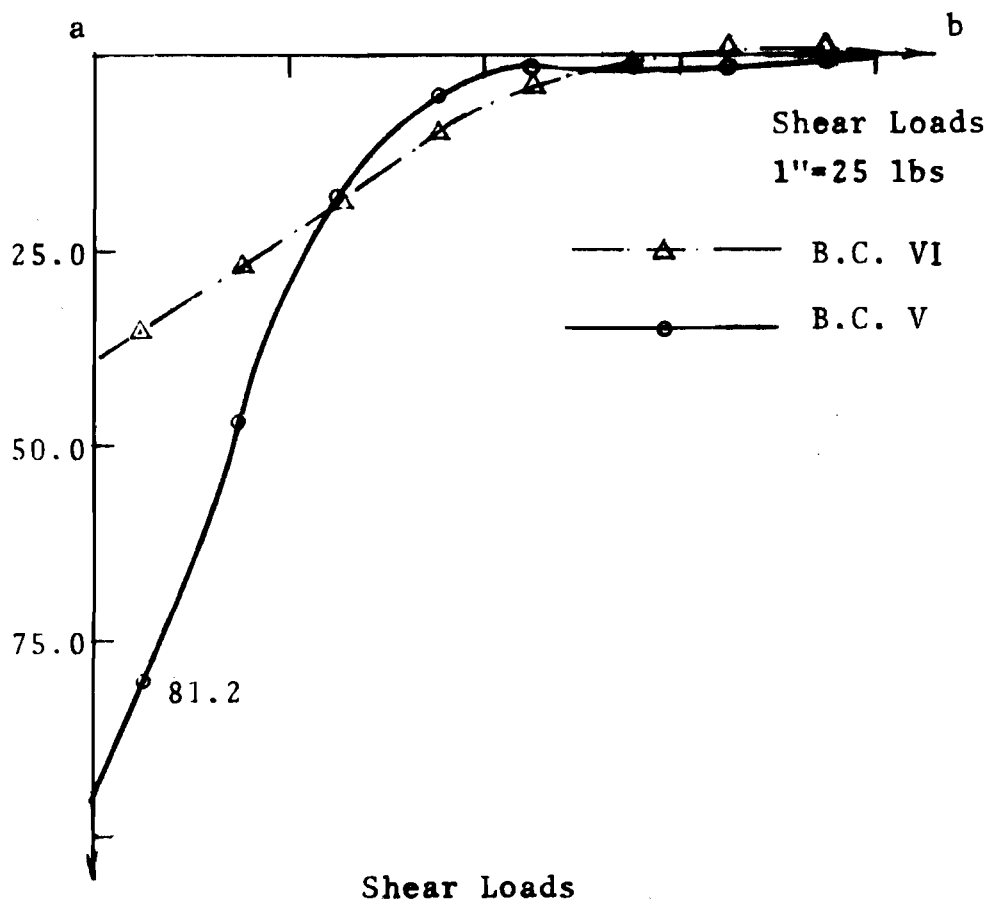
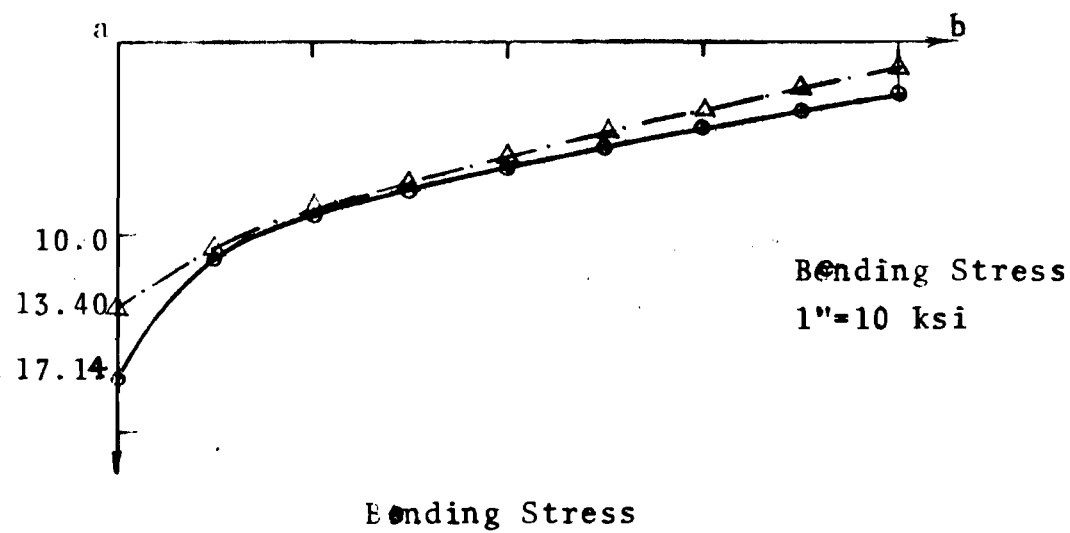


Fig. 4-31 Effect of in-plane Fixity on Bending Stress and Vertical Shearing Loads on the Tension Member (Structure '9')

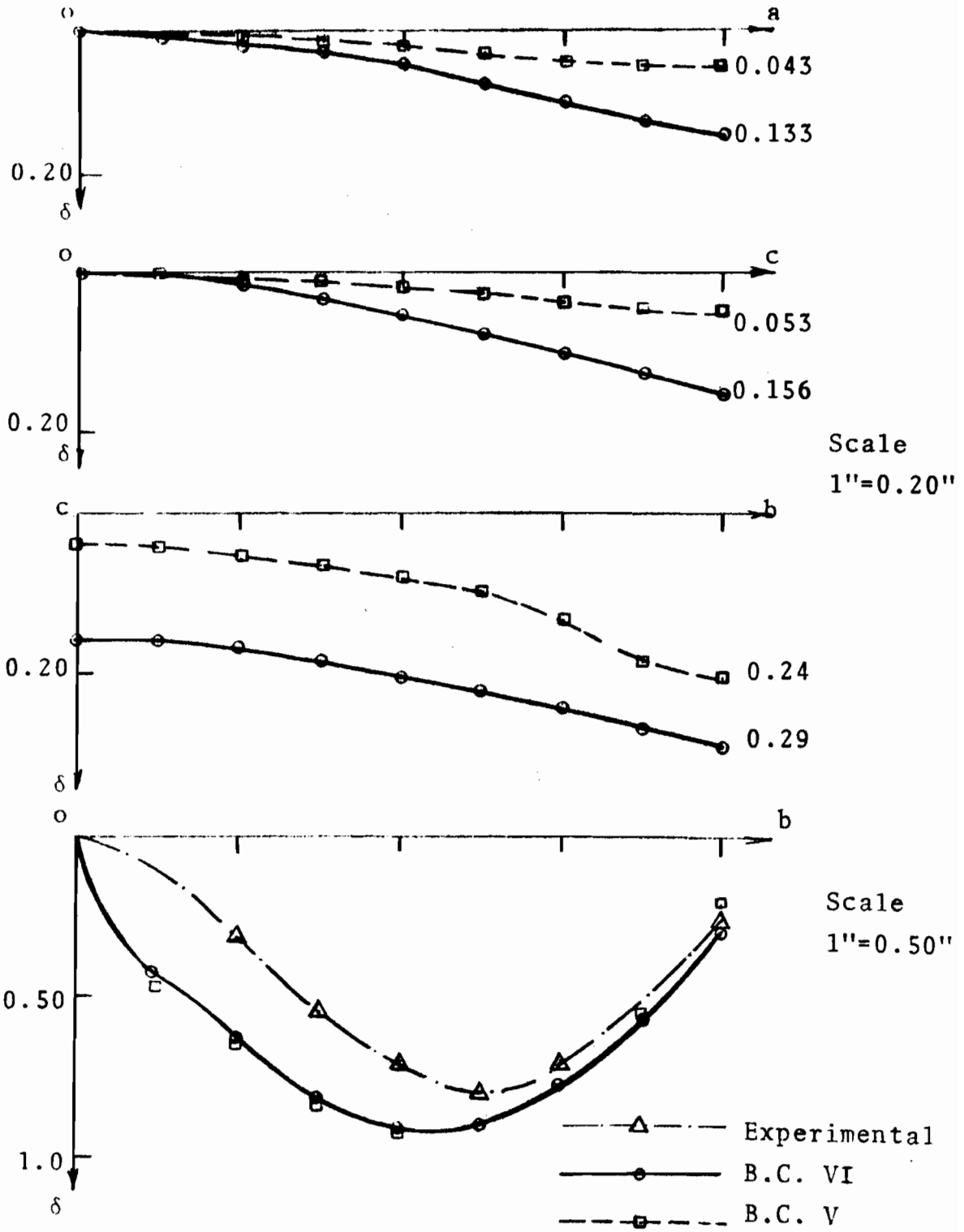


Fig. 4-32 Deflection Profiles
(Structure '11')

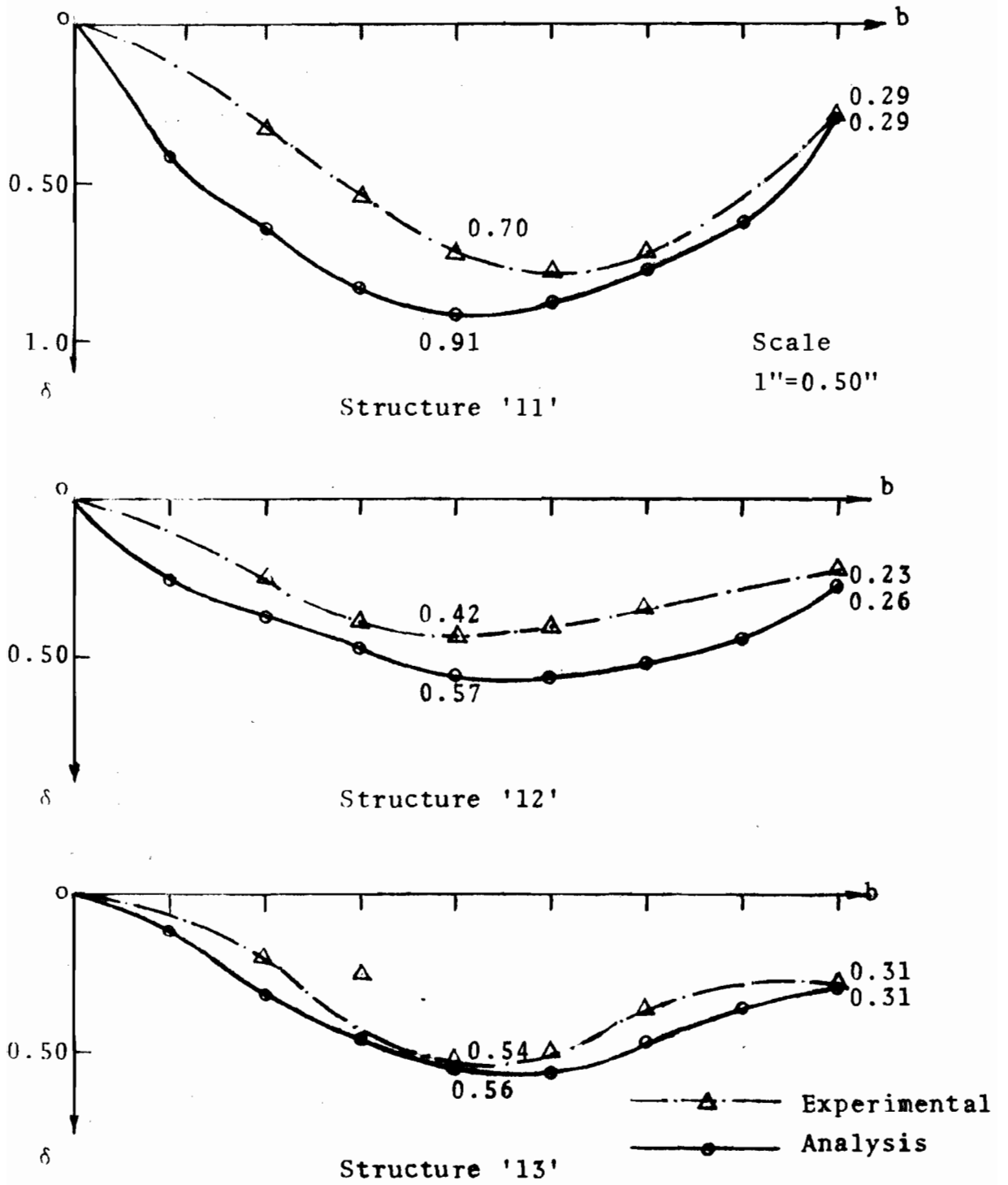


Fig. 4-33 Deflection Profiles (Structures '11', '12', '13')

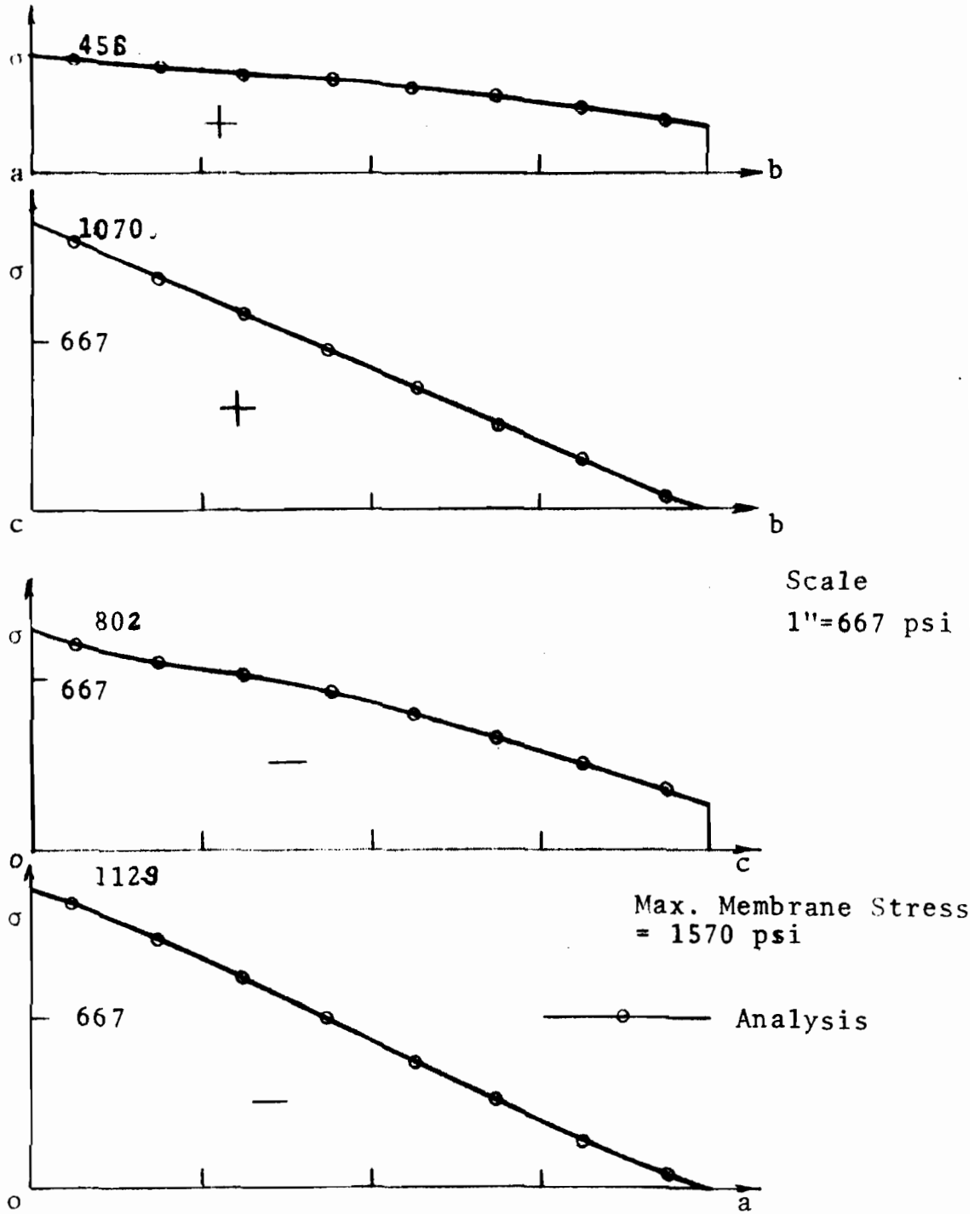


Fig. 4-34 Axial Stresses in Edge Members (Structure '11")

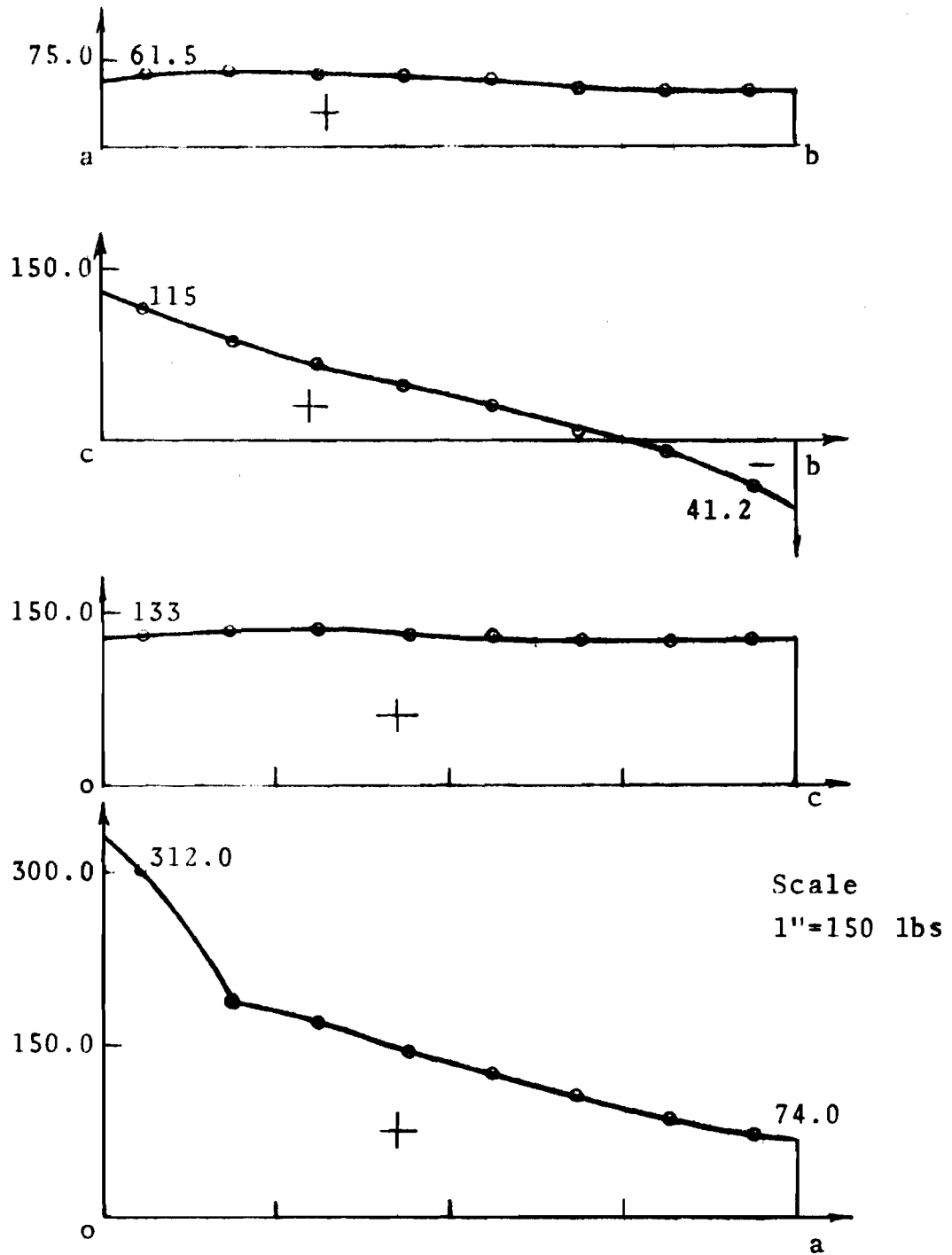
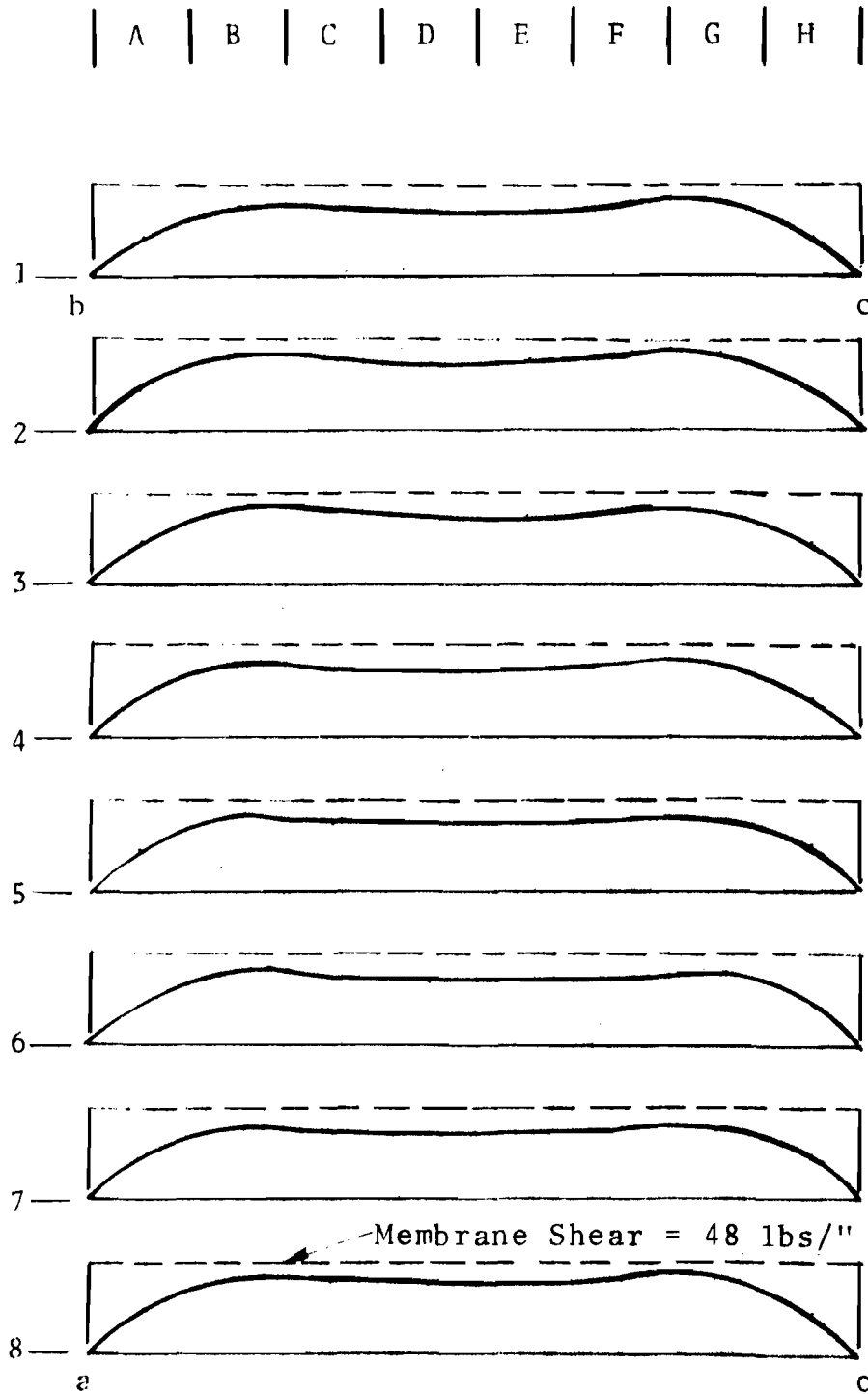


Fig. 4-35 Vertical Shear Force Diagrams (Structure '11')



Scale
1" = 100
lbs

Fig. 4-36 Shear Force N_{xy} lbs/inch
(Structure '11')

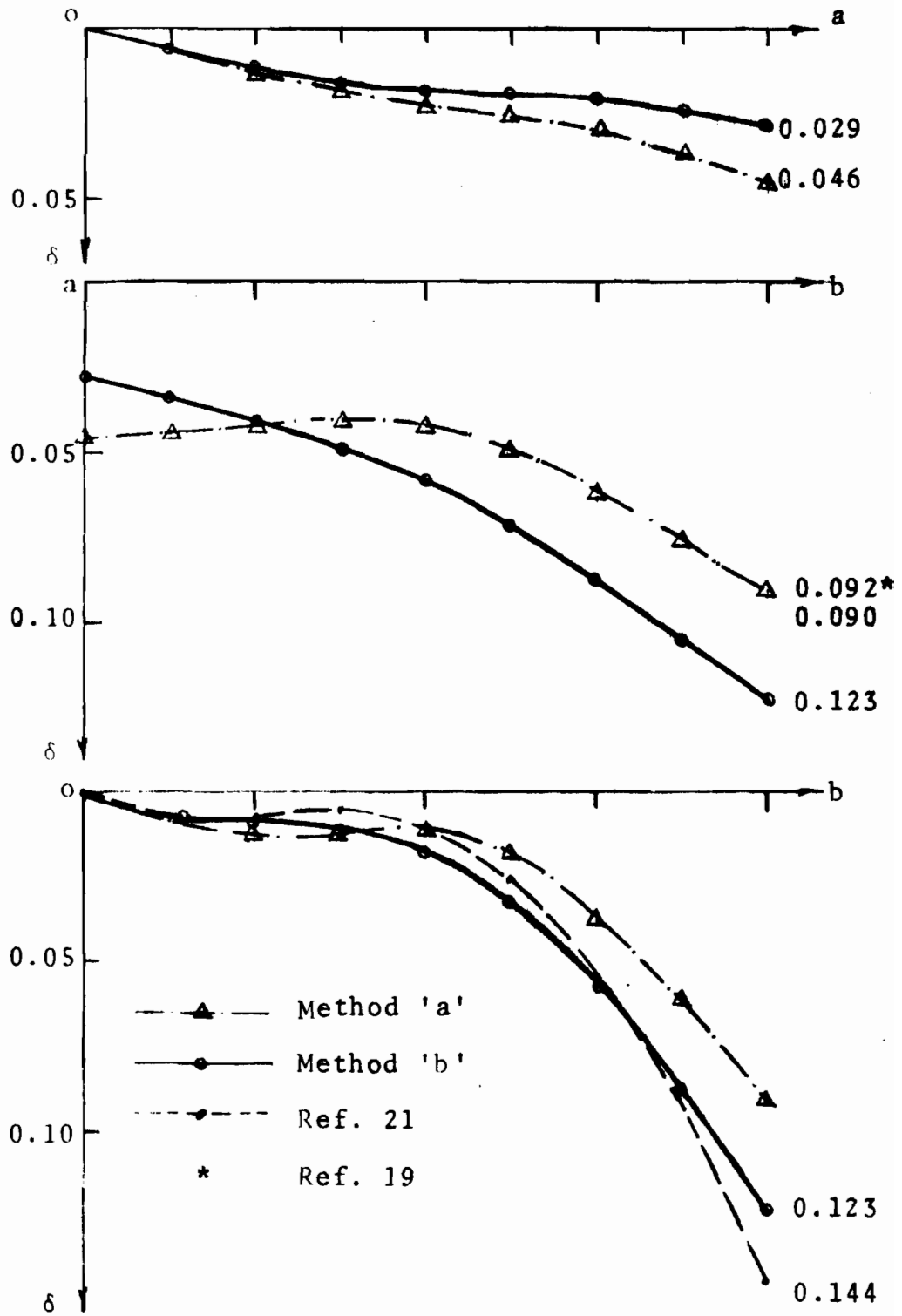
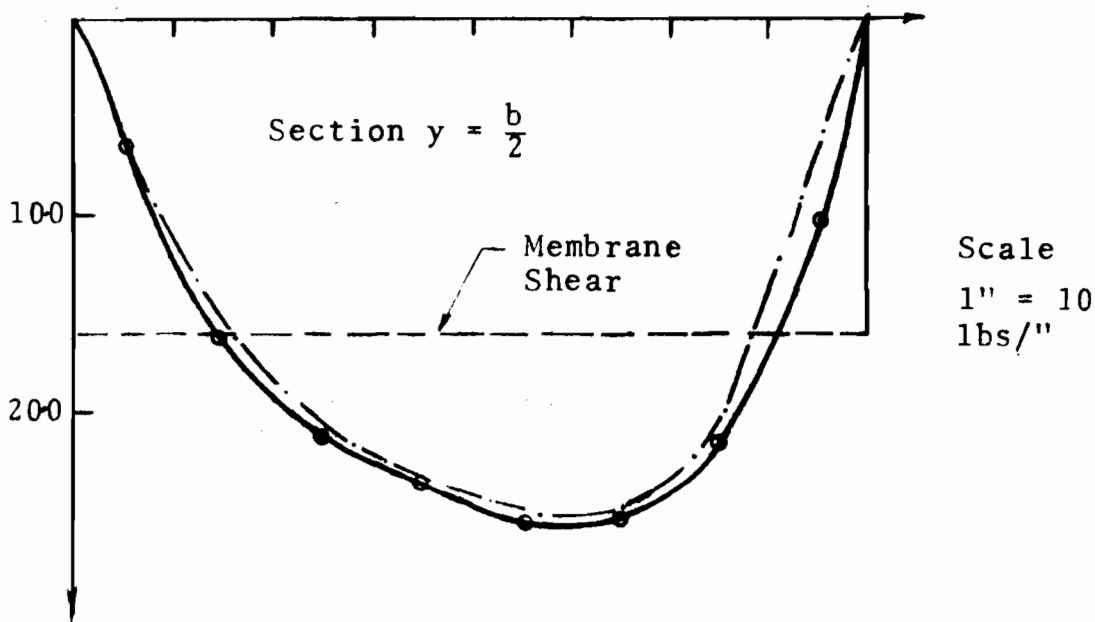
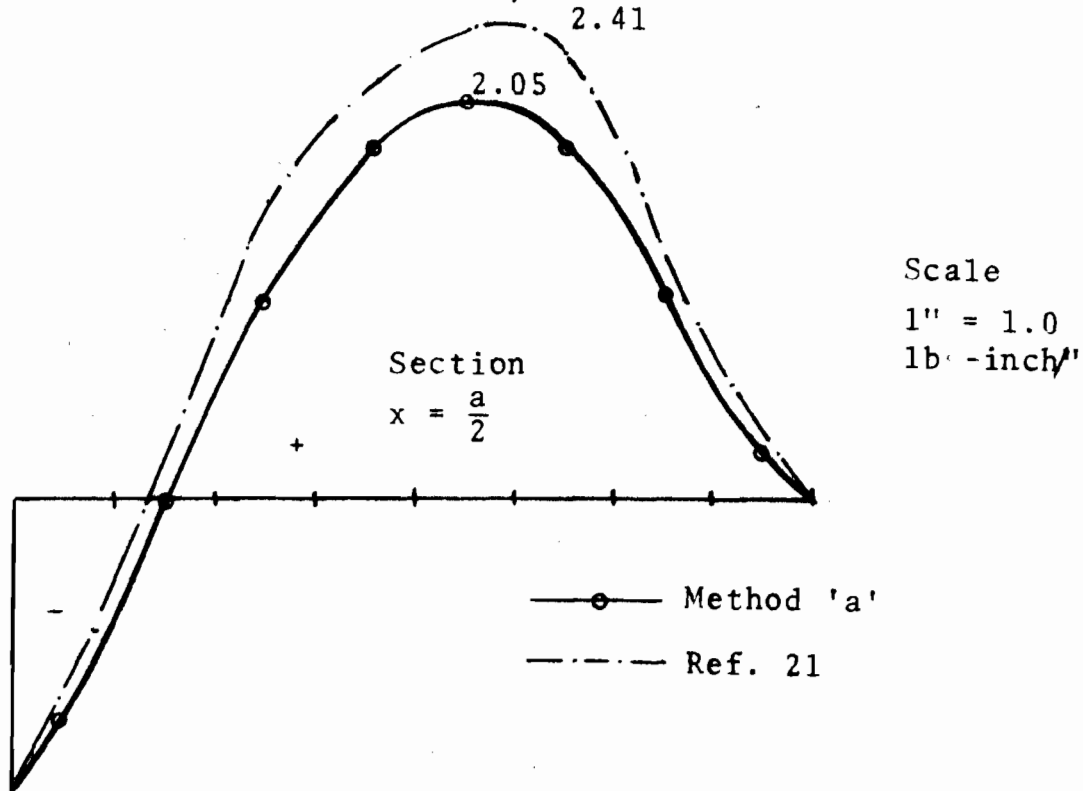


Fig. 4-37 Deflection Profiles
(Structure '15')



(a) Shear Force N_{xy} lbs/inch



(b) Bending Moment M_y lbs·inch/inch

Fig. 4-38 Shear Force and Moments
(Structure '15')

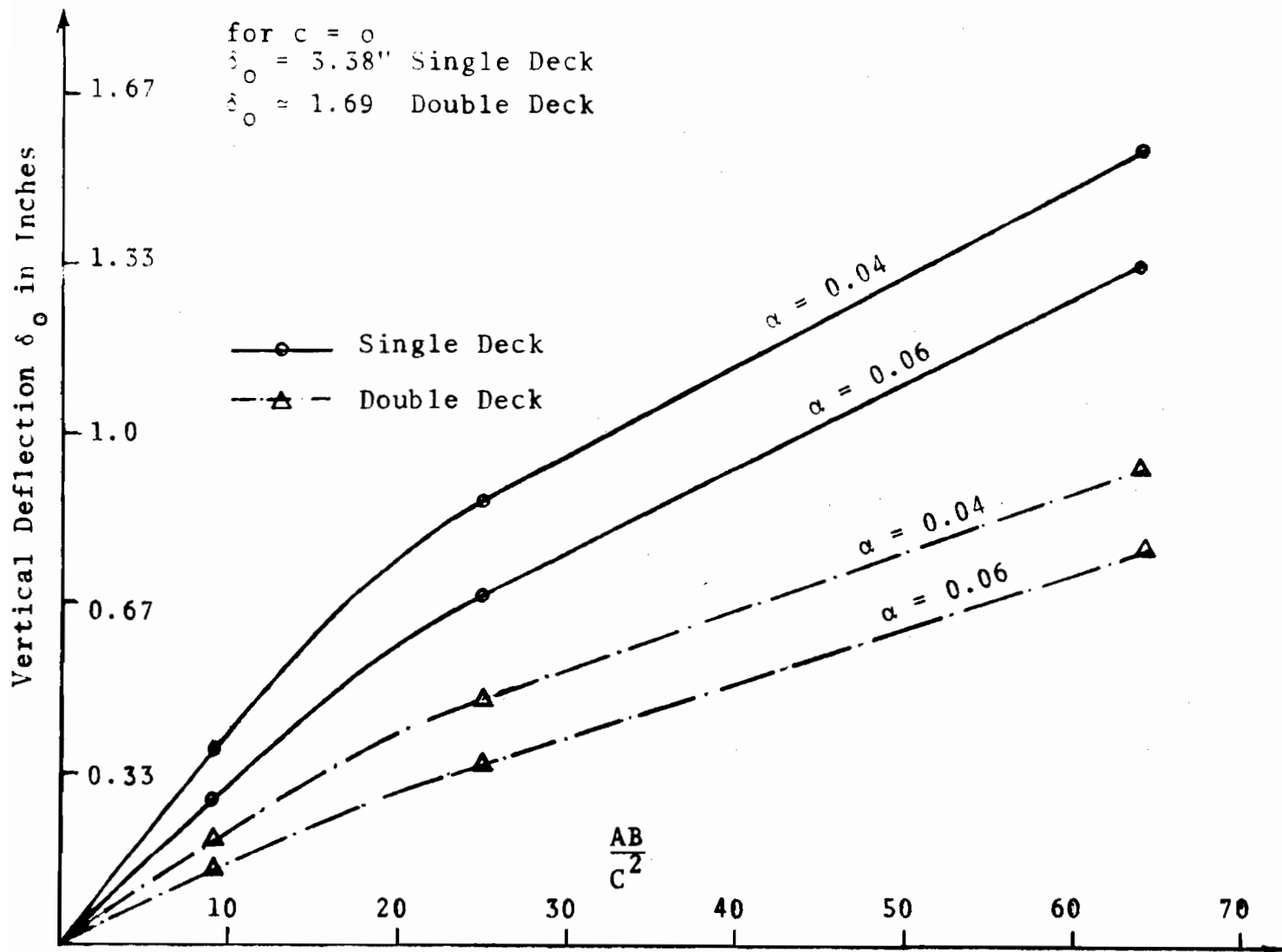


Fig. 5-1 Central Deflection ' δ_0 ' vs AB/C^2 (Structures '3' and '4')

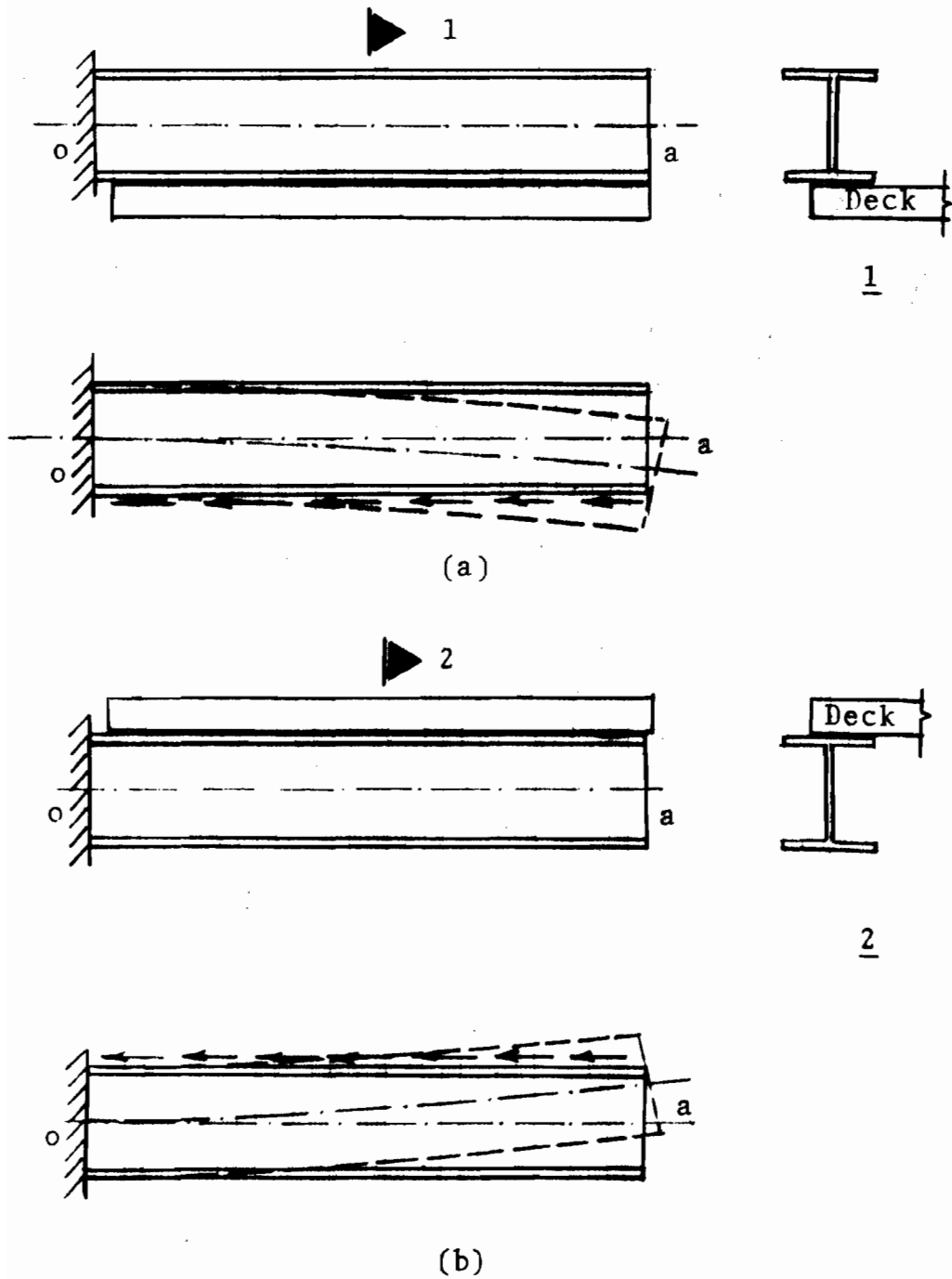


Fig. 5-2 Effect of Eccentric Connections Between Deck and Edge Member

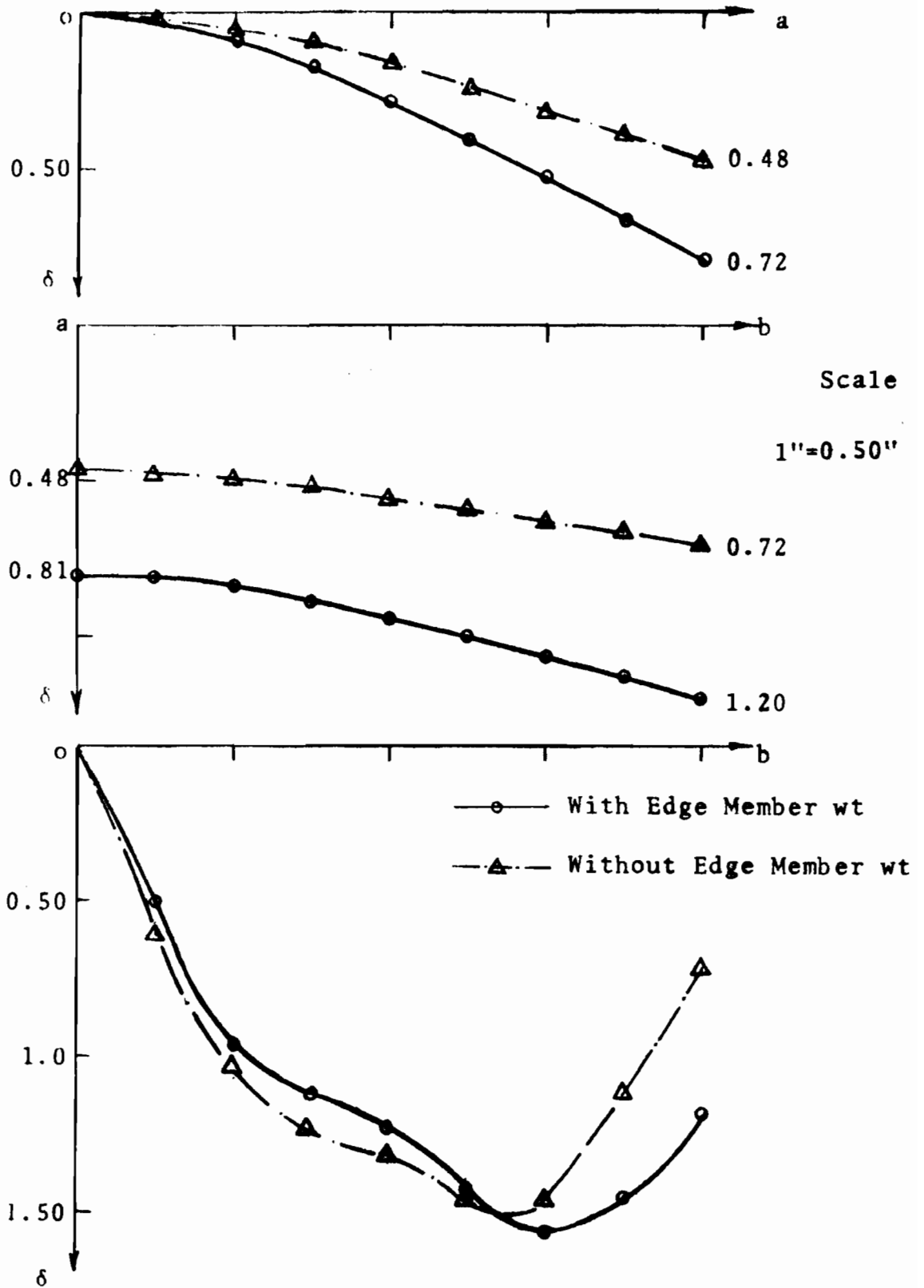
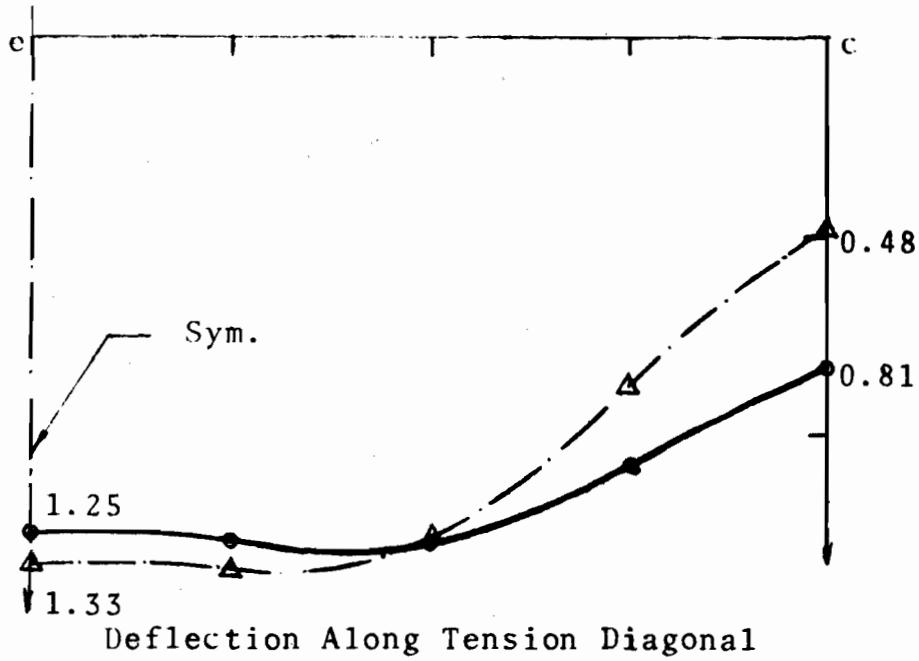
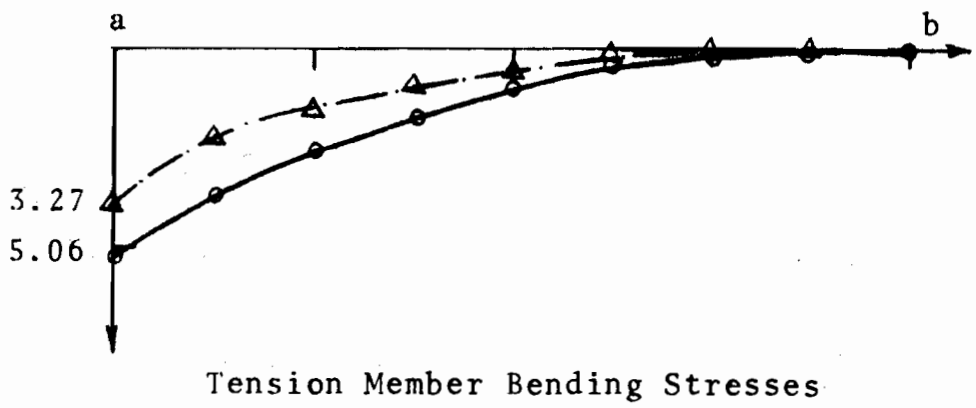


Fig. 5-3 Effect of Edge Member Weight on Deflections (Structure '14')



Scale
1"=0.50"



Scale
1"=5 ksi

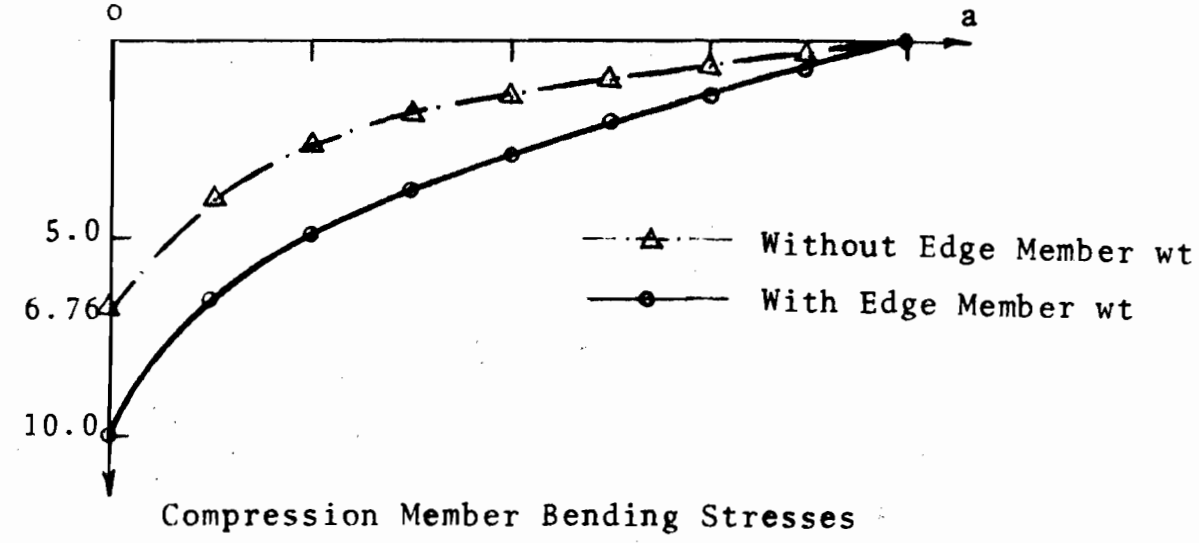


Fig. 5-4 Effect of Edge Member Weight on Deflection and Bending Stresses

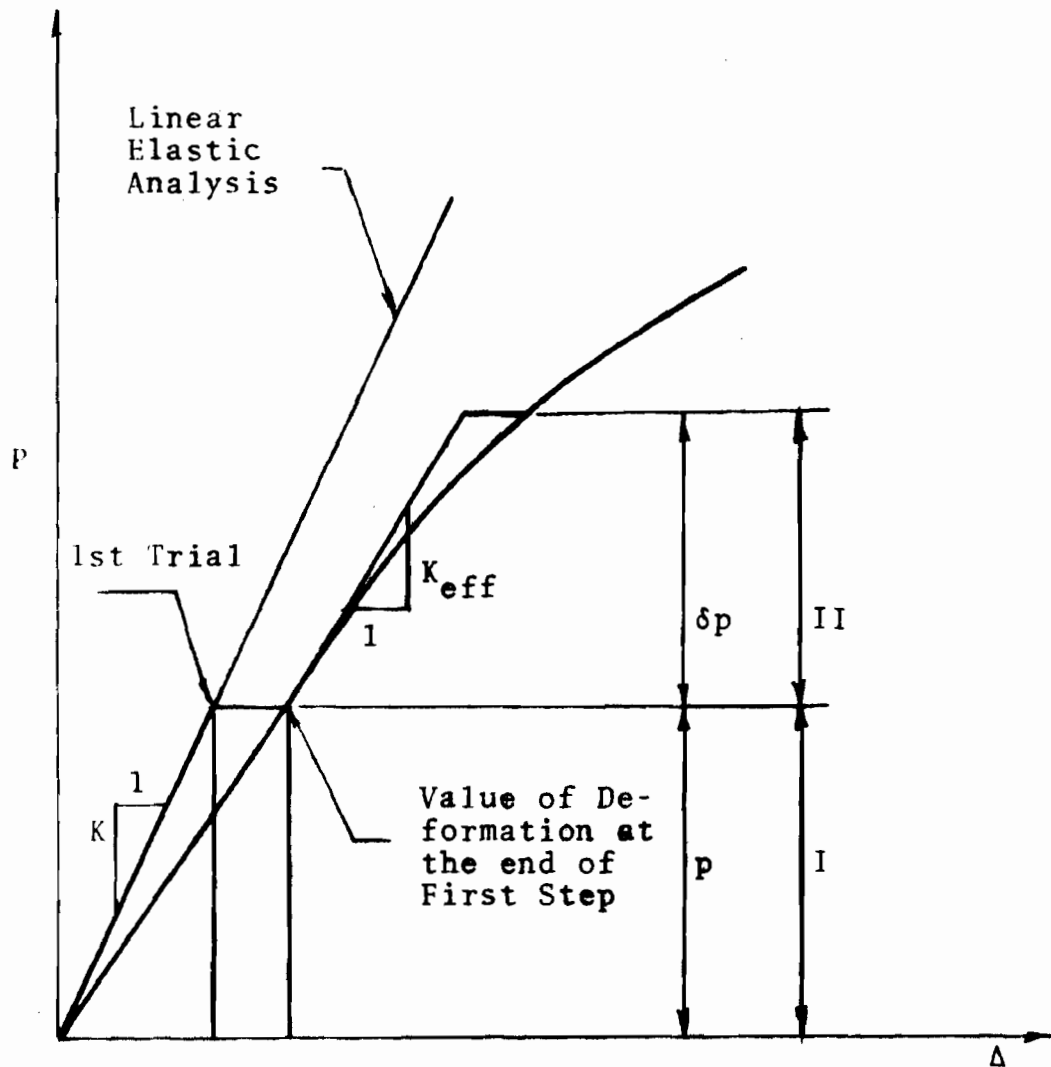


Fig. 6-1 Load Incrementation Method

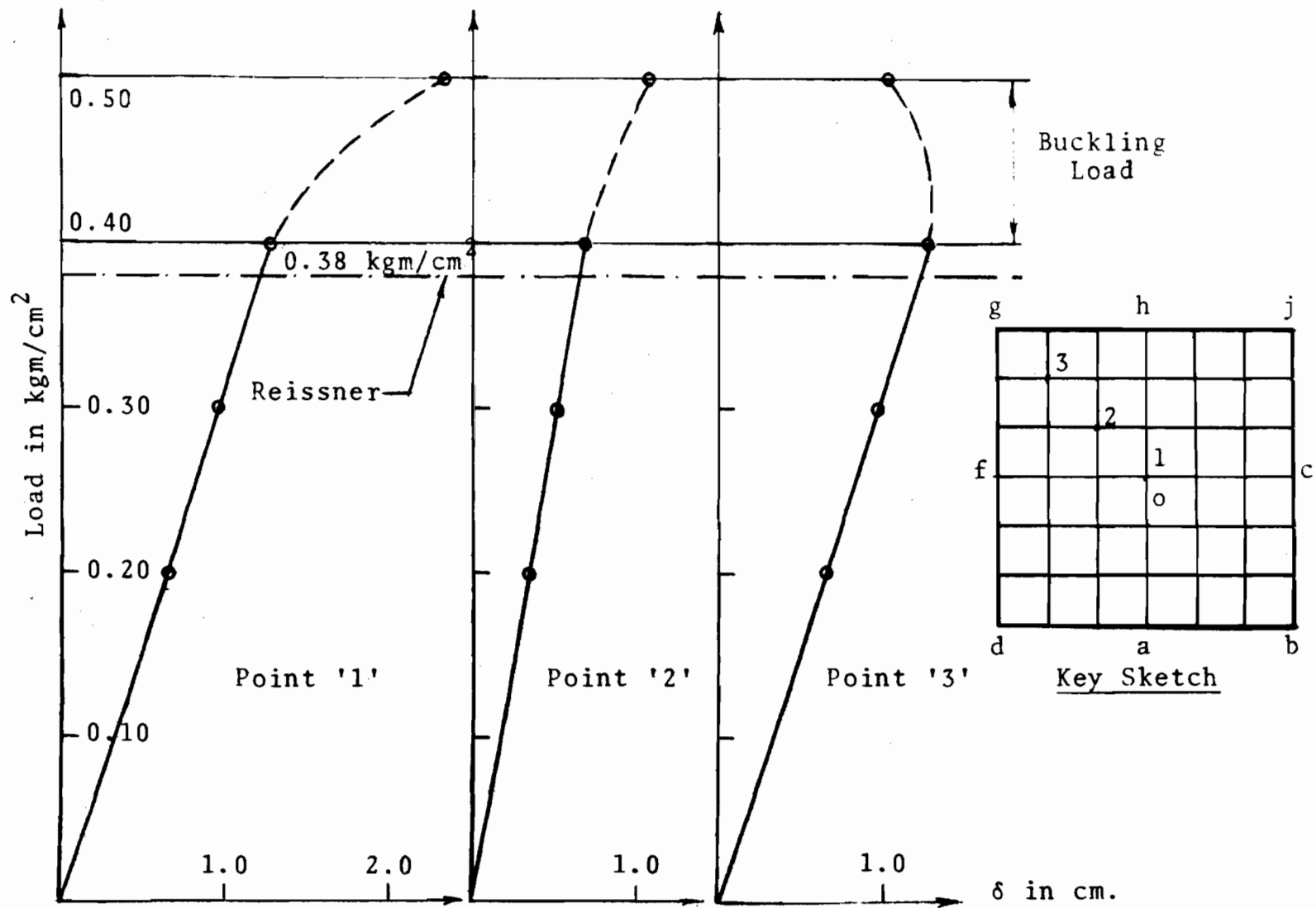
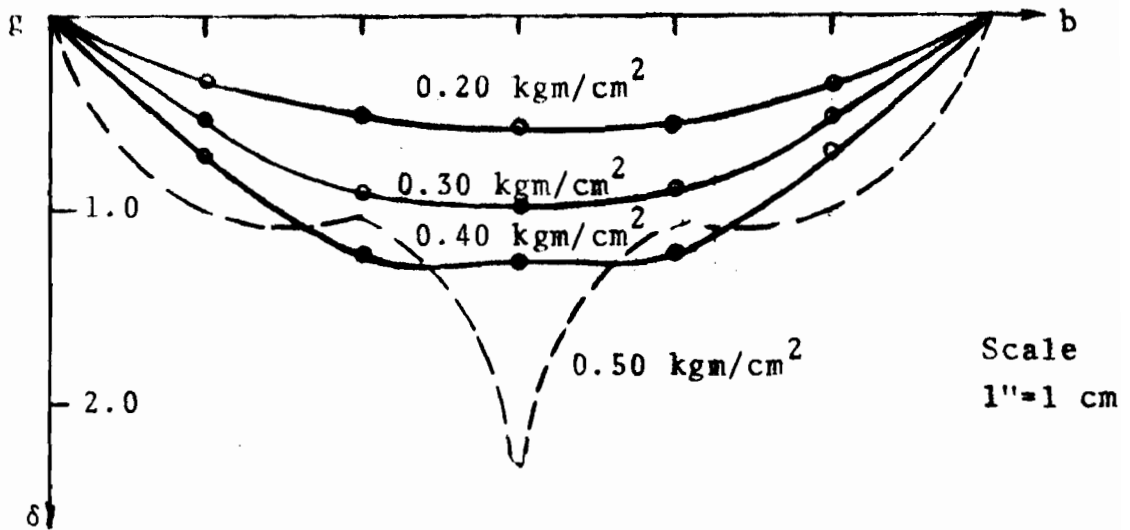
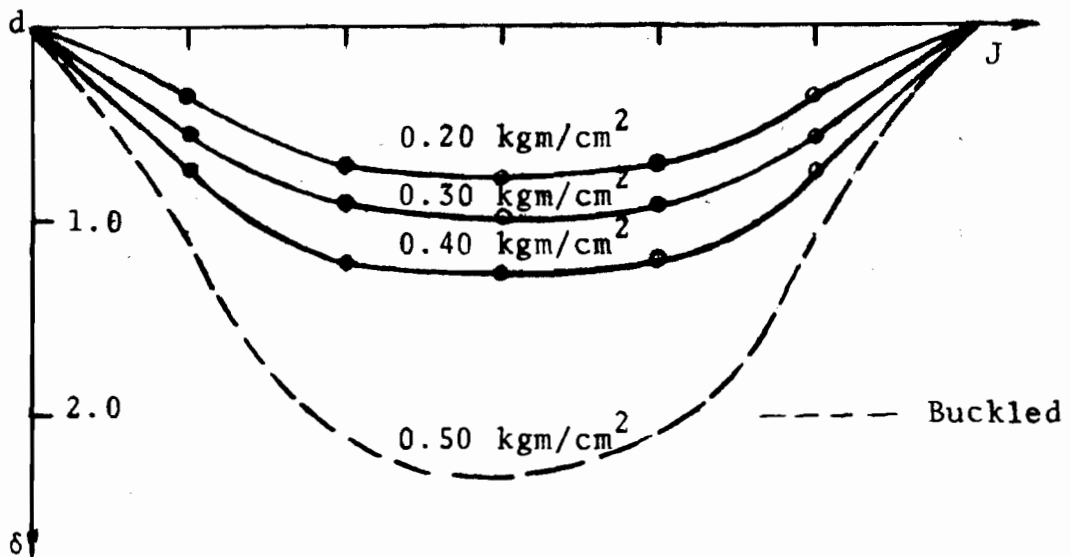


Fig. 6-2 Buckling of an Isotropic Hypar (Structure '1' Table IV-1)



Compression Diagonal 'gb'



Tension Diagonal 'dJ'

Fig. 6-3 Buckling of Structure '1' (Table IV-1)

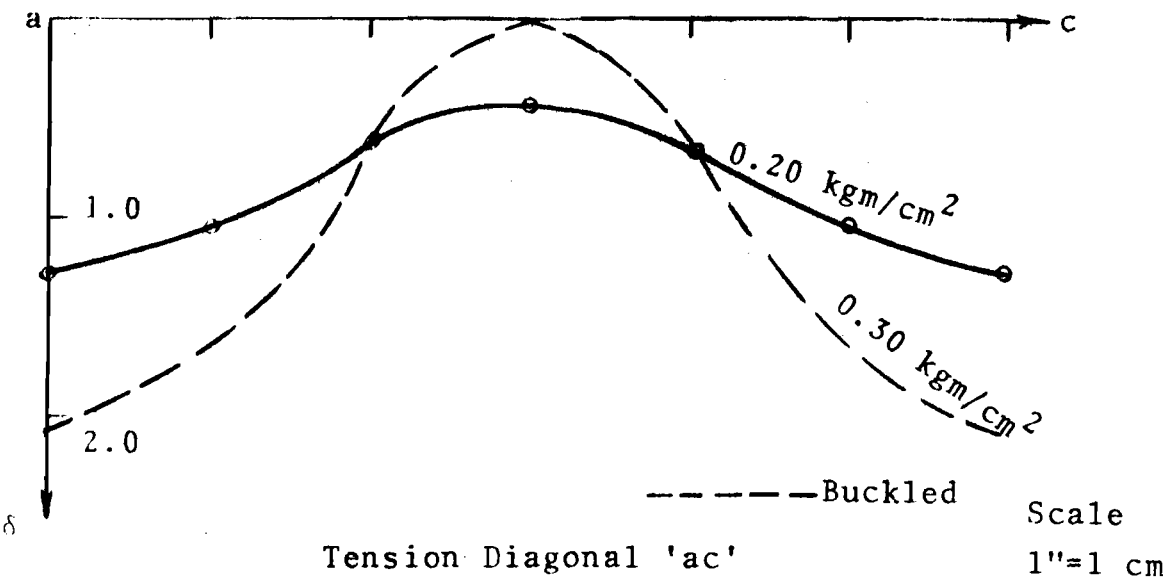
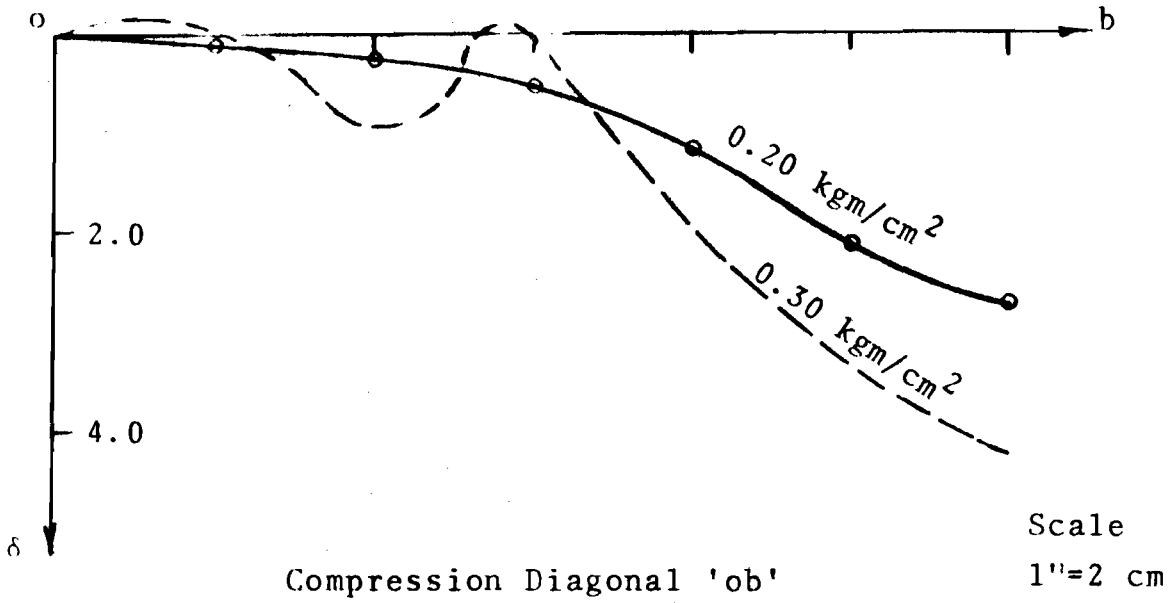


Fig. 6-4 Buckling of an Isotropic Umbrella Shell (Edge Member Sizes 6cmx3cm)

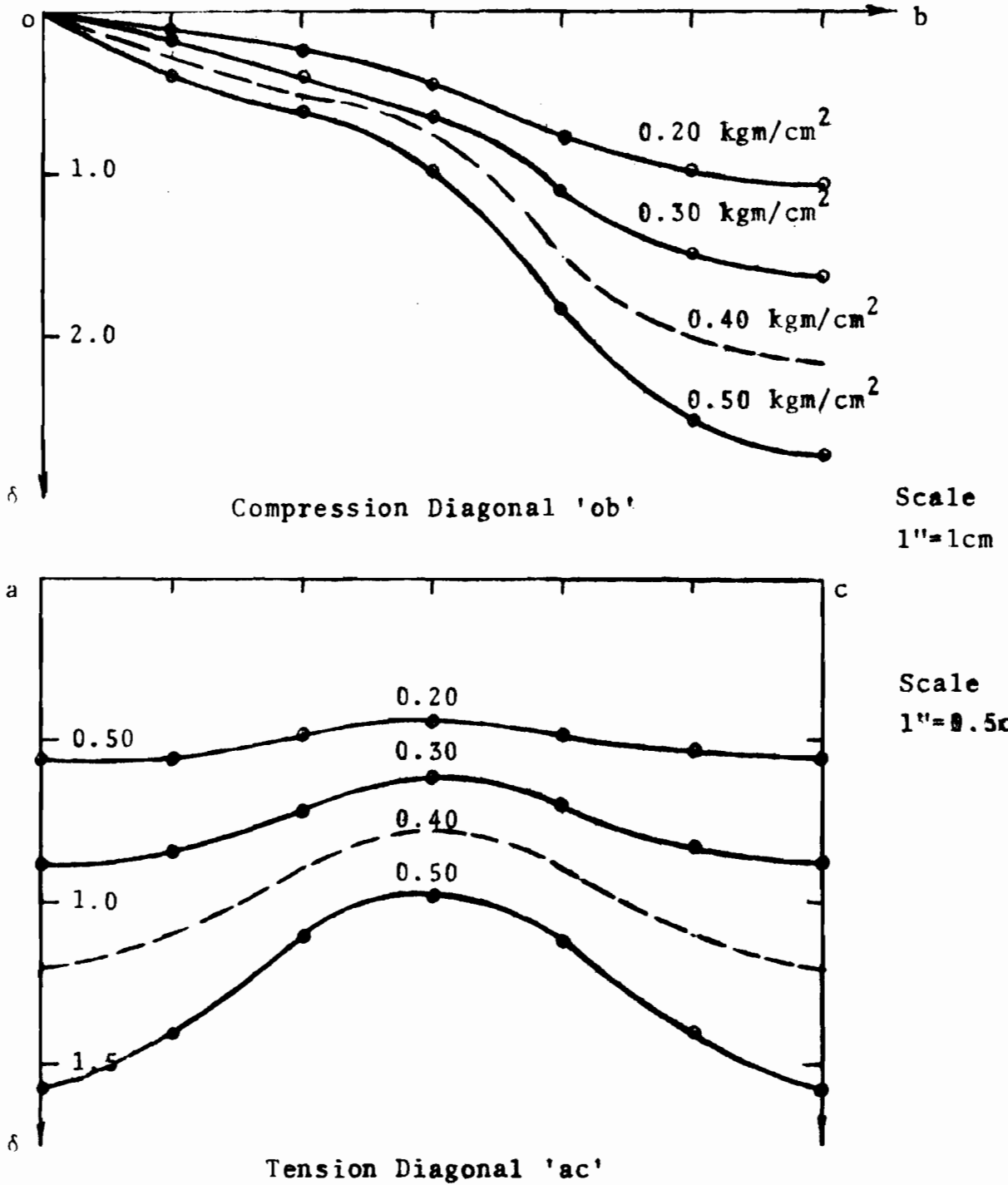


Fig. 6-4 Buckling of an Isotropic Umbrella Shell
(Edge Member Areas = 108 cm²)

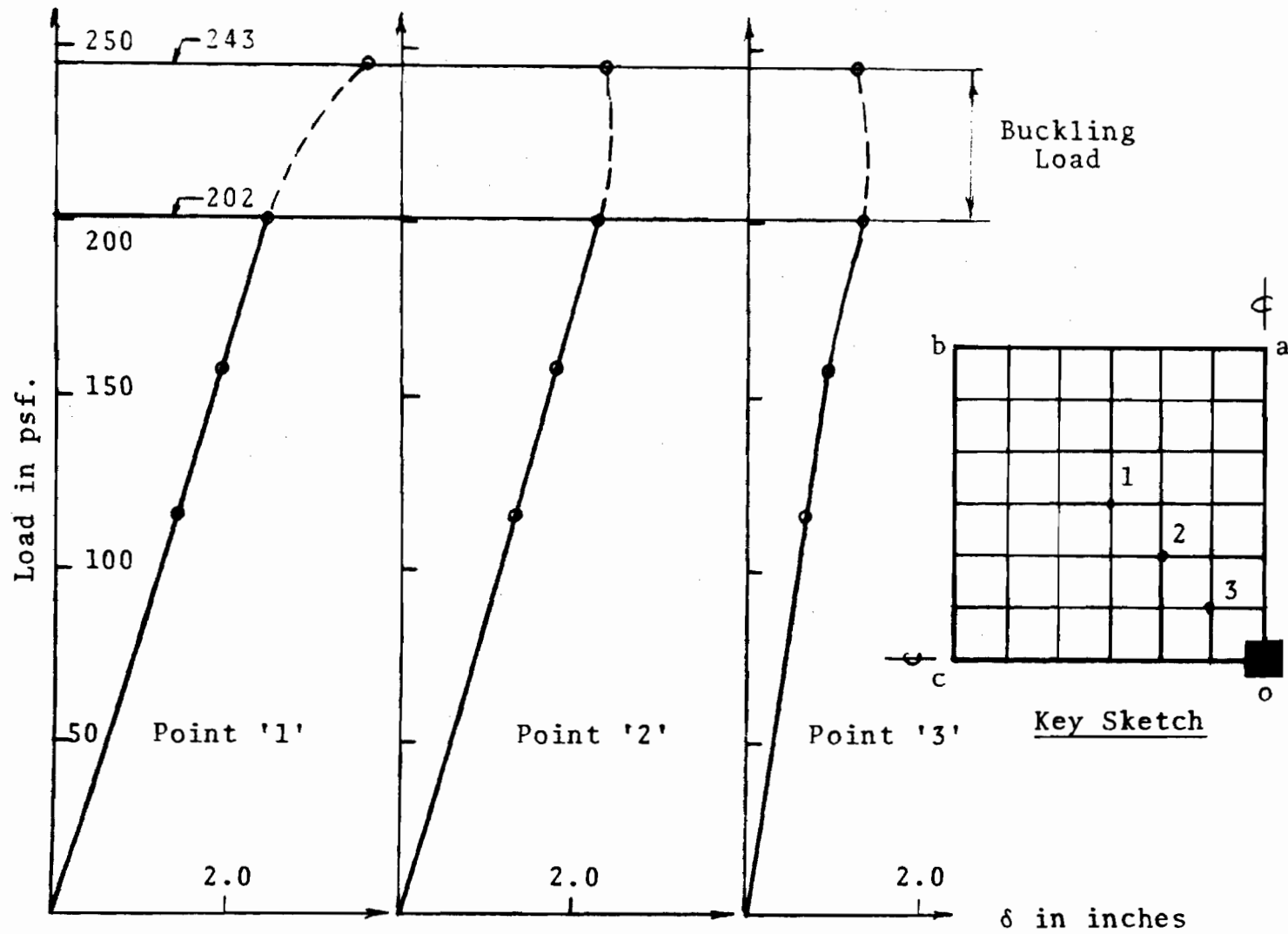


Fig. 6-6 Buckling of a 28G Double Layer All-Supported Hypar (Structure '13')

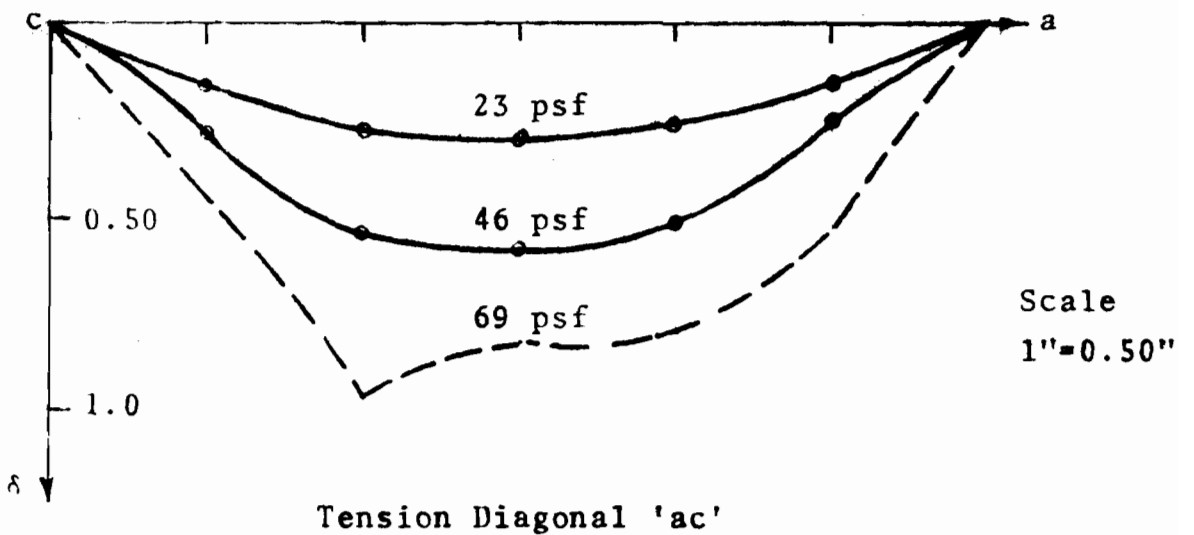
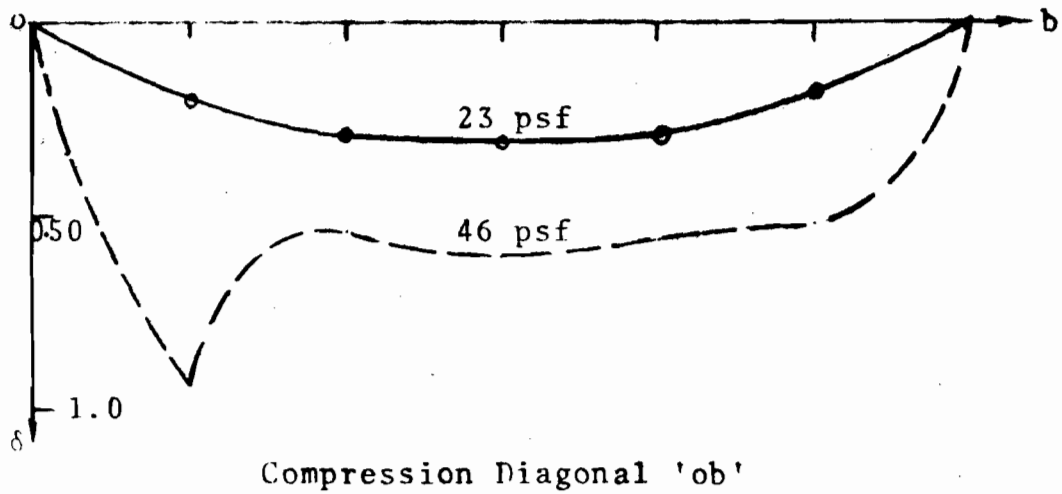
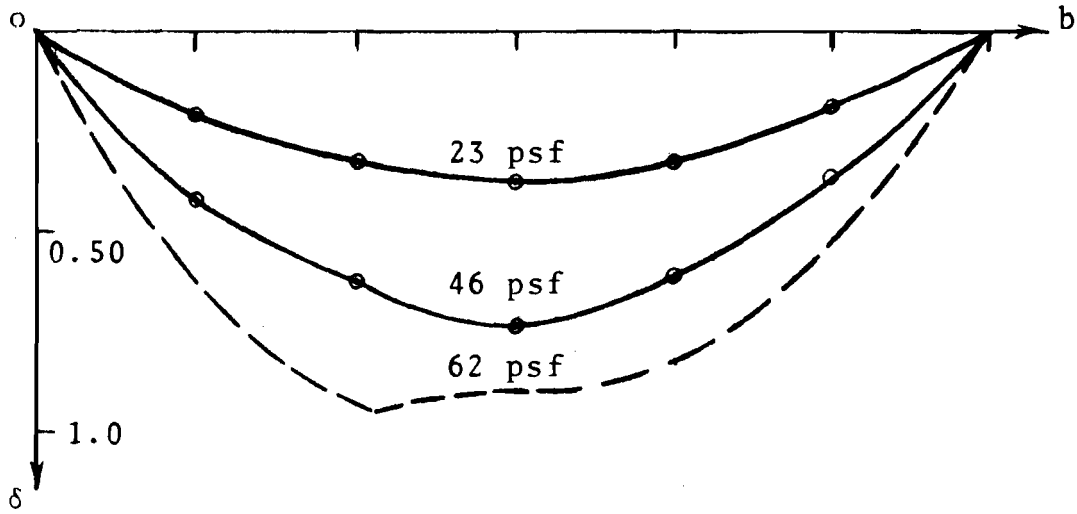
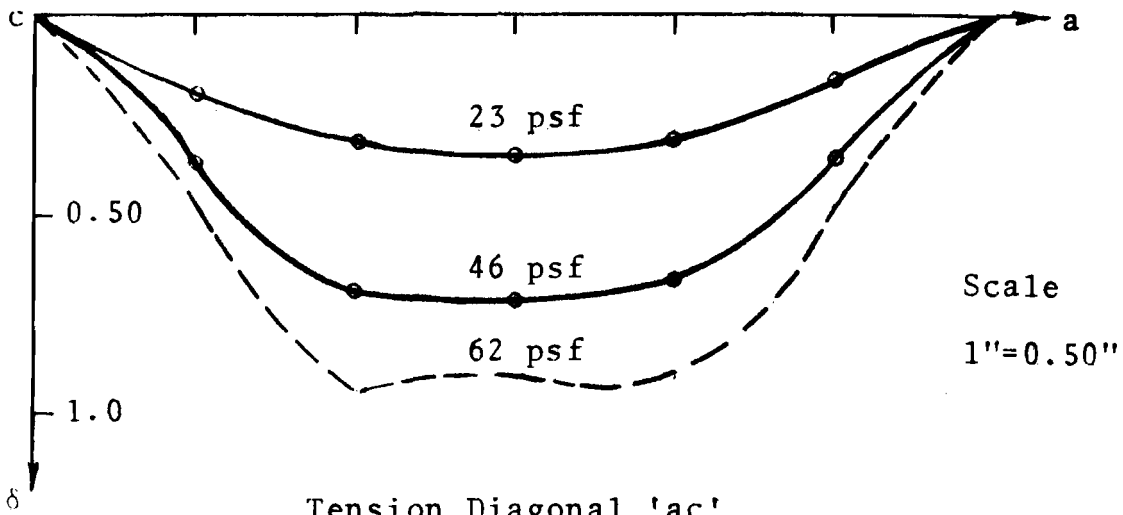


Fig. 6-7 Buckling of a 24G Single Deck All-Supported Hypar (Structure '12')

Note: Results With Flat Elements



Compression Diagonal 'ob'



Tension Diagonal 'ac'

Fig. 6-8 Buckling of a 24G Single Deck All-Supported Hypar (Structure '12')

Note: Results with Curved Elements

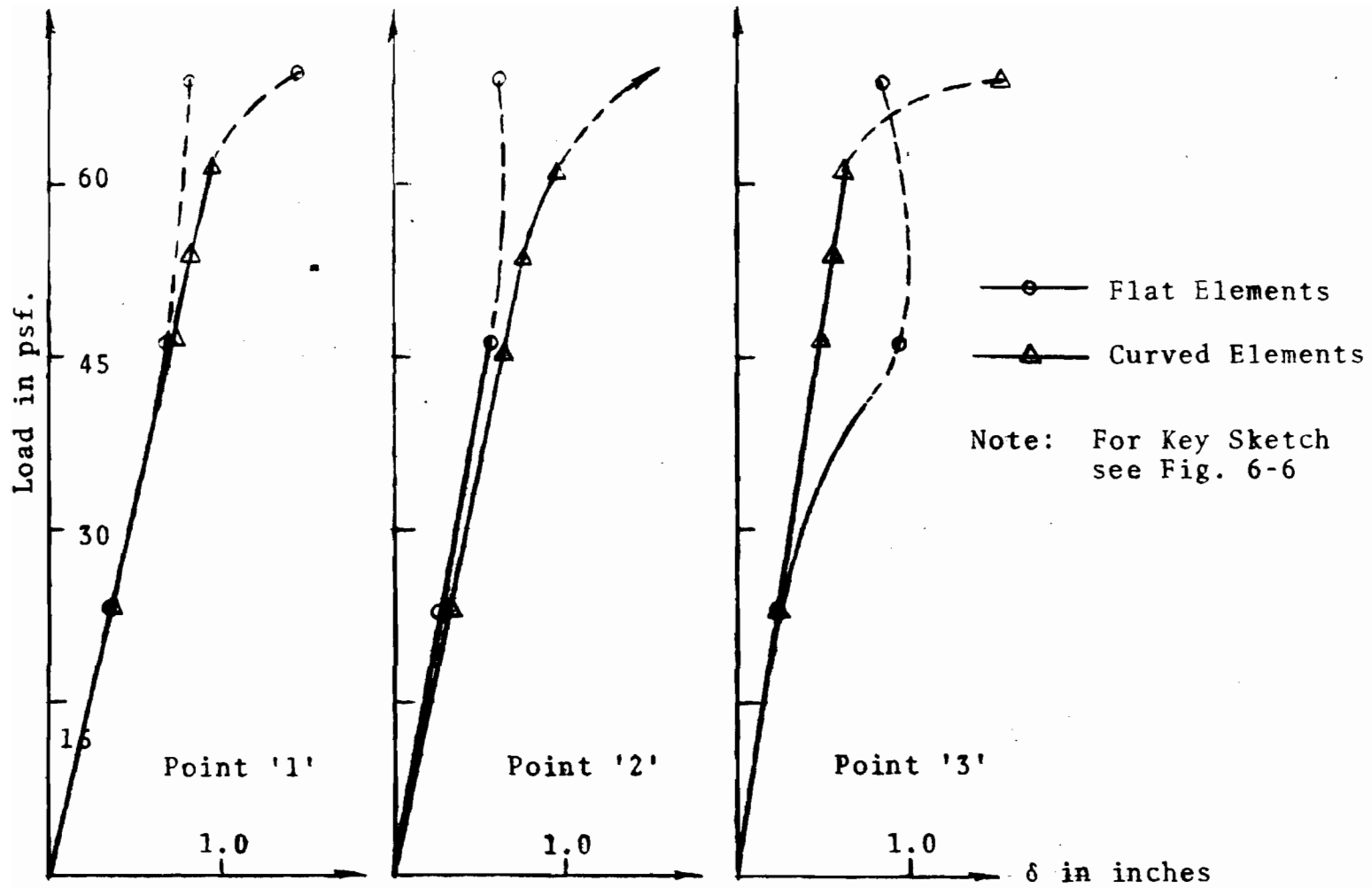


Fig. 6-9 Buckling of a 24G Single Deck All-Supported Hypar (Structure '12')

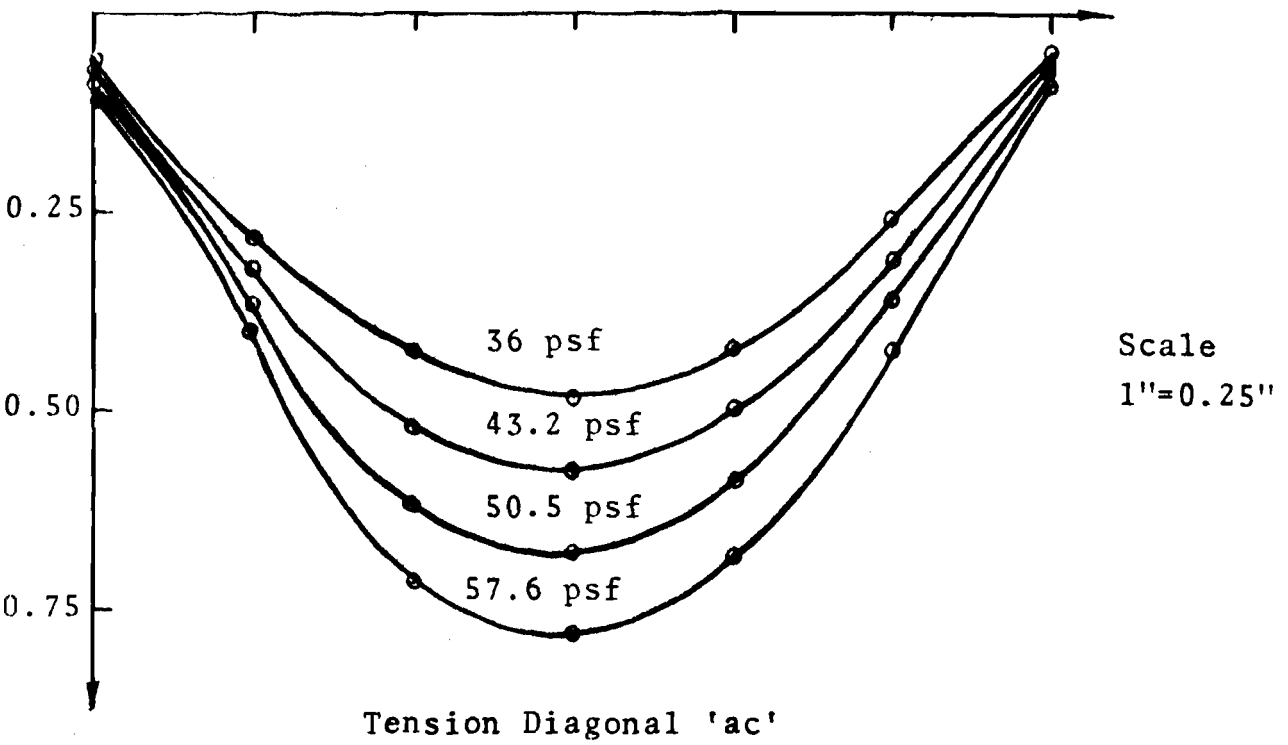
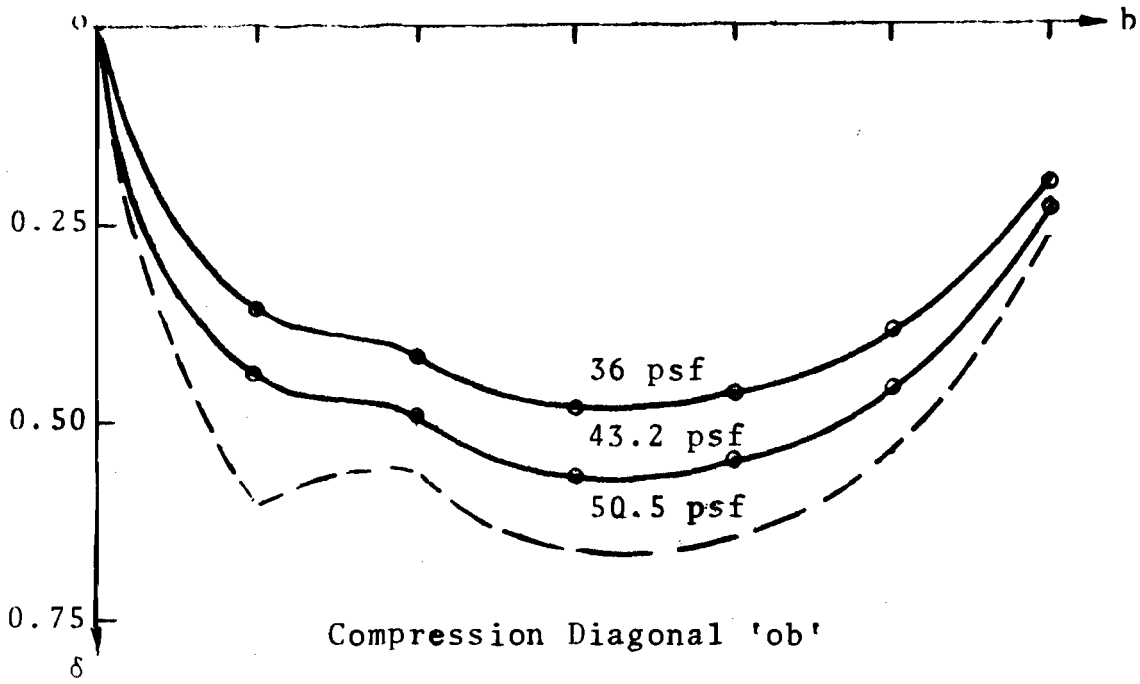


Fig. 6-10 Deflection Profiles Along Tension and Compression Diagonals (Structure '12')

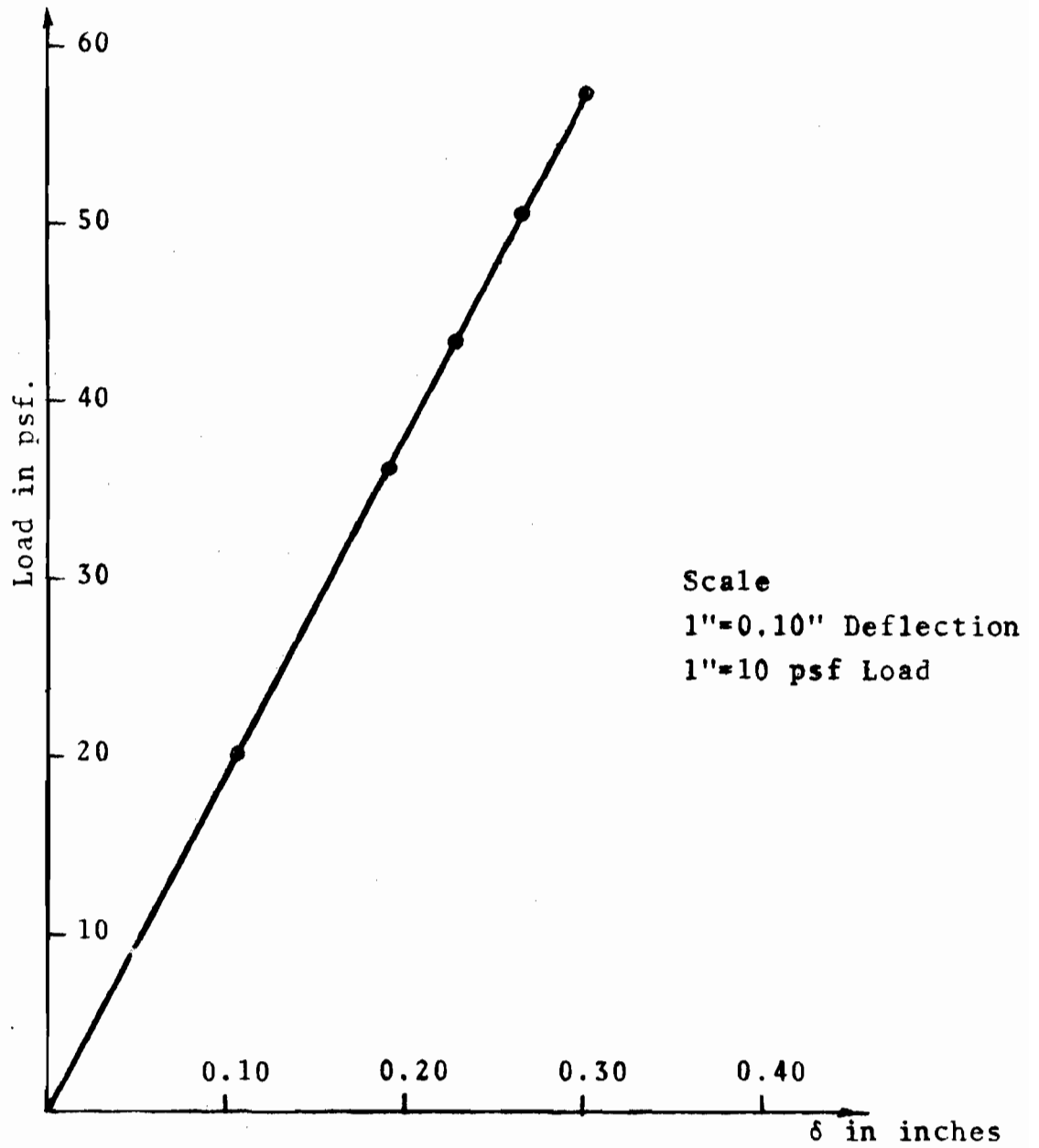


Fig. 6-11 Load vs Free Corner Deflection ' δ_b '
(Structure '12')

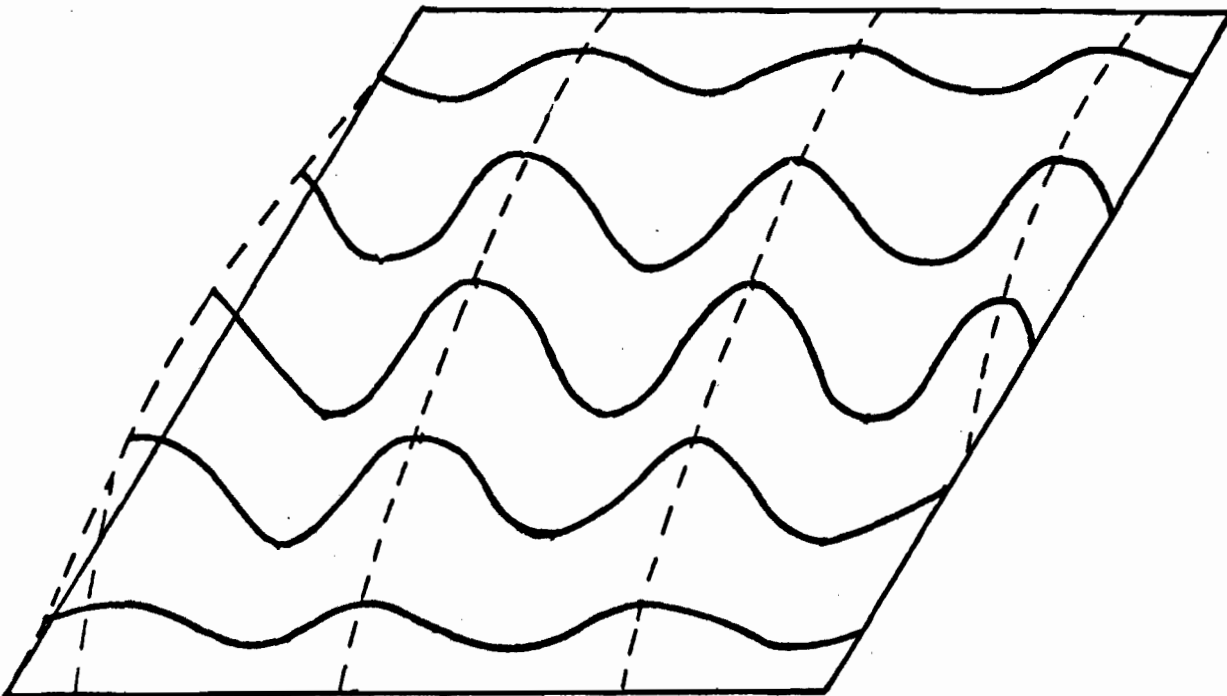


Fig. 6-12 Deck Buckling from Energy Method Analysis

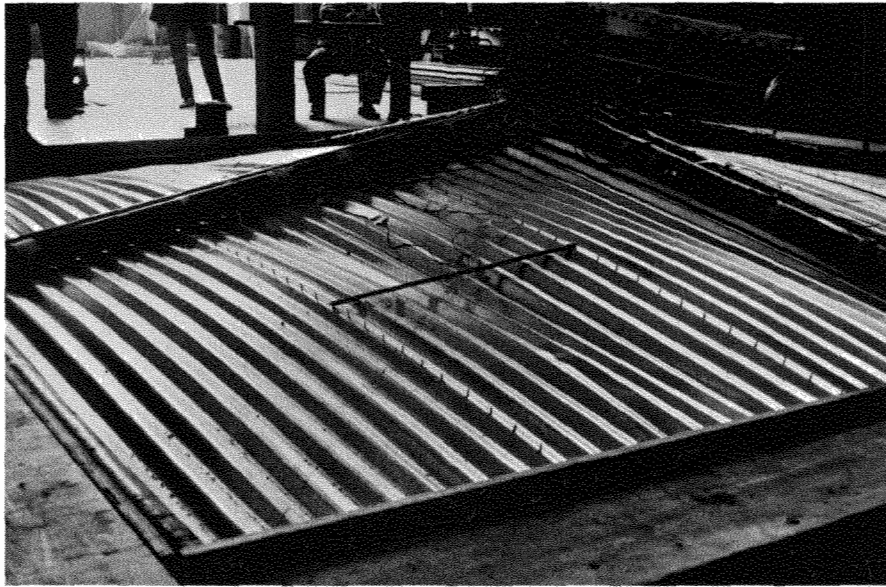
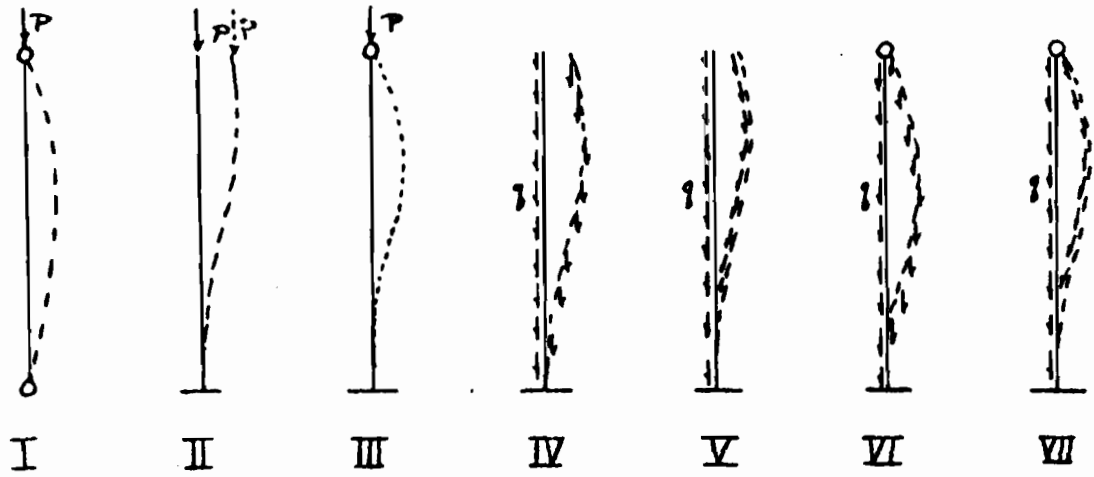


Figure 6.14 Photo of buckled hypar deck (Test No. 11).



<u>Case</u>	<u>Equation</u>	<u>k</u>
I	$P_{cr} = \pi^2 EI / (kl)^2$	1.0
II	$P_{cr} = \pi^2 EI / (kl)^2$	2.0
III	$P_{cr} = \pi^2 EI / (kl)^2$	0.699
IV	$(q1)_{cr} = \pi^2 EI / (kl)^2$	1.122
V	$(q1)_{cr} = \pi^2 EI / (kl)^2$	0.492
VI	$(q1)_{cr} = \pi^2 EI / (kl)^2$	0.436
VII	$(q1)_{cr} = \pi^2 EI / (kl)^2$	0.284

Fig. 6-13 Follower Force Buckling of Isolated Edge Members

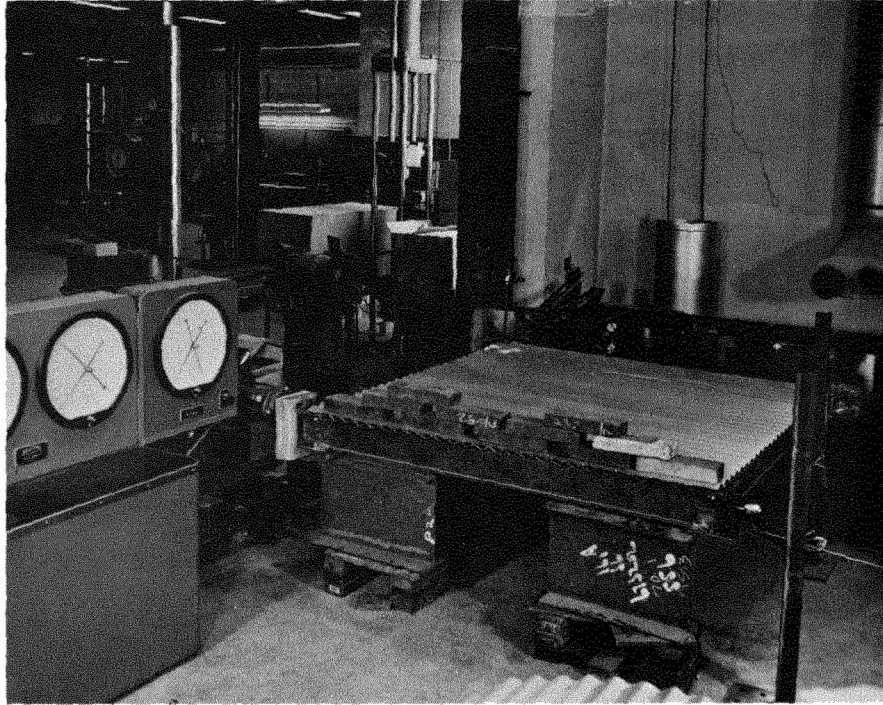


Figure 7.1 Flat shear test

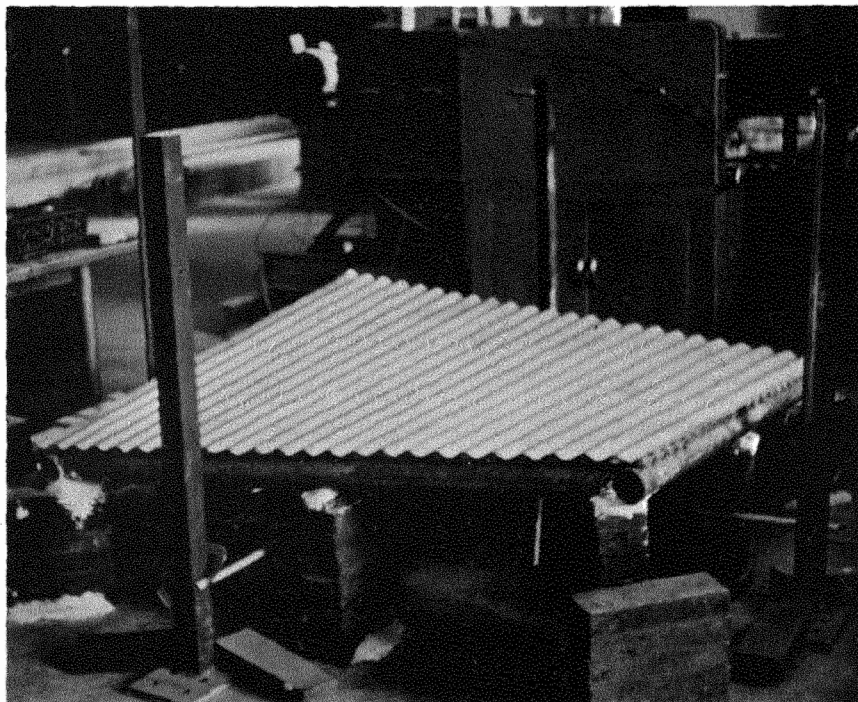


Figure 7.2 Saddle shaped hypar test no. 821

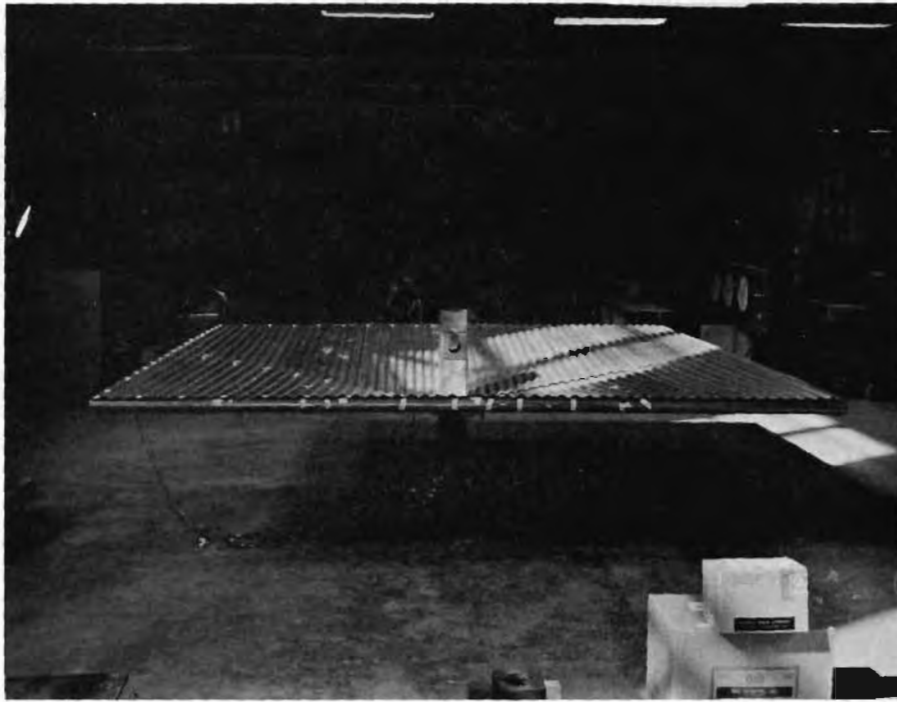


Figure 7.3(a) Umbrella Shell No. 11

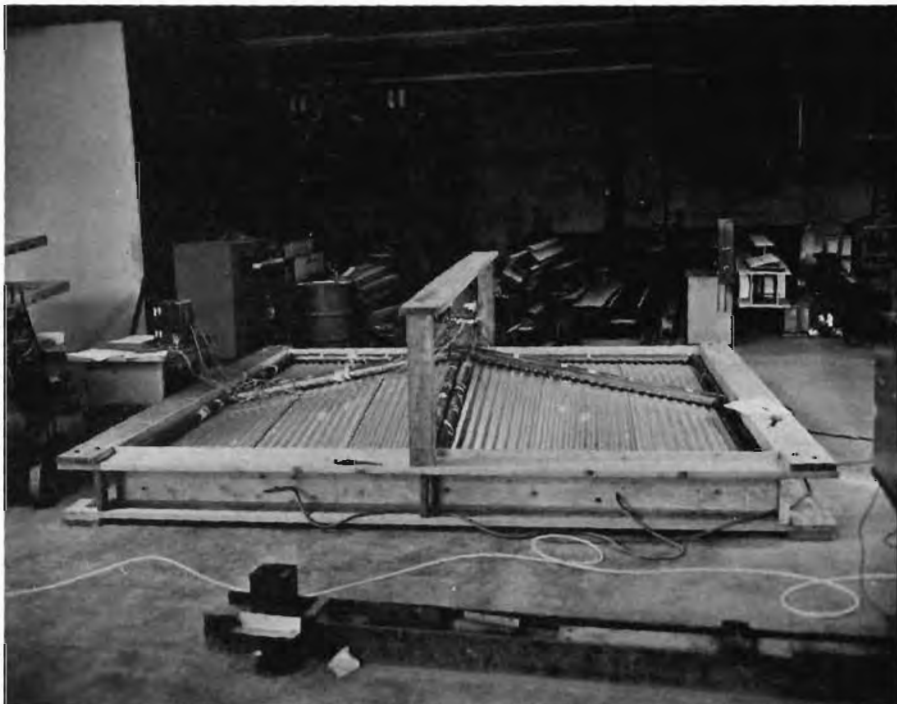


Figure 7.3(b) Test No. 11 in inverted position



Figure 7.4 Small-scale test

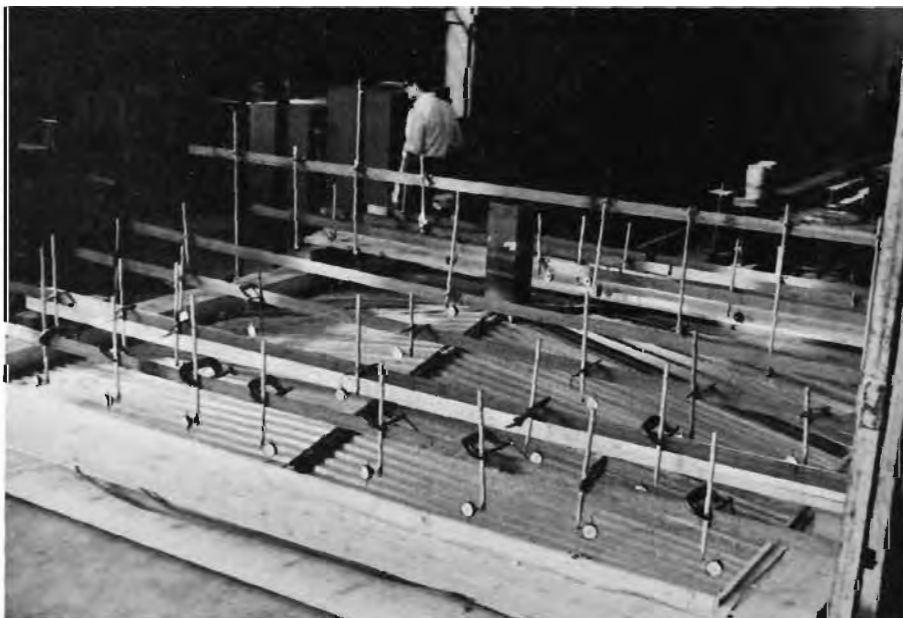
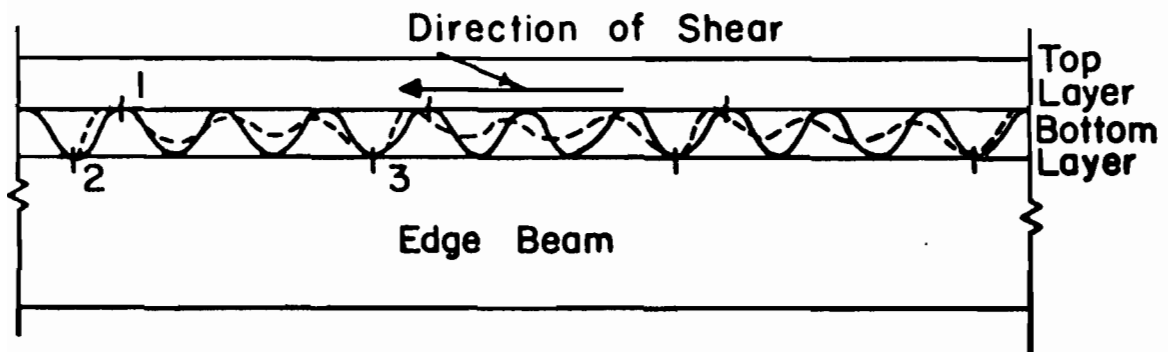
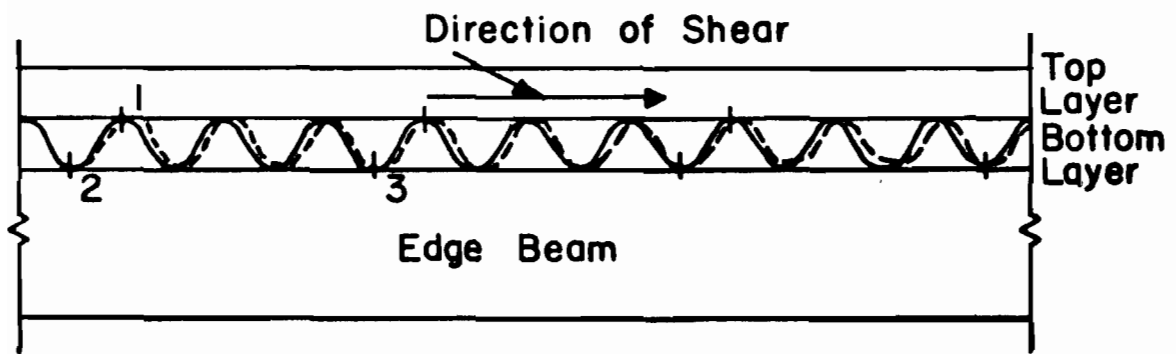


Figure 7.5 Test No. 9 in inverted position



(a) Local Compression - Large Distortion



(b) Local Tension - Tearing

Figure 7.6 Effect of Position of Screws

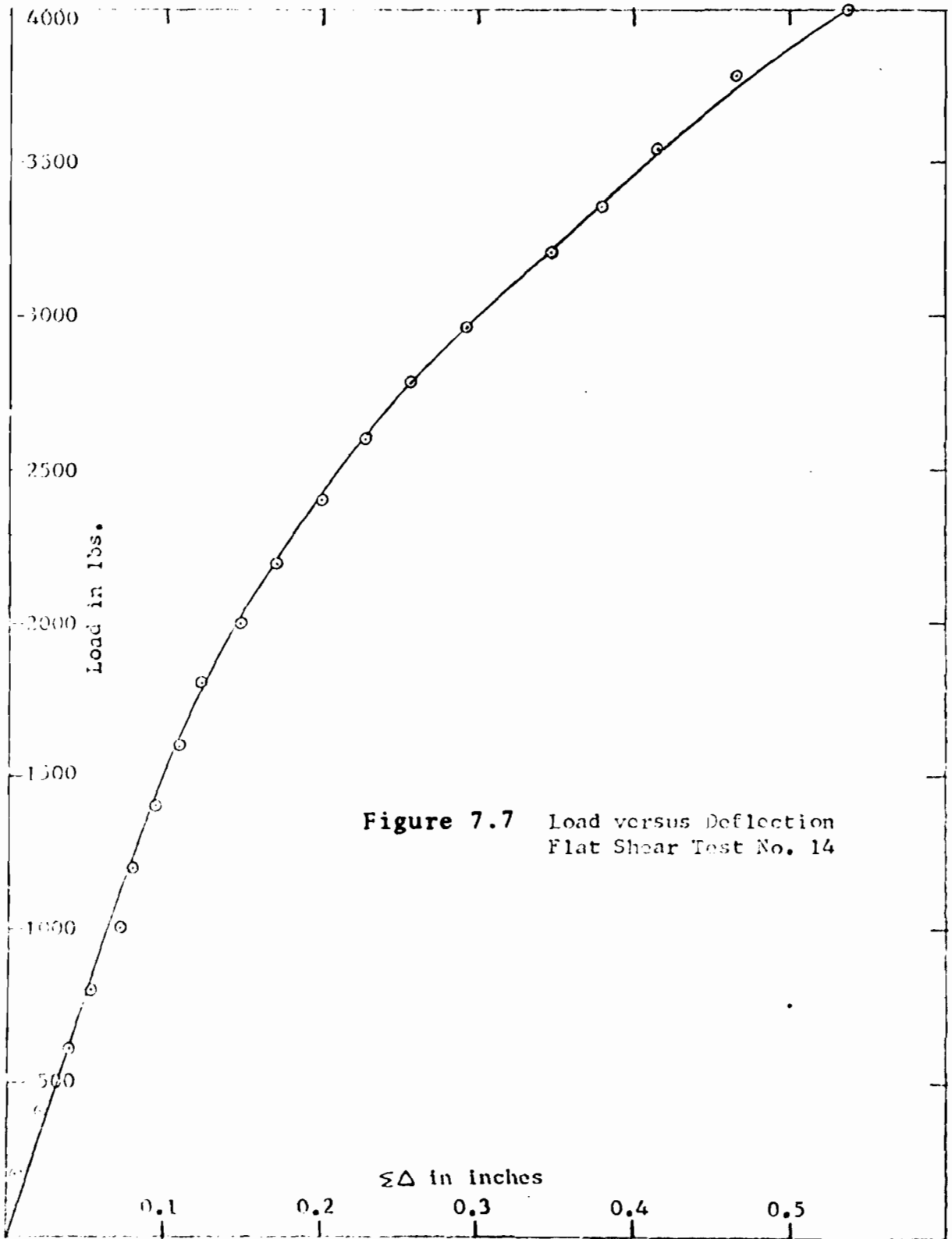
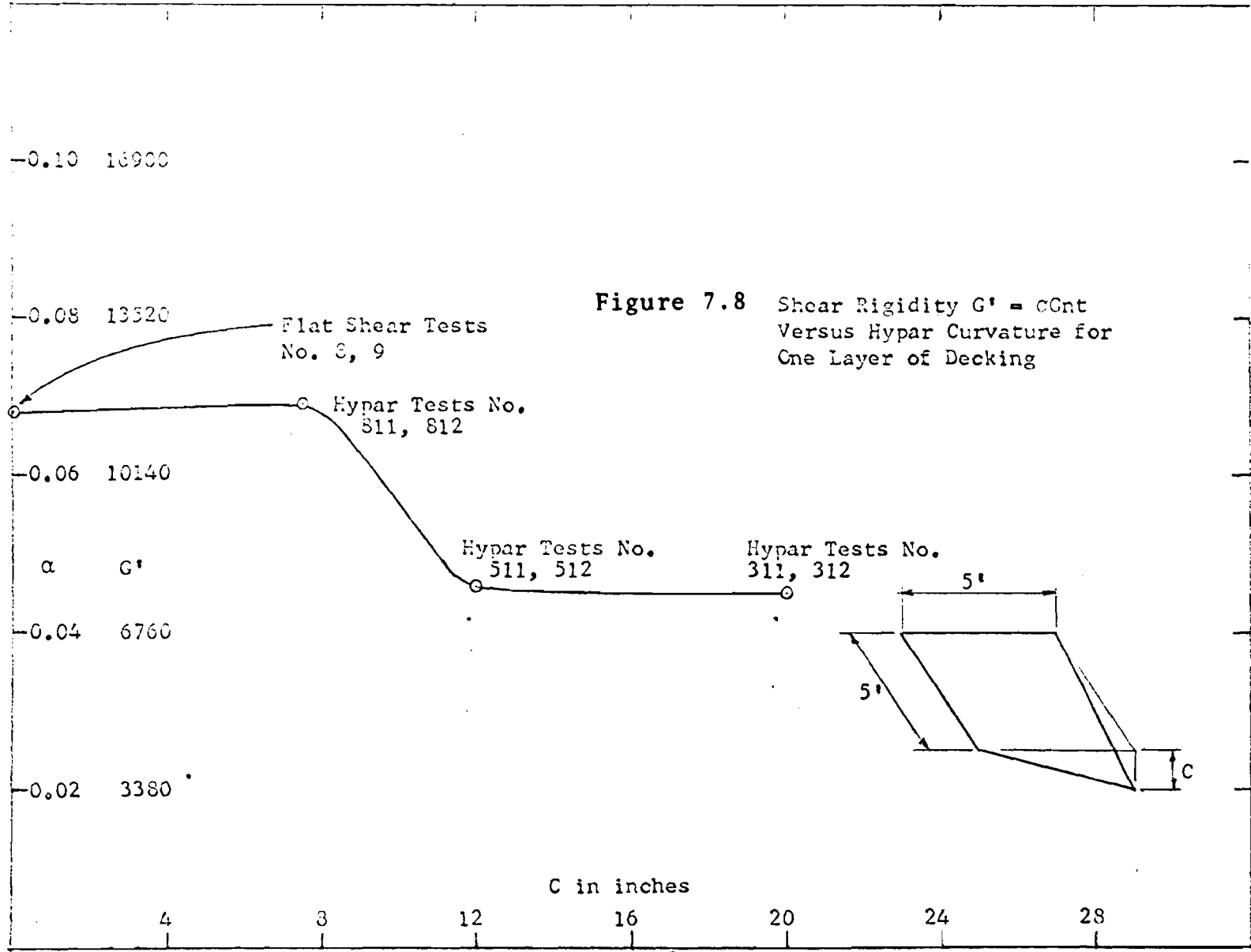
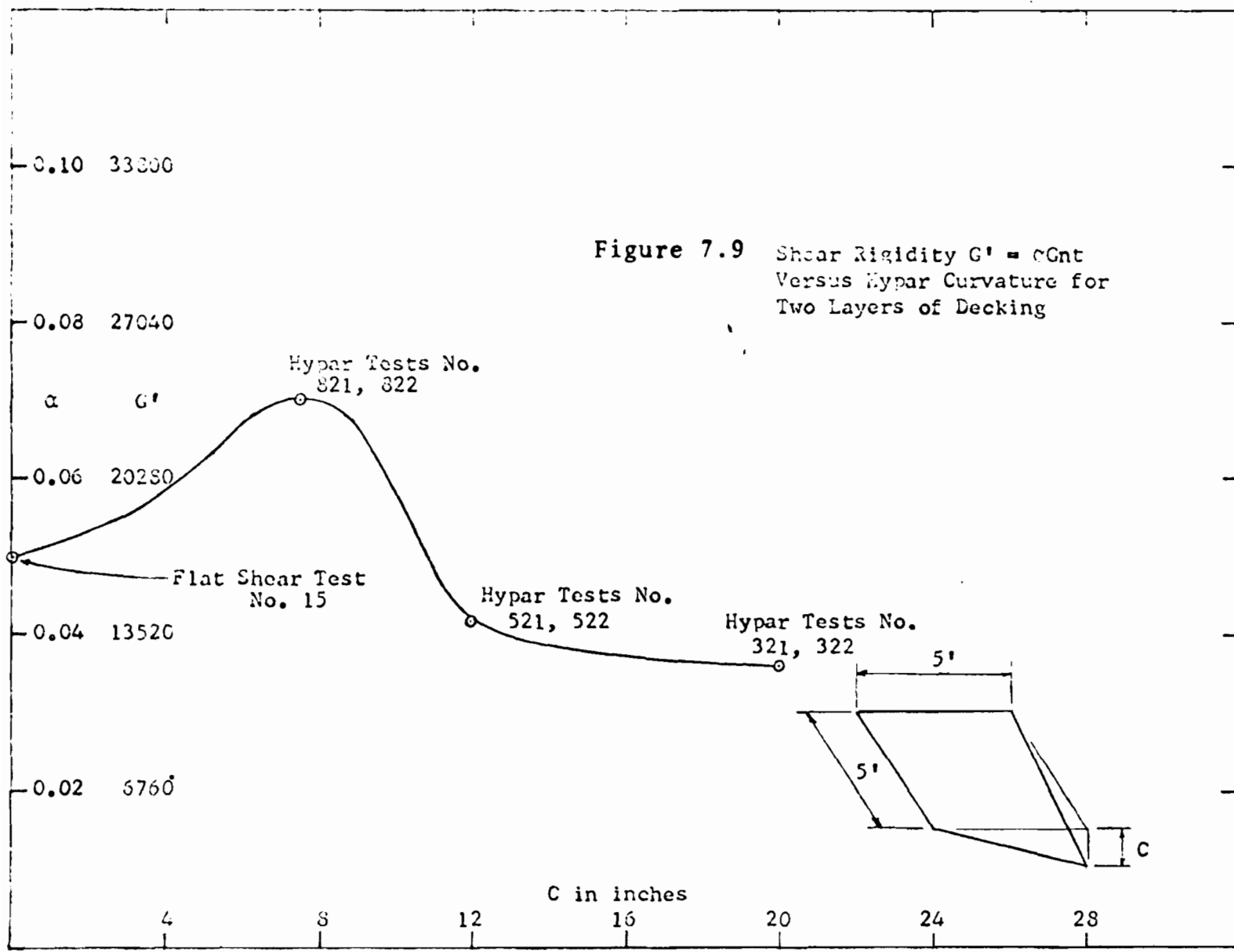


Figure 7.7 Load versus Deflection
Flat Shear Test No. 14





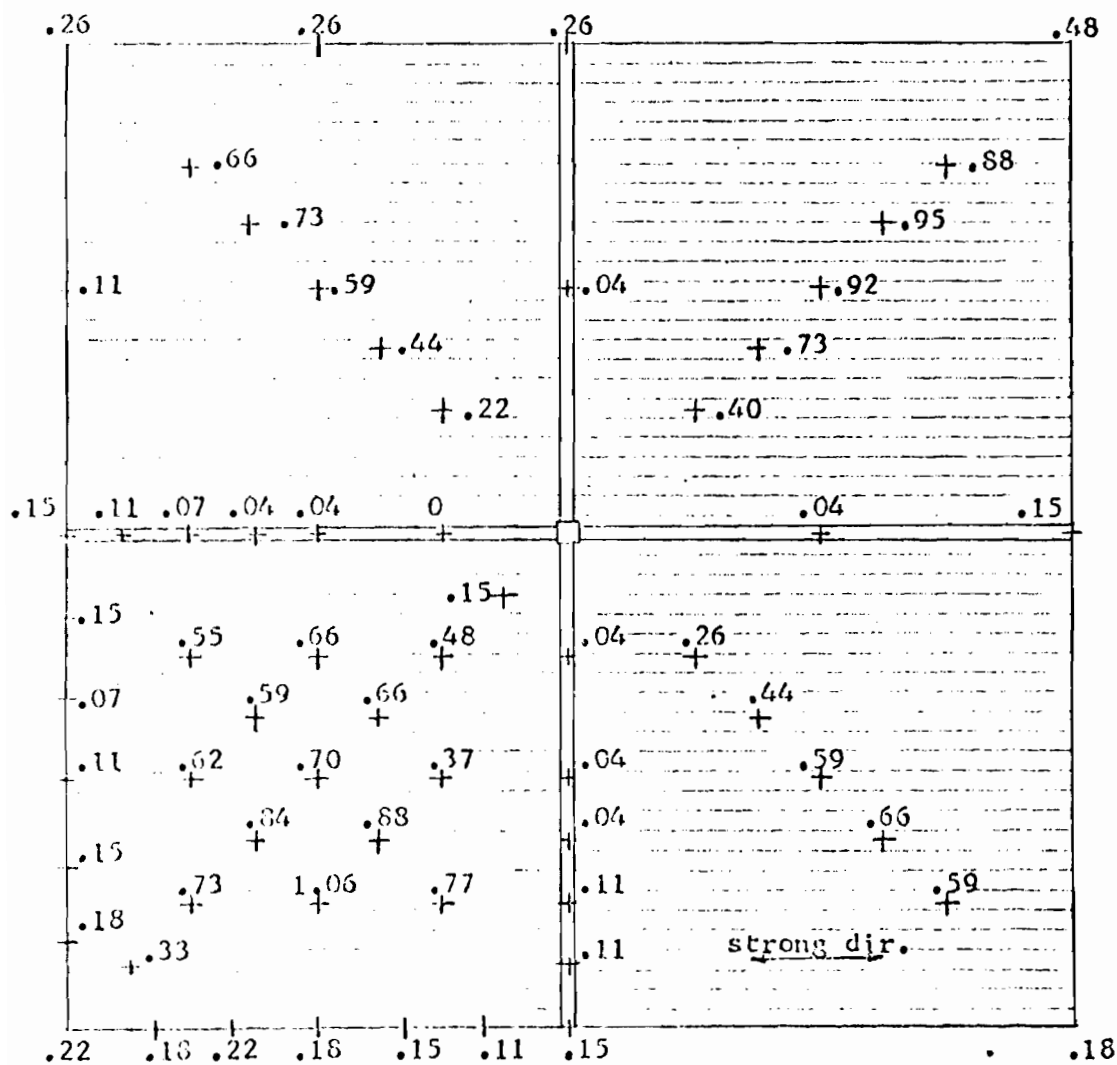


Figure 7.10(a) Experimental Vertical Deflections in inches at 40 psf, Umbrella Test No. 11

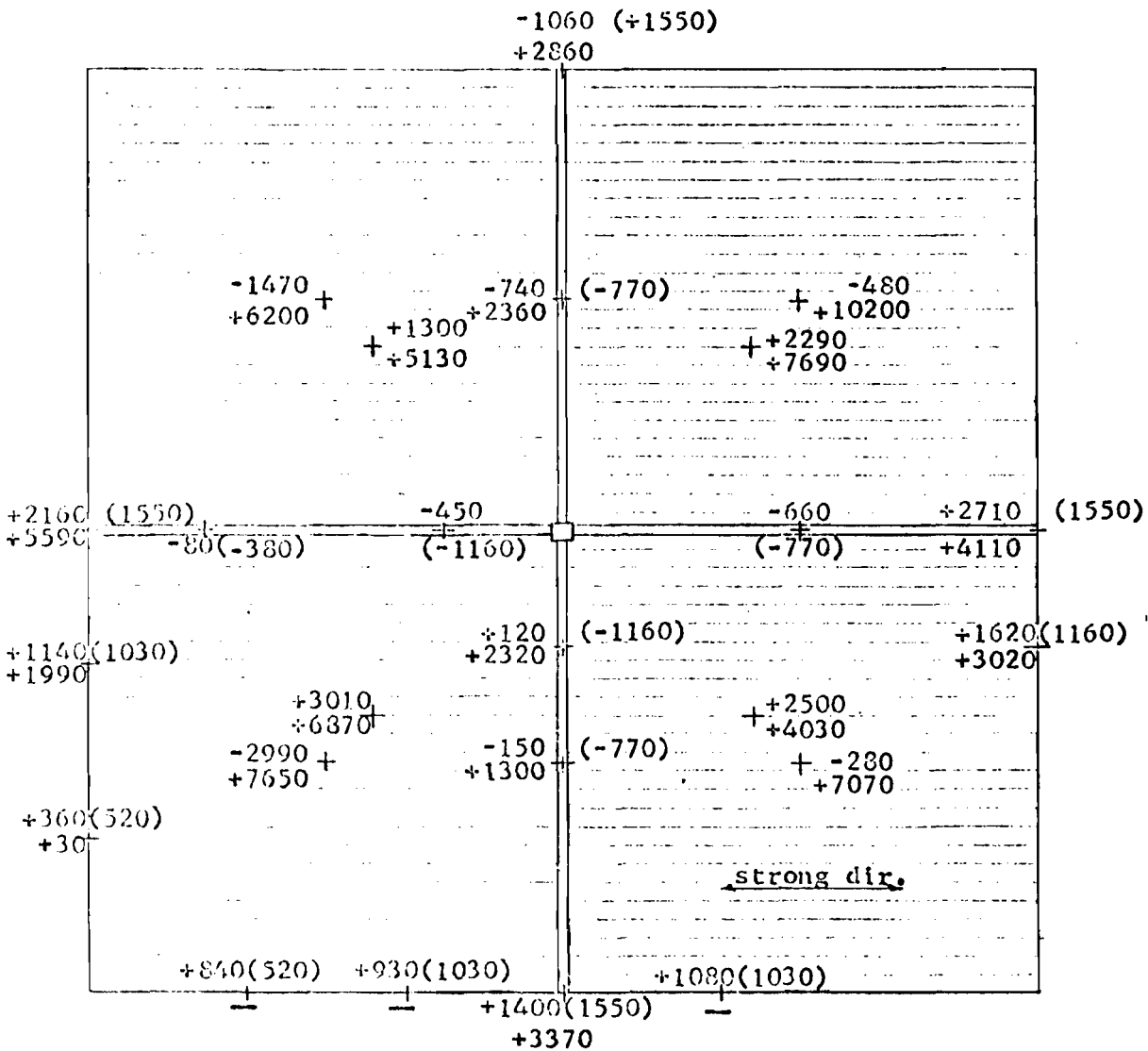


Figure 7.10(b) Experimental Stresses in psi at 40 psf Load for Umbrella Test No. 11

Axial stresses are directly above bending. Values in () are axial stresses from membrane theory.

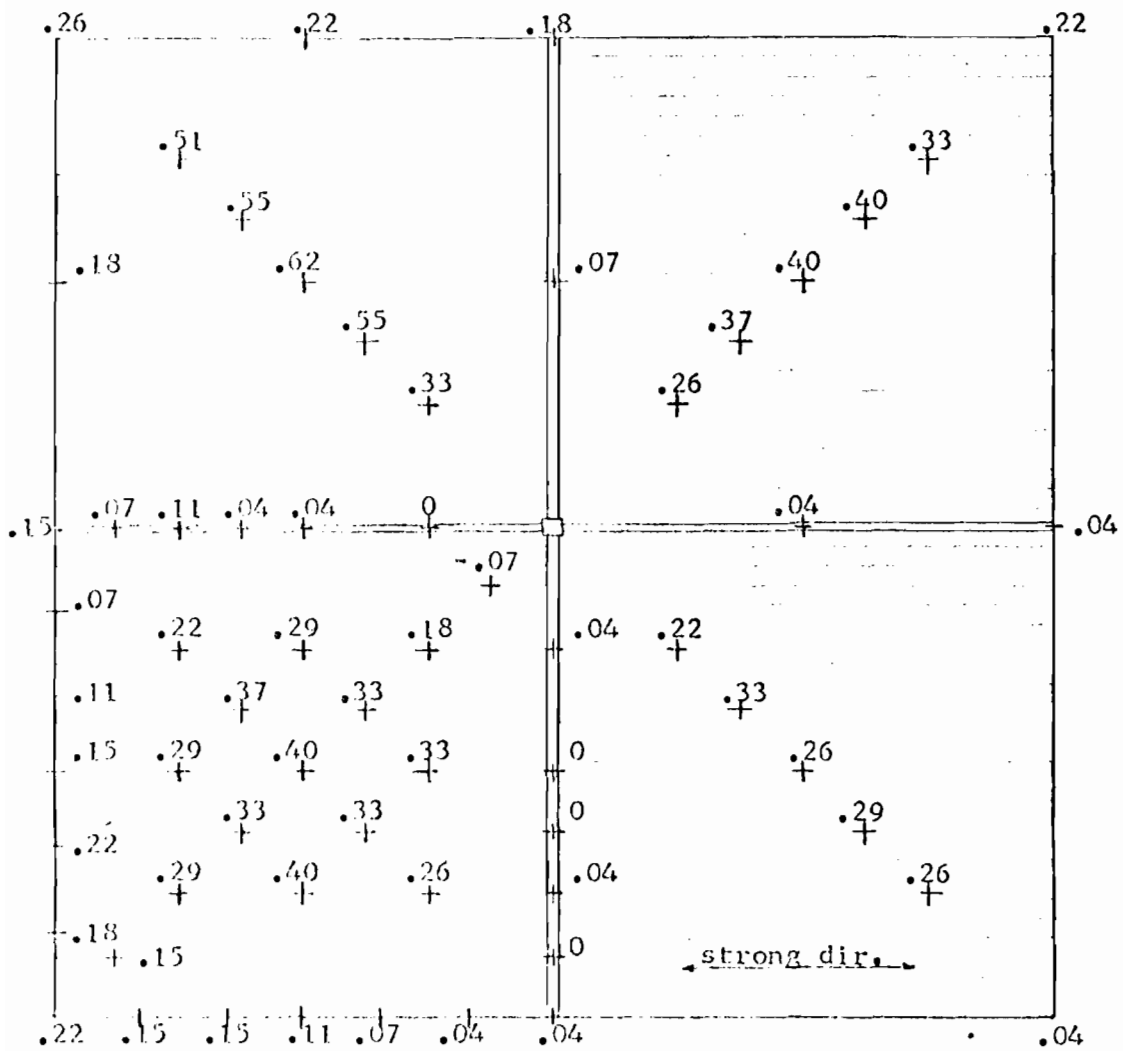


Figure 7.11(a) Experimental Vertical Deflections in inches at 40 psf, Umbrella Test No. 12

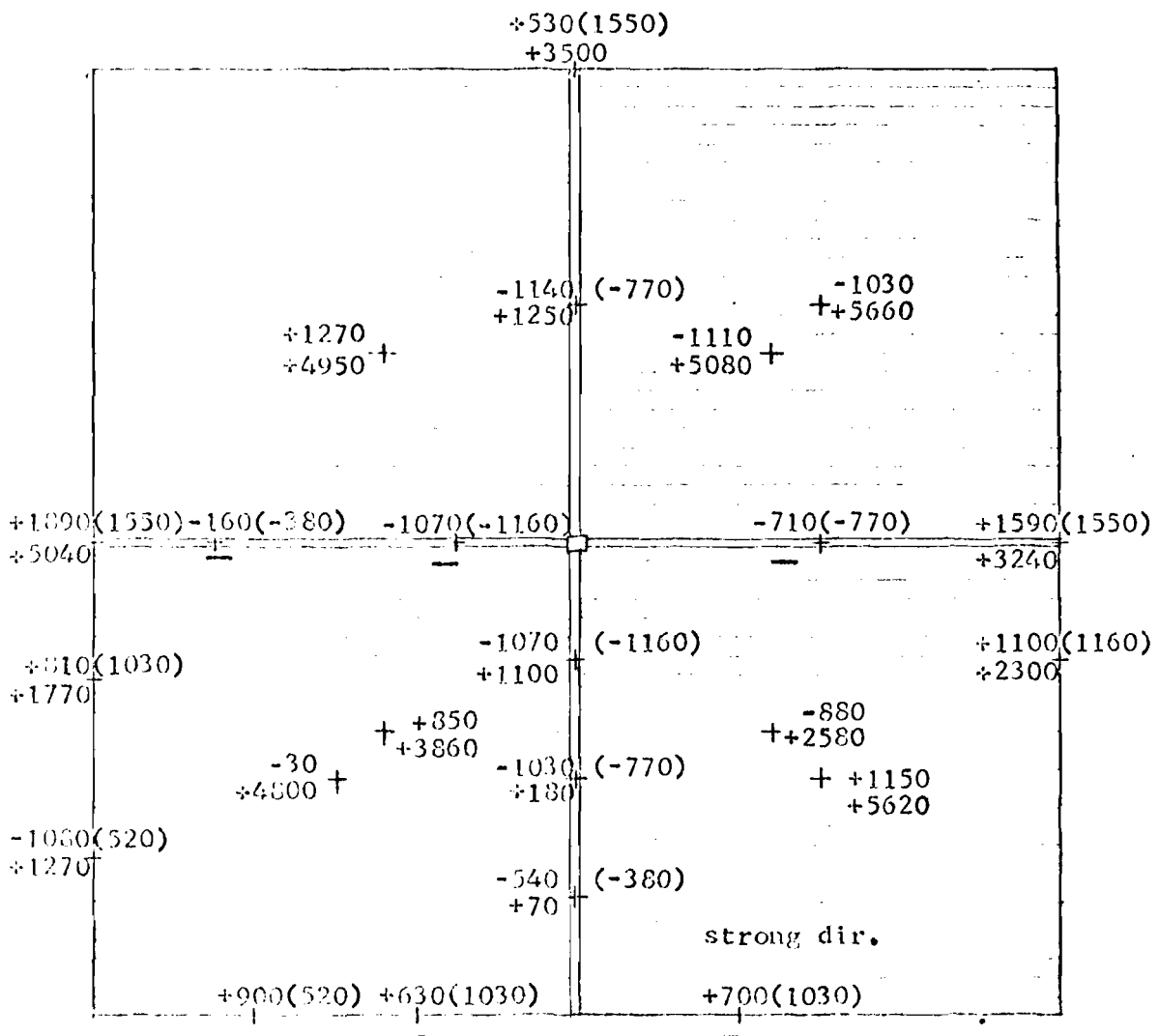


Figure 7.11(b) Experimental stresses in psi at 40 psf Load for Umbrella Test No. 12

Axial stresses are directly above bending stresses. Values in () are axial stresses from membrane theory.

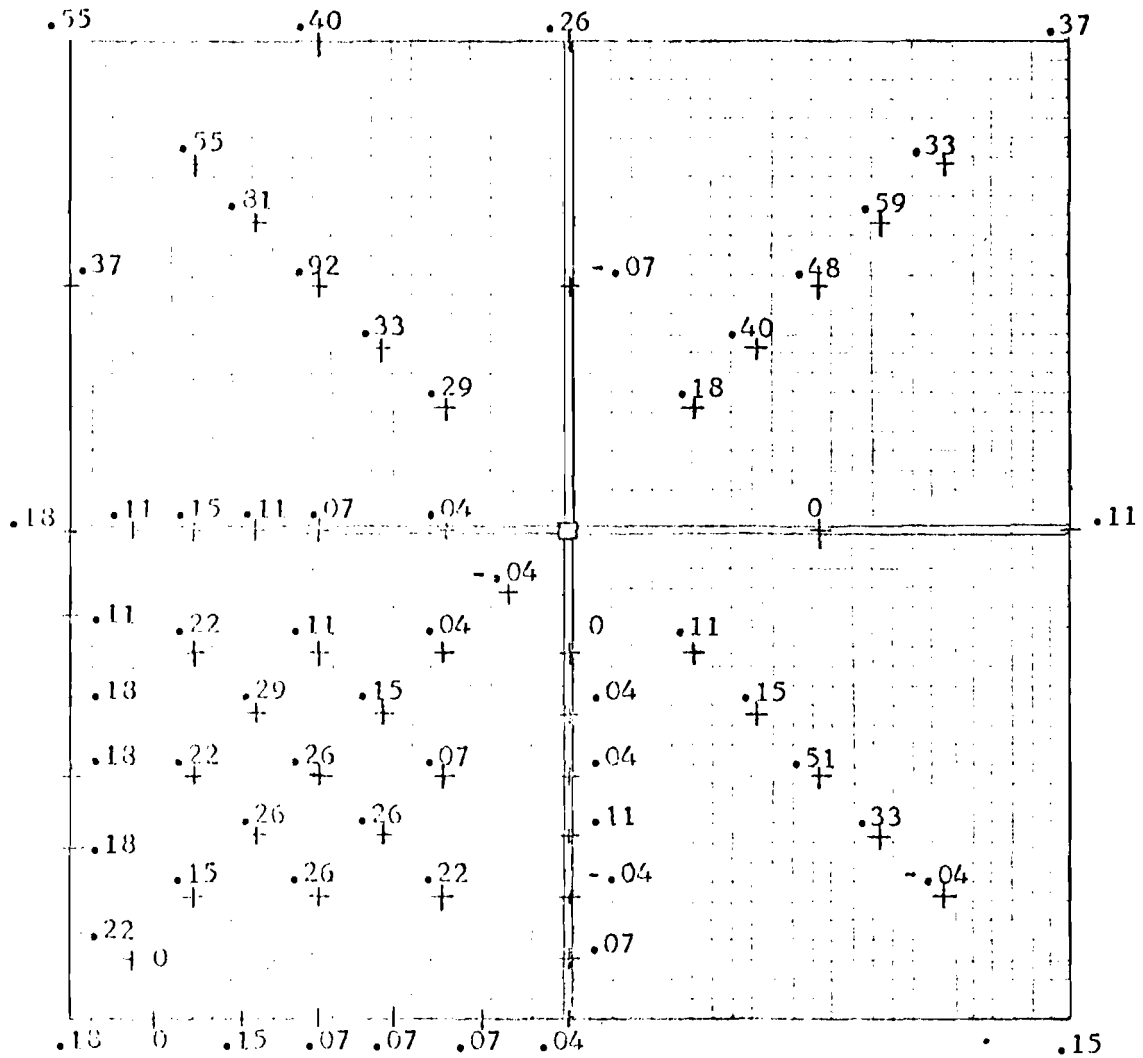


Figure 7.12(a) Experimental Vertical Deflections in inches at 40 psf, Umbrella Test No. 13.

Axial stresses are directly above bending stresses.
 Values in () are axial stresses from membrane theory.

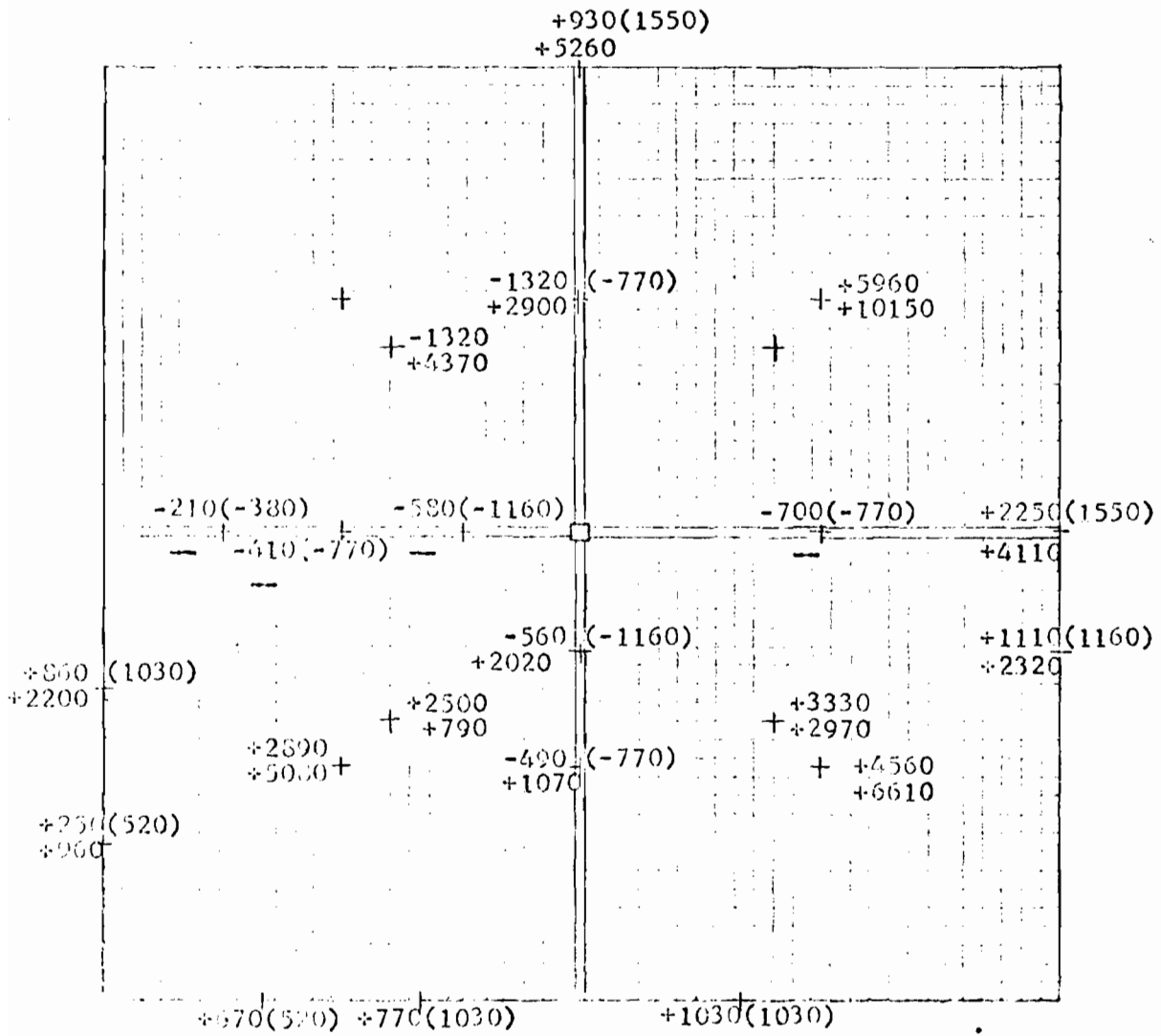


Figure 7.12(b) Experimental Stresses in psi at 40 psf Load for Umbrella Test No. 13.

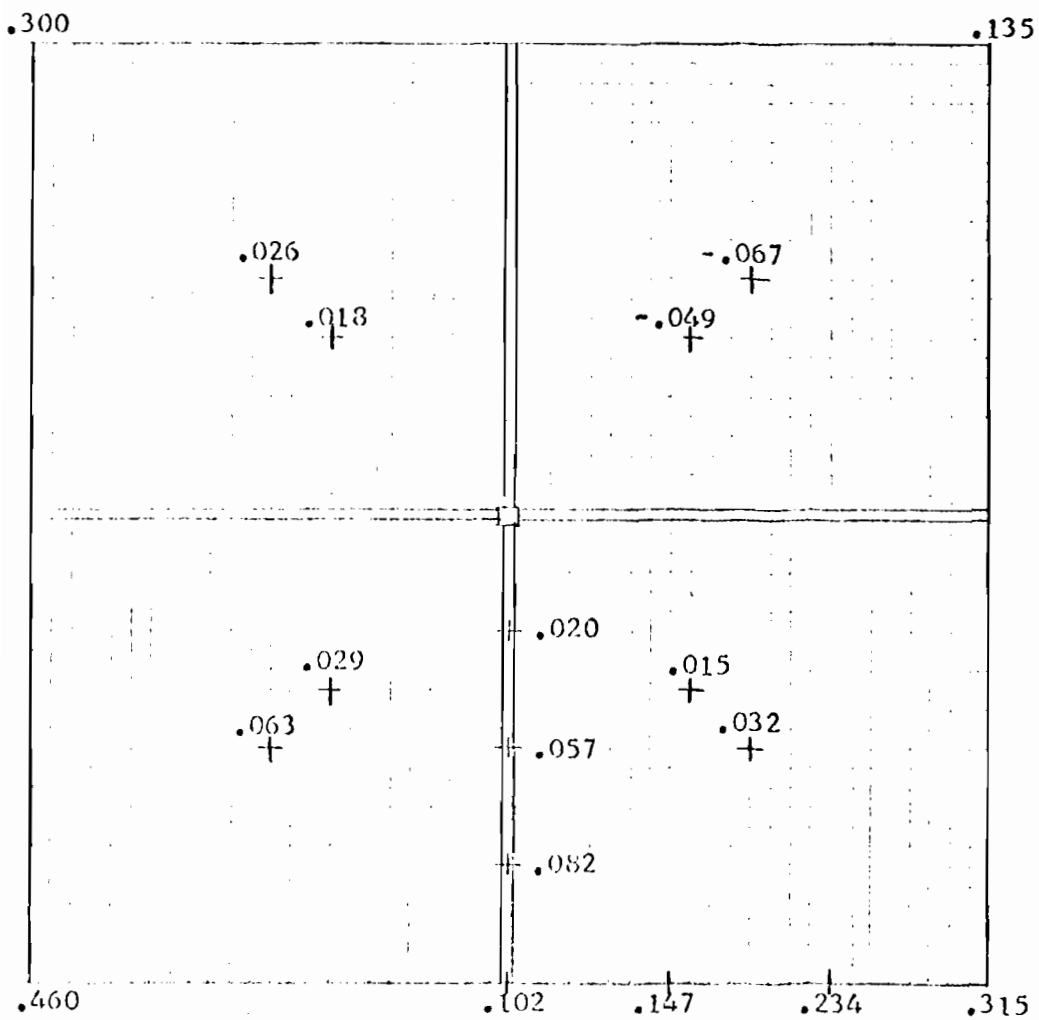


Figure 7.13 Experimental Vertical Deflections in inches at 40 psf, 2 ft x 2 ft x 0.25 ft, Umbrella Test (Section VII.1d).

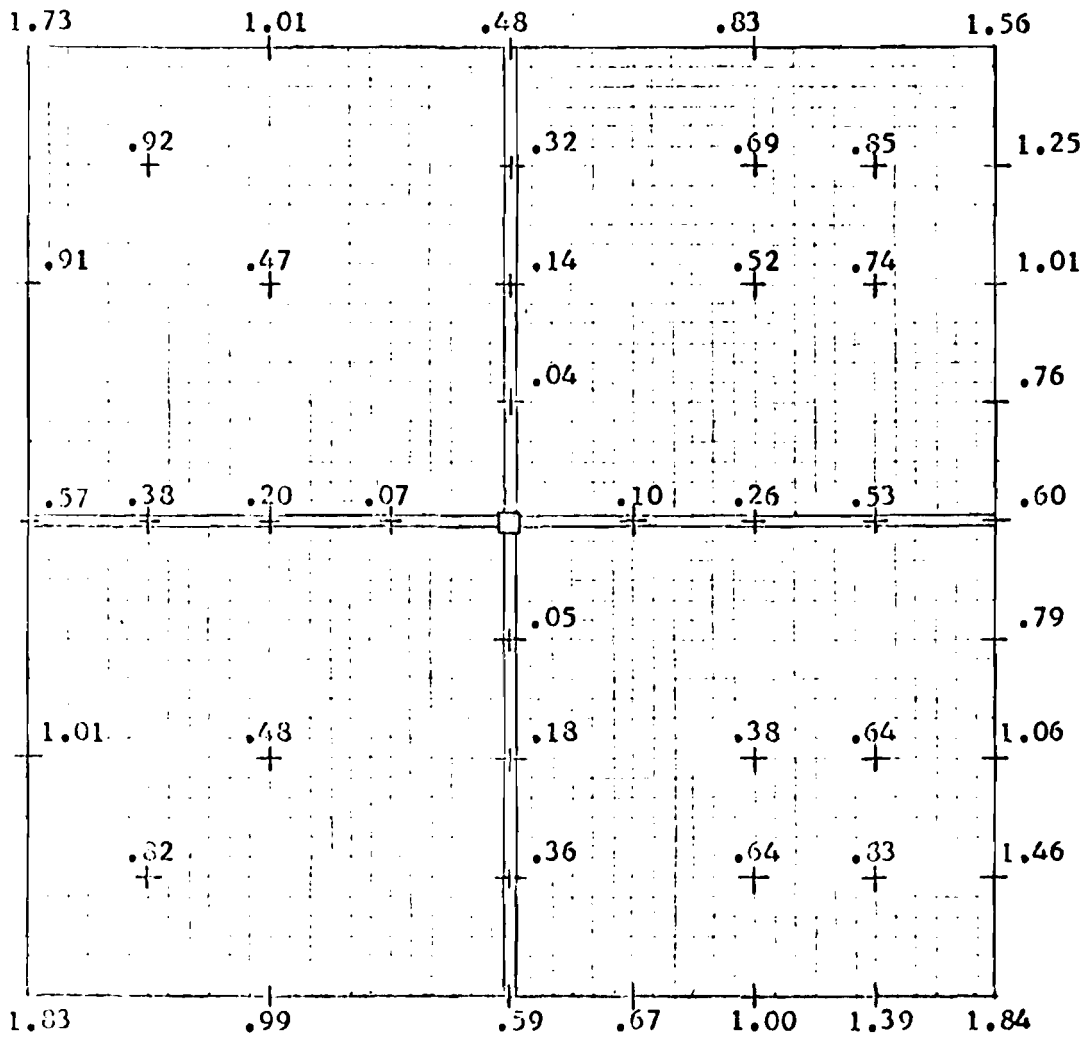


Figure 7.14(a) Experimental Vertical Deflections in inches at 40 psf, Umbrella Test No. 9.

Axial stresses are directly above bending stresses.
Deck stresses in bottom layer are to the left of those
in top layer.

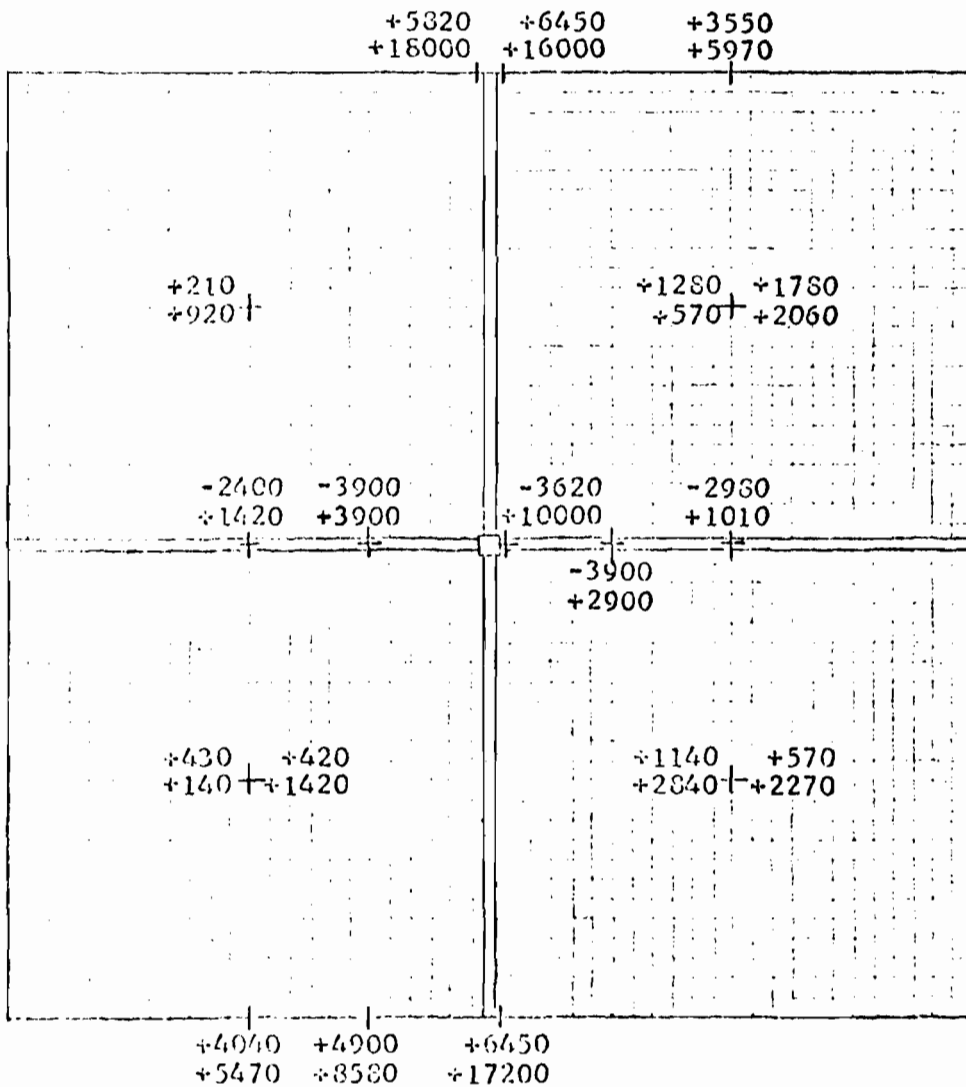


Figure 7.14(b) Experimental Stresses in psi at 40 psf, Umbrella Test No. 9.